Università degli Studi di Cagliari

DOTTORATO DI RICERCA
In Scienze e Tecnologie Chimiche

Ciclo XXIX

TITOLO TESI

Green Synthesis Approach to Coordination Polymers by Mechanochemistry

Settore scientifico disciplinari di afferenza

CHIM/03

Presentata da: Valentina Cabras

Coordinatore Dottorato Prof. Stefano Enzo

Tutor Prof. Mariano Casu
Prof. Guido Ennas

Esame finale anno accademico 2015 – 2016
Tesi discussa nella sessione d'esame marzo – aprile 2017

Università degli Studi di Cagliari

Università degli Studi di Sassari

DOTTORATO DI RICERCA
In Scienze e Tecnologie Chimiche

Ciclo XXIX

TITOLO TESI

Green Synthesis Approach to Coordination Polymers by Mechanochemistry

Settore scientifico disciplinari di afferenza

CHIM/03

Presentata da: Valentina Cabras

Coordinatore Dottorato Prof. Stefano Enzo

Tutor Prof. Mariano Casu
Prof. Guido Ennas

Esame finale anno accademico 2015 – 2016
Tesi discussa nella sessione d'esame marzo – aprile 2017

Acknowledgements

In the first place, my sincere gratitude goes to my supervisor Prof. Guido Ennas for his immense support and for helpful advice during these three years.

Also, I would like to express my thanks to Dr. Alessandra Scano and Dr. Martina Pilloni for being the best colleague and friends anyone could ever hope to work with.

Further to this, I wish to thank two research groups of the University of Cagliari headed by Prof. M.C Aragoni and Prof. Ferino for the precious collaboration. I wish also to thank CRS4 for assistance in SEM measurements, Prof. Simon Coles from the National Crystallography Service, University of Southampton and Sartec-Saras research and technology.

My sincere gratitude goes to Prof. Neil Champness who has been my supervisor during the six months I spent in the Department of Chemistry, University of Nottingham. I also take the opportunity to thank the nice people who work in lab B52 and in particular a great thank you goes to Harry for the immense help.

I would like to thank Dr. Montis and Dr. Bettoschi for their precious advice and a special thank goes to Prof. Caltagirone for her encouragement during these last months.

I also wish to thank all my friends and other PhD students at the Chemistry Department of Cagliari, an in particulary Arianna, Romina, Nicola, Federico e Viola. You are the best colleagues I could wish for.

I want to thank all my family for their encouragement and immense patience.

The present Ph.D. thesis is based on my three-years research at the University of Cagliari (Italy). It is submitted as a requirement for obtaining the Ph.D. degree with the further certificate of Doctor Europaeus. The whole research has been financed by Sardinia Regional Government (P.O.R. Sardegna F.S.E. Operational Programme of the Autonomous Region of Sardinia, European Social Fund 2007-2013 - Axis IV Human Resources, Objective l.3, Line of Activity l.3.1.).

“La presente tesi è stata prodotta durante la frequenza del corso di dottorato in Scienze e Tecnologie Chimiche dell’Università degli Studi di Cagliari, a.a. 2015 /2016- XXIX ciclo, con il sostegno di una borsa di studio finanziata dall’Università degli Studi di Sassari con le risorse del P.O.R. SARDEGNA F.S.E. 2007-2013 - Obiettivo competitività regionale e occupazione, Asse IV Capitale umano, Linea di Attività l.3.1 “Finanziamento di corsi di dottorato finalizzati alla formazione di capitale umano altamente specializzato, in particolare per i settori dell’ICT, delle nanotecnologie e delle biotecnologie, dell'energia e dello sviluppo sostenibile, dell'agroalimentare e dei materiali tradizionali”.

Valentina Cabras

Table of Contents

List of tables and schemes

List of Figures

List of abbreviations

1	bis(O-ethyldithiophosphato)Ni(II**)**
2	bis(O-methyldithiophosphato)Ni(II)
3	trans-bis[O-ethyl-(4-methoxyphenyl)dithiophosphonato]Ni(II)
4	trans-bis[O-methyl(4methoxyphenyl)dithiophosphonato]Ni(II)
acac	Acetylacetonate anion
AcOH	Acetic acid
4,4'bipy	4,4'-bipyridine
bpe	bis(pyridyn-4yl)-1,2-ethene
BTB	4,4′,4″-benzene-1,3,5-triyltribenzoic acid
BPTA	N,N' -bis(4-pyridinyl)-1,4-benzenedicarboxamide
btc/BTC	1,3,5-benzenetricarboxylate anion
$CHCl_3$	Chloroform
CH_2Cl_2	Dichlorometane
Conventional synthesis	Solution-based synthesis
dabco	[2.2.2]diazabicyclooctane
DBNDI	N,N′-Bis(4-nitrobenzene)1,4,5,8naphthalenetetracarboxydiimide
dace	1,4-diaminocyclohexane
DEF	N,N-diethylformamide
4,6-DMDBT	dimethyldibenzothiophene
DMF	N,N-dimethylformamide
DMSO	S,S-dimethylsulfoxide
DPNDI	N, N'-di(4-pyridyl)-1,4,5,8-naphthalenediimide
DPMNI	N,N'-di(4-pyridyl-methyl)-1,4,5,8naphthalenetetracarboxydiimide
DSC	Diffencial Scanning Calorimetry
EtOH	Ethanol
FTIR	Fourier transform infrared spectroscopy
Fum	fumarate anion
H_3btc	1,3,5-benzenetricarboxylic acid (trimesic acid)
HCNacac	3-cyanoacetylacetone
Hfum	fumaric acid
Him	imidazole
HMeIm	2-methylimidazole
HEtIm	2-ethylimidazole
Hina	isonicotinic acid
Ina	isonicotinate anion
LAG	Liquid assisted grinding

L1	4,4'- bipyridine
L2	1,4-bis(3-pyridyl)-butadiyne
L3	2,5-bis(4-pyridyl)-4-thia-1,3-thiazolidine
L4	2,5-bis(3-pyridyl)-4-thia-1,3-thiazolidine
L-asp	L-aspartate
MeOH	Methanol
MIL	Matérial Institut Lavoisier
mp	Melting points
NDA	Naphthalene-1,4,5,8-tetracarboxylic dianhydride
NDI	naphthalene diimide
NG	Neat grinding
NMP	N-methylpyrrolidine
ox	oxalate
pyz	pyrazine
SEM	scanning electron microscopy
TG	Thermogravimetry
TMAOH	tetramethylammonium
tpt	2,4,6-tris(4-pyridyl)-1,3,5-triazine
UMCs	coordinatively unsaturated metal centers
XRD	X-ray diffraction
XRPD	X -ray Powder Diffraction
(1·L1)$_\infty$.	[((EtO)$_2$PS$_2$)$_2$Ni·(4,4'-bipyridine)]$_\infty$
(2·L1)$_\infty$.	[((MeO)$_2$PS$_2$)$_2$Ni·(4,4'-bipyridine)]$_\infty$
(3·L1)$_\infty$.	[(MeO-C$_6$H$_4$)(EtO))PS$_2$)$_2$Ni·(4,4'-bipyridine)]$_\infty$
(4·L1)$_\infty$.	[(MeO-C$_6$H$_4$)(MeO))PS$_2$)$_2$Ni·(4,4'-bipyridine)]$_\infty$
(1·L2)$_\infty$.	[((EtO)$_2$PS$_2$)$_2$Ni·(1,4 bis (3-pyridyl)butadiyne)]$_\infty$
(2·L2)$_\infty$.	[((MeO)$_2$PS$_2$)$_2$Ni·(1,4 bis (3-pyridyl)butadiyne)]$_\infty$
(3·L2)$_\infty$.	[(MeO-C$_6$H$_4$)(EtO))PS$_2$)$_2$Ni·(1,4 bis (3-pyridyl)butadiyne)]$_\infty$
(4·L2)$_\infty$.	[(MeO-C$_6$H$_4$)(MeO))PS$_2$)$_2$Ni·(1,4 bis (3-pyridyl)butadiyne)]$_\infty$
(2·L3)$_\infty$.	[((MeO)$_2$PS$_2$)$_2$Ni·(2,5-bis(4-pyridyl)-4-thia-1,3-thiazolidine)]$_\infty$
(4·L3)$_\infty$.	[(MeO-C$_6$H$_4$)(EtO))PS$_2$)$_2$Ni·(2,5-bis(4-pyridyl)-4-thia-1,3-thiazolidine)]$_\infty$
(1·L4)$_2$.	[((EtO)$_2$PS$_2$)$_2$Ni·(2,5-bis(3-pyridyl)-4-thia-1,3-thiazolidine]$_2$
(3·L4)$_\infty$.	[(MeO-C$_6$H$_4$)(MeO))PS$_2$)$_2$Ni·(2,5-bis(3-pyridyl)-4-thia-1,3-thiazolidine]$_2$
RT	Room Temperature

Abstract

The field of Metal-Organic Frameworks, also known with the abbreviation MOFs, has been subjected to an accelerated growth in the last 15 years. The process of mixing quickly available metal precursors with organic ligands—many of which are commercially available—to produce a wide range of frameworks, is capturing the interest of chemists and materials scientists worldwide.

There is an important link between MOF chemistry and fields of inorganic and coordination chemistry, there is also a conceptual link into the field of materials chemistry that has evolved applications ranging from catalysis to energy storage. Organic chemistry is also able to contribute to the MOFs design by the synthesis of new ligands with the aim of giving different properties to the MOF wall. X-ray crystallography and solid-state chemistry provide information about the structures of MOFs so that the process of designing and synthesizing MOFs can be refined to control a targeted property of those frameworks.

My PhD thesis aims to explore, especially from the point of view of synthetic and structural, morphological, thermal and textural characterizations, the chemistry of such materials. Starting from an general overview of MOFs chemistry: design and applications, the IUPAC classification of coordination polymers (CPs), networks, and metal-organic frameworks (Chapter 1), continuing with a discussion of the most common methods of synthesis and focusing mainly on Mechanochemical synthesis (Chapter 2) which is a powerful method for environmentally-friendly strategy of CPs and MOFs synthesis. Followed by the experimental section, divided in four parts: Chapter 3 concerns the efficient mechanosynthesis of an iron(III) trimesate MOF and its usage for the adsorption of 4,6-dimethyldibenzothiophene (4,6-DMDBT) from a simulated low-sulfur diesel fuel. In Chapter 4, the structural, thermal and morphological properties of CPs based on unsatured Ni(II) dithiophosphato/ dithiophosphonato complexes and 4,4'-bipyridine as linker are outlined. Chapter 5 dials with an array study of reactivity under mechanochemical conditions of a set of CPs based on the same unsatured Ni(II) complexes with different topologies of polydentate ligands. The Chapter 6 is dedicated to the attempt to obtain thio-functionalized ligands for design, synthesis and future application in CP/ MOF architecture.

Chapter 1: Introduction

1 INTRODUCTION

1.1 Coordination Polymers and Metal-Organic Frameworks: IUPAC terminology guidelines

Coordination polymers (CPs) and metal–organic frameworks (MOFs) constitute an interdisciplinary field with its origins in solid state, inorganic and coordination chemistry that has expanded rapidly in the last two decades, and is also attracting the interest of the chemical industry and crystal engineering.[1]

The topic search using Sci-Finder Scholar for the term "coordination polymer or polymers" reveals that the term CP dates back to before the 1950s, while the term MOF dates to the late 1990s. From the statistics, one observes that the usage of the two terms has increased exponentially during the last decade along with the expansion of this new area of research.[2]

However, given the number of publications in this area and the potential application of those materials, the IUPAC division of Inorganic Chemistry has initiated a project on Coordination polymers and metal–organic frameworks: terminology and nomenclature guidelines.[3,4] A hierarchical terminology is recommended in which the most general term is coordination polymer. Coordination networks are a subset of coordination polymers and MOFs are a further subset of coordination networks. One of the criteria that a MOF needs is that it contains potential voids, but no physical measurements of porosity or other properties are demanded.

One of the preliminary terms in this terminology guidelines is the definition of coordination compound.

Coordination compound: *"A coordination compound is any compound that contains a coordination entity. A coordination entity is an ion or neutral molecule that is composed of a central atom, usually that of a metal, to which is attached a surrounding array of atoms or groups of atoms, each of which is called ligands."*[4]

In 1833, J. J. Berzelius was the first chemist to employ the term ‘‘polymer’’ to describe any compound that could be formulated as consisting of multiple units of a basic building block.[3]

The term ‘‘Coordination polymer’’ was first used by Y. Shibata in 1916 to describe dimers and trimers of various cobalt(II) ammine nitrates and has been in continuous use in the scientific literature since the 1950’s.[3]

The first (organic) polymer was proposed by H.Stauding in 1922. He discovered that the Bakelite, previously known as colloids, was in fact monomers held together with covalent bonds, to form what are now known as (organic) polymers.[3]

Furthermore, the IUPAC definition of the term “polymer” is more inclusive than the colloquial use it has among chemists and engineers. The current recommendations are as follows[5]:

Polymer: “*A substance composed of macromolecules.”*

Polyethylene, DNA and cellulose are common examples of polymers.

Polymer molecule (macromolecule): “ *A molecule of high relative molecular mass, the structure of which essentially comprises the multiple repetition of units derived, actually or conceptually, from molecules of low relative molecular mass.”*

A single chain of polyethylene is a “polymer molecule”, and that many individual polyethylene chains make up a polymer.

Coordination polymer: “*A coordination polymer is a coordination compound with repeating coordination entities extending in 1, 2, or 3 dimensions.”* [6]

Coordination polymers do not need to be crystalline; therefore, the more appropriate terms (for crystalline states) 1-periodic, 2-periodic, and 3-periodic cannot be used throughout. These compounds may in some cases, such as those being composed of mainly carboxylates, even be regarded as salts. The prefix 1D-, 2D-, or 3D- is acceptable for the indicating the degree of extension of the coordination polymer [6].

The (4,4'-bipyridine-*N*,*N*)-bridged cobalt(II) compound is a classical type of single-chain coordination polymer, Fig. 1.1. [7]

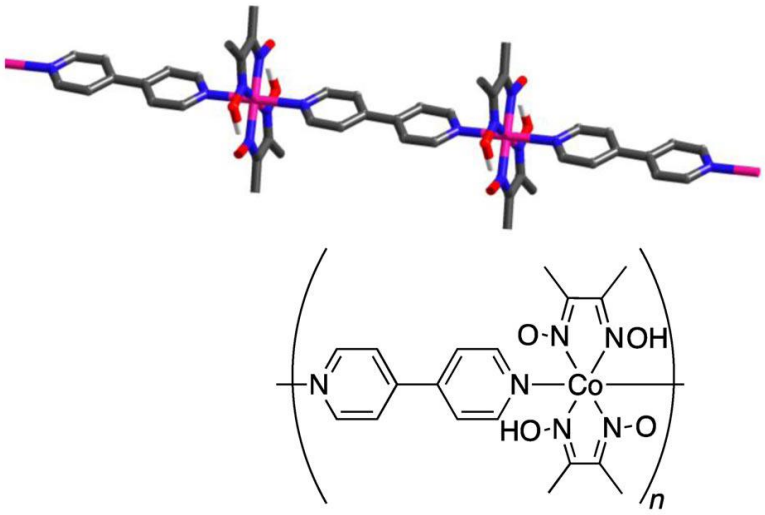

Figure1.1 An example of a 1D-coordination polymer. Hydrogen atoms on carbon have been left out for clarity. Mauve: Co; blue: N; red: O; grey: C; white: H. This picture is reproduced according to ref:7.

For coordination polymers it is reasonable to assume, and sometimes proven, that in solution, or indeed in a precrystalline state, if solid state synthesis is performed, there are polynuclear entities that without doubt can be called (polymer) macromolecules. These then crystalize or polymerize into the coordination polymer.

Coordination network: *" A coordination network is a coordination compound extending, through repeating coordination entities, in 1 dimension, but with cross-links between two or more individual chains, loops, or spiro-links, or a coordination compound extending through repeating coordination entities in 2 or 3 dimensions."* [6]

An example of cross-link coordination network is shown in Fig. 1.2. [8]

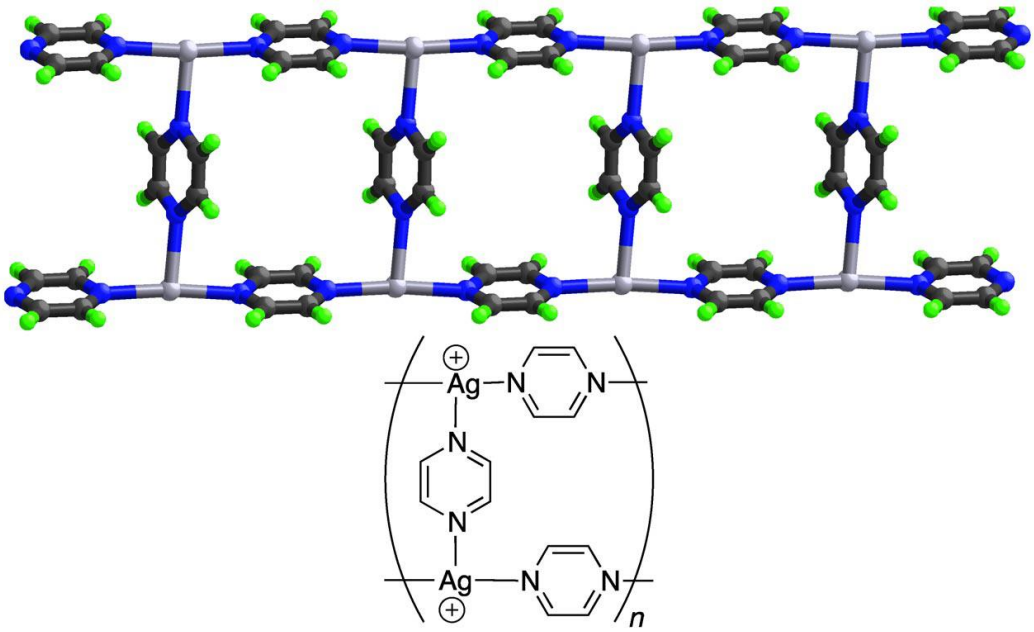

Figure 1.2. An example of cross-links coordination network, the weakly coordinating trifluoromethane-sulfonate anions are not shown. Light grey: Ag; blue: N; grey: C; green: H. This picture is reproduced according to ref: 8.

The terms "coordination network" and "coordination polymer" are not synonymous and coordination network is in fact a subset of coordination polymer.

Metal-organic framework: *"A metal–organic framework, abbreviated to MOF, is a coordination network with organic ligands containing potential voids*."[6]

In Fig. 1.3 are shown two archetypal MOFs: MOF-5 (from the Yaghi group) [9] and HKUST-1.[10]

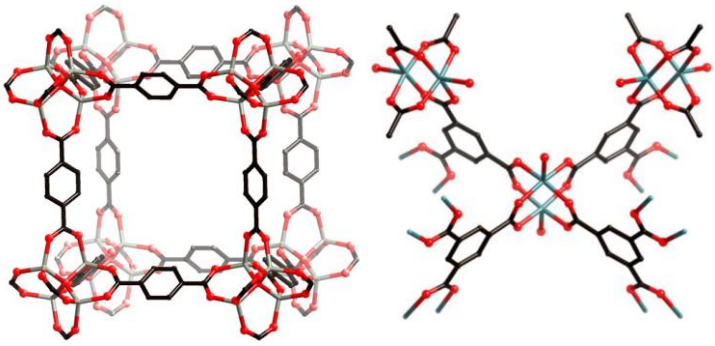

Figure 1.3. On the left is MOF-5 architecture, zinc and carboxylate-based where each [Zn4O] unit is bridged by six benzene-1,4-dicarboxylates.[9] On the right: HKUST-1architecture with copper(II) paddlewheel dimers bridged by benzene-1,3,5-tricarboxylates.[10] Hydrogen atoms are not shown. Light grey: Zn; turquoise: Cu; grey: C; red: O. This picture is reproduced according to ref: 10.

Many systems are dynamic and changes in structure, in potential porosity or solvent and/or guest filled voids may occur depending on temperature, pressure, or other external stimuli. For these reasons it is also not required that an MOF be crystalline.

IUPAC should not at the present time endorse any other terms in the area. The only term that is explicitly discouraged is "*hybrid organic–inorganic materials*" to describe MOFs. The appropriate use of the term in the context of MOFs needs to have the complete wording: "*chemically bonded hybrid inorganic–organic coordination polymer*". For the nomenclature of MOFs, the IUPAC commission agrees with the common practice of giving names based on their place of origin followed by a number.[6] Some examples are: MIL-101 (Matérial Institut Lavoisier) and HKUST-1(Hong Kong University of Science and Technology).

IUPAC presented in Fig. 1.4 and 1.5 two tentative hierarchies for CPs and MOFs.[3] However, these should not yet be regarded as final propositions from IUPAC project. For example, there remains the question whether a CP needs to have been crystallographically characterised, or if it can even be amorphous? Another point is the term Porous Coordination Polymer (CPC); in principle these could be based on inorganic ligands and thus not be a subcategory of MOFs.

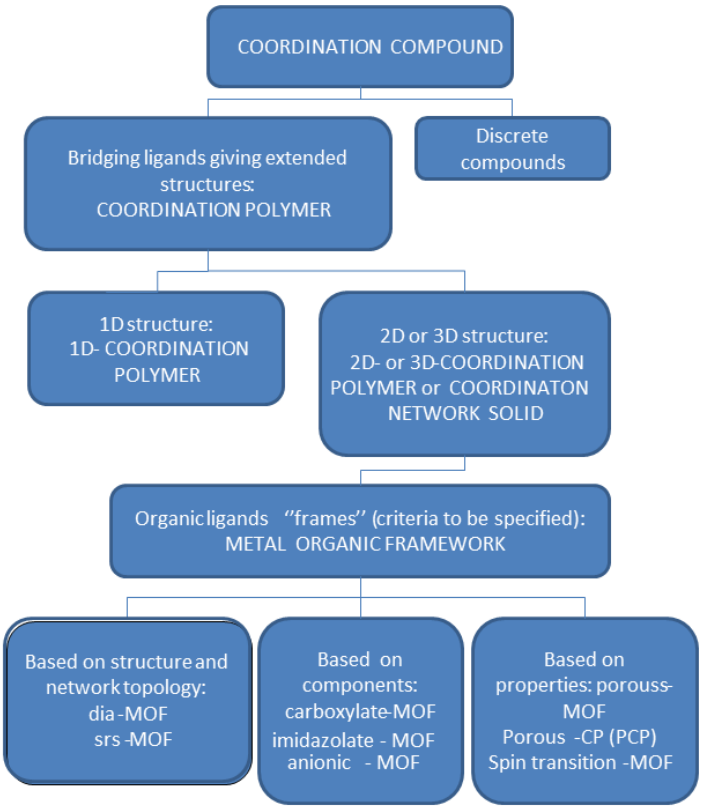

Figure 1.4. A tentative hierarchy of coordination polymers and metal–organic frameworks. The bottom descriptors are optional and not mutually exclusive. Three-letter topology codes according to O'Keeffe et al.[11,3]

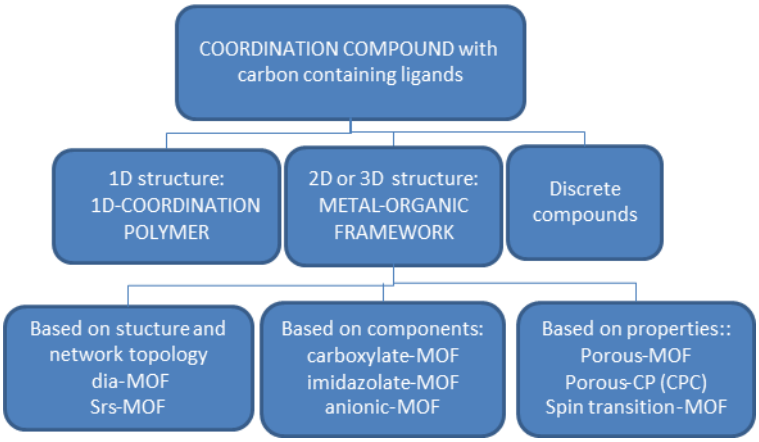

Figure 1.5. Another tentative hierarchy of coordination polymers and metal–organic frameworks. The bottom descriptors are optional and not mutually exclusive. Three-letter topology codes according to O'Keeffe et al.[11,3]

1.2 From Hofmann complexes to Metal Organic Frameworks

Porous and open-framework coordination networks have attracted considerable attention as post-zeolite materials. Zeolites are inorganic porous frameworks possessing highly ordered structures, their syntheses often require an inorganic or organic template with strong interactions forming between the inorganic framework and the template during the synthesis. As a consequence, removal of the template can result in collapse of the framework. Inorganic frameworks also suffer from a lack of diversity, as the variation of elements used seldom deviates from Al, Si and chalcogens.[12] Nevertheless, zeolite applications have generally been limited to smaller molecule applications, with few exceptions, due to their restricted pore and cavity size (< 1 nm).[13]

Recent progresses of coordination networks are pore post-modification and the possibility to obtain robust and flexible framework. This flexibility allows a dynamic behavior in porous coordination networks, which facilitate structural modifications (guest exchange or chemical reactions within the pores) without loss of its structural integrity.

The history of coordination networks started in 1897 by Hofmann and Kuspert when they discovered the first coordination network having a chemical formula of $Ni(CN)_2(NH_3)\cdot C_6H_6$[14,15] but only in 1954 did Powell and coworkers solve the structure of Hofmann's complex by X-ray analysis.[16] The crystal structure was a square network bridged by CN groups encapsulating benzene in a channel (Figure 1.6). Arrays of Ni covalently linked through CN groups create two dimensional layers that are parallel to each other. From each layer two amine groups protrude toward the adjacent layer, producing voids where benzene molecules are included.[15]

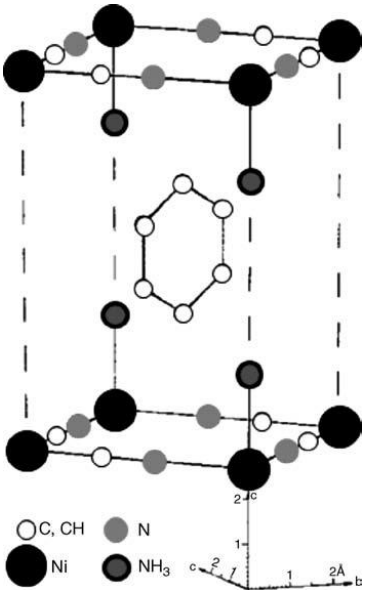

Figure 1.6. A partial crystal structure of the Hofmann complex showing benzene encapsulation within the cavity. This picture is reproduced according to ref: 15.

Expanded n-alkylamine Hofmann complexes were proposed in 1966 by Walker and Hawthorne (Figure 1.7).[17,15]The complexes were synthesized by addition of n-alkylamines to a suspension to anhydrous nickel cyanide. The crystalline samples were studied using the powder X-ray diffraction technique.

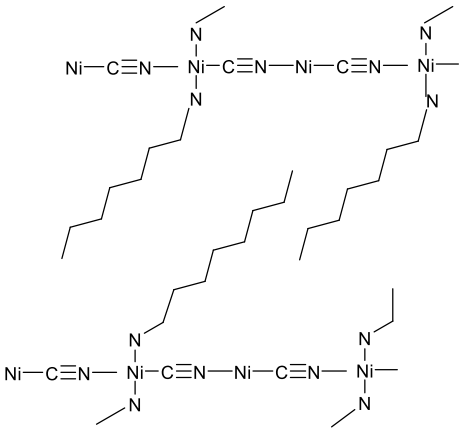

Figure 1.7. Structure of the expanded Hofmann complexes using n-alkylamines.[15] This picture is reproduced according to ref: 15.

A further Hofmann complexes evolution was reported in 1977 when Mathey synthesized aromatic diamine complexes, as shown in Figure 1.8.[18] The length of the c-axis varies depending on the length of diamines. The diamine complexes show selective encapsulation for aromatic guests and solvents. For example,

[Ni(4,4'-bipyridyl)Ni(CN)$_4$] encapsulate 0.8G (G: benzene, naphthalene, anthracene, $CHCl_3$, CH_2Cl_2, CH_3OH, but not phenanthrene, CCl_4).[15]

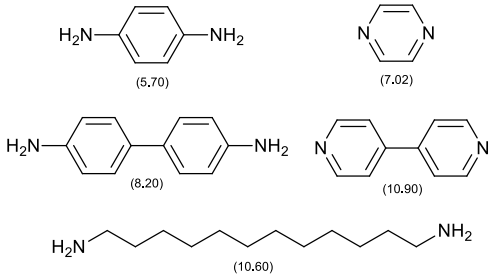

Figure 1.8. A set of diamines and corresponding c-axis values (in parentheses, Å).[15] This picture is reproduced according to ref 15.

The first organic coordination network was reported in 1989 by Robson and coworkers. They prepared three-dimensional solid polymeric materials with cavities by linking centers together with either a tetrahedral or an octahedral array of valencies by complexation of anions with tetrahedral bridging ligands. They prepared an infinite framework $\{Cu^I[C(C_6H_4{\cdot}CN_4)]\}^+$ of tetrahedral centers linked together by rod-like units. The rod-like units were obtained by substitution of the acetonitrile ligands in $[Cu^I(CH_3CN)_4]^+$ by 4,4',4'',4-tetracyanotetraphenylmethane.[15]

In this way, Robson and coworkers established a new strategy able of designing new solids with large cavities by linking organic molecules with determined size and shape.[15]

One of the first example of a coordination network with the ability to recognize organic molecules was discovered in 1994 by Fujita and coworkers [19] with the synthesis of a two-dimensional square network solid [Cd(4,4'-bipyridine)$_2$(NO$_3$)$_2$] (Figure 1.9a) containing large cavities with the possibility of guest encapsulation. The first catalytic process was prove by treating benzaldehyde and cyanotrimethylsilane with a CH_2Cl_2 suspension of powdered [Cd(4,4'-bipyridine)$_2$(NO$_3$)$_2$] (40°C, 24 h), which gave 2-(trimethylsiloxy)phenylacetonitrile) in 77% yield (Figure 1.9b).[19,15]

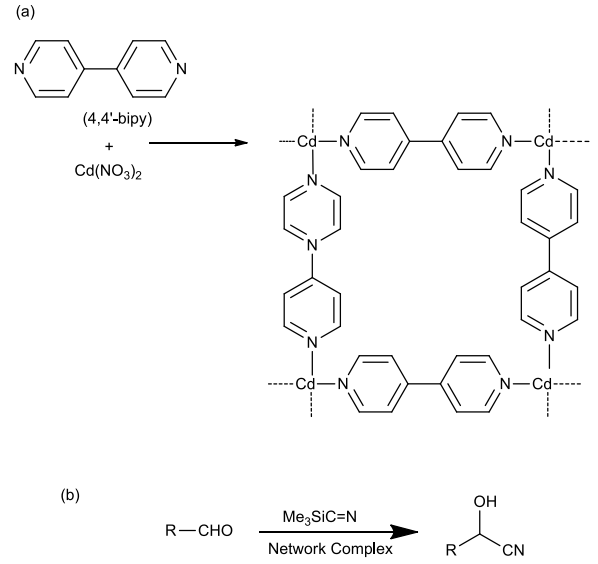

Figure 1.9. a) two-dimensional square network solid $[Cd(4,4'\text{-bipyridine})_2(NO_3)_2]$; b) catalytic process using $[Cd(4,4'\text{-bipyridyne})_2(NO_3)_2]$. This picture is reproduced according to ref:15.

In 1990, at almost the same time, Zaworotko and Yaghi reported two different examples of organic coordination networks.

Zaworotko and coworkers reported the formation of $[Zn(4,4'\text{-bipyridine})2]SiF_6$ coordination network (Figure 1.10) with large channels and 8x8 $Å^2$ pore sizes which are comparable to large zeolites pore sizes.[20] The 50% of the total volume of this material corresponds to pores. The hydrophobicity of those pores should result in the inclusion of hydrophobic molecules, using molecules with similar dimensions of the pore size.

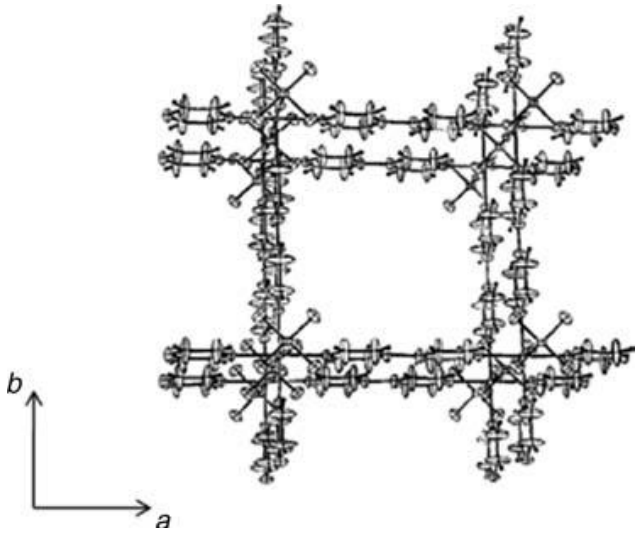

Figure 1.10. ORTEP representation of a square channel viewed along the c crystallographic axis of the $[Zn(4,4'\text{-bipyridine})_2]SiF_6$ organic coordination networks. The dimensions of the channels are the same as the dimensions of the unit cell *ca.* 11.396x11.396 $Å^2$.[15] This picture is reproduced according to ref:15.

In the same year, Yaghi and coworkers first obtained a coordination network containing three identical interpenetrated channels by hydrothermal synthesis.

The $[Cu(4,4'\text{-bipyridine})_{1.5}]NO_3\ (H_2O)_{1.25}$ network has trigonal planar Cu(I) centers that are linked by rod-like 4,4'-bipyridine ligands resulting in an extended 3D porous network (Figure 1.11).[21] The interpenetrated networks did not fill all the available space as observed in many other solids, therefore leaving an important volume of the solid as rectangular channels. The latter are filled with nitrate anions and water molecules and are linked by hydrogen bond interactions. Ion exchange properties were investigated and nitrate ions were replaced in aqueous solutions with other ions such as SO_4^{2-} and BF_4^-. Under inert atmosphere, $[Cu(4,4'\text{-bipyridine})_{1.5}]NO_3\ (H_2O)_{1.25}$ was observed to be stable up to 180°C and for hours in water at 70°C.[21,15]

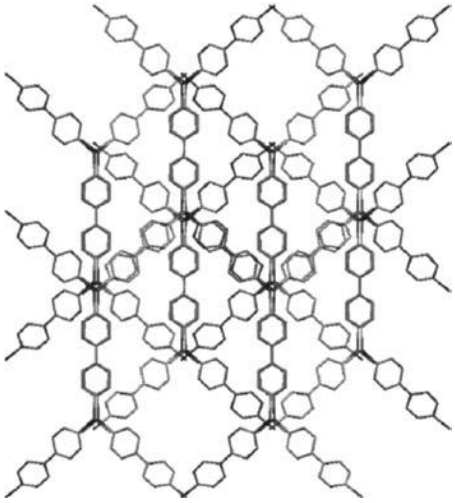

Figure 1.11. Crystal structure of $[Cu(4,4'\text{-bipyridine})_{1.5}](NO_3)\cdot(H_2O)_{1.25}$ viewed along the [100] crystallographic direction. Nitrate anions and water molecules have been omitted for clarity. This picture is reproduced according to ref: 15.

1.3 Design of Ultrahigh Porosity

Porous organic coordination networks can be prepared via self-assembly of a connector (a metal) and a link (a ligand) where connectors and ligands are bound together through a metal–ligand bond to form porous crystalline structures. It is in

the pores that a wide range of processes can be carried out. One of the important goals in the study of coordination networks is the possibility to design the pores. Now it is possible to create pores with determined sizes just by selecting ligands with determined shapes, sizes, and functionality. On the other hand, inorganic elements (metal ions or inorganic clusters) provide similar properties to traditional zeolites, including thermal and mechanical stability, optical and electronic properties. Compared to zeolite, based on a few cations (Si and Al), Metal Organic Materials can accept almost all the cations of transition metals, at least those which are di-, tri- (including rare earth) or tetravalent.[22]

Another interesting feature of Metal Organic Materials is the ability to direct structures of particular topologies that may be desirable for certain applications by using the molecular building block (MBB) approach.[23,24,25] This is a design strategy for the construction of solid-state materials, where the metal ions, coordination clusters, and organic ligands are pre-designed to have specific geometry and directionality upon coordination in situ. [1]

The first systematic approach to the construction of this class of solid-state materials had been introduced in1989, when Hoskins and Robson proposed the design of open framework based on a node-and-spacer approach, in which tetrahedral nodes can be linked by linear molecular spacers to construct an open structure based on the extension of cubic diamond.[26]

The number of potential topologies of MOFs drastically increased upon considering the large choice of functionalized organic linkers. There are two principle classes of organic ligands: N or O donor linkers. The nitrogen derivatives (cyanides, pyridine, imidazoles) are fixed directly to the cation. When O is concerned, they are mainly mono- or polycarboxylates, mono- or polyphosphonates, rarely sulfonates. Moreover, the carbon subnetwork (rigid or not) of the linker can be itself functionalized, depending on the expected applications (halogeno-, amino groups, etc).[22]

A common example of polytopic monodentate N donor ligands, is the 4,4'-bipyridine (4,4'-bipy), which possesses monodentate donor nitrogen atoms at opposite ends of the molecule and which coordinate in a linear ditopic manner.

Essentially, 4,4'-bipy acts as a longer linear spacer, and therefore extends the length of connections between nodes, ideally resulting in enlarged cavities.[15]

When 4,4'-bipy reacts with single-metal ions, the determination of each structure's network topology is directly governed by the coordination environment and geometry of the metal ion. Using terminal chelating ligand, for example ethylenediamine or 2,2'-bipy, is one successful method to control the metal coordination environment and to give a specific geometry. Fujita and coworkers reported an example of this assembly (Figure 1.12).[27] Square planar Pd(II) ions are *cis*-capped by ethylenediamine (en), the $[enPd(II)]^{2+}$ unit is the building block that provides the 90° angle necessary to coordinate two 4,4'-bipy molecules in the remaining cis positions.[15,27]

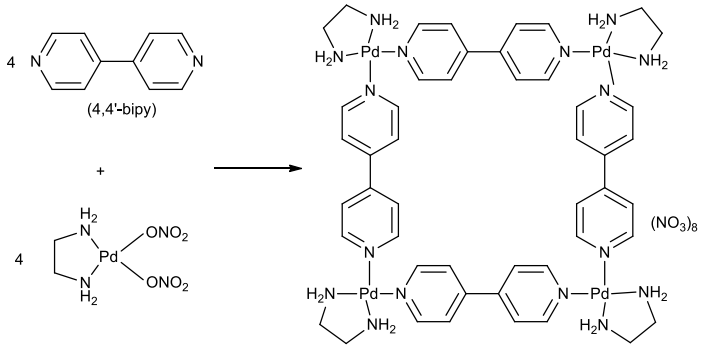

Figure 1.12. The construction of molecular squares can be achieved by using capping agents. The capping agent is ethylenediamine (en) and 4, 4' bipy molecules are coordinated in the remaining cis positions. This picture is reproduced according to ref:27.

The use of different N-donor linkers, for instance nonlinear polytopic pyridine-based ligands (Figure 1.13,a) introduces the influence of the ligand geometry into the mix construction to predict the resulting structure, where N-donor ligands have the potential to act as three-, four-, or six-connected linkers. That has resulted in an exponential increase of Metal Organic Frameworks architectures.

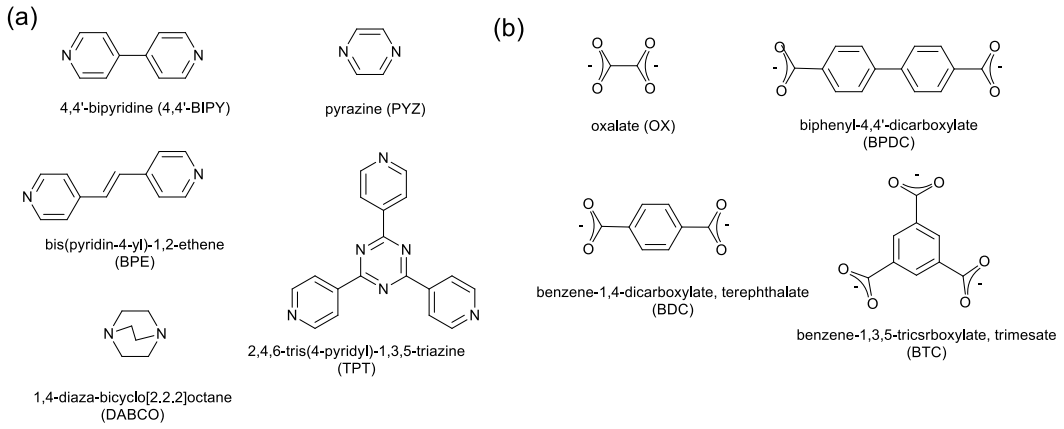

Figure 1.13. (a) examples for prototypical neutral nitrogen-heterocycle bridging ligands and (b) examples for prototypical anionic di- or tricarboxylate bridging ligands for MOFs.

The potentiality of carboxylate-based ligands (Figure 1.13,b) was explored by Yaghi and coworkers in 1998, when they first reported an example of MOF with permanent porosity. This MOF is well known as MOF-2, $Zn(BDC)\cdot(DMF)(H_2O)$, based on linear ditopic 1,4-benzenedicarboxylate (BDC) ligands. A total of four carboxylate units of different, but symmetrically equivalent, BDC building blocks are bonded to two zinc atoms in a di-monodentate fashion. Each zinc is also linked to a terminal water ligand.[28] This water can be removed upon heating, while maintaining the MOF stability.

Another extremely famous MOF is called MOF-5, $Zn_4O(BDC)_3\cdot(DMF)_8(C_6H_5Cl)$. It is constructed from octahedral Zn-O-C clusters and linear BDC to give a neutral 3D MOF with an open cubic-like network topology.[9]

MOF-5 has become the prototypical MOF for the design of a series of materials known as IRMOFs (Isoreticular Metal Organic Frameworks).[25] IRMOFs differ in the nature of functional groups decorating the pores and in the metrics of their pore structure (Figure1.14). Their formula is for the first seven members: $Zn_4O(R_{1\text{-}7}\text{-}BDC)_3$ where R increases gradually in the series, MOF-5 is the first exponent with R_1=H. In IRMOF-2 through -7, BDC links with bromo, amino, n-propoxy, n-pentoxy, cyclobutyl, and fused benzene functional groups reticulate into the desired structure wherein the groups point into the voids. From IRMOF-8 since IRMOF-16 the carboxylate-based ligands used are progressively longer and this is in agreement with the increase of the pore free volume. [25]

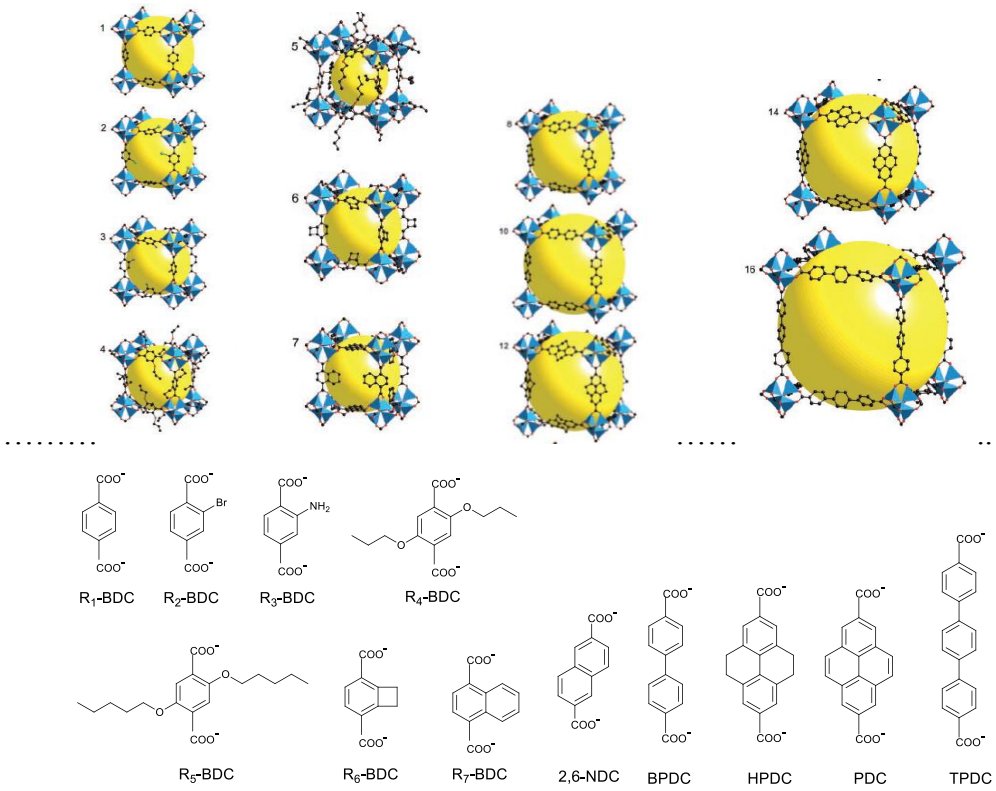

Figure 1.14. IRMOF series and on the bottom the corresponding linkers. Color scheme is as follows: Zn (blue polyhedra), O (red spheres), C (black spheres), Br (green spheres in **2**), amino-groups (blue spheres in **3**). The large yellow spheres represent the largest van der Waals spheres that would fit in the cavities without touching the frameworks. All hydrogen atoms have been omitted, and only one orientation of disordered atoms is shown for clarity. This picture is reproduced according to ref: 25.

Another important class of Metal Organic Framework was discovered at the Matérial Institut Lavoisier (MIL) by Ferey and co-workers. MIL-100 and MIL-101 are obtained from the assembly of different transition metal clusters and BDC or BTC linkers (BTC= 1,3,5-benzenetricarboxylic acid or trimesic acid, TMA) respectively. MIL-101 has very large pore sizes with a Langmuir surface area of 5900± 300 m^2/g. [15, 29,30]

In 1999, a key microporous MOF was reported based on the assembly of polytopic carboxylate ligands and metal-carboxylate clusters. It is well known with the name HKUST-1[10] or $[Cu_3(TMA)_2(H_2O)_3]_n$ and it was constructed from $Cu_2(carboxylate)_4$ square paddlewheel cluster and a tritopic ligand, trimesic acid (TMA, 1,3,5-benzenetricarboxylic acid or BTC) (Figure 1.15). This polymer forms face-centered-cubic crystals that contain an intersecting three-dimensional (3D) system of large square-shaped pores (9 Å × 9 Å) The framework is neutral and possesses large cavities, with a Brunauer–Emmett–Teller (BET) surface area of 692.2 m^2/g, a Langmuir surface area of 917.6 m^2/g, and a single-point total pore volume (typically determined using the Dubinin–Radushkevich equation) of 0.333 cm^3/g.[10]

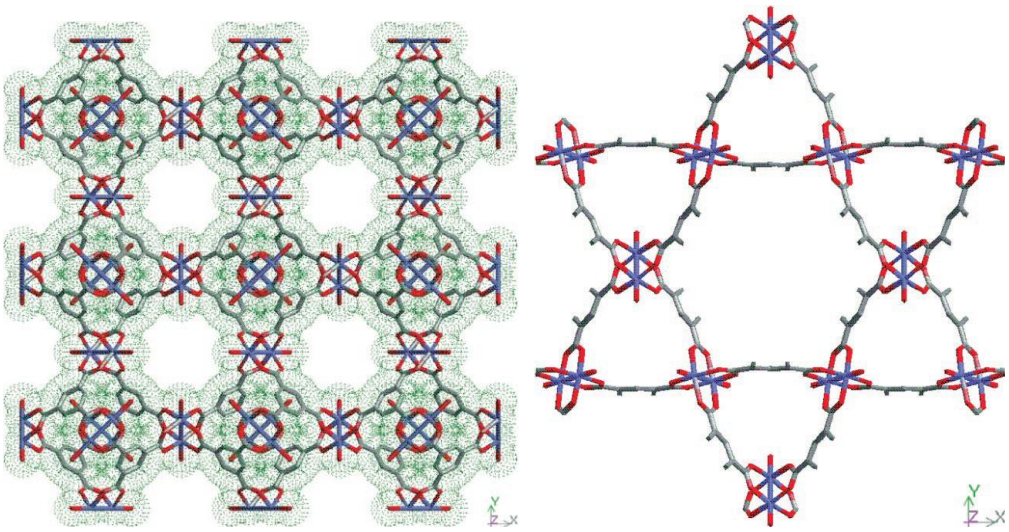

Figure 1.15. On the left: $[Cu_3(TMA)_2(H_2O)_3]_n$ coordination framework viewed down the [100] direction, showing nanochannels with fourfold symmetry. On the right: $[Cu_3(TMA)_2(H_2O)_3]_n$ coordination framework viewed along the cell body diagonal [111], showing a hexagonal shaped 18 Å window at the intersection of the nanopores. This picture is reproduced according to ref:10.

In 2008 Matzger and coworkers, using a unique mixed-ligand approach, combined a specific ratio of BDC and BTB (BTB= 4,4′,4″-benzene-1,3,5-triyltribenzoic

acid) ligands under the same reaction conditions as in the respective original MOFs, MOF-5, and MOF-177, to generate the mesoporous mixed-ligand known as, UMCM-1 (University of Michigan Crystalline Material-1). Two BDC linkers are adjacent, leaving the other four positions occupied by BTB linkers (Figure 1.16a), and these octahedra assemble into a structure containing both micropores and mesopores, which has extra-large hexagonal channels (2.7 nm × 3.2 nm) and a high apparent Langmuir surface area of 6500 m^2/g .[31]

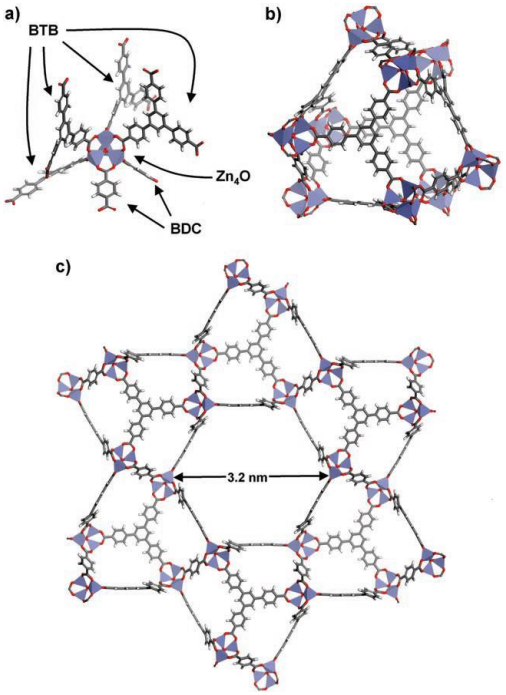

Figure 1.16. UMCM-1structure: a) A Zn_4O cluster coordinated to two BDC linkers and four BTB linkers. b) A microporous cage constructed of six BDC linkers, five BTB linkers, and nine Zn_4O clusters. c) Structure of UMCM-1 viewed along the c axis illustrating the one-dimensional mesopore. Zn_4O clusters blue tetrahedra, C gray, H white, O red. This picture is reproduced according to ref: 31.

The vast repertoire of organic chemistry also allows the synthesis of hetero-functional ligands, organic molecules that include more than one type of potential coordination functional group (e.g., O-donor and N-donor) into their structure.
This combination of donor types into a singular entity allows the formation of a greater diversity of MBBs, clusters, and structures.[15] An example of hetero-functional ligands used in Metal Organic Frameworks is shown by Schroder and coworkers in 2007. The 3,5- PDC , pyridine-3,5-bis(phenyl-4-carboxylic acid)

(H_2PBPC, Figure 1.17a) was used to construct two porous frameworks using an oxo-centered trinuclear metal-carboxylate cluster (Figure 1.17b). The resulting twelve-connected metal–organic frameworks $[Ni_3(OH)(PBPC)_3]_n \cdot n$(solvent) and $[Fe_3(O)(PBPC)_3]_n \cdot n$(solvent) (Figure 1.17c) show high porosity with surface areas up to 1553 m^3/g and an adsorption of H_2 up to 4.15 wt% at 77 K.[32]

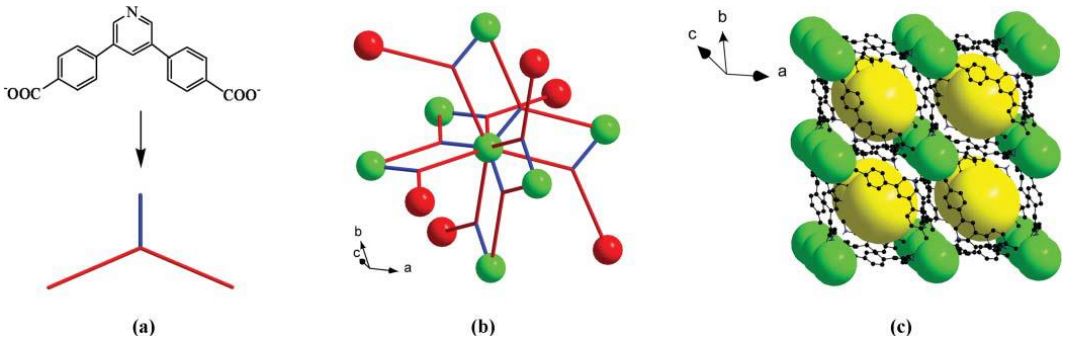

Figure 1.17. (a) the tritopic 3,5- PDC hero functional linker (b) 12-connectivity about the $[Ni_3(OH)(O_2CR)_6]$ cluster node (shown as green and red spheres) and (c) pores in $[Ni_3(OH)(PBPC)_3]_n \cdot n$(solvent) shown as yellow spheres. This picture is reproduced according to ref: 32.

In addition to the hetero-functional ligands strategy, another rational method for MOFs design and construction is the pillared-layer strategy, where 2D layers are connected with appropriate pillars, giving rise to 3D MOFs. Gao and coworkers isolated a 2D layered compound [Ni(HBTC)$(DMF)_2$ (guest)] (DMF = N,N'-dimethylamine), with DMF solvent molecules occupying polar positions on the metal centers (Figure 1.18). This 2D layered compound was an ideal candidate for the pillaring strategy. The 4,4'-bipyridine (4,4'-bipy) linker was used as the pillaring agent in order to obtain the 3D network [Ni(HBTC)(4,4'-bipy)· 3DMF]. The permanent porosity of this 3D MOF has been estimated by a N_2 adsorption isotherm measurement. By applying the Langmuir equations, the Langmuir surface area is estimated to be 1282.3 m^2/g .[33]

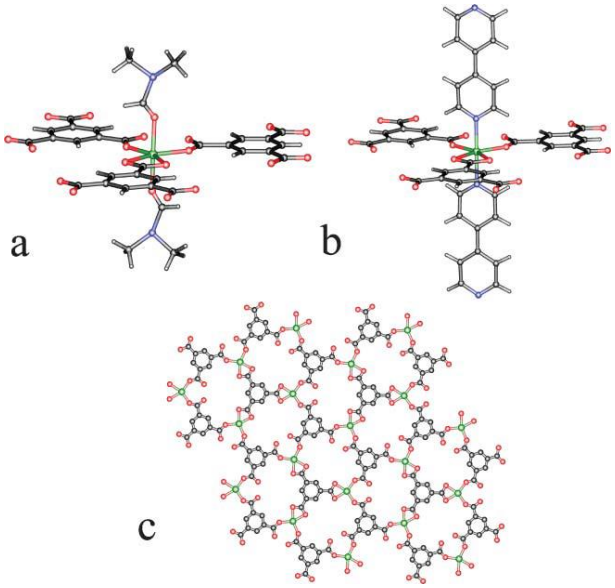

Figure 1.18. (a) Coordination environments of Ni(II) ions in the asymmetric units of [Ni(HBTC)$(DMF)_2$ (guest)] compound and (b) [Ni(HBTC)(4,4'-bipy)· 3DMF] compound . (c) a fragment of the 2D layer included both in [Ni(HBTC)$(DMF)_2$ (guest)] and [Ni(HBTC)(4,4'-bipy)· 3DMF]. For clarity the hydrogen atoms in (c) have been omitted. Ni: green; N: blue; O: red; C: black. This picture is reproduced according to ref: 33.

More recently, researchers continue to search new materials and strategies to design MOFs that have a topology and properties akin to those of zeolites. This new trend is represented by Zeolite-Like Metal Organic Frameworks (ZMOFs).The original strategy is based on choosing single-metal ions with preferred tetrahedral geometry, in combination with angular ditopic N-donor organic ligands. Such candidates have been aromatic nitrogen heterocycle-based linkers such as imidazole, pyrimidine, or tetrazole molecules.[34]

Yaghi and co-workers reported the synthesis of various ZMOFs, specifically referred to imidazole-based linkers to yield MOFs with zeolitic topologies and properties named as zeolitic imidazolate frameworks (ZIFs).[35]

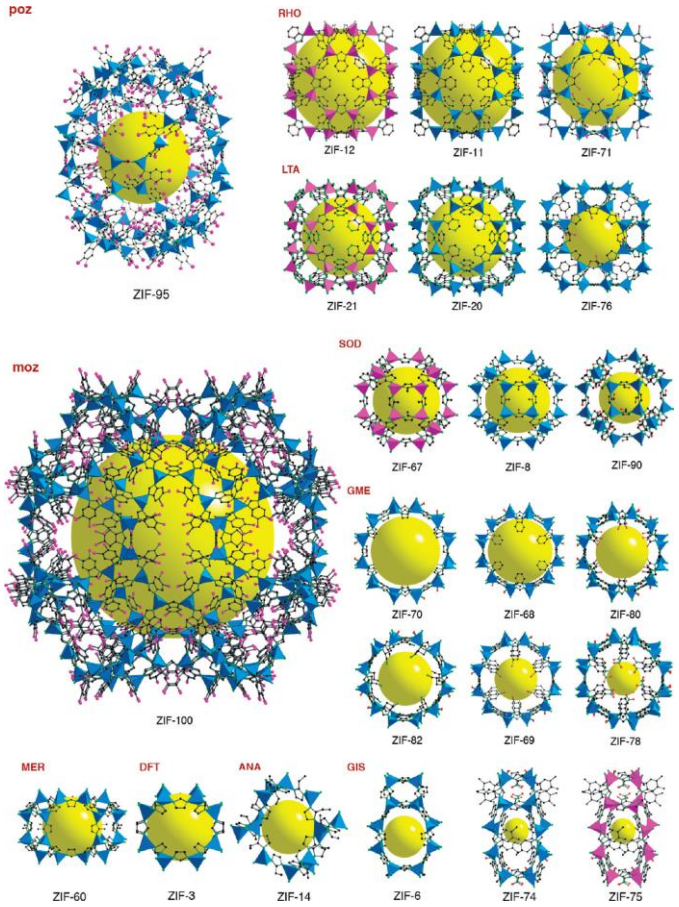

Figure 1.19. Crystal structures of ZIFs grouped according to their topology (three-letter symbol).[11]The largest cage in each ZIF is shown with ZnN_4 in blue and CoN_4 in pink polyhedra, and the links in ball-and-stick presentation. The yellow ball indicates space in the cage. H atoms are omitted for clarity (C, black; N, green; O, red; Cl, pink). This picture is reproduced according to ref: 36.

In ZIF synthesis, transition metal atoms (M, specifically Zn and Co) replace zeolite T atoms (tetrahedral linkers such as Si, Al, and P) and imidazolates (IMs) replace bridging oxides in zeolites (Figure 1.20, left). In fact, the M–IM–M angle is near 145° and that is coincident with the Si–O–Si angle preferred and commonly found in many zeolites (Figure 1.19, right).[36] The systematic variations of the linker substituents yielded a range of structures with similar topologies to those found in zeolites.

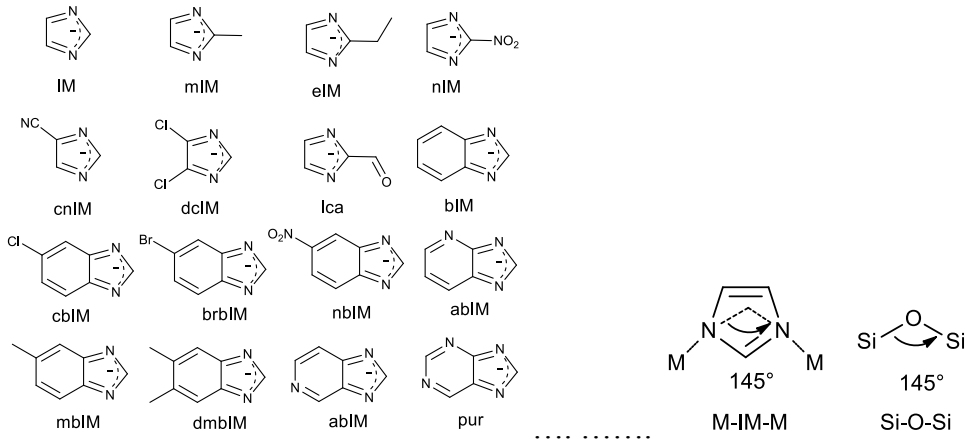

Figure 1.20. On the left: imididazolate derivates linkers used in ZIFs synthesi, on the right: the Si-O-Si preferred angle in zeolites (145°) is coincident with that of the bridging angle in the M-Im-M fragment (where M is Zn or Co and Im is imidazolate). This picture is reproduced according to ref:36.

Some members of ZIFs (ZIF-68, ZIF-69 and ZIF-70) have high thermal stability (up to 390°C) and chemical stability. Their frameworks have high porosity with surface areas up to 1970 m^2/g and they exhibit unusual selectivity for CO_2 capture from CO_2/CO mixtures and extraordinary capacity for storing CO_2: 1 dm^3 of ZIF-69 can hold ~83 liters of CO_2 at 273 kelvin under ambient pressure.[35]

A new prospective in MOFs synthesis is the use of amino acids as linkers.

An example of 3D MOF $[Ni_2(L\text{-asp})_2(bipy)]\cdot 1.28CH_3OH\cdot 0.72H_2O$ (L-asp = L-aspartate, bipy = 4,4'-bipyridine), employing an amino acid as linker is shown by Vaidhyanathan and coworkers. L-asp is an amino acid with one amine and two carboxylic acid groups[37] and each of these functional groups is capable of binding to metal centers. The compound has chiral Ni(L-asp) layers crosslinked by bipyridine to form the three-dimensional structure. The nickel centers are connected differently by the aspartate molecules forming layers. These layers are connected by the 4,4'- bipyridine forming the 3D structures. The distance between the 4,4'-bipyridine pillars connecting two Ni(L-asp) layers is 7.73 Å, and the interlayer distance between the nickel cations linked by the 4,4'-bipyridine molecules is 9.5 Å. The resulting channels which run along the b direction have a narrowest cross section of 3.8 × 4.7 Å .[37]

Other four homochiral MOFs are synthesised by mixing enantiopure valine-derived linkers, 3-methyl-2-(pyridin-4-ylmethylamino) butanoic acid and $Zn(CH_3COO)_2$ $2H_2O$ (Figure 1.21) under hydrothermal conditions in water. Those

four MOFs are isomers: structural isomers considering the two MOFs with different anions (Cl^- or Br^-) and enantiomers with respect to the ligand backbone (Figure 1.21). A three-periodic lattice with a parallel 1D helical channel was formed along the crystallographic c-axis. Molecular rearrangement results in an unprecedented zeolitic *unh*-topology in all four MOFs. In each case, two lattice water molecules (one H-bonded to halogen atoms) form a secondary helical continuous water chain inside the molecular helix.[38]

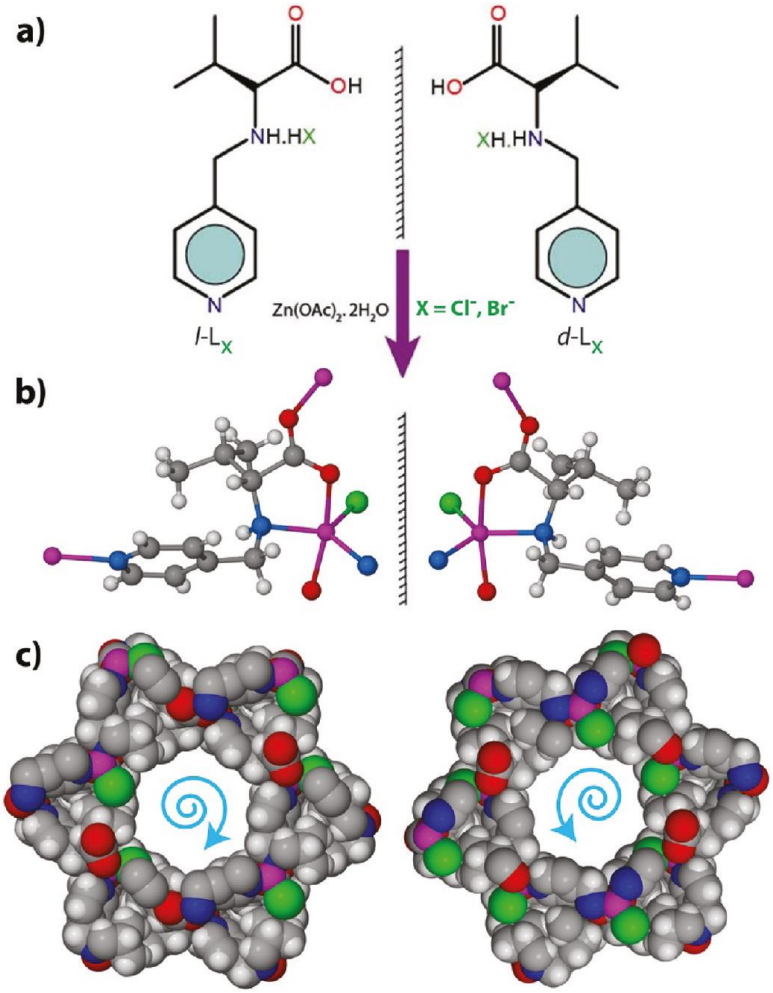

Figure 1.21. (a) Schematic representation of the links with mirror isomers (*l*-LX) and (*d*-LX) in the form of different salts, where: L= 3-methyl-2-(pyridin-4-ylmethylamino) butanoic acid and X = Cl^-, Br^-. (b) Asymmetric unit of MOFs with mirror isomers, showing a five-coordinated zinc center (pink ball). (c) Space-filling model of two enantiomers of MOF 1 and 3. Opposite helicity is shown as a blue curved arrow. Color code: C, gray; Cl, green; O, red; N, blue; Zn, pink; H, white. This picture is reproduced according to ref: 38.

1.4 Strategies for Coordination polymers and MOFs synthesis

The historical development of the field of MOFs is an excellent example of interdisciplinary research, and in particular it has been developed by the effort of two different scientific backgrounds. The first one is represented by crystal engineering and coordination chemistry that have their principles focused on the assembly of organic and inorganic building blocks in order to form porous structures. On the other hand, chemists with a background in the synthesis of zeolites started to look at the use of organic molecules not only as structure-directing agents but also as reactants to be incorporated in the framework structure. These explain the variety of synthetic methodologies and strategies adopted nowadays in the field of MOF synthesis. Coordination chemistry has introduced electrochemical and mechanochemical synthesis. On the other hand, from zeolite chemistry the concepts of solvothermal reactions, structure-directing agents, microwave-assisted synthesis or steam-assisted conversion have been introduced.[39]

Therefore, the conventional method to obtain MOFs is the solvo/hydrothermal synthesis, some alternatives routes are microwave-assisted, sonochemical, electrochemical, and mechanochemical methods

1.4.1 Solvothermal Synthesis

MOFs have been generally prepared via solvothermal synthesis by heating the reactants in a closed reaction vessel in the temperature range of 100-300°C. If water is used as the solvent the process is called hydrothermal. A solvothermal process can be defined as *"a chemical reaction in a closed system in the presence of a solvent (aqueous and non aqueous solution) at a temperature higher than that of the boiling point of such a solvent"*.[40] Consequently a solvothermal process involves also high pressures and takes reaction time from several hours to days. The solubility of reactants, in the major cases, is improved by temperature and pressure, the increase of such parameters induces an enhancement of the precursors-concentration into the solvent and favors the crystallites growing process.[40] One of the main advantages of solvothermal synthesis is the possibility

of performing heating and cooling temperature ramps to help crystal growth and the possibility of an easy industrial transposition. On the other hand, some disadvantages are as already mentioned above the long reaction time, large amount of solvent, high costs to purchase pressure-sealed metal vessels and heating ovens and high energy consumption. [41]

1.4.1.1 Biphasic Solvothermal Synthesis

Another approach that has been used extensively for the synthesis of coordination frameworks is the liquid-liquid interphase. Reaction at the interface of two immiscible solvents is a common technique for crystallizing compounds at low to moderate temperatures (<100 °C).[42] In this method, the metal salts are usually dissolved in a polar solvent and the organic ligand are preferentially soluble in opposite solvents. The surface tension at the inter-phase border between the two liquids is employed beneficially to prepare new MOFs (Figure 1.22). This approach depends on the migration of species across the inter-phase border, employs milder reaction conditions, and generally result in open structures.[43] Some advantages of this synthetic route are: the preparation of MOFs as large single-crystals which is fundamental for X-ray diffraction studies; the reactions are usually carried out in ambient conditions (e.g., pressure and temperature) or low temperatures. Drawbacks of biphasic synthesis are: very slow process, taking several days, weeks or even months; and the preparation of only a small amounts of the desired materials. [41]

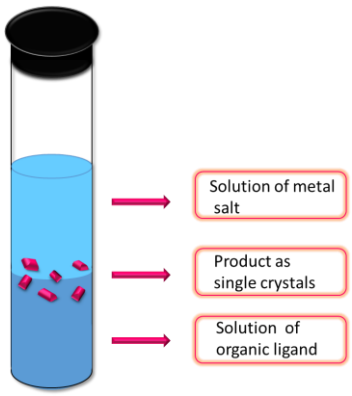

Figure 1.22. Schematic representation of liquid-liquid interface synthesis.

1.4.2 Alternative Synthesis Routes

Nowadays, alternative routes designed shorten the synthesis time and to obtain products for largescale production are becoming interesting in the field of coordination polymers and MOFs. A set of parameters such as different metal salts, solvent or mixture of solvents, presence of additives, molar ratios of the starting materials, reaction temperature and reaction time can be varied to investigate the developments of reactions.

Chemical reactions require an input form of energy that generally in solvothermal synthesis is introduced using conventional electric heating, i.e., heat is transferred from a hot source, the oven, through convection. Alternatively, energy can also be introduced by microwave irradiation (microwave-assisted synthesis), an electric potential (electrochemistry), mechanically (mechanochemistry) or through ultrasound (sonochemistry,).

The energy source is closely related to the duration, pressure, and energy per molecule that is introduced into a system, and each of these parameters can have a strong influence on the product formed and its morphology.[39] Experimental conditions play an important role in new compound synthesis that cannot be obtained otherwise. Furthermore, alternative routes can lead to compounds with different particle sizes and size distributions as well as morphologies that can have an influence on the material's properties. In porous materials different particle sizes can influence the diffusion of guest molecules, which has a direct impact on the material application, for example in catalytic reactions or in the adsorption and separation of molecules.

1.4.2.1 Microwave assisted synthesis

Microwave assisted synthesis techniques have been widely applied, firstly for organic chemistry and more recently for zeolites and MOFs synthesis.

In microwave synthesis, a substrate mixture in a suitable solvent is transferred to a teflon vessel, sealed and placed in the microwave unit, and heated for the appropriate time at the set temperature.

Microwave assisted synthesis depends on the interaction of electromagnetic waves with mobile electric charges. These can be polar solvent molecules/ions in a solution or electrons/ions in a solid. In solution, polar molecules try to align themselves in an electromagnetic field and in an oscillating field so that the molecules change their orientations permanently. Therefore, applying the appropriate frequency, collision between the molecules will take place, which leads to an increase in kinetic energy, i.e., temperature, of the system. Microwave assisted heating is a very energy efficient method of heating due to the direct interaction of the radiation with the solution/reactants. Thus, high heating rates and homogeneous heating throughout the sample is possible. The choice of appropriate solvents and selective energy input are two important elements, since starting materials may strongly interact with the microwave radiation.[39]

Potential advantages of this technique include: an easy variation and close control of the reaction parameters, the reduction of crystallization times and improvement of yields, the possibility to control the morphology of particles and to improve purity. However, large single-crystals are difficult to isolate and it does not provide an easy and quick industrial implementation.[41, 44]

The first MOF reported by microwave synthesis was Cr-MIL-100.[45] The compound was synthesized in 4h at 220 °C with 44% yield, which is comparable with that of conventional hydrothermal synthesis (220 °C and 4 days). After that, this method was expanded to Cr-MIL-101 synthesis at 210 °C in less than 1h; it has reported similar physicochemical and textural properties compared with the standard material synthesized using the conventional solvothermal heating method.[46] Microwave-assisted heating was found to be the method of choice to rapidly synthesize HKUST-1 crystals in the range of 10-20 μm in high yields (~90%) within 1 h.[47] Other MOFs like Fe-MIL-101-NH_2, IRMOF-3, and ZIF-8 were also synthesized using microwave-assisted synthesis method.[44]

1.4.3 Electrochemical synthesis

The electrochemistry synthesis principle involves metal ions continuously introduced through anodic dissolution to the reaction medium, which contains the dissolved linker molecules and a conducting salt. The metal deposition on the

cathode is avoided by using protic solvents, but in the process H_2 is formed. Another option is the use of compounds such as acrylonitrile, acrylic, or maleic esters that are preferentially reduced. Other advantages of the electrochemical route for industrial process are the possibility to run a continuous process and the possibility to obtain a higher solids content compared to normal batch reactions.[39]

The electrochemical synthesis of MOFs was first reported in 2005 by BASF researchers for the HKUST synthesis, under the name Basolite C300.[48] Bulk copper plates are arranged as the anodes in an electrochemical cell with the H_3BTC dissolved in methanol as solvent and a copper cathode. During a period of 150 min at 12-19 V and a 1.3 A, a greenish blue precipitate was formed. After activation, a dark blue colored powder (with crystals size ranging from 0.5 to 5 μm) having surface area of 1820 m^2/g was obtained. This HKUST-1 product was tested for its use in gas purification, i.e., removal of tetrahydrothiophene from natural gas, H_2 storage, and the separation of Kr-Xe mixtures.[49]

In a comparative study on the influence of the synthesis procedure on the properties of HKUST, the compound was synthesized using solvothermal, ambient pressure, and electrochemical routes in pure ethanol and ethanol/water mixtures. [47] Although XRPD investigations demonstrated that in all cases HKUST was formed, thermogravimetric experiments, elemental analyses, and sorption experiments showed the inferior quality of the electrochemically synthesized product. It was explained by the incorporation of linker molecules and/or the conducting salt in the pores during crystallization.[39]

This work was further extended to the chemistry of ZIFs. ZIF-8 was synthesized by anodic dissolution in an electrochemical cell.[50] The ZIF-8 was prepared using DMF, H_2O acetonitrile (AcN), MeOH, H_2O, a mixture of H_2O and MeOH as the solvent, tributylmethylammonium methyl sulfate (MTBS), and KCl as the electrolyte. The DMF/MTBS couple resulted in high synthesis efficiencies under mild reaction conditions (RT, 10 min).[51]

Electrochemistry is a fast and clean synthetic approach and as already anticipated it is used for the industrial production of Basolite C300. However, few others MOFs have been reported using this method.[41]

1.4.4 Sonochemical Synthesis

Sonochemical synthesis involves the introduction of high energy ultrasound to a reaction mixture.

Ultrasound is a cyclic mechanical vibration with a frequency between 20 kHz, the upper limit of human hearing, and 10 MHz. When high-energy ultrasound interacts with liquids, cyclic alternating areas of compression (high pressure) and rarefaction (low pressure) are formed. In the low pressure region, the pressure drops below the vapor pressure of the solvent and/or the reactants and small bubbles, cavities, are formed. The bubbles grow (tens of micrometers) under the alternating pressure through the diffusion of solute vapor into the volume of the bubble and consequently ultrasonic energy is accumulated. Once the bubbles reach their maximum size, they become unstable and collapse.[39]

The process of formation and collapse of bubbles in the solution after sonication, is called cavitation, it produces very high local temperatures (~5000 K) and pressures (~1000 bar)[52,53], and results in extremely fast heating and cooling rates (>10^{10} K/s).[44]

A large number of parameters govern the formation of cavities and the intensity of their collapse, and only a fraction of the input energy is transformed into cavitation. Moreover, in addition to the acoustic frequency and intensity (based on the equipment used), parameters such as the choice of liquid (vapor pressure, viscosity, and chemical reactivity), the temperature, or the gas atmosphere play an important role.[39]

Sonochemical methods accelerates the nucleation and reduces the crystallization time with a significantly smaller particles size than those by the conventional solvothermal synthesis.[44] This alternative route is fast, energy-efficient, environmentally friendly and can easily be carried out. Other advantages of this technique are the production of homogeneous particle size and morphology in short periods of time and it is a suitable method for the preparation of nano-sized MOFs. On the other hand, ultrasound waves can break crystallites hindering the formation of large single-crystals for X-ray diffraction studies.[41]

One of the first sonochemical experimentations was MOF-5. High-quality crystals (5-25 μm) of MOF-5 were obtained in 30 min by sonochemical synthesis using

NMP (1-methyl-2- pyrrolidone) as the solvent.[54] Starting from a clear solution, the reaction time and power level (maximum 200 W at 20 kHz) were varied. After 8-30 min, the product formed and the temperature was measured to be between 129 and 164 °C, depending on the power applied. At low power levels (around 20W) , impure samples were observed. Reaction times above 10 min and working at higher power levels led to the deterioration of the previously formed samples. The comparison with a conventionally synthesized sample showed almost identical physical properties.[39]

Sonochemistry synthesis was also used to obtained pillared MOFs, for example, $\{[Zn_4(BDC)_4(BPTA)_4]\cdot 5DMF\cdot 3H_2O\}_n$ (BPTA= N,N' -bis(4-pyridinyl)-1,4-benzenedicarboxamide) with nanorod morphology under ambient temperature and atmospheric pressure. Morphology and sizes of the nanostructures were investigated using different condition of initial reagents, ultrasonic irradiation powers and reaction times. Results show the particles size increased as the concentrations of initial reagents decreased.[55]

In the literature there was also reported the ultrasound synthesis of HKUST under atmospheric pressure and room temperature by using different reaction times and a mixture of solvents. Firstly, HKUST-1 was obtained in the presence of DMF (N,N-dimethylformamide)[56] after 1 min, showing that the concentration of DMF was important for the morphology of the material synthesized; the surface area and pore volume. Secondly, a few years after, [57] morphology- and size-controlled nano/microscale HKUST-1 was synthesized in an ethanol–water mixture at room temperature by adjusting the concentration of the surfactant CTAB (CTAB = cetyltrimethylammonium bromide).

1.4.5 Mechanochemical Synthesis

Mechanochemical synthesis (or mechanosynthesis) corresponds to chemical reactivity carried out by mechanical force, for example by grinding together bulk solid reactants. [58]

Mechanochemistry has a long history in synthetic chemistry and it has been employed in organic synthesis, in pharmaceutical chemistry for cocrystals synthesis, in inorganic solid-state chemistry and coordination polymers science

(MOFs).[39] The first synthesis of porous MOFs was reported in 2006[59] and the number of publications in this field in the last 10 years confirm the growing interest in this synthesis technique.

The interest in mechanochemistry for MOF synthesis is due to multiple reasons. One important point is the environmental issue; reactions can be carried out at room temperature under solvent free conditions, in which organic solvents can be avoided or added to the reactants only in trace amounts. It was for this reason and others that I selected mechanochemistry as the synthetic route used in this PhD thesis. Therefore, further details are described in Chapter 2.

1.5 Brief overview of MOFs applications

Coordination networks are useful in a wide range of applications: gas storage, gas/vapor separation, catalytic reactions, luminescent and fluorescent materials, and drug storage and delivery.

The pores of MOFs are usually occupied by solvent molecules that must be removed for most applications. Permanent porosity results when the framework remains intact, however structural collapse can occur. Moreover, the larger pores tend to collapse, therefore it is more difficult to achieve mesoporous than microporous MOFs. Microporous materials are good candidates for gas storage and gas separation applications because they have pores less than 20 Å which result in strong interactions between gas molecules and pore walls.[12]

Frameworks will often interpenetrate one another to maximize packing efficiency and consequently, the pores sizes are greatly reduced, but this may be beneficial for some applications. Indeed interpenetrated frameworks have been intentionally formed and found to lead to improved performance, for example, in H_2 storage.[60]

In order to improve the MOFs affinity towards one application rather than another, the post-synthetic modification (PSM) of MOFs has been reported.

In this case, it is necessary to first form a MOF with the desired topology, and then add the functional group to the framework. This may be applied to MOFs that are designed for catalysis and gas storage, as these applications require functional groups to modify the surface property and pore geometry.

Recently, PSM was applied to IRMOF-3, $[Zn_4O(BDC\text{-}NH_2)_3]$.[61] The MOF was submerged in a dichloromethane solution containing acetic anhydride to give the amide derivative (Figure 1.23) in >80% yield.

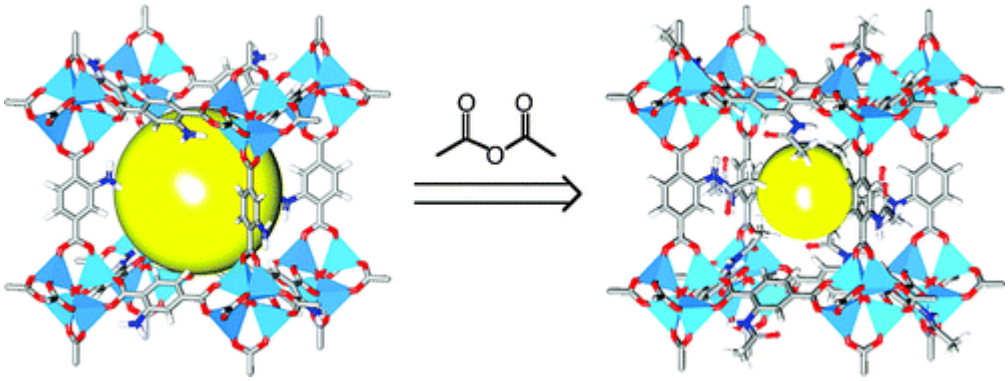

Figure 1.23. Schematic representation of IRMOF3 (on the left) and after Post Synthetic Modification using acetic anhydride to give the amide derivative (on the right). The van der Waals sphere has reduced size after PSM. This picture is reproduced according to ref: 61.

Since then, a large number of organic reactions have been used to covalently functionalize MOF backbones, and another example is shown by UMCM-1-NH_2, $[(Zn_4O)_3(BDC\text{-}NH_2)_3(BTB)_4]$ that was acylated with benzoic anhydride to produce the corresponding amide functionality within the pores.[62] The structures of both IRMOF-3 and UMCM-1-NH_2 after modification showed increased hydrogen uptake relative to the parent MOFs, even though there was a reduction in surface area.[62-63]

1.5.1 Hydrogen storage

One of the main challenges in the 21st century looks at energy storage. Hydrogen (H_2) is a clean fuel and an environmentally friendly carrier. It is an interesting alternative to the more common fossil fuels.

Hydrogen storage techniques involve the use of high pressure tanks, cryogenic tanks, chemisorption, and physisorption. Hydrogen storage in MOFs is based on physisorption, weak interactions (mainly van der Waals interactions), between the adsorbed hydrogen and the adsorbent, leading to fast kinetics, full reversibility, and manageable heat during hydrogen fueling. However, the promising data from physisorption-based hydrogen storage are all obtained at a cryogenic state (normally 77 K), and the adsorption becomes insignificant at ambient temperature.[12]

In 2003 the first study of hydrogen adsorption for MOF-5 was reported. This material is able to adsorb up to 4.5 wt% of H_2 under cryogenic conditions and 1 bar of pressure.[64] Subsequently, the hydrogen adsorption data has been reported for hundreds of MOFs.

One way to increase the interaction between hydrogen and MOFs is to tailor the pore size in the MOF to maximize interaction between hydrogen and MOFs.[12] However, increasing the surface area is not always an effective tool for increasing the volumetric hydrogen adsorption, which can be accomplished by increasing the adsorption enthalpy of hydrogen (Q_{st}).[65] In this contest, MOFs with unsaturated metal centers (UMC) have been used to enhance the hydrogen uptake.

Unsaturated metal centers (UMCs) can be generated by the removal of the coordinated solvent molecules under vacuum.[66] The interaction between hydrogen and the UMCs is much higher than that with pure carbon materials, and the isosteric heat of adsorption can sometimes go as high as 12–13 kJ/mol,[67] very close to the projected optimum 15.1 kJ/mol.[68] Lee et al. prepared isostructural MOFs with and without UMCs, and compared their hydrogen sorption capacities.[69] MOFs containing UMCs have higher hydrogen uptake both at low pressure (2.87 wt% *vs.* 2.07wt% at 77 K/1 bar) and high pressure (5.22 wt% *vs.* 3.70wt% at 77 K/50 bar) than MOFs with saturated metal centers.[12]

The U.S. Department of Energy (DOE) system targets (5.5 wt% and 40 g/liter at –40° to 60°C below 100 bar) for hydrogen adsorption.[70] Researchers from Mercedes-Benz have already drawn up MOF hydrogen fuel tanks in a fuel cell–powered demonstration model, the F125.[71]

1.5.2 Methane Storage

Methane (CH_4), a component of natural gas, also seems to be an attractive fuel because of its abundance and burning process. It burns more cleanly than the other fossil fuels, and produces relatively more energy than other fossil flues. [41] The storage of methane in MOFs comes up as a promising alternative to achieve the ambitious U.S. DOE targets under moderate pressures (35–65 bar) and at ambient temperature.[72]

In 2000, Kitagawa and coworkers. reported one of the first studies of high-pressure methane adsorption in MOFs. In particular the preparation of [$CuSiF_6$(4,4'-bipy)], a new MOF potentially able to adsorb methane, which had an uptake capacity of 104 m^2/g at 36 atm and 298 K.[73]

In 2013, Peng and coworkers, reported the study of methane uptake properties of six of the most promising MOF materials [74]: PCN-14, UTSA-20, HKUST-1, Ni-MOF-74 (Ni-CPO-27), NU-111, and NU-125 (Figure 1.24). HKUST-1 exhibited a room-temperature volumetric methane uptake that exceeds any value reported to date. At ambient temperature the volumetric CH_4 uptake for this material is about 230 cm^3/cm^3 at 35 bar and 270 cm^3/cm^3 at 65 bar.

These values reach the new volumetric target recently set by the DOE if the packing efficiency loss is ignored. Despite these excellent results, other issues remain such as, for instance, the cost and the chemical stability of these materials.[41]

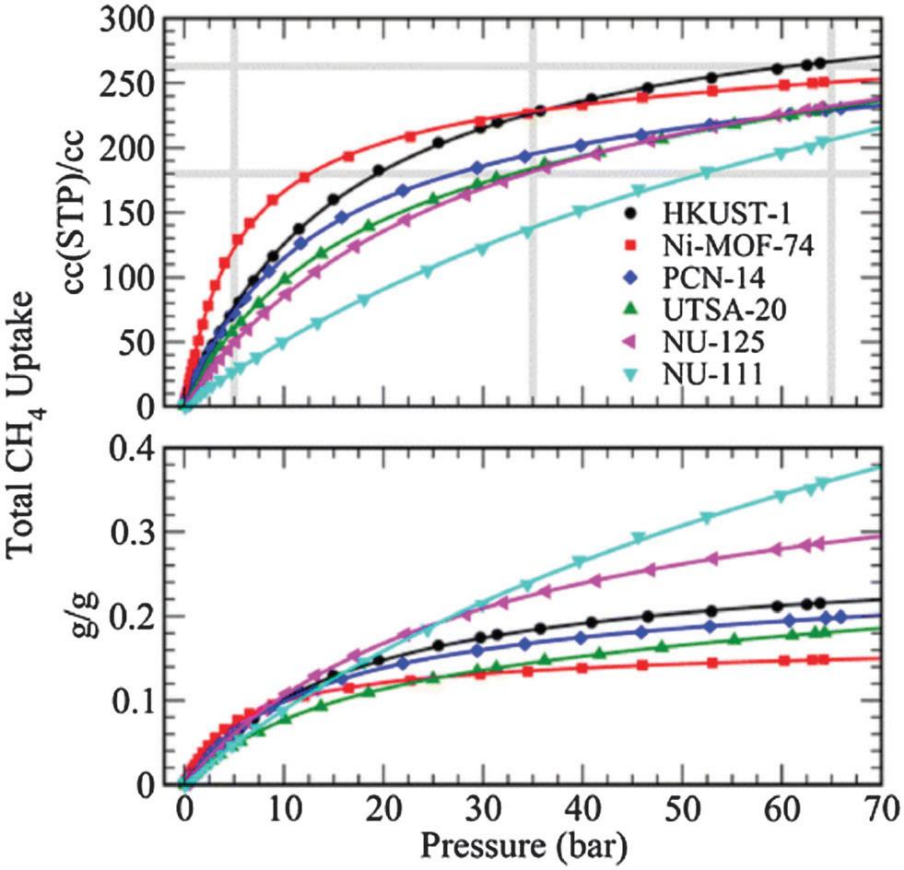

Figura 1.24. Total volumetric(top) and gravimetric(bottom) uptakes for six MOFs studied. The gray horizontal lines show the old and new DOE targets for volumetric methane storage. The gravimetric target is 0.5 g of methane per gram of sorbent. This picture is reproduced according to ref:74.

1.5.3 Carbon dioxide adsorption

MOFs are promising materials in the application of reversible carbon dioxide adsorption. Carbon dioxide is a major contributor to the greenhouse effect. It has been reported that during the last half century the concentration of CO_2 in the atmosphere increased from about 310 to over 380 ppm, being expected to achieve 550 ppm by 2050 even if CO_2 emissions stabilize in the next four decades.[41] Industries and the combustion of fossil combustibles are the major causes of the intense CO_2 increase. Because of this, several strategies have been developed for the sequestration/reduction of CO_2 and the U.S. DOE established a program envisaging the retention of 90% of CO_2 emissions via the post-combustion process allowing an increase in the cost of electricity by no more than 35% by 2020.[75]

The first MOF employed for carbon dioxide adsorption was MOF-2 [Zn(BDC)].[28]. The large quadrupole moment of carbon dioxide molecules causes them to interact with the framework more strongly than hydrogen and methane.[63] MOFs should possess specific characteristics to be used as efficient CO2 adsorbers :(i) porosity, with good accessibility to the channels; (ii) thermal stability; (iii) the presence of organic ligands derived from nitrogen-containing heterocycles and/or the (iv) existence of functional groups (e.g., –NH2 or –OH groups) in the pores to interact with CO_2; (v) insertion of metal ions; and (vi) the presence of UMCs.[41]

One of the best excess carbon dioxide uptakes reported to date was observed in a ultrahigh porosity MOF, MOF-200 (2437 mg/g at 50 bar and 298 K).[76] A gas tank filled with MOF-200 would store 17 times as much carbon dioxide at 35 bar, respectively, as the corresponding pressurized tank without MOF.[63]

Flexible MOFs , for instance MIL-53, based on different metal ions (Al, Cr, Fe) and BDC ligand, show great potentiality in selective adsorption and separation of gases and other small molecules. During the adsorption and desorption of CO_2, MIL-53 exhibits the "breathing" process, which has been associated with a phase transition of these MOF structures.[77] For example MIL-53(Cr), has two phases, one with narrow trapezoidal pores, named NP (2.6 Å ×13.6 Å) and another

called LP with large, almost square, pores (8.5 Å ×8.5 Å). Increasing the loaded CO_2, the MIL-53(Cr) structure converts from the NP to the LP form.[78]

1.5.4 Heterogeneous catalysis

Economic and environmental reasons are driving the scientific research towards the recyclability of heterogeneous catalyst. Zeolites are the most common materials used in industrial heterogeneous catalysis. The preparation of catalytic-active MOFs does not aim to replace zeolite materials, but to fill a number of important gaps never achieved to date for these materials, as for instance, in enantioselective heterogeneous catalysis.[41] Advantages of MOFs as catalyst are seen in the easy separation of a heterogeneous catalyst, the tailoring of the pore size to yield selectivity, and/or shape and size selectivity by creating an appropriate environment around the catalytic center in the restricted space available. MOFs with the following characteristics: a) ligands functionalized to activate the reactions, as for example, Brönsted acids to organo-catalysis; b) the presence of unsaturated metal centers, UMCs; and c) the potentiality to incorporate metal complexes into the organic ligand and pores/channels,[79] are good candidates for hereogeneous catalysis.

In 1994, the first example of catalysis in an extended framework was reported, involving the cyanosilylation of aldehydes in a Cd-based framework [Cd(4, 4'-bipy)$_2$(NO$_3$)$_2$] as a result of axial ligand removal.[19] In 2006, it was shown that removal of solvent from HKUST-1 exposes UMCs that act as Lewis acid catalysts to the isomerization of terpene derivatives, such as the rearrangement of α-pinene oxide to campholenic aldehyde and the cyclization of citronellal to isopulegol. By using the ethylene ketal of 2-bromopropiophenone as a test substrate, it was demonstrated that the active sites in HKUST-1 are hard Lewis acids.[80]

MIL-101 [Cr$_3$X(H$_2$O)$_2$O(BDC)$_3$; X = F, OH] has also been identified as a Lewis acid catalyst. Pure MIL-101 has a significantly higher catalytic activity in the cyanosilylation of benzaldehyde than reported for HKUST-1 and other MOFs. Moreover, it is a suitable support for palladium which can be incorporated via incipient wetness impregnation. Compared to Pd/MOF-5 and commercial

supported palladium catalysts, Pd/MIL-101 shows a better catalytic performance in the hydrogenation of styrene and cyclooctene, and a high and sustained activity in the gas phase hydrogenation of acetylene–ethylene mixtures, the essential advantage of Pd/MIL-101 over Pd/MOF-5 being its stability towards air, moisture and also (reducing) reaction conditions up to at least 373 K.[81]

1.5.5 Luminescence

Luminescence is the process where light is produced by the emission of energy from a material,[82] and contains two basic forms: 1) fluorescence which is spin-allowed, possessing typical lifetimes ranging between nano- to microseconds; and 2) phosphorescence, being spin-forbidden, and having lifetimes which can reach several seconds.[83] Light emission may appear either from individual organic ligands or metallic centers, or from both these components.

Coordination polymers and MOFs containing lanthanide ions are used as sensors or electroluminescent devices. Crystalline coordination polymers having a predictable topologies are interesting luminescent materials. Removing solvent molecules from the framework allows an increase in luminescence intensity since the solvent molecules can quench the emission. Permanent porosity, combined with the rigidity of the framework, may also lead to increased luminescence lifetimes and other features not inherent in traditional inorganic complexes.[84]

Over the years, the interest in luminescent MOFs has been developed for their promising potential to be applied, for instance, as sensors to detect Volatile Organic Compounds, VOCs (including benzene, toluene, xylenes, cyclohexene etc), for bioimaging, intracellular sensing and biomedicine. [41]

In 2011, the porous $[Zn_2(BDC)_2(DPNDI)]_n$ framework reported by Kitagawa research group, was tested as a luminescent MOF. $[Zn_2(BDC)_2(DPNDI)]_n$ was prepared under solvothermal conditions from a mixture of H_2BDC and N,N'-di(4-pyridyl)-1,4,5,8-naphthalenediimide (DPNDI) as organic linkers and $Zn(NO_3)_2$ in DMF.[85] The DPNDI linker has a low fluorescence quantum yield, nevertheless it could strongly interact with aromatic VOCs and the obtained $[Zn_2(BDC)_2(DPNDI)]_n$ MOF exhibited a strong color change in the visible region of the spectrum, this is a direct consequence of the aromatic VOC adsorption. The

incorporation of benzene, toluene, xylene, anisole and iodobenzene into the desolvated $[Zn_2(BDC)_2(DPNDI)]_n$, led to new products (i.e., $[Zn_2(BDC)2(DPNDI)]_n4VOC$) displaying intense blue, cyan, green, yellow, and red photoluminescence, respectively. This chemoresponse was of a non-linear nature owing to the coupling of structural transformation with the amount of adsorbed guest molecules.

1.6 References

1. Yaghi, O. M.; Li, H.; Davis, C.; Richardson, D.; Groy, T. L., Synthetic Strategies, Structure Patterns, and Emerging Properties in the Chemistry of Modular Porous Solids. *Accounts of Chemical Research* **1998,** *31* (8), 474-484.

2. Biradha, K.; Ramanan, A.; Vittal, J. J., Coordination polymers versus metal-organic frameworks. *Crystal Growth and Design* **2009,** *9* (7), 2969-2970.

3. Batten, S. R.; Champness, N. R.; Chen, X. M.; Garcia-Martinez, J.; Kitagawa, S.; Öhrström, L.; O'Keeffe, M.; Suh, M. P.; Reedijk, J., Coordination polymers, metal-organic frameworks and the need for terminology guidelines. *CrystEngComm* **2012,** *14* (9), 3001-3004.

4. Dukov, I. L., Nomenclature of inorganic chemistry - IUPAC recommendations 2005. *Chemistry* **2007,** *16* (6), 561-568.

5. A. D. Jenkins, P. K., R. F. T. Stepto, U. W. Suter. Pure Appl. Chem. 68, 2287 (1996).

6. Batten, S. R.; Champness, N. R.; Chen, X. M.; Garcia-Martinez, J.; Kitagawa, S.; Öhrström, L.; O'Keeffe, M.; Suh, M. P.; Reedijk, J., Terminology of metal-organic frameworks and coordination polymers (IUPAC recommendations 2013). *Pure and Applied Chemistry* **2013,** *85* (8), 1715-1724.

7. Kubel, F.; Strahle, J., Synthesis and properties of new one-dimensional conductors. 18. Polymeric dimethyl-and diphenylglyoximato complexes of cobalt and iron with 4, 4-bipyridine as a bridging ligand. Crystal structure of bis (dimethylglyoximato)-4, 4-bipyridinecobalt (II). *Z Naturforsch B: Anorg Chem Org Chem* **1982,** *37*, 272-5.

8. Venkataraman, D.; Lee, S.; Moore, J. S.; Zhang, P.; Hirsch, K. A.; Gardner, G. B.; Covey, A. C.; Prentice, C. L., Coordination Networks Based on Multitopic Ligands and Silver(I) Salts: A Study of Network Connectivity and Topology as a Function of Counterion. *Chemistry of Materials* **1996,** *8* (8), 2030-2040.

9. Li, H.; Eddaoudi, M.; O'Keeffe, M.; Yaghi, O. M., Design and synthesis of an exceptionally stable and highly porous metal-organic framework. *Nature* **1999,** *402* (6759), 276-279.

10. Chui, S. S. Y.; Lo, S. M. F.; Charmant, J. P. H.; Orpen, A. G.; Williams, I. D., A chemically functionalizable nanoporous material [Cu3(TMA)2 (H2O)3](n). *Science* **1999,** *283* (5405), 1148-1150.

11. O'Keeffe, M.; Peskov, M. A.; Ramsden, S. J.; Yaghi, O. M., The Reticular Chemistry Structure Resource (RCSR) Database of, and Symbols for, Crystal Nets. *Accounts of Chemical Research* **2008,** *41* (12), 1782-1789.

12. Kuppler, R. J.; Timmons, D. J.; Fang, Q. R.; Li, J. R.; Makal, T. A.; Young, M. D.; Yuan, D.; Zhao, D.; Zhuang, W.; Zhou, H. C., Potential applications of metal-organic frameworks. *Coordination Chemistry Reviews* **2009,** *253* (23-24), 3042-3066.

13. Paillaud, J.-L.; Harbuzaru, B.; Patarin, J.; Bats, N., Extra-Large-Pore Zeolites with Two-Dimensional Channels Formed by 14 and 12 Rings. *Science* **2004,** *304* (5673), 990.

14. Hofmann, K. A.; Küspert, F., Verbindungen von Kohlenwasserstoffen mit Metallsalzen. *Zeitschrift für anorganische Chemie* **1897,** *15* (1), 204-207.

15. MacGillivray, L. R., *Metal-Organic Frameworks: Design and Application*. **2010**.

16. Rayner, J. H.; Powell, H. M., 67. Structure of molecular compounds. Part X. Crystal structure of the compound of benzene with an ammonia-nickel cyanide complex. *Journal of the Chemical Society (Resumed)* **1952,** (0), 319-328.

17. Walker, G. F.; Hawthorne, D. G., Complexes between n-alkylamines and nickel cyanide. *Transactions of the Faraday Society* **1967,** *63* (0), 166-174.

18. Mathey, Y.; Mazières, C.; Setton, R., Formation of 3-dimensional structures using bifunctional ligand bridges between nickel cyanide planes. *Inorganic and Nuclear Chemistry Letters* **1977,** *13* (1), 1-3.

19. Fujita, M.; Kwon, Y. J.; Washizu, S.; Ogura, K., Preparation, clathration ability, and catalysis of a two-dimensional square network material composed of cadmium(II) and 4,4'-bipyridine. *Journal of the American Chemical Society* **1994,** *116* (3), 1151-1152.

20. Subramanian, S.; Zaworotko, M. J., Porous solids by design: [Zn(4,4'-bpy)2(SiF6)]n·xDMF, a single framework octahedral coordination polymer with large square channels. *Angewandte Chemie (International Edition in English)* **1995,** *34* (19), 2127-2129.

21. Yaghi, O. M.; Li, H., Hydrothermal synthesis of a metal - Organic framework containing large rectangular channels. *Journal of the American Chemical Society* **1995,** *117* (41), 10401-10402.

22. Ferey, G., Hybrid porous solids: past, present, future. *Chemical Society Reviews* **2008,** *37* (1), 191-214.

23. Stein, A.; Keller, S. W.; Mallouk, T. E., Turning Down the Heat: Design and Mechanism in Solid-State Synthesis. *Science* **1993,** *259* (5101), 1558.

24. Férey, G., Building Units Design and Scale Chemistry. *Journal of Solid State Chemistry* **2000,** *152* (1), 37-48.

25. Eddaoudi, M.; Kim, J.; Rosi, N.; Vodak, D.; Wachter, J.; Keeffe, M.; Yaghi, O. M., Systematic Design of Pore Size and Functionality in Isoreticular MOFs and Their Application in Methane Storage. *Science* **2002,** *295* (5554), 469.

26. Hoskins, B. F.; Robson, R., Infinite polymeric frameworks consisting of three dimensionally linked rod-like segments. *Journal of the American Chemical Society* **1989,** *111* (15), 5962-5964.

27. Fujita, M.; Tominaga, M.; Hori, A.; Therrien, B., Coordination Assemblies from a Pd(II)-Cornered Square Complex. *Accounts of Chemical Research* **2005,** *38* (4), 369-378.

28. Li, H.; Eddaoudi, M.; Groy, T. L.; Yaghi, O. M., Establishing Microporosity in Open Metal−Organic Frameworks: Gas Sorption Isotherms for Zn(BDC) (BDC = 1,4-Benzenedicarboxylate). *Journal of the American Chemical Society* **1998,** *120* (33), 8571-8572.

29. Férey, C.; Mellot-Draznieks, C.; Serre, C.; Millange, F.; Dutour, J.; Surblé, S.; Margiolaki, I., Chemistry: A chromium terephthalate-based solid with unusually large pore volumes and surface area. *Science* **2005,** *309* (5743), 2040-2042.

30. Férey, G.; Serre, C.; Mellot-Draznieks, C.; Millange, F.; Surblé, S.; Dutour, J.; Margiolaki, I., A hybrid solid with giant pores prepared by a combination of targeted chemistry, simulation, and powder diffraction. *Angewandte Chemie - International Edition* **2004,** *43* (46), 6296-6301.

31. Koh, K.; Wong-Foy, A. G.; Matzger, A. J., A crystalline mesoporous coordination copolymer with high microporosity. *Angewandte Chemie - International Edition* **2008,** *47* (4), 677-680.

32. Jia, J.; Lin, X.; Wilson, C.; Blake, A. J.; Champness, N. R.; Hubberstey, P.; Walker, G.; Cussen, E. J.; Schröder, M., Twelve-connected porous metal-organic frameworks with high H2 adsorption. *Chemical Communications* **2007,** (8), 840-842.

33. Gao, C.; Liu, S.; Xie, L.; Ren, Y.; Cao, J.; Sun, C., Design and construction of a microporous metal-organic framework based on the pillared-layer motif. *CrystEngComm* **2007,** *9* (7), 545-547.

34. Eddaoudi, M.; Sava, D. F.; Eubank, J. F.; Adil, K.; Guillerm, V., Zeolite-like metal-organic frameworks (ZMOFs): design, synthesis, and properties. *Chemical Society Reviews* **2015,** *44* (1), 228-249.

35. Banerjee, R.; Phan, A.; Wang, B.; Knobler, C.; Furukawa, H.; O'Keeffe, M.; Yaghi, O. M., http://www.w3.org/1999/xhtml, Synthesis of Zeolitic Imidazolate Frameworks and Application to CO_2 Capture. *Science* **2008,** *319* (5865), 939-943.

36. Phan, A.; Doonan, C. J.; Uribe-Romo, F. J.; Knobler, C. B.; O'Keeffe, M.; Yaghi, O. M., Synthesis, Structure, and Carbon Dioxide Capture Properties of Zeolitic Imidazolate Frameworks. *Accounts of Chemical Research* **2010,** *43* (1), 58-67.

37. Vaidhyanathan, R.; Bradshaw, D.; Rebilly, J. N.; Barrio, J. P.; Gould, J. A.; Berry, N. G.; Rosseinsky, M. J., A family of nanoporous materials based on an amino acid backbone. *Angewandte Chemie - International Edition* **2006,** *45* (39), 6495-6499.

38. Sahoo, S. C.; Kundu, T.; Banerjee, R., Helical Water Chain Mediated Proton Conductivity in Homochiral Metal–Organic Frameworks with Unprecedented Zeolitic unh-Topology. *Journal of the American Chemical Society* **2011,** *133* (44), 17950-17958.

39. Stock, N.; Biswas, S., Synthesis of Metal-Organic Frameworks (MOFs): Routes to Various MOF Topologies, Morphologies, and Composites. *Chemical Reviews* **2012,** *112* (2), 933-969.

40. Demazeau, G., Solvothermal processes: a route to the stabilization of new materials. *Journal of Materials Chemistry* **1999,** *9* (1), 15-18.

41. Silva, P.; Vilela, S. M. F.; Tomé, J. P. C.; Almeida Paz, F. A., Multifunctional metal-organic frameworks: From academia to industrial applications. *Chemical Society Reviews* **2015,** *44* (19), 6774-6803.

42. Forster, P. M.; Thomas, P. M.; Cheetham, A. K., Biphasic solvothermal synthesis: A new approach for hybrid inorganic-organic materials. *Chemistry of Materials* **2002,** *14* (1), 17-20.

43. Mahata, P.; Natarajan, S., Diversity in porous metal-organic framework materials. *Journal of the Indian Institute of Science* **2014,** *94* (1), 79-93.

44. Lee, Y. R.; Kim, J.; Ahn, W. S., Synthesis of metal-organic frameworks: A mini review. *Korean Journal of Chemical Engineering* **2013,** *30* (9), 1667-1680.

45. Sung, H. J.; Lee, J. H.; Chang, J. S., Microwave synthesis of a nanoporous hybrid material, chromium trimesate. *Bulletin of the Korean Chemical Society* **2005,** *26* (6), 880-881.

46. Jhung, S. H.; Lee, J. H.; Yoon, J. W.; Serre, C.; Férey, G.; Chang, J. S., Microwave synthesis of chromium terephthalate MIL-101 and its benzene sorption ability. *Advanced Materials* **2007,** *19* (1), 121-124.

47. Schlesinger, M.; Schulze, S.; Hietschold, M.; Mehring, M., Evaluation of synthetic methods for microporous metal–organic frameworks exemplified by the competitive formation of [Cu2(btc)3(H2O)3] and [Cu_2(btc)(OH)(H_2O)]. *Microporous and Mesoporous Materials* **2010,** *132* (1–2), 121-127.

48. Mueller, U. P., H.; Hesse, M.; Wessel, H. WO **2005**; 049892.

49. Mueller, U.; Schubert, M.; Teich, F.; Puetter, H.; Schierle-Arndt, K.; Pastre, J., Metal-organic frameworks-prospective industrial applications. *Journal of Materials Chemistry* **2006,** *16* (7), 626-636.

50. Martinez Joaristi, A.; Juan-Alcañiz, J.; Serra-Crespo, P.; Kapteijn, F.; Gascon, J., Electrochemical Synthesis of Some Archetypical Zn^{2+}, Cu^{2+}, and Al^{3+} Metal Organic Frameworks. *Crystal Growth & Design* **2012,** *12* (7), 3489-3498.

51. Bhattacharjee, S.; Jang, M.-S.; Kwon, H.-J.; Ahn, W.-S., Zeolitic Imidazolate Frameworks: Synthesis, Functionalization, and Catalytic/Adsorption Applications. *Catalysis Surveys from Asia* **2014,** *18* (4), 101-127.

52. Suslick, K. S.; Hammerton, D. A.; Cline, R. E., Sonochemical hot spot. *Journal of the American Chemical Society* **1986,** *108* (18), 5641-5642.

53. Gedanken, A., Using sonochemistry for the fabrication of nanomaterials. *Ultrasonics Sonochemistry* **2004,** *11* (2), 47-55.

54. Son, W.-J.; Kim, J.; Kim, J.; Ahn, W.-S., Sonochemical synthesis of MOF-5. *Chemical Communications* **2008,** (47), 6336-6338.

55. Bigdeli, M.; Morsali, A., Sonochemical synthesis of a nano-structured zinc(II) amidic pillar metal–organic framework. *Ultrasonics Sonochemistry* **2015,** *27*, 416-422.

56. Khan, N. A.; Jhung, S. H., Facile syntheses of metal-organic framework $Cu_3(BTC)_2(H_2O)_3$ under ultrasound. *Bulletin of the Korean Chemical Society* **2009,** *30* (12), 2921-2926.

57. Liu, Q.; Jin, L.-N.; Sun, W.-Y., Facile fabrication and adsorption property of a nano/microporous coordination polymer with controllable size and morphology. *Chemical Communications* **2012,** *48* (70), 8814-8816.

58. Friscic, T., New opportunities for materials synthesis using mechanochemistry. *Journal of Materials Chemistry* **2010,** *20* (36), 7599-7605.

59. Pichon, A.; Lazuen-Garay, A.; James, S. L., Solvent-free synthesis of a microporous metal–organic framework. *CrystEngComm* **2006,** *8* (3), 211-214.

60. Ma, S.; Eckert, J.; Forster, P. M.; Yoon, J. W.; Hwang, Y. K.; Chang, J.-S.; Collier, C. D.; Parise, J. B.; Zhou, H.-C., Further Investigation of the Effect of Framework Catenation on Hydrogen Uptake in Metal−Organic Frameworks. *Journal of the American Chemical Society* **2008,** *130* (47), 15896-15902.

61. Wang, Z.; Cohen, S. M., Postsynthetic covalent modification of a neutral metal-organic framework. *Journal of the American Chemical Society* **2007,** *129* (41), 12368-12369.

62. Wang, Z.; Tanabe, K. K.; Cohen, S. M., Tuning hydrogen sorption properties of metal-organic frameworks by postsynthetic covalent modification. *Chemistry - A European Journal* **2010,** *16* (1), 212-217.

63. Furukawa, H.; Cordova, K. E.; O'Keeffe, M.; Yaghi, O. M., The chemistry and applications of metal-organic frameworks. *Science* **2013,** *341* (6149).

64. Rosi, N. L.; Eckert, J.; Eddaoudi, M.; Vodak, D. T.; Kim, J.; O'Keeffe, M.; Yaghi, O. M., Hydrogen storage in microporous metal-organic frameworks. *Science* **2003,** *300* (5622), 1127-1129.

65. Wong-Foy, A. G.; Matzger, A. J.; Yaghi, O. M., Exceptional H2 Saturation Uptake in Microporous Metal−Organic Frameworks. *Journal of the American Chemical Society* **2006,** *128* (11), 3494-3495.

66. Dincă, M.; Long, J. R., Hydrogen Storage in Microporous Metal–Organic Frameworks with Exposed Metal Sites. *Angewandte Chemie International Edition* **2008,** *47* (36), 6766-6779.

67. Chen, B.; Zhao, X.; Putkham, A.; Hong, K.; Lobkovsky, E. B.; Hurtado, E. J.; Fletcher, A. J.; Thomas, K. M., Surface Interactions and Quantum Kinetic Molecular Sieving for H_2 and D_2 Adsorption on a Mixed Metal−Organic Framework Material. *Journal of the American Chemical Society* **2008,** *130* (20), 6411-6423.

68. Bhatia, S. K.; Myers, A. L., Optimum Conditions for Adsorptive Storage. *Langmuir* **2006,** *22* (4), 1688-1700.

69. Lee, Y.-G.; Moon, H. R.; Cheon, Y. E.; Suh, M. P., A Comparison of the H2 Sorption Capacities of Isostructural Metal–Organic Frameworks With and Without Accessible Metal Sites: $[\{Zn_2(abtc)(dmf)_2\}_3]$ and $[\{Cu_2(abtc)(dmf)_2\}_3]$ versus $[\{Cu_2(abtc)\}_3]$. *Angewandte Chemie International Edition* **2008,** *47* (40), 7741-7745.

70. Suh, M. P.; Park, H. J.; Prasad, T. K.; Lim, D.-W., Hydrogen Storage in Metal–Organic Frameworks. *Chemical Reviews* **2012,** *112* (2), 782-835.

71. www.emercedesbenz.com/autos/, M.-B. F.; mercedes-benz/concept-vehicles/mercedes-benz-f125-; research-vehicle-technology.

72. Düren, T.; Sarkisov, L.; Yaghi, O. M.; Snurr, R. Q., Design of New Materials for Methane Storage. *Langmuir* **2004,** *20* (7), 2683-2689.

73. Noro, S.-i.; Kitagawa, S.; Kondo, M.; Seki, K., A New, Methane Adsorbent, Porous Coordination Polymer $[\{CuSiF_6(4,4'\text{-bipyridine})_2\}_n]$. *Angewandte Chemie International Edition* **2000,** *39* (12), 2081-2084.

74. Peng, Y.; Krungleviciute, V.; Eryazici, I.; Hupp, J. T.; Farha, O. K.; Yildirim, T., Methane Storage in Metal–Organic Frameworks: Current Records, Surprise Findings, and Challenges. *Journal of the American Chemical Society* **2013,** *135* (32), 11887-11894.

75. Zhang, Z.; Zhao, Y.; Gong, Q.; Li, Z.; Li, J., MOFs for CO2 capture and separation from flue gas mixtures: the effect of multifunctional sites on their adsorption capacity and selectivity. *Chemical Communications* **2013,** *49* (7), 653-661.

76. Furukawa, H.; Ko, N.; Go, Y. B.; Aratani, N.; Choi, S. B.; Choi, E.; Yazaydin, A. Ö.; Snurr, R. Q.; O'Keeffe, M.; Kim, J.; Yaghi, O. M., Ultrahigh Porosity in Metal-Organic Frameworks. *Science* **2010,** *329* (5990), 424.

77. Serre, C.; Millange, F.; Thouvenot, C.; Noguès, M.; Marsolier, G.; Louër, D.; Férey, G., Very Large Breathing Effect in the First Nanoporous Chromium (III)-Based Solids: MIL-53 or CrIII (OH){O_2C-C_6H_4-CO_2} {HO_2C-C_6H_4-CO_2H} × H2O y. *Journal of the American Chemical Society* **2002,** *124* (45), 13519-13526.

78. Li, J.-R.; Ma, Y.; McCarthy, M. C.; Sculley, J.; Yu, J.; Jeong, H.-K.; Balbuena, P. B.; Zhou, H.-C., Carbon dioxide capture-related gas adsorption and separation in metal-organic frameworks. *Coordination Chemistry Reviews* **2011,** *255* (15), 1791-1823.

79. Janiak, C.; Vieth, J. K., MOFs, MILs and more: concepts, properties and applications for porous coordination networks (PCNs). *New Journal of Chemistry* **2010,** *34* (11), 2366-2388.

80. Alaerts, L.; Séguin, E.; Poelman, H.; Thibault-Starzyk, F.; Jacobs, P. A.; De Vos, D. E., Probing the lewis acidity and catalytic activity of the metal-organic framework [Cu_3(btc)$_2$] (BTC = Benzene-1,3,5-tricarboxylate). *Chemistry - A European Journal* **2006,** *12* (28), 7353-7363.

81. Henschel, A.; Gedrich, K.; Kraehnert, R.; Kaskel, S., Catalytic properties of MIL-101. *Chemical Communications* **2008,** (35), 4192-4194.

82. Cui, Y.; Yue, Y.; Qian, G.; Chen, B., Luminescent functional metal–organic frameworks. *Chemical reviews* **2011,** *112* (2), 1126-1162.

83. Allendorf, M.; Bauer, C.; Bhakta, R.; Houk, R., Luminescent metal–organic frameworks. *Chemical Society Reviews* **2009,** *38* (5), 1330-1352.

84. Li, Z.; Zhu, G.; Guo, X.; Zhao, X.; Jin, Z.; Qiu, S., Synthesis, Structure, and Luminescent and Magnetic Properties of Novel Lanthanide Metal−Organic Frameworks with Zeolite-like Topology. *Inorganic Chemistry* **2007,** *46* (13), 5174-5178.

85. Takashima, Y.; Martínez, V. M.; Furukawa, S.; Kondo, M.; Shimomura, S.; Uehara, H.; Nakahama, M.; Sugimoto, K.; Kitagawa, S., Molecular decoding using luminescence from an entangled porous framework. *Nature communications* **2011,** *2*, 168.

Chapter 2: Mechanochemical synthesis form inorganic materials to coordination polymers

2 Mechanochemical synthesis: from inorganic materials to coordination polymers

2.1 Introduction

The functional materials research can be divided into three broad aspects: 1) the discovery of potential applications; 2) the development of reliable and general synthetic designs and 3) the development of efficient synthetic strategies.[1] The third aspect is the subject of this chapter; which is an overview of one of the alternative synthetic strategies, mechanochemical synthesis (sometimes called mechanosynthesis) including historical aspects, from the earliest example of mechanochemical reaction to metal-complexes and coordination polymers synthesis.

Mechanochemistry refers to reactions, normally of solids, induced by the input of mechanical energy, such as by grinding in ball mills. It is becoming more intensely studied because it can promote reactions between solids quickly and quantitatively, with either no added solvent or only nominal amounts.[2] The mechanical grinding of the dry reactants does not involve external heating, but only heating that results from the conversion of the mechanical energy of grinding into heat.[3] Although mechanochemistry has a long history, the interest in this synthetic method has increased in the last 30 years with the rise in the number of publications and patents. Mechanochemisty has found followers in broad areas of chemistry, ranging from inorganic chemistry to organic and supramolecular chemistry, with the recent incorporation of coordination polymers (including Metal Organic Frameworks). The interest in mechanochemistry results from the growing expansion in environmentally friendly and sustainable processes. While traditional solution-based methods require high temperatures and pressures, mechanosynthesis has the advantage of avoiding the use of solvent [4] or reducing the volume.[5] Other benefits of mechanosynthesis are high yields and products purity [6] as well as with the reduction of reaction times.[7]

2.2 The Mechanochemistry terminology

Frequently, the term mechanochemistry is used in a broad sense, covering any chemical reaction mechanically induced, for instance by grinding etc. The IUPAC definition of a mechano-chemical reaction is the following*: 'Chemical reaction that is induced by the direct absorption of mechanical energy'*.[8]

Proceeding with the description of the terminology, the term grinding is generally used to describe mechanical action by hard surfaces on a material, normally to break up the material and reduce its particle size. It can refer to manual methods (mortar and pestle) or non-manual ones, such as ball milling, or extrusion etc.[2] An additional terminology is related to solids grinding in the presence or in absence of liquids. The completely absence of solvent is known as neat grinding,[4] the reduction of the amount of solvent to catalytic or near stoichiometric amounts is called LAG, liquid assisted grinding.[5,9] Originally 'solvent drop grinding' was used to indicate the use of small amount of solvent but it has been superseded by 'liquid assisted grinding' which is the term used currently. LAG is equivalent to the term 'kneading', also used in the same context.[10] Very small amounts of added liquid can dramatically accelerate, and even enable, mechanochemical reactions between solids.

Often the solvent molar amount added is similar to those of the reactants themselves. Another piece of terminology is the term 'solvent free'. It may indicate that no solvent is intentionally added to the reaction, but solvents can be present in the starting materials as molecular solvates or in hydrated metal salts or as moisture in non-formally hydrated materials and also in the atmosphere. Furthermore, species such as acetic acid and water may be obtained as reaction products. Therefore a solvent-free reaction does not necessarily correspond to a solvent-free process.[2]

2.3 Historical development of Mechanochemistry

The beginning of mechanochemistry goes back into prehistory, where the use of rubbing and grinding had to result in chemical transformation, such as making fire

by friction or by striking iron with a flint. The earliest document related to chemistry is the 'On Stone' written by Theophrastus of Eresus in 315 B.C in which there is reported the reduction of cinnabar to mercury by grinding in a copper mortar and pestle. Grinding and its traditional instrument, the mortar and pestle, can be regarded as the first engineering technology.[11] Despite this earlier discovery, the first systematic studies of mechanochemical reactions were carried out only at the end of the 19th century and speedy advancement was delayed until the 1960s.

In 1820, Faraday described the reduction of silver chloride by grinding with zinc, tin, iron, and copper in a mortar and this method was called the ''dry way'' of inducing reactions.[12] He reported that silver chloride reacted with zinc in a fast and highly exothermic reaction, raising the possibility that he actually observed a mechanochemically induced self-sustaining reaction.

In 1866 Matthew Carey Lea investigated the first experiment on the use of mechanical action to induce a chemical response.[13] The most remarkable finding of Lea was related to the decomposition of mercuric and silver chlorides. Both these compounds decomposed while triturated in a mortar, although they are known to melt or sublime undecomposed upon heating.[14]

Almost in the same year another chemist Walthère Spring carried out a large-scale systematic investigation of the mechanical action effects on chemical processes and it anticipated further investigations.[15] Although Lea and Spring had had a very different career paths and life circumstances, their investigations have marked the beginning of systematic research in mechanochemistry. The main motivation of the research of Spring and Lea was to understand the fundamental nature of chemical reactions under pressure and shear. Grinding, sliding, and other forms of mechanical action are important components of many technological processes and they are often accompanied by chemical changes.[11]

In 1919 Wilhelm Ostwald wrote the textbook of General Chemistry where he included mechanochemistry as one of sub-disciplines of chemistry together with thermochemistry, electrochemistry, sonochemistry or photochemistry.[16]

The progress in mechanochemistry was relatively slow during the first half of the 20th century; more important developments in experimental techniques such as X-

ray crystallography discovery occurred. Although mechanochemistry went through a slow growth period, it had benefited a lot for general progresses in underlying science, and the practical potential of mechanochemistry was recognized and it became a major source of motivation for further research.[11]

F. M. Flavitsky, fascinated by the idea that reactions could take place between solids, studied many solid state reactions induced by grinding.[17] He was interested in qualitative chemical analysis and he investigated 36 solid chemicals that could be used to identify 13 cations and 19 anions by rubbing small quantities of the unknown substance with an appropriate sequence of reactants. His method required very small samples and no solvent (although the role of moisture from the air was unclear) and it was accurate, fast and simple. Students at the University of Saint Petersburg performed qualitative analysis of inorganic mixtures using Flavitsky's method beginning in 1949. It is likely that this was the first time mechanochemistry found its employment in the teaching laboratory.[11]

Efforts in mechanochemistry development were interrupted during the Second World War but at the same time the developments with military relevance and the mechanical initiation and sensitivity of explosives became an interesting researched subject.[18] The accepted model assumed that the mechanical impact or shock wave created hot spots where ignition started. It was only very recently that a mechanochemical, non-thermal mechanism of detonation was considered .[19]

The hot-spot model was extended to explain chemical reactions caused by sliding but not all scientists accepted this point of view, some of them argued that sliding broke bonds directly, and the resulting free bonds caused the chemical reactivity.[20] In 1933, Fink and Hofmann affirmed that the fast oxidation of metal surfaces during sliding was the result of the mechanical action, and argued that the observed temperature increase was the consequence of oxidation, rather than the direct result of friction and the cause of the reaction.[21,11]

The most important progress in mechanochemistry is closely related to new advancements in grinding technology and mill design. As already mentioned, the first instrument for grinding has been the mortar and pestle and it is still useful nowadays for qualitative investigations of mechanically induced reactions. Despite these advantages, manual grinding using a mortar and pestle is slow and

the power input is difficult to quantify.[11] Therefore, when the industrial production required an efficient method to mill tons of cement and metal ores (particularly gold) to sub-millimetre size, the tumbling mill was developed. Tumbler mills used balls, pebbles or rods as milling bodies and they could be quite energetic, if the drop height was sufficiently large.[22]

In 1922, Andrew Szegvari [23] invented the stirred-ball attritor mill and in 1923 Retsch [24] developed the first motorized mill that simulated the hand grinding in a mortar.

In a tumbling mill, the dropping distance and therefore the energy of the impacts are low and in order to achieve more energetic impacts in 1961 the Fritsch company invented the planetary mill in which the milling drum was placed on a centrifuge to simulate a substantially larger acceleration of gravity.[23,11] Planetary mills provide a mixture of impact and friction that can be varied by the choice of the milling parameters and they are widely used in many laboratories in mechanochemistry.

However, the most popular laboratory mill is a shaker mill known as SPEX 8000, developed in 1957. It is suitable for *mechanical alloying* and for the mechanochemical processing of small samples on the laboratory scale. Mechanochemistry in the modern age began with *mechanical alloying*, the process of combining elements or alloys to produce a single homogenous alloy, in high velocity ball mills. During such processes there is a significant reduction in crystallite and particle sizes, such that products are often either nanoparticles or amorphous phases,[25] which is sometimes desired as providing a top-down route to nanomaterials.[2] First experiments using the SPEX 8000 were aimed to produce alloys and were carried out at the International Nickel COmpany (INCO) in the late 1960s.[26] The aim of INCO researchers was to prepare oxide dispersion strengthened nickel alloys. The main difficulty with traditional technologies was that molten nickel kept rejecting the oxide particles due to the lack of wetting. To overcome this problem, the oxide particles were coated with a layer of metal in a high-energy ball mill. When the attention was turned to the ball milling process, a fine composite powder with carefully selected composition was produced and

successfully processed into bulk metal by powder metallurgical methods, always staying below the melting point. The principle of mechanical alloying was born.[26] The interest in mechanical alloying increased after the discovery of its ability to produce amorphous alloys systems: bimetallicalloy Y–Co,[27] Fe-Zr,[28] Ni-Ti,[29] Cu-M (M = Ti, Zr, Hf) and Pd-Zr[30] and Ni–Nb[31] and SemiMetal-Metal Alloys Ni,Co-B,[32,33] Pd-Si [34] and Nb-Ge.[35] Amorphous alloys prepared by rapid solidification had been the subjects of intense research for over 20 years, and the opportunity to apply the same methodology to similar materials had attracted the interest of a remarkable group of researchers. Furthermore, as glass formation is governed by different principles depending on the preparation method, mechanical alloying extended the composition range available in amorphous form.[36] Research in this method of mechanochemistry was intensified and a large number of conferences on this subject were organized. In 1995, the Materials Transactions of the Japan Institute of Metals published a special issue dedicated to mechanical alloying and a new periodical,[37] the ‘‘International Journal of Mechanochemistry and Mechanical Alloying’’, was established in 1994.[11]

Though inorganic materials represent the most established area of mechanochemicals synthesis, good results were also obtained for organic materials synthesis, and research in the latter area intensified substantially only recently. The most important and beneficial opportunities in organic mechanosynthesis are the increased reaction rates and the elimination of solvents. Moreover, mechanochemical reactions exhibit high selectivity and the favored products are often different from the ones dominating in conventional solution-based synthesis.[38] Two categories of organic mechanochemical reactions can be identified based on the interactions involved.[39] If covalent bonds rupture and new bonds form, the product is a new compound. It may be different from the product of solution-based synthesis. If only secondary interactions, such as hydrogen bonds, are affected,

the process is a supramolecular reaction, such as the formation of cocrystals.[4] A cocrystal can be identified as a ‘‘multi-component molecular crystal’’,[40] this includes solvates and hydrates, and does not discriminate between formally charged systems (salts) versus neutral ones as defined by the extent of proton

transfer along a hydrogen bond.[41] Mechanical mixing of molecular crystals, manually or by ball milling, is often effective for preparing cocrystals,[42] some of them can only be obtained via mechanical processing. Kuroda et al. obtained three-component cocrystals based on racemic bis-β-naphthol, benzoquinone and anthracene.[43,44] It is noteworthy that the resulting cocrystal could not be obtained from solution.[45]

Mechanochemistry and cocrystallisation are becoming increasingly established as versatile approaches to discovering new solid forms of pharmaceutically active compounds.[2]

The use of mechanochemical methods in organometallic synthesis (coordination complexes and coordination polymers) is relatively new, but it is a very active and promising research area. The development of greener, more selective processes and new compounds attracts increasing attention.[11]

2.4 Mechanical Milling: Equipment and Process Variables

Mechanical milling is a relatively simple powder processing method capable of industrial exploitation on different scales.[46] In a typical mechanical milling experiment, a suitable powder mixture of reagents is placed in a high energy mill, along with a suitable milling tool.[47] Periodic movement of the reactor allows the milling tools to collide with each other and with the reactant powder, subjecting the latter to mechanical load. The reduction of particle size and the blending of particles in new phase is the objective of milling. The typical mill used for these purposes has been the high energy ball mill such as tumbler ball mills, vibratory, planetary and attritor mills.[48] An extensive coverage about different mills for Mechanical Milling is discussed in Suryanarayana book [49] but in this context we are mostly interested in high energy ball mills because they are the most commonly used.

The tumbler ball mill (Figure 2.1) is a rotating cylindrical vessel that rolls about its axis. The balls may roll down the surface of the chamber in a series of parallel layers or they may fall freely and impact the powder and the other balls below them. The tumbler ball mill is operated closed to the critical speed over which the

balls are pinned to the inner walls of the mill because of the centrifugal force dominating over centripetal force.[48]

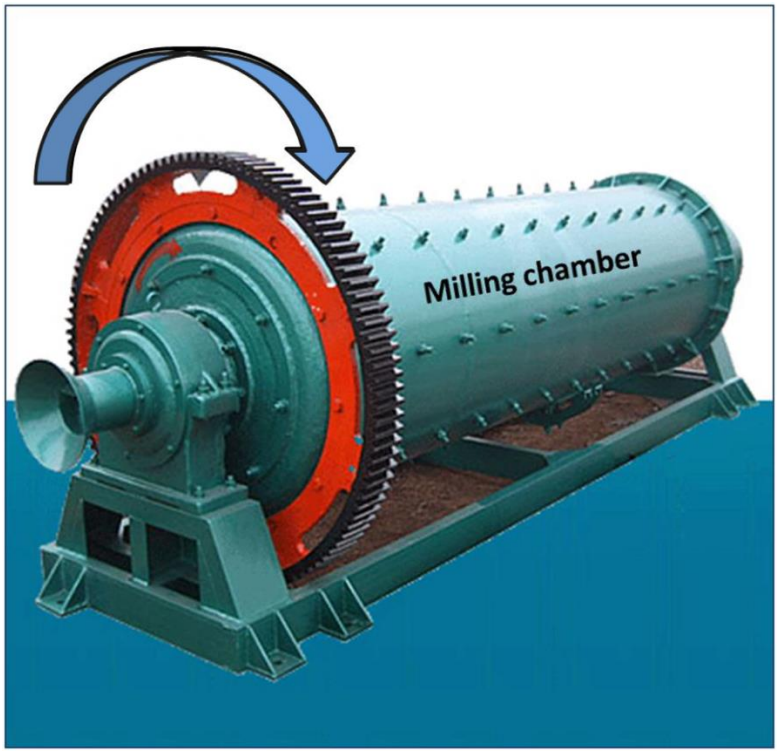

Figure 2.1. A tumbler ball mill. This picture is reproduced according to ref:48.

Another mill is the attritor mill in which the agitator has a vertical rotating shaft with horizontal arms. The latter causes a differential movement between the balls and the powder and provides a much higher degree of surface contact than is achieved in tumbler ball mills. The kinetic energy imparted depends on the speed of rotation of the tumbler mill cylinder or the attritor shaft for tumbler ball mill and attritor mill respectively.[50] A particular and very efficient attritor mill is the Simoloyer model which may be describe as the high kinetic horizontal rotatory mill (Figure 2.2). It is equipped with horizontal arms and knives.[51]

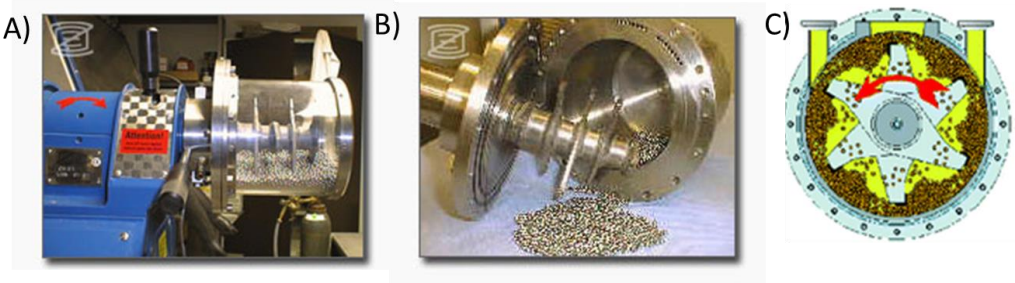

Figure 2. 2. A) the front part of the Simoloyer mill, B) the cross section of the grinding unit and C) frontal view while rotating with balls. This picture is reproduced according to ref:52.

For pilot-size production the vibratory mill is used. The container is vibrated and the impact forces acting on the powders are a function of the rate of milling, amplitude of vibration, and mass of the milling medium. High energy milling forces can be obtained by using high vibrational frequencies and small amplitudes of vibration.[48] A common vibratory mill is the SPEX 8000 shaker that has been used for laboratory scale research. The vessel is moved at high frequency in a complex cycle that involves motion in three orthogonal directions. The centre of the jar vibrates in two directions (x and y axis) with the same frequency and different amplitude, its slanted axis rotates around the third direction (z axis).[53] Rotation and vibration movements have the same frequency (Figure 2.3).

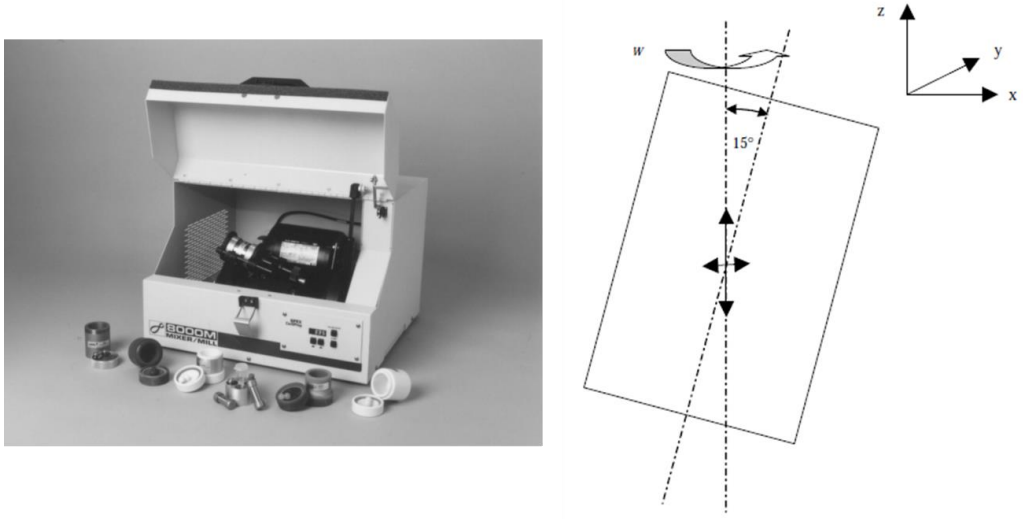

Figure 2.3. Picture of a SPEX 8000 mixer/mill on the left, schematic representation of the movement of the SPEX 800 on the right. This picture is reproduced according to ref:53.

As the motion of this mill can be considered more complex, W. Chen and coworkers investigated a numerical modeling method to develop a theoretical description of the milling process using the SPEX 8000 shaker mill.[53] The purpose of their study was to examine dynamic impacts inside the milling apparatus and develop a correlation between theoretical results and experimental data.

It is noteworthy that the driving force for the milling process is the innumerable impacts between ball and ball, and ball and vessel. Energy dissipation during the impact contributes to changes in the milled powder, as the latter is trapped between impacting surfaces. Energy dissipation arises from ball-ball and ball-vessel wall collisions, and is calculated in the term of the energy dissipation rate by the following equation: [53]

$$E_d = \sum_{k=1}^{N_c} \frac{\Delta E_k}{t_s} = \sum_{k=1}^{N_c} \frac{(E_1 - E_2)_k}{t_s} \qquad (1)$$

E_1 and E_2 are the energies of a binary impacting system before and after a collision, respectively; *k* represents the collision index, and N_c is the total number of collisions during the time interval, t_s. For a ball-ball collision, the energy of the impacting system is calculated as following:

$$E_{1,2} = \frac{1}{2} m_i v_i^2 + \frac{1}{2} I_i \omega_i^2 + E_{p_i} + \frac{1}{2} m_j v_j^2 + \frac{1}{2} I_j \omega_j^2 + E_{p_j} \qquad (2)$$

1, *2* subscripts are referred to the impact energy before (E_1) and after the collision (E_2) respectively; *i*, *j* are two crashing balls indices; *v* is the translational velocity; ω is the rotational speed of each impacting ball; *m* is the mass and *I* is the moment of inertia of the ball; and E_p is the potential energy of the ball under gravity (E_p=*mgh*, where *h* is height of mass center, and *g* is the gravitational acceleration). For a ball-vessel wall interaction, the energy of the impacting system is:

$$E_{1,2} = \frac{1}{2} m_i \Delta v_i^2 + \frac{1}{2} I_i \omega_i^2 + E_{p_i} \qquad (3)$$

Δv_i is the relative impact velocity between the ball *i* and the vessel wall with which the ball collides.

The Chen study based both on the experimental results for initiation (or trigger) of the thermite reaction $2Al + Fe_2O_3 \longrightarrow 2Fe + Al_2O_3$ and theoretical model report E_d for four different ball sizes and three various ball-to-powder ratios.[53] Note that the ball to powder mass ratio, also named charge ratio, C_R, ($C_R = m_b/m_p$ where m_b is the ball mass and m_p is the powder mass) is related to the dissipation energy by the following equation:

$$\frac{E_d t_{init}}{m_p} \propto C_R \cdot t_{init} \qquad (4)$$

When t_{init} is the milling time required to initiate the thermite reaction.

Some trends were observed:

a) keeping constant C_R largest ball size involves biggest E_d

b) generally, for all ball sizes, most collisions occur at an angle that is in range 80-90°. Such impact can be classified as oblique or *glancing impacts*, while minor fraction of collisions occurring at the angles less than 30° (which can be called *head-on collision*). However *glancing impact*s do not contribute significantly to the milling progress while *head-on collisions* are formed to be more effective;

c) another observation is that the collision energy dissipation rate is proportional to the total ball mass and is nearly independent of the ball size.

Experimental and theoretical calculation for the thermite reaction indicated that the milling progress is most significantly affect by milling media collisions with the energy within a specific threshold, while the collision with smaller and greater energies are less effective. In this particular reaction the 5 mm ball size represent the most efficient milling condition for the examined charge ratios (C_R= 2.5, 5,10)

Another mill used for laboratory scale synthesis is the planetary mill. It takes its name from the motion of the components, much similar to the motion of planets. It consists of two or more jars that rotate around its axis (with angular velocity ω) installed on a disc, which is also rotating, in a generally opposite direction with speed Ω ($\omega = - R (\Omega)$,[54] where R usually ranging from 1 to 5 (Figure 2.4)). Depending on the relative speeds of these two rotations this motion causes the ball bearings to move around the surfaces of the walls (*attrition mode*) or jump across

the vessel and impact against the sides (*collision mode*).[55] Inside the jars, the grinding is caused by high-energy impacts between the balls (whose movement is due to the centrifugal and Coriolis forces) and the walls of the jar and the powders of reagents, typically, covering the surfaces of balls and jar. The energy available for grinding and, consequently, the characteristics of the final product depend closely on many parameters, related both to the geometry that the physical properties of the constituent parts of the mill prossess. Among these can certainly be included the size of spheres and jars, the elasto-plastic properties of the materials, the friction effect, the angular speed of the rotating parts, the grinding time and, finally, the amount of introduced material and the degree of filling of the jar, φ_b.[56] Planetary mills often have larger capacities than shaker mills, but generally have also a lower impact frequency and for this reason they are considered being of lower efficiency than shaker mills.[55]

Magini and coworkers calculated the power transferred from the planetary mill to the system during collisions: [57]

$$P = \varphi_b \Delta E_b N_b f_b \qquad (5)$$

When the vessel is completely filled by balls and no movement is possible $\varphi_b = 0$, on the other hand $\varphi_b = 1$ is possible when the vial is filled with one ball. ΔE_b [$\Delta E_b = 1/2 m_b(v_b^2 - v_s^2)$] is the total energy released during the collisions by the ball having mass m_b and velocity before and after collision v_b and v_s respectively; N_b represent a finite number of balls, $f_b = K(\Omega-\omega)/2\pi$, the frequency with which balls are launched (K is a constant).

This model is confirmed by experimental results and allow practical indications in order to set up the suitable milling conditions with different planetary mills and milling materials in order to modulate the process path and to obtain the wanted end product.[57]

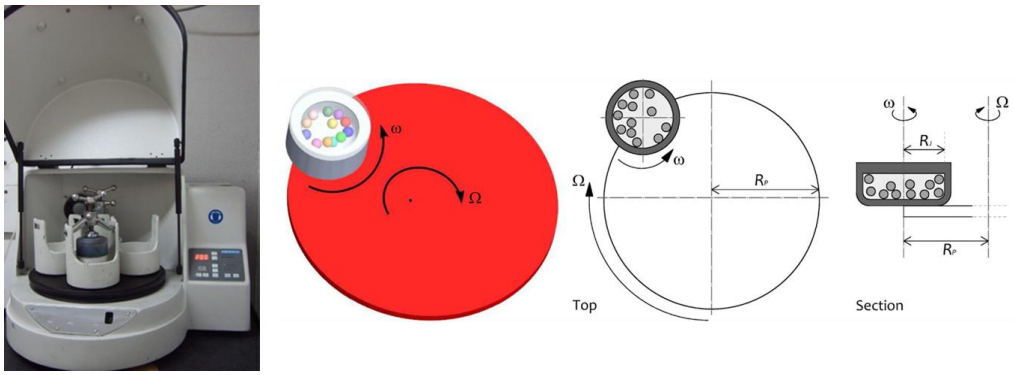

Figure 2.4. Planetary ball mill picture on the left, and 3D and 2D schematic representations of the planetary balls mill on the right. In 2D views is defined the radius of the jar, Rj, and the distance between the axes of rotation (angular velocity ω) and revolution (angular speed Ω), Rp (also coincident with the radius of the dish). This picture is reproduced according to ref:56.

The energy transfer during the mechanical milling is governed by many parameters such as the type of mill, the powder supplied to drive the milling chamber, milling speed, size and size distribution of the balls, dry or wet milling, temperature of milling and the duration of milling.[58] Another useful parameter associated with ball milling is the ball-to-powder ratio; the mass of balls over the mass of reactants.[55]

The kinetic energy of the balls is a function of their mass and square velocity. Steel and tungsten carbide are dense materials (d= 7.8 g/cm^3 and d= 15.8 g/cm^3 respectively) and sometimes are preferable to less dense materials like ceramic balls (d_{agate}=2.6 g/cm^3, $d_{zirconia}$= 5.7 g/cm^3) but in other kind of experiments the latter are more suitable. The size distribution should be optimized on the basis of the mill used.[59] A dilute distribution of balls minimizes the collision frequency (impact mode is therefore dominant), while a dense packing reduces the mean free path of the ball motion and promotes the friction mode. The material of which the milling media and the powder are made of and therefore the kinetic energy of the ball can influence the temperature during milling. The grinding speed and the duration of milling affect the kinetics, for example the faster the milling speed, the higher the energy input, and generally the reaction is faster. On the other hand high speeds can result in higher temperatures, that may cause side reactions or pollution from the jar material.[55]

2.5 Mechanistic aspects

The central event in mechanical milling is the collision between balls and powder. Powder particles are trapped between the colliding balls during milling and undergo deformation and/or fracture processes which define the ultimate structure of the powder. The nature of these processes depends upon the mechanical behavior of the powder components.[48] Mechanistic studies are different depending on the reaction condition, reaction type and reactive material. Organic reactions, especially for cocrystals synthesis, have been much more thoroughly investigated than coordination compound reactions. There are a lot of similarities in both areas and consequently, analogies can be drawn.[60] The physical effects that grinding have on molecular crystals include: (i) breaking down particles to smaller sizes, giving greater surface area and breaking up any product coating layers to expose fresh surfaces, (ii) intimate mixing of reactants, (iii) introducing defects and eventually amorphization of the material, and (iv) frictional heating, both local and bulk.[2]

Neat grinding, NG, is the simplest form of mechanosynthesis, as it involves grinding a physical mixture of two or more reactants using a mortar and a pestle or a mechanical ball mill. Neat grinding reactions are considered to take place in a dry environment but as already mentioned most neat grinding reactions involve the use of hydrated metal salts (e.g., acetates or nitrates) as precursors.[61,62] Therefore, water or acid can be liberated during a mechanochemical reaction. The formation of water or acid could serve as a liquid phase that facilitates the mechanochemical reaction (as in LAG method) or templates the formation of a specific structure.[1]

LAG, also known as the kneading method, was introduced with the cocrystal mechanosynthesis. In contrast to neat grinding, LAG utilizes the addition of small quantities of a liquid phase to assist or enable the mechanochemical reaction. LAG synthesis for cocrystals has resulted in quantitative yields, short reaction times, and a greater scope of reactants and products.[1]

Cocrystallisation reactions are accelerated by liquid-assisted grinding (LAG) giving products of higher crystallinity compared to neat grinding. Cocrystals obtained via LAG are likely related to enhanced molecular diffusion and the plasticizing effect of the liquid phase, suggesting a means to avoid amorphous impurities that usually result from neat grinding.[1] The term liquid-assisted grinding does not presuppose that the liquid added plays the role of solvent but in some cases correlations of reactivity with reactant solubility have been noted,[63] suggesting that solvation and therefore solubility effects can be significant. The nature of the added liquid can also determine the product obtained without being included within it.[64] Recently, in the field of coordination chemistry similar observations have been made. LAG synthesis was found to improve the rate of mechanochemical synthesis.

Another mechanosynthesis method is neat grinding followed by annealing. It is represented by the heating of the product initially obtained by neat grinding, it can carry on a consequent reaction and the formation of new products. An example of a coordination polymer obtained with annealing was demonstrated by Kuroda. The formation of discrete monomeric β diketonate complexes with axially coordinated water molecules can be carried out by grinding 3-cyanoacetylacetone with acetates of divalent transition metals.[65,66] This product annealing results in the expulsion of water and the formation of a 3D metal-organic polymer.

2.6 Mechanochemical reactivity leading to coordination bonds

Coordination polymers and metal organic frameworks can be constructed using different mechanochemical methodologies discussed in the previous section, such as NG and LAG synthetic strategies, in order to obtain different types of reactions that lead to the formation of coordination bonds. There are different reaction types for coordination polymers construction: 1) ligand addition, 2) ligand exchange, 3) acid-base reactions.

2.6.1 Coordination polymers by ligand addition

Probably the simplest methodology to coordination polymer construction via mechanochemistry is the addition of neutral ligands. An example of this reaction type was reported by Pichon and James using NG for the $Cu(acac)_2(bipy)_n$ 1-D polymer mechanosynthesis, starting from cupper(II) acetylacetonate and 4,4'-bipy. The ligand addition is a type of reaction with a stepwise mechanism that has been observed during neat grinding of anhydrous $ZnCl_2$ with the diamine [2.2.2]-diazabicyclooctane (dabco).[67] The first step is the formation of an intermediate hydrate $ZnCl_2(dabco)\cdot 4H_2O$ phase, which upon heating or further grinding led to the 1-D zigzag dehydrate polymer $ZnCl_2(dabco)$. The same reaction carried out in dry air and with non-hydrated reactants can lead directly to the $ZnCl_2(dabco)$ polymer.[67] The same reaction using the less hydroscopic 4,4'-bipyridine led directly to the analogous 1-D zigzag dehydrate polymer.[68]

An example of a NG reaction using anhydrous and hydrated $CoCl_2$ shows that the 2-D sheet polymer is obtained only with the hydrate metal salt, with the anhydrous form the formation of the desired polymer is not possible.[68] Therefore, the water produced by desolvation of the reagent plays an important role for the mechanochemical reactivity. The 2-D sheet polymer using anhydrous $CoCl_2$ is possible only by using the LAG method. The addition of a liquid phase is not only useful to accelerate or enable a mechanochemical reaction, but also an opportunity for molecular inclusion in hosts. An example is the $CuCl_2(dace)$ host polymer, obtained from $CuCl_2$ and 1,4-diaminocyclohexane (dace), that with the inclusion of DMSO gives rise to $CuCl_2(dace)_n\cdot DMSO$ by LAG in DMSO. The analogous coordination polymer by NG is not obtained.[69]

2.6.2 Coordination polymers by ligand exchange

Another frequent reaction type in mechanosynthesis of coordination polymers is ligand substitution. The mechanochemical formation of new metal-ligand bonds

often involves breaking connections between metals and water, with water removal.

Manual grinding of silver acetate and dabco (diamine [2.2.2]-diazabicyclooctane) displaces the acetate ligands by dabco with the immediate water absorption from the air that gives $AgOAc(dabco)_2 \cdot 5H_2O$.[67] This is an example of the surrounding atmosphere importance for mechanosynthesis.

2.6.3 Coordination polymers by acid-base reactions

This coordination polymer reaction approach involves the proton transfer from an acid species to basic species, for example hydroxide, carbonate or oxides. There is also the possibility of adding an external base or incorporating basic anions into reactants.[1] An example of the first type is the possibility of using potassium hydroxide to achieve the dehydrohalogenation of 4,4'-bipyridinium tetrachlorometallate salts with the elimination of potassium chloride and water as byproducts (Figure 2.5a).[70] The alternative way of basic anions incorporation is shown in the LAG reaction of a metal precursor with an acidic reagent, such as a bis(pyridinium) salt or a carboxylic acid towards the formation of the desired coordination polymer and the formation of carbon dioxide and water as byproducts (Figure 2.5b).[1]

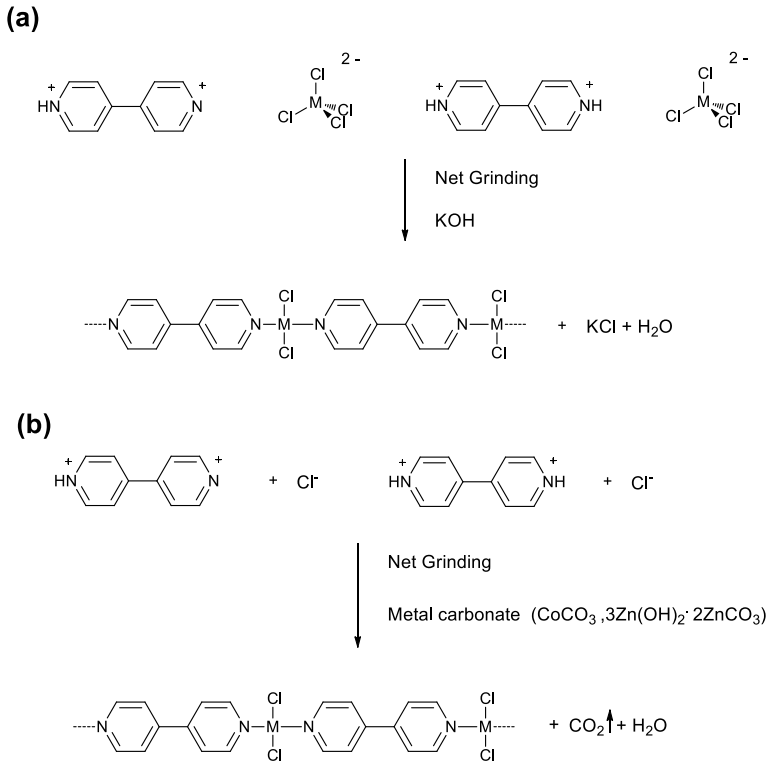

Figure 2.5. Coordination polymers by acid-base reaction: (a) addition of potassium hydroxide , an external reagent, and (b) use of a metal salt of a basic anion, such as carbonate or hydroxide.[1]

In this context, it is also possible to use slightly soluble metal oxides; these are very attractive for their low cost and because their only byproduct is water. Several coordination polymers have been constructed by using zinc oxide with different organic ligands. An example of coordination polymers with metal oxide are shown by T. Friscic˘ and coworkers.[71] They obtained from zinc oxide and fumaric acid (fum) different products by using various solvents for LAG synthesis. In methanol and ethanol they obtained an anhydrous 3-D non-porous coordination polymer of zinc fumarate. In a water and ethanol 1:1 mixture a dihydrate form was obtained and the structure was solved by X-ray powder diffraction and it was identified as a 2-D polymer. Moreover, the same reaction using increasing amounts of water reveals two different 1-D structures, tetrahydrate and pentahydrate. It is noteworthy that in this example LAG syntheses result in four different structures by changing only the solvent phases (Figure 2.6).

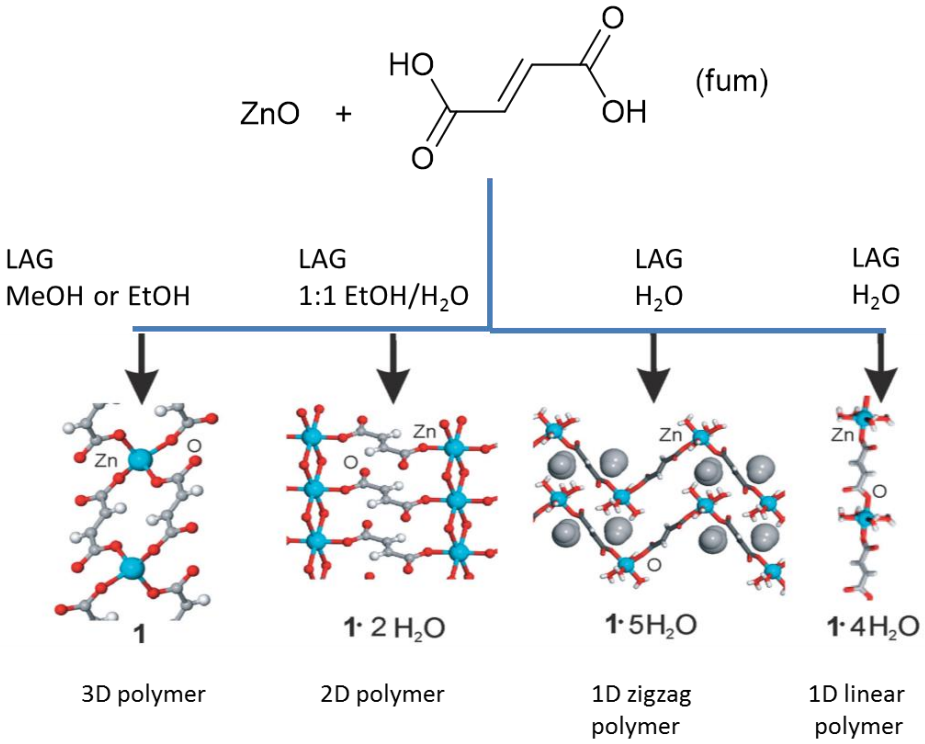

Figure 2.6. Comparison of different products obtained from zinc oxide and fumaric acid (fum) by using various solvents for LAG syntheses. Guest water molecules are shown in gray. This picture is reproduced according to ref :71.

2.7 MOFs by mechanosynthesis

The first MOF obtained by NG was the microporous 3-D copper(II) isonicotinate. It was synthesized by the reaction between copper(II) acetate monohydrate and isonicotinic acid (HINA).[61] In a few minutes of grinding a product was obtained that was almost completely coincident with the simulated, XRPD pattern, with included water molecules and a partial inclusion of acetic acid. After heating the resulting desolvated product has an identical XRPD pattern with the expected pattern. Pichon used a similar approach to the HKUST-1 NG synthesis.[62] This nanoporous framework was obtained in quantitative yield by grinding $Cu(OAc)_2 \cdot H_2O$ and 1,3,5-benzeentricarboxylic acid (H_3BTC). The XRPD pattern of this material was compared with the same product given by solvent-based synthesis. Broader peaks in the NG samples were due to the smaller particle size. The same HKUST-1 material was also reported by using LAG in different solvents (100 μL AcOH, MeOH, EtOH, DMF).[72] The LAG approach does not

accelerate the $Cu_3(BTC)_2$ formation. On the contrary, the same LAG experiment was performed on the $Cu(INA)_2$ MOF formation from the same metal salt $Cu(OAc)_2 \cdot H_2O$ and the isonicotinic acid (HINA). In the latter example the addition of a liquid phase, AcOH (acetic acid), dramatically accelerates the reaction and that may reflect the higher solubility of HINA than H_3BTC in this solvent. However, a benefit of using LAG is also found in the case of $Cu_3(BTC)_2$, where the addition of solvent leads to slightly sharper peaks in XRPD pattern and better-defined crystallites in SEM images. A further investigation of $Cu(INA)_2$ synthesis was achieved by mechanochemical activation and ageing.[61] This process was performed by grinding the reaction mixture for 1 minute resulting in a partial formation of the MOF and an ageing of 6 hours in which the $Cu(INA)_2$ is quantitatively obtained with larger and morphologically better-defined crystals compared with the sample obtained in case of continuous grinding.

Mechanochemistry has also been used for the synthesis of MOFs pillared such as [Zn(BDC)(bipy)] and [Zn(BDC)-(dabco)(H_2O)].[73] Different types of Zn(BDC) structures were obtained by grinding H_2BDC and zinc oxide or zinc carbonate in LAG syntheses (using 100 μL of H_2O, MeOH or DMF). These primary materials were reacted with additional bridging ligands, 4,4'-bipyridine or dabco by NG synthesis in order to provide 3-D [Zn(BDC)(bipy)] and 2-D [Zn(BDC)-(dabco)(H_2O)] structures respectively (Figure 2.7).

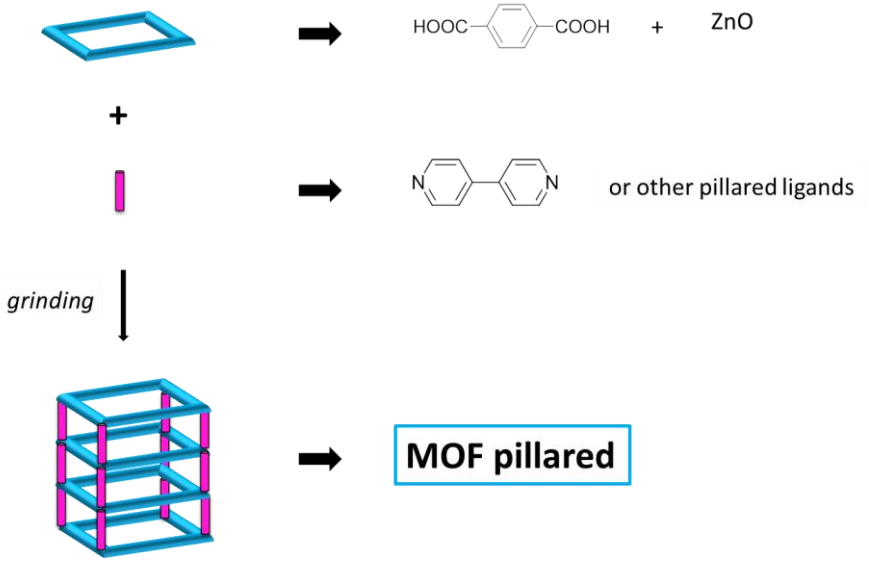

Figure2.7. Schematic representation of MOF pillared by ball milling.

Furthermore, another family of materials, ZIFs (Zeolitic imidazolate fremeworks) was synthesised by mechanochemical methods. A set of ZIFs based on zinc oxide and imidazole (Him), 2-methylimidazole (HMeIm) and 2-ethylimidazole (HEtIm) was obtained by LAG and ILAG (ion-and liquid-assisted grinding) synthesis.[74] A mechanochemical reactivity study was performed using DMF, DEF and EtOH solvents and NH_4NO_3, $(NH_4)_2SO_4$ and $NH_4CH_3SO_3$ as salt additives for ILAG method. As already demonstrated for other MOFs the ILAG synthesis accelerates the formation of the desired structures. The topological control in ILAG synthesis of ZIFs appears to arise from the ability of salt additives to control the rate of spontaneous interconversion of porous and non-porous structure.

The first successful ILAG mechanosynthesis of pillared MOFs was reported by Friščić and coworkers.[75] They synthesized $[Zn_2(bdc)_2(dabco)]$ MOF which has several tetragonal isomers and one hexagonal by using salts that are specific for the tetragonal product, for example NH_4NO_3 or for the hexagonal phase, K_2SO_4. That nitrates and sulfates induce the formation of different isomers suggests an anion-templating mechanism.[76] XRPD analysis revealed that KNO_3 is not observed in the product if its quantity is below 7 mg (w~5%). In contrast, NH_4NO_3 could not be detected even at 22 mg loadings (w~13%).[75] These observations support the anion-templating mechanism and suggest that different salts become included in the MOF in variable amounts.[76] The role of the salt additive in ILAG mechanosynthesis of pillared MOFs is different from the role in ZIFs. While the synthesis of pillared MOFs using ILAG shows an anion-related effect, ZIF synthesis strongly depends on the use of weakly acidic ammonium salts.[77]

Very recently, also MOF-5 from the archetypal family of IRMOFs was obtained with a mechanochemical strategy starting from an oxo-zinc benzoate as precursor.[78] After 60 minutes milling of oxo-zinc benzoate and H_2BDC in presence of DEF (N,N-diethylformamide) the MOF-5 was obtained and characterized with XRPD that revealed the isostructurality with the same material obtained by solvent-based reaction.

2.8 Aim of this research

As already established above, mechanochemistry is a green method for various chemical reactions with particular importance in this PhD thesis for the construction of covalents bonds.

The first part of the three-year research project deals with the mechanochemical synthesis of porous coordination polymers, MOFs. In the literature there has been reported a wide range of carboxylate-based MOF, with promising performances also in ball milling synthesis (2.6). Due to the importance of MOFs in a wide range of applications, we focused the research project on an iron (III) carboxylate metal organic framework isostructural with MIL-100(Fe).

MIL-100(Fe) was first discovered by Horcajada [79] and co-workers in 2007, when they synthesized that material by solvothermal synthesis with HF. Its structure was solved from synchrotron X-ray powder diffraction data using coordinates of MIL-100(Cr) as the starting mode. MIL-100(Fe) consists of trimers of iron octahedral sharing a common vertex, indicated as (μ_3-O). The trimers are linked by the benzene-1,3,5-tricarboxylate (BTC) moieties resulting in the formation of a supertetrahedral structure. This structure exhibits two types of mesoporous cages of 25 and 29Å, accessible through microporous windows of 5.5 and 8.6 Å (Figure 2.8). The MIL-100(Fe) thermal stability was measured to be greater than 270°C and the permanent porosity was studied with N_2 adsorption experiment where the characteristic isotherm curve typical of microporous materials was observed.[79]

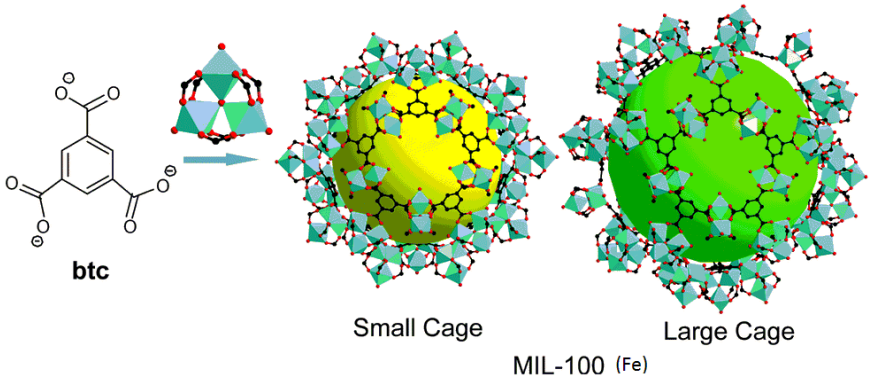

Figure 2.8. Illustration of MIL-100 obtained from the BTC linker (benzene-1,3,5-tricarboxylate) and the Fe^{3+} trigonal-prismatic cluster. Color scheme: chromium (turquoise); O (red); C (black). This picture is reproduced according to ref:80.

As is well known in literature (and previously reported in section 1.5.4) the presence of coordinatively unsaturated metal centers (UMCs) into porous MOFs is very useful because these UMCs can strongly interact with organic molecules in catalysis. MIL-100(Fe) exhibits unsaturated metal centers and it is one of the most interesting MOFs for catalytic applications. The same research group that first proposed the solvothermal synthesis also examined its catalytic properties in the Friedel–Craft benzylation of benzene by benzyl chloride (Figure 2.9), and found that MIL-100(Fe) could afford diphenylmethane with high activity and selectivity (nearly 100%) after a short induction period (5 min).[79]

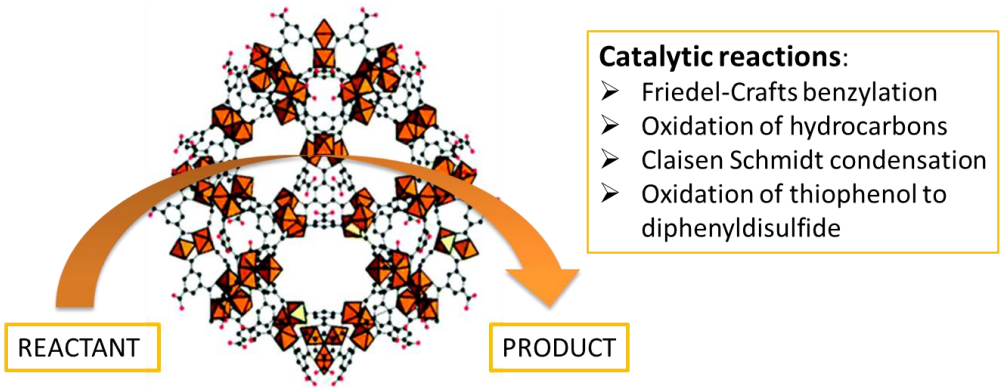

Figure 2.9. Schematic representation of MIL-100 (Fe) catalytic properties.[81]

Based only on the presence in literature of the microwave synthesis[82] as an alternative route for MIL-100 (Fe) building, we have applied for the first time mechanochemical synthesis as a novel and alternative way to obtain this material. A heterogeneous catalysis experiment was also performed concerning the evaluation in diesel fuel desulfurization.

The mechanochemical strategy was also adopted in the second part of the research project where we focused our attention on coordination polymers based on square-planar Ni(II) complexes and a set of N-donor molecules.

The traditional synthetic approaches for the construction of coordination polymers is the use of covalent coordinative bonds between transition metal ions, also called nodes, and suitable polydentate organic ligands, also named spacers or

linkers.[83] The employment of "naked" metal ions increased the number of products potentially available and therefore introduces a certain grade of uncertainty.[84] In order to reduce this degree of freedom, we used preformed coordination compounds as nodes with coordinative unsaturation to be able to coordinate neutral donor molecules.[85] We base this part of the project on a set of neutral square planar nickel(II) dithiophosphato [$Ni(PS_2(OR)_2)_2$] and dithiophosphonato [$Ni(ROdtp)_2$] complexes [dtp = $((CH_3O\text{-}C_6H_4)(RO)PS_2)$; R = Me, Et]. These square planar building blocks have high tendency to form octahedral complexes with pyridine and its derivatives.[86]

The IUPAC terminology for phosphor-1,1 dithiolate class of compounds is reported in Figure 2.10, indicating dithiopho*sphat*es (phosphorodithioate), dithiopho*sphi*nates (phosphinodithioate), dithiopho*spho*nates (phosphonodithioate) and amidodithiopho*spho*nates (amidophosphonodithioate) with regard to the different substituents bonded to the phosphor atom.[87]

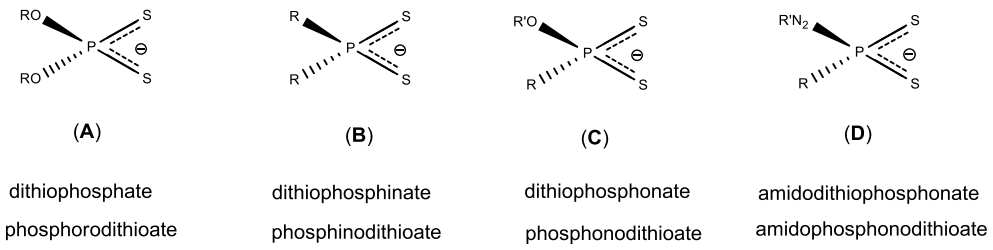

Figure 2.10. Different types of phosphor-1,1,-dithiolates based on various substituents on the P atom.[87]

Phosphor-1,1 dithiolate compounds can be described by four resonance structures. The predominate structure depends on the metal type, oxidation state and coordination geometry.[87]

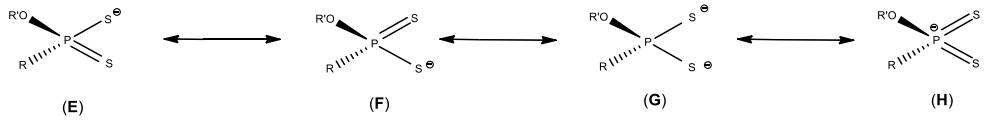

Figure 2.11. Contributing resonance structures for dithiophosphonato ligands.[87]

For complexes for which the ligand binds in a μ1-fashion (monodentate) with one sulfur atom only, the resonance structures E and F have been observed and

examples of this type can be found in some Pb(II), Hg(II), and Zn(II) complexes. Resonance structure G predominates in many dinuclear Au(I) complexes and in Ni(II) isobidentate chelating mononuclear complexes. Evidence of G is usually shown by the two equal P-S bond lengths in the solid state. Structure H is actually unknown for metal dithiophosphonates but included here for completeness.[88] In Figure 2.12 are reported the major coordination modes categorized for mononuclear metal centers with mono- or biconnectivity. Where with connectivity is intended the number of connections between the metal ion and the sulfur atom (aniso- or iso-bidentate coordination).[87, 89]

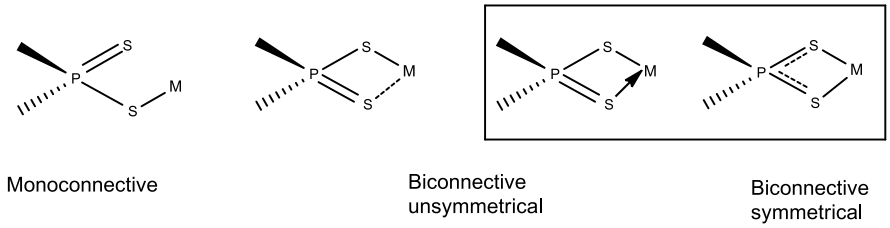

Figure 2.12. Different connectivity for mononuclear metal centers.

Nickel(II) dithiophosphato [$Ni(PS_2(OEt)_2)_2$], bis(O-ethyldithiophosphato)Ni(II**)** (**1**) and [$Ni(PS_2(OEt)_2)_2$], bis(O-methyldithiophosphato)Ni(II) (**2**) are constituted of centrosymmetric units in which the two dithiophosphato units are coordinated to the central nickel atom through the sulfur atoms in a square-planar environment and the phosphorus atoms bond to the substituents, -OEt or -OMe for **1** and **2** respectively (Figure 2.13 and 2.14a). Moreover, nickel(II) dithiophosphonates [$Ni(EtOdtp)_2$], trans-bis[O-ethyl-(4-methoxyphenyl)dithiophosphonato]Ni(II) (**3**) and [$Ni(EtOdtp)_2$], trans-bis[O-methyl(4methoxyphenyl)dithiophosphonato]Ni(II) (**4**) [dtp = ($(CH_3O\text{-}C_6H_4)PS_2$)] consist of centrosymmetric units in which the two dithiophosphonato units coordinated to the central nickel atom as S,S-bidentate ligands (Figure 2.13). The phosphorus atoms reside in a square-planar sphere with the 4-methoxyphenyl (anisole) and the –OR groups *trans* disposed with respect to the coordination plane define by the P(1), S(1) and S(2) atoms (Figure 2.14b).

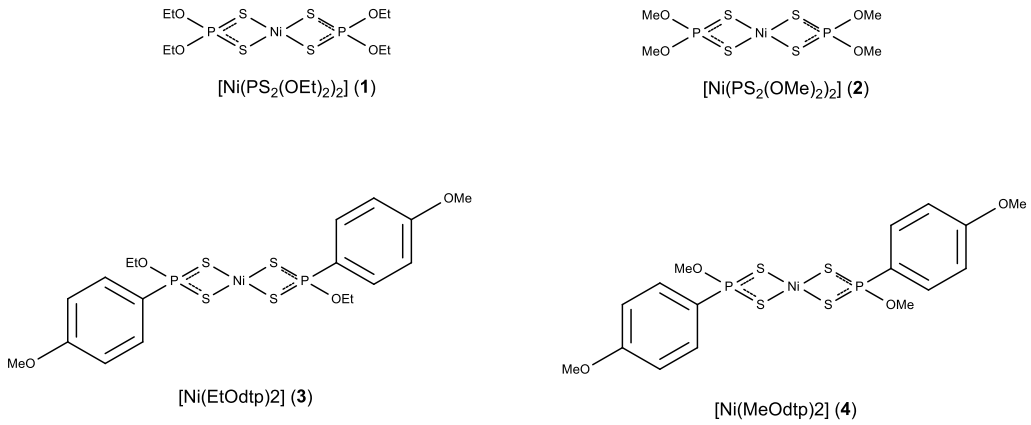

Figure 2.13. Dithiophosphato and Dithiophosphonato Ni(II) complexes formula structures.

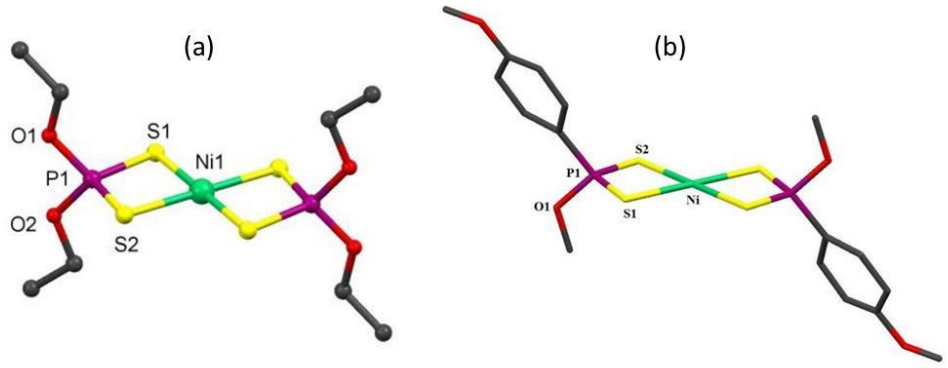

Figure 2.14 (a) Ball-and-stick representation of a nickel(II) dithiophosphato and (b) capped sticks representation of a nickel(II) dithiophosphonato (hydrogen atoms are omitted for clarity).

Aragoni and coworkers demonstrated that neutral square-planar Ni^{II} complexes can be bonded together with various nitrogen donors, such as pyridine, resulting in Ni^{II} octahedral complexes formation.[86] This tendency to form octahedral complexes with pyridine, has led to further investigations on the development of coordination polymers by using square-planar Ni^{II} complexes able to axially coordinate with N–R–N bidentate ligands. The same research group reported the solution based synthesis of coordination polymers by using 4,4'-bipyridine (bipy) as bidentate ligand that for topology reasons is unable to chelate the metal ion.[90,91] The polymeric structure was obtained where the bipy molecules coordinate two

independent complex units acting as linkers. Recently, further solution based synthesis with more complex ligands have been performed.[92]

We developed this second part of the research project with the collaboration of the research group of Prof. M.C Aragoni (University of Cagliari) due to their expertise in dithiophosphato and dithiophosphonato Ni(II) complexes and in the organic synthesis of new linkers. They have prepared and made available for my mechanochemical experimentation the metal complexes (**1)**,(**2)**, (**3)** e (**4**) and a set of organic linkers: 1,4-bis(3-pyridyl)-butadiyne (**L2**), 2,5-bis(4-pyridyl)-4-thia-1,3-thiazolidine (**L3)** and 2,5-bis(3-pyridyl)-4-thia-1,3-thiazolidine (**L4**) (Figure 2.15). **L1 (**4,4'- bipyridine) is commercially available.

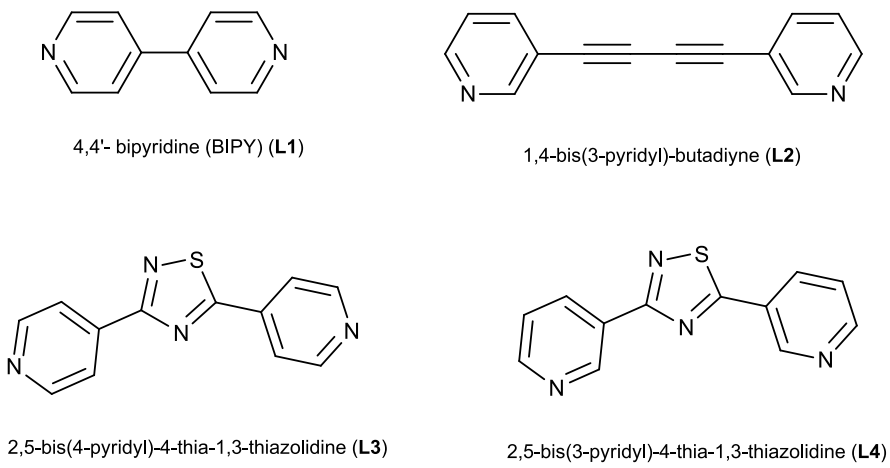

Figure 2.15 Formula structures of polypyridyl ligands used as organic linkers.

The third part of the PhD project has been carried out in the research group of Prof. Neil R. Champness at the *School of Chemistry*, *University of Nottingham* (UK). This part of the project is focused on the conventional solution based synthesis of N-donors ligands to be used for coordination polymers synthesis. The project has concerned the investigation of naphthalene-1,4,5,8-tetracarboxylic diimides (NDIs) as the simplest member of the rylene class of molecules (Figure 2.16). NDIs have high electron affinities and mobilities, intense absorbance in the visible spectrum and excellent chemical and thermal stabilities. NDIs molecules

exhibit an imide and core regions. Variation of substituents in these two regions leads to the modification of the electronic properties.[93]

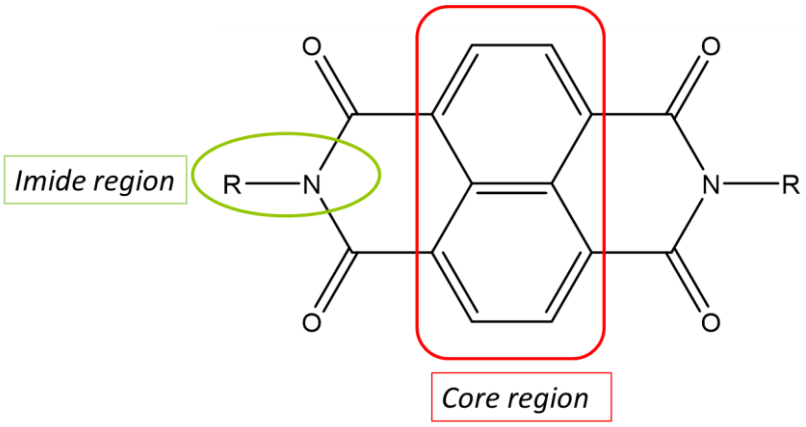

Figure 2.16 General structure of NDIs with the imide region (green) and core region (red).

In addition to the variation of substituents on imide and core regions, another modification can be made to NDIs molecules. The substitution of oxygen with sulfur, also named thionation, has been used to change carbonyl groups into thiocarbonyls. It is already known that thionation can be used to modify optical and electronic properties of a molecule without having large-scale changes to the molecular structure.[94,95] In literature there are very few examples where carbonyl thionation is used to modify the properties of rylene diimides, some of those examples were obtained in Champness research group.[96] In this context, I developed 6 months of experience in NDIs synthesis and then consequently thionation.

2.9 References

1. MacGillivray, L. R., *Metal-organic frameworks: design and application*. John Wiley & Sons: **2010**.

2. James, S. L.; Adams, C. J.; Bolm, C.; Braga, D.; Collier, P.; Friscic, T.; Grepioni, F.; Harris, K. D. M.; Hyett, G.; Jones, W.; Krebs, A.; Mack, J.; Maini, L.; Orpen, A. G.; Parkin, I. P.; Shearouse, W. C.; Steed, J. W.; Waddell, D. C., Mechanochemistry: opportunities for new and cleaner synthesis. *Chemical Society Reviews* **2012,** *41* (1), 413-447.

3. Bowmaker, G. A., Solvent-assisted mechanochemistry. *Chemical Communications* **2013,** *49* (4), 334-348.

4. Trask, A. V.; Jones, W., Crystal engineering of organic cocrystals by the solid-state grinding approach. In *Organic solid state reactions*, Springer: **2005**; pp 41-70.

5. Braga, D.; Giaffreda, S. L.; Grepioni, F.; Pettersen, A.; Maini, L.; Curzi, M.; Polito, M., Mechanochemical preparation of molecular and supramolecular organometallic materials and coordination networks. *Dalton transactions* **2006,** (10), 1249-1263.

6. Karki, S.; Friščić, T.; Jones, W., Control and interconversion of cocrystal stoichiometry in grinding: stepwise mechanism for the formation of a hydrogen-bonded cocrystal. *CrystEngComm* **2009,** *11* (3), 470-481.

7. Shan, N.; Toda, F.; Jones, W., Mechanochemistry and co-crystal formation: effect of solvent on reaction kinetics. *Chemical Communications* **2002,** (20), 2372-2373.

8. IUPAC Compendium of Chemical Terminology, n. e. t.; Wilkinson., G. B. C. b. A. D. M. a. A.; Blackwell Scientific Publications, O. X. o.-l.; by, c. v. h. g. i. o.-c.; M. Nic, J. J., B. Kosata; updates compiled by A. Jenkins. ISBN; 0-9678550-9-8. doi:10.1351/goldbook, h. g. i. o.; MT07141.html.

9. Friščić, T.; Trask, A. V.; Jones, W.; Motherwell, W., Screening for inclusion compounds and systematic construction of three-component solids by liquid-assisted grinding. *Angewandte Chemie* **2006,** *118* (45), 7708-7712.

10. Friscic, T.; Jones, W., Recent advances in understanding the mechanism of cocrystal formation via grinding. *Crystal Growth and Design* **2009,** *9* (3), 1621-1637.

11. Takacs, L., The historical development of mechanochemistry. *Chemical Society Reviews* **2013,** *42* (18), 7649-7659.

12. M. Faraday, Q. J. S., Lit., Arts, **1820**, 8, 374.

13. Lea, M. C., Researches on the latent image. *The British Journal of Photography* **1866,** *13*, 84.

14. Lea, M. C., On endothermic decompositions obstained by pressure; Part II, Transformations of energy by shearing stress. *American Journal of Science* **1893,** (276), 413-420.

15. Spring, W. V., *Recherches sur la propriété que possèdent les corps de se souder sous l'action de la pression*. Hayez: **1880**.

16. Ostwald, W., *Die chemische Literatur und die Organisation der Wissenschaft*. Akad. Verlag. Gesel.: **1919**; Vol. 1.

17. F. M. Flavitsky, Z. R. F. K. O. v., **1902**, 34, 8.

18. Bowden, F. P.; Yoffe, A. D., *Initiation and growth of explosion in liquids and solids*. CUP Archive: **1952**.

19. Gilman, J., During detonation chemistry may precede heat. *Materials science and technology* **2006,** *22* (4), 430-437.

20. Tabor, D., *The Friction and Lubication of Solids*. Oxford University Press: 1964.

21. Fink, M.; Hofmann, U., Oxydation von Metallen unter dem Einfluss der Reibung. *Zeitschrift für anorganische und allgemeine Chemie* **1933,** *210* (1), 100-104

22. Lynch, A.; Rowland, C., The History of Grinding. Society for Mining, Metallurgy and Exploration. *Inc.(SME), Littleton* **2005**.

23. Union Process web site, h. w. u. c.; about.html, r. o. S., **2012.**

24. J. Buie, h. w. l. c. a. v. a.; 4511/, L. M. M., retrieved on September 11,; **2012**.

25. Solsona, P.; Doppiu, S.; Spassov, T.; Surinach, S.; Baró, M., Evolution of amorphous and nanocrystalline phases in mechanically alloyed Mg 1.9 M 0.1 Ni (M= Ti, Zr, V). *Journal of alloys and compounds* **2004,** *381* (1), 66-71.

26. Benjamin, J.; Arzt, E.; Schultz, L., in 'New materials by mechanical alloying'. Oberursel, Germany: Deutsche Gesellschaft fur Metallkunde: **1989**.

27. Ermakov, A.; Yurchikov, E.; Barinov, V., Amorphous transition in intermetallic compounds induced by high ball milling. *Phys Met Metallogr* **1981,** *52* (6), 50-58.

28. Ennas, G.; Magini, M.; Padella, F.; Susini, P.; Boffitto, G.; Licheri, G., Preparation of amorphous Fe-Zr alloys by mechanical alloying and melt spinning methods. *Journal of Materials Science* **1989,** *24* (9), 3053-3058.

29. Cocco, G.; Enzo, S.; Schiffini, L.; Battezzati, L., X-ray diffraction study of the amorphization process by mechanical alloying of the Ni-Ti system. *Materials Science and Engineering* **1988,** *97*, 43-46.

30. Mulas, G.; Deledda, S.; Monagheddu, M.; Cocco, G.; Cutrufello, M.; Ferino, I.; Solinas, V. In *Metal supported catalysts prepared by Mechanical Alloying processes*, Materials Science Forum, Trans Tech Publ: **2000**; pp 889-894.

31. Koch, C.; Cavin, O.; McKamey, C.; Scarbrough, J., Preparation of ''amorphous'' $Ni_{60}Nb_{40}$ by mechanical alloying. *Applied Physics Letters* **1983,** *43* (11), 1017-1019.

32. Corrias, A.; Ennas, G.; Licheri, G.; Marongiu, G.; Paschina, G., Mechanical alloying of cobalt and boron powders. *Materials Science and Engineering: A* **1991,** *145* (1), 123-125.

33. Corrias, A.; Ennas, G.; Marongiu, G.; Musinu, A.; Paschina, G.; Zedda, D., The synthesis of nanocrystalline nickel boride powders by ball milling of elemental components. *Materials Science and Engineering: A* **1995,** *204* (1), 211-216.

34. Ennas, G.; Magini, M.; Padella, F.; Pompa, F.; Vittori, M., On the formation of Pd_3Si by mechanical alloying solid-state reaction. *Journal of non-crystalline solids* **1989,** *110* (1), 69-73.

35. Politis, C., Amorphous superconducting Nb_3Ge and $Nb_3Ge_{1-x}Al_x$ powders prepared by mechanical alloying. *Physica B+ C* **1985,** *135* (1-3), 286-289.

36. Murty, B.; Ranganathan, S., Novel materials synthesis by mechanical alloying/milling. *International materials reviews* **2013**.
37. Mater. Trans., J., **1995**, 36(2).

38. Todres, Z. V., *Organic mechanochemistry and its practical applications*. CRC Press: **2006**.

39. Braga, D.; Maini, L.; Giaffreda, S. L.; Grepioni, F.; Chierotti, M. R.; Gobetto, R., Supramolecular complexation of alkali cations through mechanochemical reactions between crystalline solids. *Chemistry–A European Journal* **2004,** *10* (13), 3261-3269.

40. Bond, A. D., What is a co-crystal? *CrystEngComm* **2007,** *9* (9), 833-834.

41. Childs, S. L.; Stahly, G. P.; Park, A., The salt-cocrystal continuum: the influence of crystal structure on ionization state. *Molecular Pharmaceutics* **2007,** *4* (3), 323-338.

42. Braga, D.; Maini, L.; Grepioni, F., Mechanochemical preparation of co-crystals. *Chemical Society Reviews* **2013,** *42* (18), 7638-7648.

43. Kuroda, R.; Higashiguchi, K.; Hasebe, S.; Imai, Y., Crystal to crystal transformation in the solid state. *CrystEngComm* **2004,** *6* (76), 464-468.

44. Kuroda, R.; Imai, Y.; Tajima, N., Generation of a co-crystal phase with novel coloristic properties via solid state grinding procedures. *Chemical Communications* **2002,** (23), 2848-2849.

45. Cheung, E. Y.; Kitchin, S. J.; Harris, K. D.; Imai, Y.; Tajima, N.; Kuroda, R., Direct structure determination of a multicomponent molecular crystal prepared by a solid-state grinding procedure. *Journal of the American Chemical Society* **2003,** *125* (48), 14658-14659.

46. Delogu, F., *Experimental and Theoretical Studies in Modern Mechanochemistry, 2010*. Transworld Research Network: **2010**.

47. Garroni, S.; Soru, S.; Enzo, S.; Delogu, F., Reduction of grain size in metals and metal mixtures processed by ball milling. *Scripta Materialia* **2014,** *88*, 9-12.

48. Yadav, T. P.; Yadav, R. M.; Singh, D. P., Mechanical milling: a top down approach for the synthesis of nanomaterials and nanocomposites. *Nanoscience and Nanotechnology* **2012,** *2* (3), 22-48.

49. Suryanarayana, C., Powder metal technologies and applications. *ASM handbook* **1998,** *7*, 80-90.

50. Yadav, T.; Mukhopadhyay, N.; Tiwari, R.; Srivastava, O., On the evolution of a nanocrystalline phase from the Al-Cu-Fe quasicrystalline alloy during high energy ball milling. *Transactions of the Indian Institute of Metals* **2005,** *58* (6), 1169-1176.

51. http://gmbh.zoz.de/_AKTUELL/pdf_content/publications/v14.pdf.

52. http://gmbh.zoz.de/?page_id=1255.

53. Chen, W.; Schoenitz, M.; Ward, T.; Dave, R. N.; Dreizin, E. L., Numerical simulation of mechanical alloying in a shaker mill by discrete element method. *KONA Powder and Particle Journal* **2005,** *23* (0), 152-162.

54. Multiphysics, C., LA MULTIFISICA ACCESSIBILE A TUTTI. **2016**.

55. Garay, A. L.; Pichon, A.; James, S. L., Solvent-free synthesis of metal complexes. *Chemical Society Reviews* **2007,** *36* (6), 846-855.

56. Broseghini, M.; Gelisio, L.; D'Incau, M.; Ricardo, C. A.; Pugno, N.; Scardi, P., Modeling of the planetary ball-milling process: The case study of ceramic powders. *Journal of the European Ceramic Society* **2016,** *36* (9), 2205-2212.

57. Burgio, N.; Iasonna, A.; Magini, M.; Martelli, S.; Padella, F., Mechanical alloying of the Fe− Zr system. Correlation between input energy and end products. *Il nuovo cimento D* **1991,** *13* (4), 459-476.

58. Benjamin, J. S., Mechanical alloying—A perspective. *Metal Powder Report* **1990,** *45* (2), 122-127.

59. Zhang, D., Processing of advanced materials using high-energy mechanical milling. *Progress in Materials Science* **2004,** *49* (3), 537-560.

60. Baisch, U.; Rubini, K.; Braga, D., Remarkable structural similarities between organic co-crystals and a metal–organic coordination network—insights into hydrogen bonded aliphatic ammonium chlorides. *CrystEngComm* **2008,** *10* (12), 1939-1947.

61. Pichon, A.; Lazuen-Garay, A.; James, S. L., Solvent-free synthesis of a microporous metal–organic framework. *CrystEngComm* **2006,** *8* (3), 211-214.

62. Pichon, A.; James, S. L., An array-based study of reactivity under solvent-free mechanochemical conditions—insights and trends. *CrystEngComm* **2008,** *10* (12), 1839-1847.

63. Weyna, D. R.; Shattock, T.; Vishweshwar, P.; Zaworotko, M. J., Synthesis and structural characterization of cocrystals and pharmaceutical cocrystals: mechanochemistry vs slow evaporation from solution. *Crystal Growth and Design* **2009,** *9* (2), 1106-1123.

64. Trask, A. V.; Motherwell, W. S.; Jones, W., Solvent-drop grinding: green polymorph control of cocrystallisation. *Chemical communications* **2004,** (7), 890-891.

65. Kuroda, R.; Yoshida, J.; Nakamura, A.; Nishikiori, S.-i., Annealing assisted mechanochemical syntheses of transition-metal coordination compounds and co-crystal formation. *CrystEngComm* **2009,** *11* (3), 427-432.

66. Yoshida, J.; Nishikiori, S. i.; Kuroda, R., Formation of 1 D and 3 D Coordination Polymers in the Solid State Induced by Mechanochemical and Annealing Treatments: Bis (3-cyano-pentane-2, 4-dionato) Metal Complexes. *Chemistry–A European Journal* **2008,** *14* (34), 10570-10578.

67. Braga, D.; Giaffreda, S. L.; Grepioni, F.; Polito, M., Mechanochemical and solution preparation of the coordination polymers Ag [N $(CH_2CH_2)_3$ N]$_2$ [CH_3COO]· $5H_2O$ and Zn [N$(CH_2CH_2)_3$ N]Cl_2. *CrystEngComm* **2004,** *6* (75), 459-462.

68. Adams, C. J.; Colquhoun, H. M.; Crawford, P. C.; Lusi, M.; Orpen, A. G., Solid-State Interconversions of Coordination Networks and Hydrogen-Bonded Salts. *Angewandte Chemie* **2007,** *119* (7), 1142-1146.

69. Braga, D.; Curzi, M.; Johansson, A.; Polito, M.; Rubini, K.; Grepioni, F., Simple and quantitative mechanochemical preparation of a porous crystalline material based on a 1D coordination network for uptake of small molecules. *Angewandte Chemie International Edition* **2006,** *45* (1), 142-146.

70. Adams, C. J.; Kurawa, M. A.; Lusi, M.; Orpen, A. G., Solid state synthesis of coordination compounds from basic metal salts. *CrystEngComm* **2008,** *10* (12), 1790-1795.

71. Friščić, T.; Fábián, L., Mechanochemical conversion of a metal oxide into coordination polymers and porous frameworks using liquid-assisted grinding (LAG). *CrystEngComm* **2009,** *11* (5), 743-745.

72. Yuan, W.; Garay, A. L.; Pichon, A.; Clowes, R.; Wood, C. D.; Cooper, A. I.; James, S. L., Study of the mechanochemical formation and resulting properties of an archetypal MOF: $Cu_3(BTC)_2$ (BTC= 1, 3, 5-benzenetricarboxylate). *CrystEngComm* **2010,** *12* (12), 4063-4065.

73. Yuan, W.; Friščić, T.; Apperley, D.; James, S. L., High reactivity of metal–organic frameworks under grinding conditions: parallels with organic molecular materials. *Angewandte Chemie* **2010,** *122* (23), 4008-4011.

74. Beldon, P. J.; Fábián, L.; Stein, R. S.; Thirumurugan, A.; Cheetham, A. K.; Friščić, T., Rapid Room-Temperature Synthesis of Zeolitic Imidazolate Frameworks by Using Mechanochemistry. *Angewandte Chemie International Edition* **2010,** *49* (50), 9640-9643.

75. Friščić, T.; Reid, D. G.; Halasz, I.; Stein, R. S.; Dinnebier, R. E.; Duer, M. J., Ion-and Liquid-Assisted Grinding: Improved Mechanochemical Synthesis of Metal–Organic Frameworks Reveals Salt Inclusion and Anion Templating. *Angewandte Chemie* **2010,** *122* (4), 724-727.

76. Vilar, R., Anion recognition and templation in coordination chemistry. *European Journal of Inorganic Chemistry* **2008,** *2008* (3), 357-367.

77. Stolle, A., *Ball milling towards green synthesis: applications, projects, challenges*. Royal Society of Chemistry: 2014.

78. Prochowicz, D.; Sokołowski, K.; Justyniak, I.; Kornowicz, A.; Fairen-Jimenez, D.; Friščić, T.; Lewiński, J., A mechanochemical strategy for IRMOF assembly based on pre-designed oxo-zinc precursors. *Chemical Communications* **2015,** *51* (19), 4032-4035.

79. Horcajada, P.; Surblé, S.; Serre, C.; Hong, D.-Y.; Seo, Y.-K.; Chang, J.-S.; Greneche, J.-M.; Margiolaki, I.; Férey, G., Synthesis and catalytic properties of MIL-100 (Fe), an iron (III) carboxylate with large pores. *Chemical Communications* **2007,** (27), 2820-2822.

80. Lu, W.; Wei, Z.; Gu, Z.-Y.; Liu, T.-F.; Park, J.; Park, J.; Tian, J.; Zhang, M.; Zhang, Q.; Gentle III, T., Tuning the structure and function of metal–organic frameworks via linker design. *Chemical Society Reviews* **2014,** *43* (16), 5561-5593.

81. Liu, J.; Chen, L.; Cui, H.; Zhang, J.; Zhang, L.; Su, C.-Y., Applications of metal–organic frameworks in heterogeneous supramolecular catalysis. *Chemical Society Reviews* **2014,** *43* (16), 6011-6061.

82. Horcajada, P.; Chalati, T.; Serre, C.; Gillet, B.; Sebrie, C.; Baati, T.; Eubank, J. F.; Heurtaux, D.; Clayette, P.; Kreuz, C., Porous metal-organic-framework nanoscale carriers as a potential platform for drug delivery and imaging. *Nature materials* **2010,** *9* (2), 172-178.

83. Dolomanov, O. V.; Blake, A. J.; Champness, N. R.; Schröder, M.; Wilson, C., A novel synthetic strategy for hexanuclear supramolecular architectures. *Chemical Communications* **2003,** (6), 682-683.

84. Bourne, S. A.; Lu, J.; Moulton, B.; Zaworotko, M. J., Coexisting covalent and noncovalent nets: parallel interpenetration of a puckered rectangular coordination polymer and aromatic noncovalent nets. *Chemical Communications* **2001,** (9), 861-862.

85. Aragoni, M. C.; Arca, M.; Devillanova, F. A.; Hursthouse, M. B.; Huth, S. L.; Isaia, F.; Lippolis, V.; Mancini, A.; Soddu, S.; Verani, G., Investigation into the reactivity of the coordinatively unsaturated phosphonodithioato [Ni $(MeOpdt)_2$] towards 2, 4, 6-tris (2-pyridyl)-1, 3, 5-triazine: goals and achievements. *Dalton Transactions* **2007,** (21), 2127-2134.

86. Aragoni, M. C.; Arca, M.; Demartin, F.; Devillanova, F. A.; Graiff, C.; Isaia, F.; Lippolis, V.; Tiripicchio, A.; Verani, G., Reactivity of phosphonodithioato Ni II complexes: solution equilibria, solid state studies and theoretical calculations on the adduct formation with some pyridine derivatives. *Journal of the Chemical Society, Dalton Transactions* **2001,** (18), 2671-2677.

87. van Zyl, W. E.; Woollins, J. D., The coordination chemistry of dithiophosphonates: An emerging and versatile ligand class. *Coordination Chemistry Reviews* **2013,** *257* (3), 718-731.

88. Drew, M. G.; Hopkins, W. A.; Mitchell, P. C.; Colclough, T., Preparation, properties, and X-ray crystal structure of tris (O, O'-di-isopropyl phosphorodithioato) iron (III),[Fe $\{S_2P(OPr_i)_2\}_3$]. Comparison of structure and bonding in phosphorodithioato- and dithiocarbamato-complexes. *Journal of the Chemical Society, Dalton Transactions* **1986,** (2), 351-354.

89. Haiduc, I.; Sowerby, D. B.; Lu, S.-F., Stereochemical aspects of phosphor-1, 1-dithiolato metal complexes (dithiophosphates, dithiophosphinates): Coordination patterns, molecular structures and supramolecular associations—I. *Polyhedron* **1995,** *14* (23), 3389-3472.

90. Aragoni, M. C.; Arca, M.; Champness, N. R.; Chernikov, A. V.; Devillanova, F. A.; Isaia, F.; Lippolis, V.; Oxtoby, N. S.; Verani, G.; Vatsadze, S. Z., Designed Assembly of Low-dimensional Molecular Units: Novel Neutral Coordination Polymers Based on (Phosphonodithioato) NiII Complexes. *European Journal of Inorganic Chemistry* **2004,** (10), 2008-2012.

91. Aragoni, M. C.; Arca, M.; Champness, N. R.; De Pasquale, M.; Devillanova, F. A.; Isaia, F.; Lippolis, V.; Oxtoby, N. S.; Wilson, C., Synthesis and structural characterisation of coordination polymers designed using discrete phosphonodithioato Ni II complexes and dipyridyl donor ligands. *CrystEngComm* **2005,** *7* (60), 363-369.

92. Aragoni, M. C.; Arca, M.; Coles, S.; Crespo-Alonso, M.; Coles, S.; Davies, R.; Hursthouse, M.; Isaia, F.; Lai, R.; Lippolis, V., Coordination polymers and polygons using di-pyridyl-thiadiazole spacers and substituted phosphorodithioato NiII complexes: potential and limitations for inorganic crystal engineering. *CrystEngComm* **2016**.

93. Bhosale, S. V.; Jani, C. H.; Langford, S. J., Chemistry of naphthalene diimides. *Chemical Society Reviews* **2008,** *37* (2), 331-342.

94. Pensack, R. D.; Song, Y.; McCormick, T. M.; Jahnke, A. A.; Hollinger, J.; Seferos, D. S.; Scholes, G. D., Evidence for the Rapid Conversion of Primary Photoexcitations to Triplet States in Seleno-and Telluro-Analogues of Poly (3-hexylthiophene). *The Journal of Physical Chemistry B* **2014,** *118* (9), 2589-2597.

95. Tilley, A. J.; Pensack, R. D.; Lee, T. S.; Djukic, B.; Scholes, G. D.; Seferos, D. S., Ultrafast Triplet Formation in Thionated Perylene Diimides. *The Journal of Physical Chemistry C* **2014,** *118* (19), 9996-10004.

96. Llewellyn, B. A.; Davies, E. S.; Pfeiffer, C. R.; Cooper, M.; Lewis, W.; Champness, N. R., Thionated perylene diimides with intense absorbance in the near-IR. *Chemical Communications* **2016,** *52* (10), 2099-2102.

Chapter 3: Metal Organic Framework: Fe^{III} 1,3,5-benzene tricarboxylate

This chapter is the result of the collaboration with: (i) another research group from the University of Cagliari (Headed by Prof. Ferino),(ii) ENEA: Italian National Agency for New Technologies Energy and Sustainable Economic Development, and (iii) Sartec-Saras research and technology.

M. Pilloni, F. Padella, G. Ennas, S. Lai, M. Bellusci, E. Rombi, F. Sini, M. Pentimalli, C. Delitala, A. Scano, V. Cabras, I. Ferino , "Liquid-assisted mechanochemical synthesis of an iron carboxylate Metal Organic Framework and its evaluation in diesel fuel desulfurization." *Microporous and Mesoporous Materials* 213 (**2015**): 14-21.

This study is published on *Microporous and Mesoporous Materials* and reported in this PhD thesis with their permission.

3 Metal Organic Framework: Fe^{III} 1,3,5-benzene tricarboxylate

3.1 Introduction

As already mentioned in the first chapter, Metal Organic Frameworks, MOFs, have attracted great interest for their application in gas storage, separation, catalysis and sensing. The cavities within their stable network can be tailored to accommodate different guest molecules. The huge interest for these materials has originated in the past decade and a large number of papers in different research areas has been produced. Among the different MOFs, MIL-100(Fe), MIL: *Materials of Institut Lavoisier*, is one of the most interesting structures and in the past decade it has been used in many applications as an adsorbent and a catalyst.

In the aim of the research (Chapter 2, 2.7) we have already introduced the material as a polar framework built up by trimers of carboxylate oxygen octahedra sharing μ_3-O corners, with the Fe (III) ions located in the center of octahedra. MIL-100(Fe) has a rigid zeotype crystal structure, consisting of 2.5 and 2.9 nm mesoporous cages accessible through window sizes of ca. 0.55 and 0.86 nm, respectively. One of the two octahedra of the trimers in terminal position is bonded with a water molecule and the other with a fluoride or hydroxyl group.[1,2] The water molecules can be removed, leaving Fe (III) a coordinatively unsaturated metal center (UMC), which can act as electron acceptors (Lewis acid sites) to form π bonds. It is possible to reduce Fe(III) sites to Fe(II) under controlled conditions, thus changing the preferential sorption properties of this material, and so offering new opportunities in particular for separation processes. For example, remarkable results were obtained in the CO removal from CO_2 [3] and in the separation of propane, propylene and isobutene mixtures.[4] The MIL-100(Fe) is stable to moisture and to hydrothermal

conditions, and is an useful adsorbent material in water sorption technologies,[5,6] contrary to other MOFs, which suffer of hydrothermal instability. In catalysis, this MOF has been used both as a solid catalyst, taking advantage of redox property of trivalent iron species,[1] and as a 3D mesoporous system for the encapsulation of other catalytic species.[2] MIL-100(Fe) seems also interesting as a carrier in drug delivery[7] by virtue of its low acute toxicity in vivo.[8] Promising capacities in removing contaminants from fuel at mild conditions have been reported as well.[9,10]

The usually reported method for MIL-100(Fe) and more generally for MOFs synthesis, is the solvothermal one. However, the solvothermal method imposes, already at the laboratory scale, hard reaction conditions, such as high temperature and pressure, use of large solvent amounts, and long synthesis times. Such reaction conditions would represent a serious drawback in the scale-up of the synthesis. In recent years , large-scale synthesis methods of well-known MOFs, such as MOF-5, MIL-53 (Al), HKUST-1, ZIF-8, and MIL-100(Fe), have been developed using both solvothermal and non-conventional procedures, including electrochemical and microwave methods. Only in few cases commercial products have been obtained as a result of such efforts. Furthermore, the scale-up procedures so far proposed do not completely match the criteria for industrial-scale syntheses.[11] A promising alternative for the large-scale production of MOFs could be based on a mechanochemical approach. [12] Through this technique high yields can be obtained in short reaction times working under mild conditions (room temperature, ambient pressure) using small solvent amounts (LAG method) or even without solvent (NG method). Moreover, low-cost starting materials can be used with this technique. The Neat Grinding, NG, and Liquid-Assisted Grinding ball-milling synthetic methods,[13] have been already reported for MOFs synthesis (chapter 2, paragraph 2.4). As already mentioned the MOFs synthesis is favored by the presence of a liquid phase[14,15] and several structures can be obtained from the same precursors by using different solvents. A careful solvent selection, as well as its accurate dosing, is required in order to obtain 3D structures[16] with the desired final properties.[17]

In this first part of the PhD project we propose a mechanochemical approach as an alternative synthetic route for MOFs preparation, in view of a possible large scale production. The ball milling LAG method was used to synthesize a non-fluorinated MIL-100(Fe) structure under mild conditions. Several papers dealing with the synthesis of carboxylate MOFs using the LAG method have been recently published.[14,15,16] However, to the best of our knowledge, the applicability of such method for preparing a non-fluorinated MIL-100(Fe) structure has not so far been reported in the open literature. Furthermore, while catalytic amounts of solvent are usually added to the reaction mixture in the LAG method, in this work an alkali solution has been used to increase the yield and to avoid the presence of unreacted 1,3,5-benzenetricarboxylic acid (H_3BTC) in the final product. Tetramethylammonium hydroxide (TMAOH) has been selected as a base.[18]

An iron (III) carboxylate framework isostructural with MIL-100(Fe) was obtained and characterized as to its structure (by X-ray powder diffraction, XRPD, and Fourier transform infrared spectroscopy, FTIR) and morphology (by scanning electron microscopy, SEM). The thermal stability was evaluated by thermogravimetry (TG) and the textural features were assessed by nitrogen physisorption. Adsorption microcalorimetry of ammonia was used as a direct and reliable method for determining both the concentration and the strength of the acid sites present on the sample. For comparison, a commercial iron trimesate (Basolite F300, one of the several MOFs produced in large scale by BASF using electrochemical methods)[11,19] was characterised as well.

The adsorption performance of the ball-milled sample for the removal of 4,6-dimethyldibenzothiophene (4,6-DMDBT) from 4,6DMDBT/*n*-heptane solutions simulating a diesel fuel was also investigated. The stringent regulations on the sulfur content of fuels make adsorption technology an interesting, environmentally-friendly alternative to the conventional catalytic hydrodesulfurization processes.[20] Being energy- and hydrogen-consuming, the latter seems hardly sustainable for the removal of refractory dibenzothiophenes with one or two methyl groups at 4- or/and 6-position from gasoil streams, where such compounds are particularly abundant. Though a MIL-100(Fe) MOF

has already been used as a component of copper-based adsorbents for the separation of benzothiophene from n-octane solutions,[10] investigations of the adsorption behavior of unmodified non-fluorinated MIL-100(Fe) structures are rare [21] and no papers on the use of such adsorbents prepared by ball-milling have so far reported. The present liquid-phase 4,6-DMDBT adsorption experiments were carried out on the as-synthesized MOF sample at room temperature and atmospheric pressure. *n*-Heptane was selected as a single-component surrogate diesel fuel because its cetane number is comparable to that for current European diesel fuel.[22] 4,6-DMDBT was regarded as a model compound for the refractory organosulfur fraction in a diesel fuel. For comparison, 4,6-DMDBT adsorption experiments were also carried out on the commercial iron trimesate sample (Basolite F300).

3.2 Experimental section

3.2.1 Materials and Methods

For synthesis, 1,3,5 benzenetricarboxylic acid (H_3BTC, 95% Sigma Aldrich), iron (III) nitrate nonahydrate ($Fe(NO_3)_3 \cdot 9H_2O$, 98% Sigma), tetramethyl ammonium hydroxide (TMAOH, 97% Sigma Aldrich), were used as received without further purification. Basolite F300 was purchased from Sigma Aldrich. For batch adsorption experiments, 4-6-dimethyldibenzothiophene (purum > 98%, Aldrich) and n-heptane (HPLC grade, Suprasolv Merck KGaA) were used as received.

XRPD patterns were recorded at 40 kV and 30 mA on a SEIFERT X3000 diffractometer using CuK_α radiation in Bragg Brentano geometry and equipped with a graphite monochromator and scintillation counter. The data were collected between 3.00° and 80.00° in 2θ, 0.05°2θ step size, and using opportune slits. In order to obtain satisfactory signal-to-noise ratio in the X-ray pattern an appropriate acquisition time was selected. The Maud software[23] was used for Rietveld refinements,[24] and the peaks profile was modeled by the pseudo-Voigt

profile function. X-ray diffraction patterns deriving from partially crystalline materials were analyzed superimposing the scattering contribution deriving from the disordered region of the material to the contribution due to the crystalline component of the sample, as calculated from the MIL-100(Fe)-type crystalline phase.[1] The crystallinity is defined as the ratio of the amount of crystalline sample to the total amount of sample material and can be measured by a variety of methods relying on different structural features.[25] The degree of crystallinity, x_{CR}, (weight fraction of the crystalline content) of the materials was determined from the XRPD patterns, by employing the Ruland-Vonk method and the correlate following equation:[26,27]

$$\frac{\int_{S_{min}}^{S_{max}} I_T(s)s^2 ds}{\int_{S_{min}}^{S_{max}} I_{CR}(s)s^2 ds} = \frac{\int_{S_{min}}^{S_{max}} \overline{f}_T^{\,2}(s)s^2 ds}{x_{CR}\int_{S_{min}}^{S_{max}} \overline{f}_T^{\,2} D(s)s^2 ds} \quad (1)$$

where I_{CR}, I_T are the intensity of coherent scattering, $\overline{f}_{CR}$, $\overline{f}_T$ are the average scattering factors of crystalline and total contribution respectively, D(s) is a disorder factor, *s* is the scattering variable on reciprocal space (=2sinϑ/λ). This formula can be rewritten as:

$$R(s) = \frac{k(s)}{x_{CR}} \quad (2)$$

where $\lim_{s^2 \to 0} k(s)=1$ and R(s) oscillate on a parabolic curve with $1/x_{CR}$ as intercept to $s^2=0$.

The scale factor, background contribution, lattice parameter, unit cell, average crystallite size, micro-strain were refined. The R_{wp}-factor:

$$R_{wp} = \left[\frac{\sum_{i=1}^{N} w_i\left(I_i^{exp} - I_i^{calc}\right)^2}{\sum_{i=1}^{N}\left(w_i I_i^{exp}\right)^2}\right]^{1/2} \quad (3)$$

where the weight factor $w_i = 1/(I_i^{exp})^{1/2}$ and I_i^{exp}, I_i^{calc} are the observed and the computed intensity value respectively. The R_{wp} was used as an indicator of fit goodness.

Scanning electron micrographs were obtained by High Resolution SEM LEO 130, the samples were prepared by sprinkling the powder onto double-sided sticky carbon tape.

FTIR spectra were obtained by a Bruker Vector 22 spectrophotometer within the 4000–400 cm^{-1} range using the KBr disc method.

Thermal analysis was carried out on a Perkin-Elmer Pyris Diamond TGA/DTAinstrument under Argon atmosphere (60 mL min^{-1}) with a heating rate of 10 K min^{-1}.

N_2 sorption isotherms were obtained on a Sorptomatic 1990 CE apparatus (Fisons Instruments) operated at 77 K. Prior to the sorption experiment, MFe_{LAG} was outgassed for 17 hours at 200°C. For Basolite F300, 80°C was selected as the temperature of the outgassing step, in order to avoid collapsing of the structure, which was observed with higher-temperature outgassing protocols. From the adsorption data the Specific Surface Area (SSA) was calculated by Brunauer–Emmett–Teller (BET) equation according to consistency criteria.[28] The pore volume was determined by the t-plot method, using the de Boer equation.[29]

A Tian-Calvet heat-flow calorimeter (C80, Setaram) was used in adsorption microcalorimetry experiments using ammonia as a probe molecule. Prior to the adsorption run, the samples were outgassed overnight at 200 (MFe_{LAG}) and 80°C (Basolite F300). Adsorption was carried out at 80°C by admitting successive doses of ammonia and recording the thermal effect. The equilibrium pressure relative to each adsorbed amount was measured by means of a differential pressure gauge (Datametrics) and the thermal effect recorded. The run was stopped at a final equilibrium pressure of 133.3 Pa. The adsorption and calorimetric isotherms were obtained from each adsorption run. The adsorption isotherms relate the amount of probe gas with the corresponding equilibrium pressure. The calorimetric isotherms relate the integral heat of adsorption, Q_{int}, with the corresponding equilibrium pressure. Combining the two sets of data, a plot of the differential heat of adsorption, Q_{diff}, as a function of the adsorbed ammonia was drawn, which gives information on the influence of the surface coverage on the energetics of the adsorption.

3.2.2 Adsorption of 4,6-DMDBT

Adsorption experiments were carried out in batch conditions at 25°C and atmospheric pressure in a modified FC6S Jar Test Apparatus (VELP Scientifica) by contacting 0.1 g of adsorbent with 4,6-DMDBT solutions in n-heptane (50 mL). Prior to the adsorption runs, the adsorbent was pre-treated in oven at either 105 or 130°C overnight. Based on TG curves, these temperatures were chosen to examine the efficiency of dehydratation on adsorption. Four-hour contact time and 200 rpm stirring were found to be safe conditions for collecting equilibrium data and were adopted for obtaining the adsorption isotherms. The 4,6-DMDBT content for the 4,6- DMDBT/n-heptane system was determined by HPLC before and after each experiment; the initial concentration of the adsorbate was varied between 3.4×10^{-5} and 1.8×10^{-2} mol L^{-1} according to procedures developed by Sartec. The HPLC apparatus (Agilent Technologies 1100 series) was equipped with a Lichrospher 100 NH_2 250×4 mm ID, 5 μm column, and UV and Refractive Index detectors; n-heptane was used as the eluant.

3.2.3 Synthesis

H_3BTC (0.471 g), Fe $(NO_3)_3$ $9H_2O$ (1.29 g), 8.8 g of 3 mm diameter balls were placed in a 80 mL Teflon coated stainless-steel grinding jar and 5 mL of an aqueous solution of TMAOH (0.22 M)was added. The mixture was milled using a vibratory ball-mill (Spex 8000, CertiPrep, Metuchen, NJ), and a thick paste was collected after 1 h of grinding (Figure 3.1). The sample was then dispersed in water and centrifuged three times at 2500 rpm. After washing, the sample was air-dried at room temperature. The resulting dry sample (labeled as MFe_{LAG}) was light- orange colored.

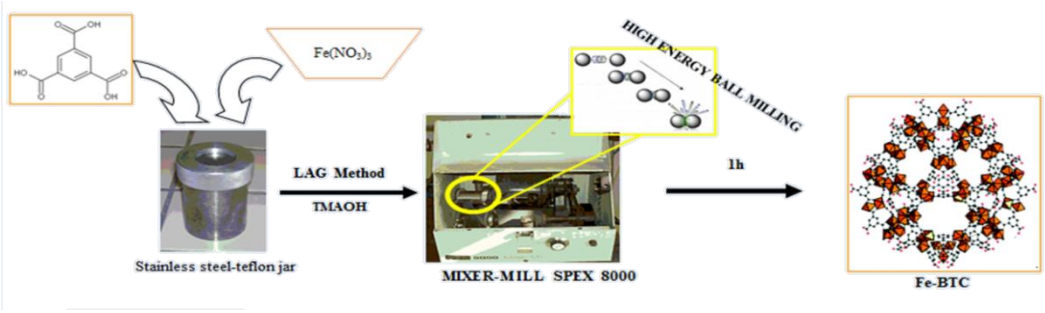

Figure 3.1 Schematic representation of mechanochemical reaction between H_3BTC and $Fe(NO_3)_3 \cdot 9H_2O$ resulting in MFe_{LAG}

3.3 Results and discussion

3.3.1 Structure and morphology

In Figure 3.2 experimental XRPD patterns of MFe_{LAG} is reported, in comparison with the ones resulting from the Basolite F300 sample and the MIL-100(Fe) Bragg peaks obtained from crystallographic data resulting from [1]. The reference material exhibits a cubic structure with space group Fd-3m and cell parameter a_0 = 7.34 nm.[1] The ball-milled sample possesses higher crystallinity with respect to the commercial F300 powder (as evidenced at qualitative level by the relatively sharp peaks in the pattern of figure 3.2). In comparison with the MIL-100(Fe) pattern (i.e. calculated from the standard material) MFe_{LAG} shows broadening and overlapping of peak profiles.

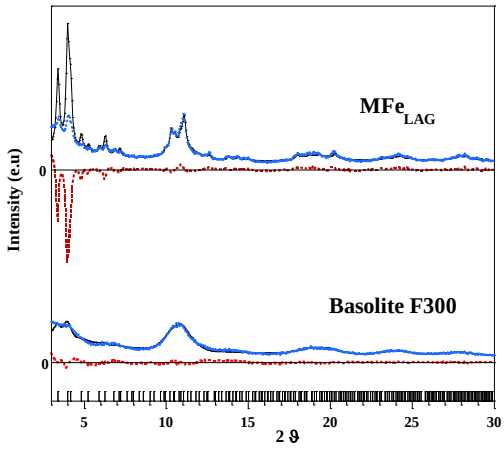

Figure 3.2. X-ray diffraction patterns of MFe_{LAG}(ball milling) and commercial Basolite F300 samples: experimental data (blue dots), Rietveld simulation (black solid lines) and curve difference (red dash lines). On the bottom MIL-100(Fe) Bragg peaks are reported.

Diffractogram arising from the Basolite F300 sample consists of multiple broad halos in the whole examined 2ϑ range, deriving from massive broadening of peaks, typical of a highly disordered phase.[30] The diffraction data for Basolite F300 were quantitatively analyzed by the Rietveld refinement using a model that includes a greatly disordered phase superimposed with a MIL-100(Fe)-type crystalline phase. The Rietveld refinement of MFe_{LAG} sample can be discussed by separately analyzing the 3.00-5.00 and 5.00-30.00° 2ϑ degree intervals. While X-ray data analysis produces a good fit in the range 5.00-30.00° 2ϑ (R_{wp} = 0.0866), in the 3.00-5.00 range a good fit is clearly not obtained. At 3.40° and 4.00° 2ϑ, related to (220) and (311) planes respectively differences in the intensity result. Such evidences can derive from physisorbed water molecules, filling the pores in the material. As already reported for other materials with large internal volume,[31,32] the intensity of reflections at low angles in the XPRD pattern is strongly dependent on the amount of the species present in the pores and from their scattering power. Despite the unsatisfactory fitting in the low-angle region, we believe that the Rietveld refined parameters are appropriate for describing the cubic crystal system of MFe_{LAG}. The resulting cell parameter is 7.283 nm, slightly shorter than that for MIL-100(Fe) reference. As expected for a sample obtained by mechanosynthesis, a small crystallite size (ca. 47 nm) and a slight microstrain (0.3%) are calculated.

The degree of crystallinity X_{CR} was calculated using the Ruland-Vonk method by the equation (2). The intensity of coherent scatterings for crystalline and total contribution, I_{CR} and I_T, result from the Rietveld refinement. The amorphous contribution to MIL-100(Fe) structure was simulated using several gaussian haloes. A plot of R(s) versus s^2 and an extrapolation to $s^2=0$ gives X_{CR} values for BasoliteF300 and MFe_{LAG} samples (Figure 3.3).

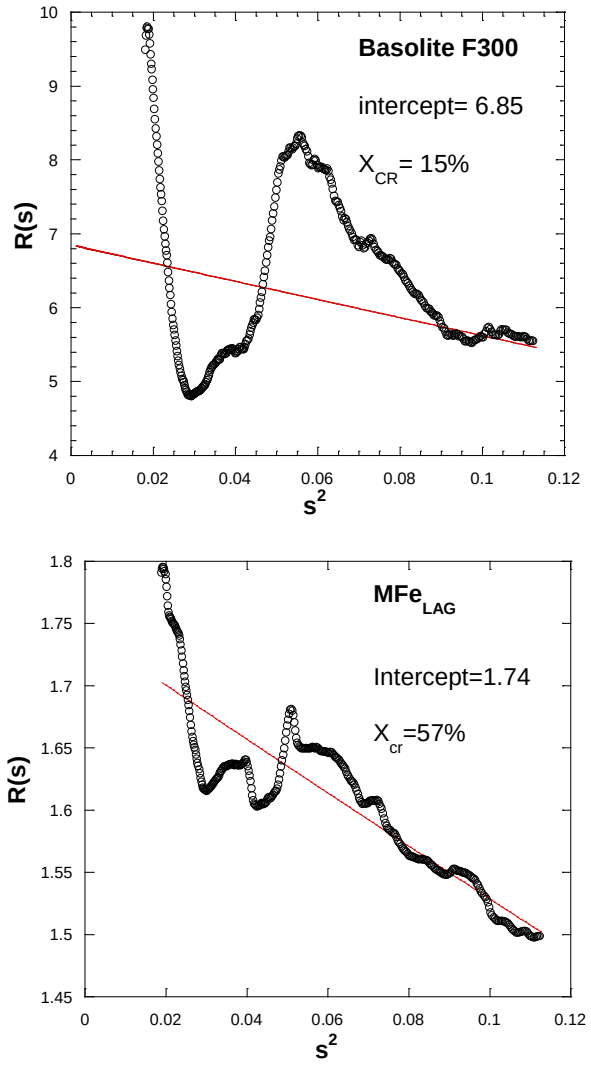

Figure 3.3. Ruland plot for MFe_{LAG} and Basolite F300 samples.

As calculated from Ruland analysis, MFe_{LAG} sample consists in a partially crystalline material having 57%wt of crystalline fraction. Basolite F300 exhibits a minimal crystalline fraction as low as about 15% with a consequent large extend of disordered structure (i.e. 85%). The ordered fraction results isostructural with MIL-100(Fe).

The XRPD results show that the liquid assisted mechanochemical method is useful to obtain a phase isostructural with MIL-100(Fe). The mechanism that can be tentatively involved in order to account for the high yield of a reaction carried out in the presence of added liquid relies on the idea that the added liquid acts as a solvent for one or more of the reactant solids, favoring the mass transport of material from the reactants to the product phase. In the LAG method

the amount of solvent is rather small and it is realistic to assume that diffusion plays a major role in comparison with the case in which the convection mechanism is involved.[33] Correlations between reactivity and reactant solubility have also been observed in cocrystal formation.[34] As known for the MOF synthesis, the possibility of obtaining the required structure depends also on the nature of the added liquid.[16] In our case the LAG method is carried out by using an aqueous solution containing TMAOH. For the ligand addition to a metal salt, as in the case of the present reaction, the acid-base reactivity is one of the driving forces, and the control of acid-base relationship between reagents is strategic for an effective synthesis, as described recently for mechanochemical synthesis of IRMOF.[35] The possibility that the reaction evolves through the formation of an amidate ligand, generated from TMAOH and carboxylic acid, can also be considered.

SEM micrographs (Figure 3.4) show that the two samples have similar morphologies, MFe_{LAG} appearing as smaller aggregates in comparison with Basolite F300.

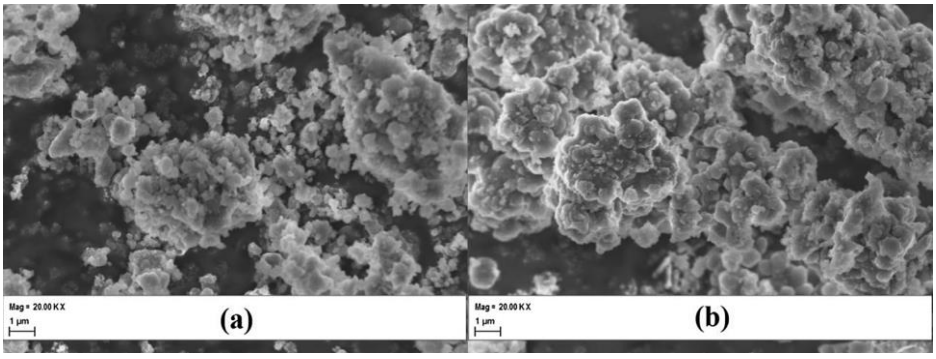

Figure 3.4 SEM images (20 Kx) of (a) MFe_{LAG} and (b) Basolite F300.

The FTIR spectra of MFe_{LAG} and Basolite F300 (Figure 3.5) are those expected for these iron trimesates.[2,36] Both spectra present hydroxyl stretching vibrations in the 3600-2500 cm^{-1} region, typical of adsorbed water molecules. Stretching of carboxylate group is visible in the 1700-1500 cm^{-1} region, as well as C-C stretching in the aromatic ring in the 1500-1300 cm^{-1} region. It worthy of note that in the FTIR spectrum of Basolite F300 additional vibration bands at 1720, 1064 and 1000 cm^{-1}, ascribable to free 1,3,5-benzenetricarboxylic acid, are

present, as already reported.[37] The lack of unreacted 1,3,5-benzenetricarboxylic acid in MFe_{LAG} is probably related to the use of TMAOH during the synthesis, as above explained.

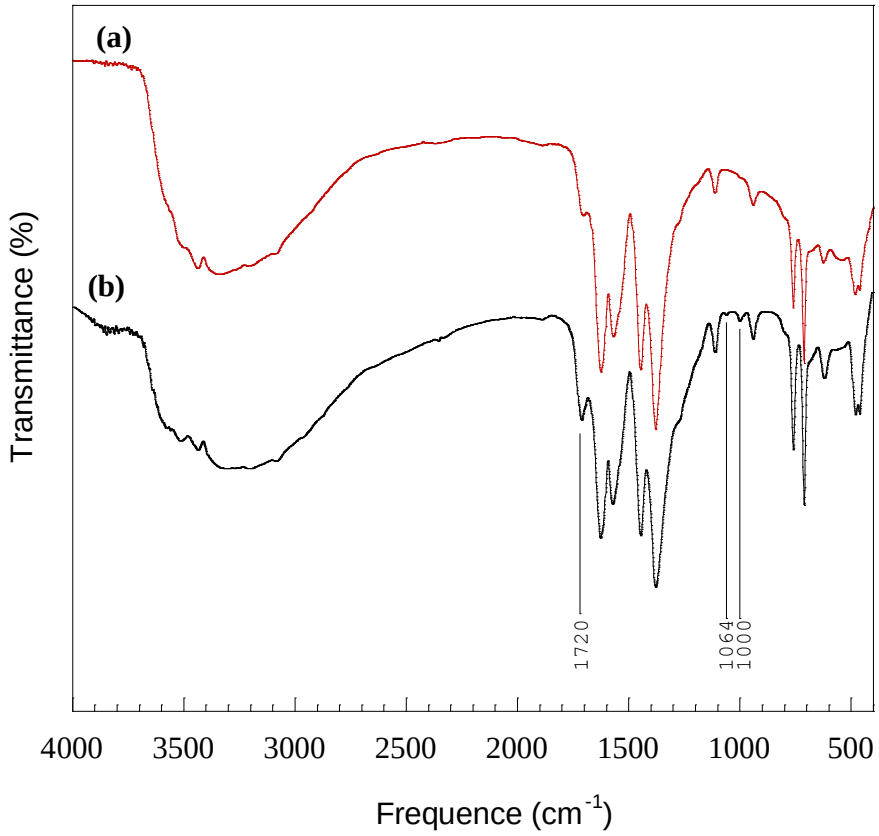

Figure 3.5 FTIR spectra of (a) MFe_{LAG} and (b) Basolite F300.

3.3.2 Thermal stability

Figure 3.6 shows the thermogravimetric (TG) curves under Ar flow and the corresponding derivative curves (dTG) for MFe_{LAG} and Basolite F300. The TG curve for MFe_{LAG} shows a weight loss of ca. 33 wt% in the range 25-120°C, as a consequence of dehydration. Such an evidence for the presence of a high amount of water in the sample supports the XRPD data interpretation: water molecules located inside the MOF pores induce a decrease in the XRPD peaks intensity in the 3.00-4.00° 2ϑ range. The weight loss of about 39 wt % observed in the range 274-400°C is related to the collapse of the framework. Decomposition into hematite occurs at higher temperatures (600°C), as confirmed by XRPD analysis (data not shown). This is in agreement with the literature on MIL-100(Fe)

prepared through solvothermal routes, which report thermal stability of the samples up to 250°C.[1,2,36]

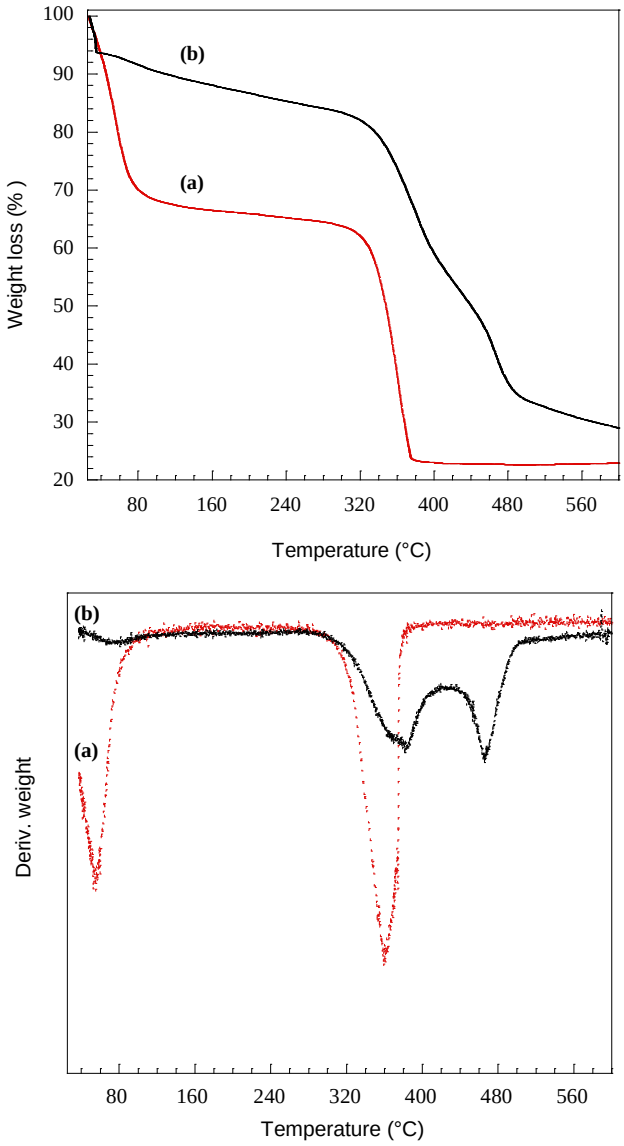

Figure 3.6 TG (left) and dTG (right) curves for (a) MFeLAG and (b) Basolite F300. Argon flow rate, 60 mL min^{-1}; heating rate, 10°C min^{-1}; alumina crucible.

Based on TG results, the composition of MFe_{LAG} is in agreement with the formula $Fe_3O(OH)\ (H_2O)_2\{C_6H_3(CO_2)_3\}_2\ nH_2O$ with n~19. From the above formula (with n~19) an iron content of 16 wt% is calculated, which is in good agreement with the experimentally determined (ICP-AES) value (15 wt%). For the dehydrated structure (n = 0) the iron content (i.e. 26 wt%) is consistent with the value based on structure obtained by Horcajada and coworkers.[1] For Basolite

F300 a gradual and continuous weight loss of ca.11 wt% (i.e. much lower than that observed for MFe_{LAG}) occurs in the range 25-130°C probably due to water and/or synthesis solvent physisorbed. Above 25°C, Basolite F300 loses weight in two different steps, in the 260-426 and 426-509°C range respectively. While the first step can be ascribed to structure degradation of framework, as observed in the same temperature range on MFe_{LAG}, the second step is due to the presence of a residual amount of free 1,3,5-benzenetricarboxylic acid, which was actually detected by FTIR (cf. Figure 3.4). Upon treating at 600°C, Basolite F300 is converted into hematite. By comparing the TG results in Figu6, it can be observed that after complete dehydration the curve for MFe_{LAG} attains a plateau, indicating that its structure (and hence the porous network) is retained after the release of the guest molecules, while a gradual, continuous weight loss occurs in the case of Basolite F300.

3.3.3 Textural features

The nitrogen physisorption isotherm for $MFeL_{AG}$ activated at 200°C is shown in Figure 3.7. According to [28], it can be classified of type Ib. The steep rise in nitrogen uptake in the region of low relative pressures results from monolayer adsorption on the walls of supermicropores/narrow mesopores followed by their filling, while the long, virtually horizontal plateau extending up to $p/p_0 \rightarrow 1$ is indicative of a negligible extent of multilayer adsorption on the external open surface. This is consistent with the MFe_{LAG} structure, characterized by the presence of cages of ca. 25 and 29 Å, accessible through microporous windows (ca. 5.5 and 8.6 Å). The very narrow hysteresis loop at p/p_0 very close to 1 is not related to the presence of amount of larger mesopores but can be ascribed to nitrogen condensation within the interparticle voids resulting by agglomeration of small particles, whose existence was actually revealed by SEM (Figure 3.4). A similar isotherm has been reported for mechanochemically-prepared HKUST-1.[16] The calculated pore volume and specific surface area values are 0.386 $cm^3\ g^{-1}$ (% Relative Standard Deviation, RSD = 1) and 1033 $m^2\ g^{-1}$ (%RSD = 2) respectively. Though mechanochemical synthesis can lead to materials whose

surface area is comparable to that of samples obtained by other synthetic approaches,[12] in the present case the surface area of the milled sample is lower than that of solvothermal samples,[2,36] as already observed by others.[18] The isotherm for Basolite F300 activated at 80°C, also shown in Figure 3.7, is quite similar to that for MFe_{LAG}, but the nitrogen uptake is remarkably lower. Accordingly, remarkably lower pore volume and surface area values are calculated, 0.151 $cm^3\ g^{-1}$ (% RSD = 1) and 365 $m^2\ g^{-1}$ (%RSD = 2) respectively. The negligible area of the very small hysteresis loop at p/p_0 very close to 1 is consistent with the large size of the particles (cf. Figure 3.4) and the correspondingly low volume of the interparticles voids in the aggregates.

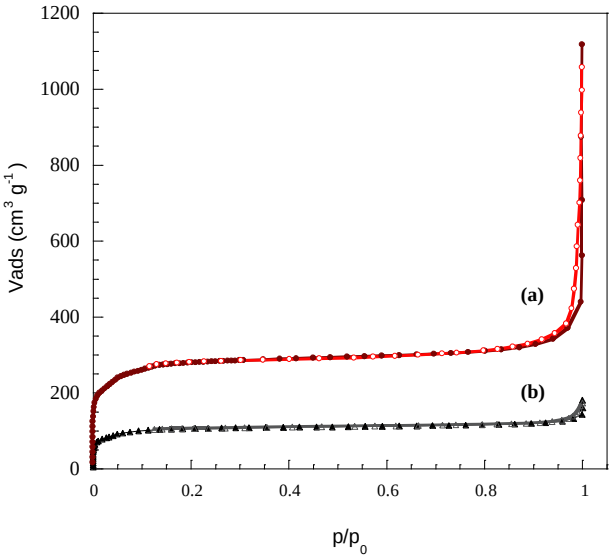

Figure 3.7. Nitrogen adsorption-desorption isotherms for (a) MFe_{LAG} and (b) Basolite F300 at 77 K. Full and open symbols refer to adsorption and desorption, respectively.

The different textural features of Basolite F300 in comparison with those for MFe_{LAG} are not unexpected, in view of the differences observed by XRPD characterization. The relationship between the pore structure and the MOF crystalline phase has been studied in different works by single crystal XRD[32] in combination with small-angle X-ray scattering and wide-angle X-ray scattering experiments.[38] The MOFs, built from the linkage of metal clusters with the organic units, are open 3D network, which allows efficient adsorption of guest molecules into its inner space. Ideally, their architecture can be described as a 3D channel structure consisting of reciprocally orthogonal and perfectly ordered 1D open channels that may result in a high specific surface and pore volume.

Actually, the real pore structure and pore network deviate considerably from this ideal architecture, and in no case a synthetic method can yield the perfect MOF crystal with theoretically maximum SSA or pores density.[38] In this work we correlate the textural properties of MFe_{LAG} and Basolite F300 with the Rietveld results obtained from XRPD data, gathering that the higher SSA and pore volume of the ball-milled sample reflect its higher fraction of crystallinity in comparison with commercial sample in which the disordered structure is predominant. In agreement with the above statement, in [31] such crystallographic defects in MOF-5 with low SSA have been noticed.

Noteworthy, the surface area value claimed in the technical sheet of Basolite F300 (1300-1600 $m^2\ g^{-1}$) is by far higher than that experimentally determined in the present work (398 $m^2\ g^{-1}$), as already found by others.[37]

Table 3.1. Schematic representation of the SSA (B.E. T) with correlation to the synthesis method.

MOF	Synthesis method	SSA (B.E.T)
Basolite F300	Electrochemical method	365 m^2/g
MFe_{LAG}	Mechanochemical method	1033 m^2/g

3.3.4 Acid properties

The ammonia adsorption calorimetry results for MFe_{LAG} and Basolite F300 are summarized in Figure 3.8, where the differential heat of adsorption, Q_{diff}, is plotted vs. the ammonia uptake. For both the ball-milled and the commercial sample the differential heat decreases from 125 to 115 to ca. 20-25 kJ mol^{-1} as the coverage increases, until a total ammonia uptake of ca. 2850-3110 μmol $g^{-1}$is attained. At high coverage values, physisorption can take place and its contribution to the ammonia uptake should be neglected in the assessment of the acid sites concentration, n_A. Typically, the heat released during physisorption is twice as big as the condensation heat [39] which, in the case of ammonia at 80°C, is 20.2 kJ mol^{-1}.[40] Accordingly, the fraction of ammonia uptake in Figure 3.8 corresponding to differential heats below 40 kJ mol^{-1} was ascribed to physical

adsorption and was neglected in calculating the acid sites concentration. The obtained n_A values are 1895 and 1805 μmol g^{-1} for MFe_{LAG} and Basolite F300, respectively. The observed decreasing trend in the Q_{diff} vs. uptake curves indicates heterogeneity of the sites, which is not unexpected in view of the different nature of the ammonia-adsorbing sites. Besides UMC Fe(III) Lewis sites, other species, such as structural Fe-OH groups and coordinated water species, acting as Brønsted sites, would also be present. IR evidence for the presence of Brønsted acidity arising from water molecules coordinated to UMC Al(III) was obtained for a non-fluorinated aluminum trimesate MOF (MIL-100(Al)).[41]

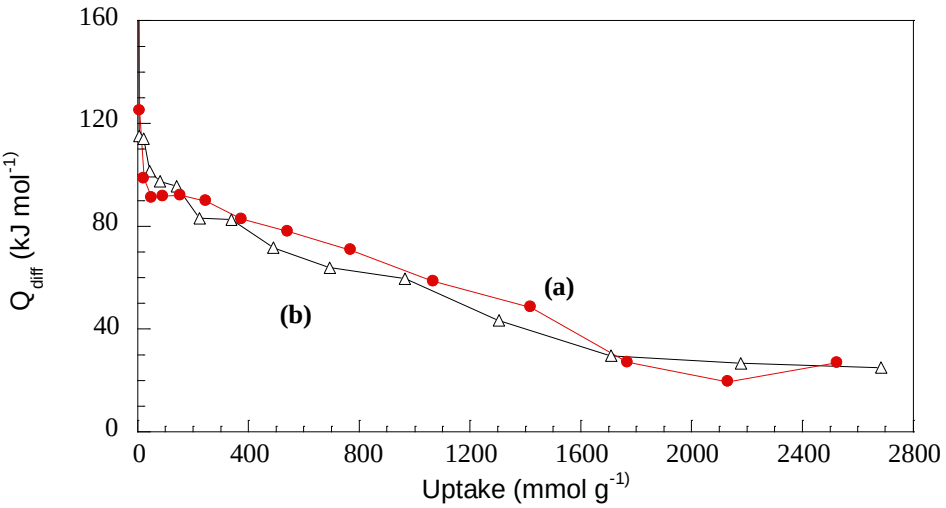

Figure 3.8. Differential heats adsorption (Q_{diff}) for ammonia adsorption observed at 80°C for (a) MFe_{LAG} (red curve with circles) and (b) Basolite F300 (black curve with triangles).

Brønsted interactions between ammonia and coordinated water have been reported, besides NH_3-UMC Fe(III) interactions, in ammonia removal under dynamic conditions from fluorinated MIL-100(Fe).[42] It should also be considered that the presence of terminal carboxylate moieties, virtually negligible for perfectly ordered materials, would become significant for partially disordered samples as those dealt with in the present work; the higher the disorder degree, the higher the amount of such moieties. In the case of Basolite F300, the presence of residual amounts of free 1,3,5- benzenetricarboxylic acid (cf. FTIR results) would also contribute to the acidity of the sample. Though MFe_{LAG} and Basolite F300 are similar as to the acid sites concentration, their

site-strength distribution is significantly different. While for the commercial sample virtually continuous heterogeneity is observed in the Q_{diff} vs. n_A plot, a plateau is visible at ca. 90 kJ mol^{-1} for MFe_{LAG}. The difference in the site-energy distribution between the two samples is better appreciated in Figure 3.9, where $-dn_A/dQ_{diff}$ values obtained by graphical derivation of the curves of Figure 3.8 are plotted versus Q_{diff}. For MFe_{LAG}, the sharp peak at 90 kJ mol^{-1} is indicative of the presence of a homogeneous family of strong acid sites (supposedly Lewis ones), whose population is 285 μmol g^{-1}. Only a small peak in the 102-196 kJ mol^{-1} region is present in the energy distribution plot of Basolite F300. This indicates that the population of homogeneous strong sites on this sample is rather low (165 μmol/g), as expected in view of its poor crystallinity.

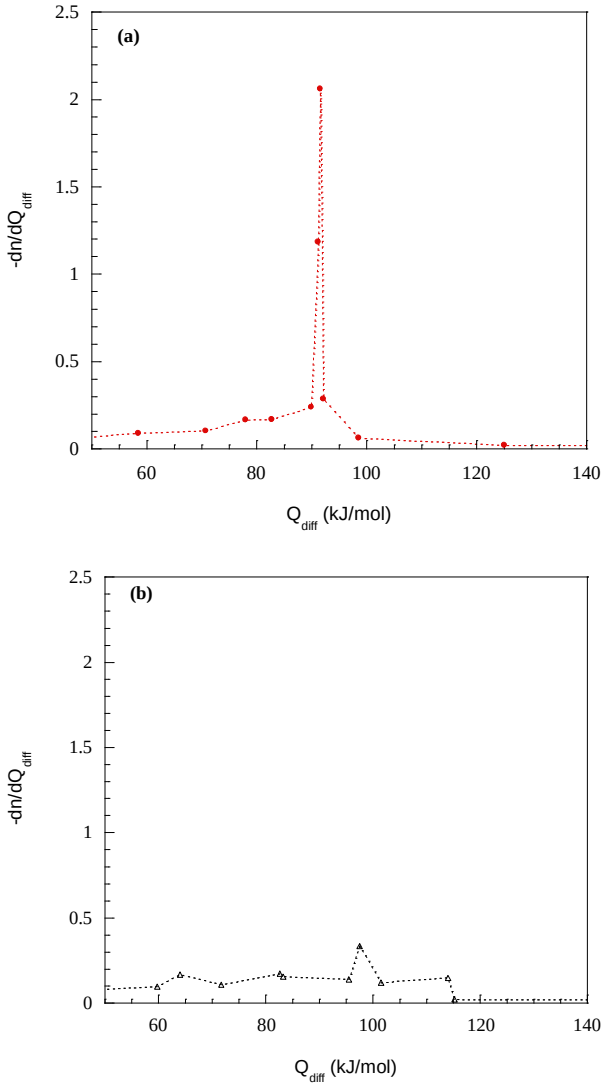

Figure 3.9. Site-energy distribution plots for (a) MFe_{LAG} and (b) Basolite, as obtained through graphical derivation of Fig. 7 curves.

3.3.5 Adsorption of 4,6-DMDBT

The adsorption equilibrium data obtained by contacting either MFe_{LAG} and Basolite F300 with 4,6-DMDBT/n-heptane mixtures are reported in Figure 3.10, where the adsorbed amount (expressed as mmol of sulfur per g of adsorbent) is plotted vs. the residual 4,6-DMDBT concentration in the liquid phase (mmol L^{-1}). Both the samples are able to adsorb 4,6-DMDBT, though to a different extent. For both the adsorbents, the experimental points are fitted by a Langmuir isotherm:

$$q_e = \frac{Q_{max} K_L C_e}{1 + K_L C_e}$$

Where q_e is the equilibrium adsorbed amount (mmol g^{-1}), C_e the equilibrium concentration in the fluid phase (mmol L^{-1}), Q_{max} the maximum adsorption capacity of the sorbent (mmol g^{-1}), and $K_L$the adsorption equilibrium constant (L $mmol^{-1}$).

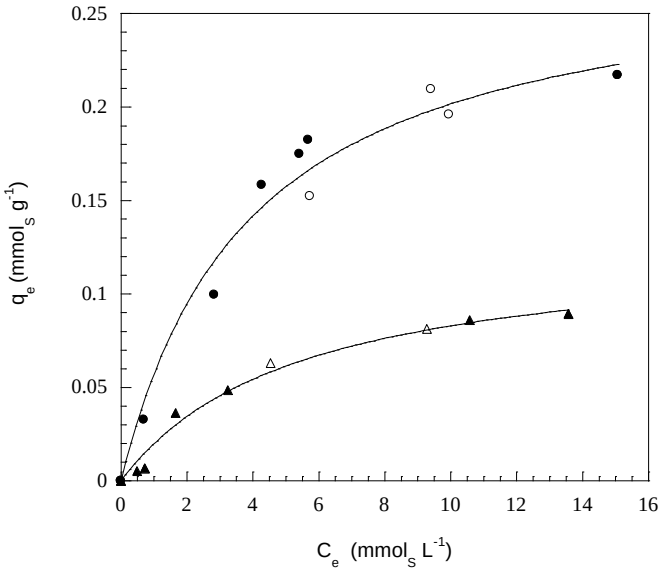

Figure 3.10. 4,6-DMDBT adsorption from 4,6-DMDBT/n-heptane solutions at 298 K under atmospheric pressure on MFe_{LAG} (circles) and Basolite F300 (trianglrs). C_e and q_e represent the 4,6-DMDBT equilibrium concentration in the liquid phase and the equilibrium adsorbed amount, respectively. Full and open symbols refer to samples activated at 105 and 130°C, respectively.

For both MFe_{LAG} and Basolite F300, an activation temperature of the sample of 105 or 130°C results in the same adsorption behavior, the corresponding data points being fitted by the same curve. This confirms that the dehydratation, required for the establishing of the organosulfur compound adsorption, can be achieved at such low temperatures that no framework collapse can occur (cf. TG results, Figure 3.6). The superior performance of MFe_{LAG} is manifest from the comparison of its calculated maximum adsorption capacity (0.29 mmol g^{-1}) with that of the commercial sample (0.13 mmol g^{-1}). The maximum adsorption capacity value for MFe_{LAG} is quite in agreement with very recent results for 4,6-DMDBT adsorption on a MIL-100(Fe) sample prepared by solvothermal synthesis,[21] Q_{max} being 7.94 $mg_S/g_{adsorbent}$ for the latter sample and 9.28 $mg_S/g_{adsorbent}$ for ours. The K_L value is higher for MFe_{LAG} (0.26 L $mmol^{-1}$) than for Basolite F300 (0.18 L $mmol^{-1}$), which suggests a stronger interaction of the organosulfur compound with the ball-milled adsorbent. This is not unexpected, in view of the acid-base nature of the interaction between the adsorbent and 4,6-DMDBT and the presence on MFe_{LAG} of a relatively large family of acid sites of uniform, remarkable strength (cf. Fig. 3.9). The overall acid sites concentration determined by ammonia adsorption (1895 and 1805 mmol g^{-1} for MFe_{LAG} and Basolite F300, respectively) is far higher than the Q_{max} values (290 and 130 μmol g^{-1} for MFe_{LAG} and Basolite F300, respectively), which clearly indicates that only a small fraction of the acid sites detected by ammonia are able to interact with 4,6-DMDBT. Noteworthy, the Q_{max} value for the ball-milled sample is quite close to the population of those sites originating the sharp peak in Figure 3.9a (285 μmol g^{-1}); for the commercial sample, the value Q_{max} is comparable to the population of the sites originating the small peak in Figure 3.9b (165 μmol g^{-1}). Though there is no direct evidence about the nature of these sites, their uniform, high strength suggests that they are the UMC Fe(III) species of the MOF framework. Such sites, generated by dehydratation,[3] are located inside the large cages of the framework, which can be accessed through the pentagonal and hexagonal windows by 4,6-DMDBT molecules (4.2 × 5.6 × 9.1 Å) with an appropriate orientation, and can adsorb the organosulfur compound with either a head-on or a side-on configuration. In the former case, the

adsorbate would stand up in a vertical geometry with the lone pair of sulfur interacting with the surface acid site. In the side-on adsorption configuration, the conjugated π electrons would be involved, with the adsorbate lying flat on the adsorption site. According to [21], the dominant adsorption mechanism would depend on the MOF type, a side-on configuration being predominant in the case of the MIL-100(Fe) structure. We tentatively propose here that such adsorption mode can be further stabilized by π-π interation taking place between the aromatic rings of the organosulfur compound and the linker units of the MOF. This would be possible in view of the electron-donating effect of the methyl groups, which would enhance the electron-rich character of the adsorbate, while the electron-withdrawing effect of the carboxilate moieties would give to the MOF framework an electron-poor character. Though a detailed description of the adsorption mechanism is lacking in the literature, it is suggested in different papers that π-π stacking/interactions are involved in the adsorption of aromatic compounds over different MOFs,[43,44] MIL-100(Fe) included.[45] The lack of 4,6-DMDBT adsorption on the rest (i.e. the largest part) of the acid sites detected by microcalorimetry can be tentatively explained as follows. The Brønsted sites associated to the framework (i.e. structural hydroxyl groups and water molecules coordinated to UMC metal sites) are probably too weak [41] for interacting with a weakly basic molecule as 4,6-DMDBT. As to the other ammonia-adsorbing sites, i.e. terminal carboxyl moieties resulting from the incomplete growth of the framework, and, in the case of Basolite F300, residual 1,3,5-benzenetricarboxylic acid, it can be thought that because of the absence of a regular framework no π-π interactions stabilizing the adsorbate on the acid site can take place, hence disfavoring the establishing of the adsorption phenomenon.

3.4 Conclusions

Liquid-assisted grinding is an effective strategy for the synthesis with quantitative yields of high quality metal-organic frameworks, as shown by the preparation of an iron(III) trimesate MOF of predominant crystalline cubic phase with good thermal stability, high surface area and pore volume. In comparison, the structural and textural features of commercial iron trimesate Basolite F300 appear rather poor. Both the ball-milled and the commercial sample have a quite high concentration of acid sites, as determined by ammonia adsorption calorimetry, with more pronounced heterogeneity of the sites in the case of Basolite F300. The ball-milled sample performs much better than the commercial one in the ambient temperature adsorption of 4,6-DMDBT from a simulated low-sulfur diesel fuel. It seems that the sites responsible for 4,6-DMDBT adsorption are those able to interact with ammonia with a differential heat of ca. 90 kJ mol^{-1}, supposedly the UMC Fe(III) species of the MOF framework.

3.5 References

1. Horcajada, P.; Surblé, S.; Serre, C.; Hong, D.-Y.; Seo, Y.-K.; Chang, J.-S.; Greneche, J.-M.; Margiolaki, I.; Férey, G., Synthesis and catalytic properties of MIL-100 (Fe), an iron (III) carboxylate with large pores. *Chemical Communications* **2007,** (27), 2820-2822.

2. Canioni, R.; Roch-Marchal, C.; Sécheresse, F.; Horcajada, P.; Serre, C.; Hardi-Dan, M.; Férey, G.; Greneche, J.-M.; Lefebvre, F.; Chang, J.-S., Stable polyoxometalate insertion within the mesoporous metal organic framework MIL-100 (Fe). *Journal of Materials Chemistry* **2011,** *21* (4), 1226-1233.

3. Yoon, J. W.; Seo, Y. K.; Hwang, Y. K.; Chang, J. S.; Leclerc, H.; Wuttke, S.; Bazin, P.; Vimont, A.; Daturi, M.; Bloch, E., Controlled reducibility of a metal–organic framework with coordinatively unsaturated sites for preferential gas sorption. *Angewandte Chemie International Edition* **2010,** *49* (34), 5949-5952.

4. Plaza, M.; Ribeiro, A.; Ferreira, A.; Santos, J.; Hwang, Y.; Seo, Y.-K.; Lee, U.-H.; Chang, J.-S.; Loureiro, J.; Rodrigues, A., Separation of C3/C4 hydrocarbon mixtures by adsorption using a mesoporous iron MOF: MIL-100 (Fe). *Microporous and Mesoporous Materials* **2012,** *153*, 178-190.

5. Henninger, S. K.; Jeremias, F.; Kummer, H.; Janiak, C., MOFs for use in adsorption heat pump processes. *European Journal of Inorganic Chemistry* **2012,** *2012* (16), 2625-2634.

6. Seo, Y. K.; Yoon, J. W.; Lee, J. S.; Hwang, Y. K.; Jun, C. H.; Chang, J. S.; Wuttke, S.; Bazin, P.; Vimont, A.; Daturi, M., Energy-Efficient Dehumidification over Hierachically Porous Metal–Organic Frameworks as Advanced Water Adsorbents. *Advanced Materials* **2012,** *24* (6), 806-810.

7. Horcajada, P.; Chalati, T.; Serre, C.; Gillet, B.; Sebrie, C.; Baati, T.; Eubank, J. F.; Heurtaux, D.; Clayette, P.; Kreuz, C., Porous metal-organic-framework nanoscale carriers as a potential platform for drug delivery and imaging. *Nature materials* **2010,** *9* (2), 172-178.

8. Baati, T.; Njim, L.; Neffati, F.; Kerkeni, A.; Bouttemi, M.; Gref, R.; Najjar, M. F.; Zakhama, A.; Couvreur, P.; Serre, C., In depth analysis of the in vivo toxicity of nanoparticles of porous iron (III) metal–organic frameworks. *Chemical Science* **2013,** *4* (4), 1597-1607.

9. Maes, M.; Trekels, M.; Boulhout, M.; Schouteden, S.; Vermoortele, F.; Alaerts, L.; Heurtaux, D.; Seo, Y. K.; Hwang, Y. K.; Chang, J. S., Selective Removal of N-Heterocyclic Aromatic Contaminants from Fuels by Lewis Acidic Metal–Organic Frameworks. *Angewandte Chemie* **2011,** *123* (18), 4296-4300.

10. Khan, N. A.; Jhung, S. H., Low-temperature loading of Cu+ species over porous metal-organic frameworks (MOFs) and adsorptive desulfurization with Cu+-loaded MOFs. *Journal of hazardous materials* **2012,** *237*, 180-185.

11. Stock, N.; Biswas, S., Synthesis of metal-organic frameworks (MOFs): routes to various MOF topologies, morphologies, and composites. *Chemical reviews* **2011,** *112* (2), 933-969.

12. Crawford, D.; Casaban, J.; Haydon, R.; Giri, N.; McNally, T.; James, S. L., Synthesis by extrusion: continuous, large-scale preparation of MOFs using little or no solvent. *Chemical Science* **2015,** *6* (3), 1645-1649.

13. Friščić, T.; Trask, A. V.; Jones, W.; Motherwell, W., Screening for inclusion compounds and systematic construction of three-component solids by liquid-assisted grinding. *Angewandte Chemie* **2006,** *118* (45), 7708-7712.

14. Friščić, T.; Reid, D. G.; Halasz, I.; Stein, R. S.; Dinnebier, R. E.; Duer, M. J., Ion-and Liquid-Assisted Grinding: Improved Mechanochemical Synthesis of Metal–Organic Frameworks Reveals Salt Inclusion and Anion Templating. *Angewandte Chemie* **2010,** *122* (4), 724-727.

15. Friščić, T.; Fábián, L., Mechanochemical conversion of a metal oxide into coordination polymers and porous frameworks using liquid-assisted grinding (LAG). *CrystEngComm* **2009,** *11* (5), 743-745.

16. Yuan, W.; Friščić, T.; Apperley, D.; James, S. L., High reactivity of metal–organic frameworks under grinding conditions: parallels with organic molecular materials. *Angewandte Chemie* **2010,** *122* (23), 4008-4011.

17. Yang, H.; Orefuwa, S.; Goudy, A., Study of mechanochemical synthesis in the formation of the metal–organic framework Cu 3 (BTC) 2 for hydrogen storage. *Microporous and Mesoporous Materials* **2011,** *143* (1), 37-45.

18. Yang, J.; Zhao, Q.; Li, J.; Dong, J., Synthesis of metal–organic framework MIL-101 in TMAOH-Cr $(NO_3)_3$-H_2BDC-H_2O and its hydrogen-storage behavior. *Microporous and Mesoporous Materials* **2010,** *130* (1), 174-179.

19. Czaja, A. U.; Trukhan, N.; Müller, U., Industrial applications of metal–organic frameworks. *Chemical Society Reviews* **2009,** *38* (5), 1284-1293.

20. Srivastava, V. C., An evaluation of desulfurization technologies for sulfur removal from liquid fuels. *Rsc Advances* **2012,** *2* (3), 759-783.

21. Wu, L.; Xiao, J.; Wu, Y.; Xian, S.; Miao, G.; Wang, H.; Li, Z., A combined experimental/computational study on the adsorption of organosulfur compounds over metal–organic frameworks from fuels. *Langmuir* **2014,** *30* (4), 1080-1088.

22. Farrell, J.; Cernansky, N.; Dryer, F.; Law, C.; Friend, D.; Hergart, C.; McDavid, R.; Patel, A.; Mueller, C. J.; Pitsch, H. *Development of an experimental database and kinetic models for surrogate diesel fuels*; 0148-7191; SAE Technical Paper: **2007**.

23. Lutterotti, L.; Matthies, S.; Wenk, H., MAUD: a friendly Java program for material analysis using diffraction. *IUCr: Newsletter of the CPD* **1999,** *21* (14-15).

24. Young, R., The Rietveld Method, IUCr. *Monographs on Crystallography, Oxford University Press, Oxford* **1993**.

25. Terinte, N.; Ibbett, R.; Schuster, K. C., Overview on native cellulose and microcrystalline cellulose I structure studied by X-ray diffraction (WAXD): Comparison between measurement techniques. *Lenzinger Berichte* **2011,** *89*, 118-131.

26. Vonk, C., Investigation of non-ideal two-phase polymer structures by small-angle X-ray scattering. *Journal of applied crystallography* **1973,** *6* (2), 81-86.

27. Ruland, W., X-ray determination of crystallinity and diffuse disorder scattering. *Acta Crystallographica* **1961,** *14* (11), 1180-1185.

28. Walton, K. S.; Snurr, R. Q., Applicability of the BET method for determining surface areas of microporous metal-organic frameworks. *Journal of the American Chemical Society* **2007,** *129* (27), 8552-8556.

29. Robens, E.; Rouquerol, F.; Rouquerol, J.; Sing, K., Adsorption by powders and porous solids. Academic Press, London, UK: **1999**.

30. Dhakshinamoorthy, A.; Alvaro, M.; Garcia, H., Commercial metal–organic frameworks as heterogeneous catalysts. *Chemical Communications* **2012,** *48* (92), 11275-11288.

31. DeCoste, J. B.; Peterson, G. W.; Jasuja, H.; Glover, T. G.; Huang, Y.-g.; Walton, K. S., Stability and degradation mechanisms of metal–organic frameworks containing the $Zr_6O_4(OH)_4$ secondary building unit. *Journal of Materials Chemistry A* **2013,** *1* (18), 5642-5650.

32. Hafizovic, J.; Bjørgen, M.; Olsbye, U.; Dietzel, P. D.; Bordiga, S.; Prestipino, C.; Lamberti, C.; Lillerud, K. P., The inconsistency in adsorption properties and powder XRD data of MOF-5 is rationalized by framework interpenetration and the presence of organic and inorganic species in the nanocavities. *Journal of the American Chemical Society* **2007,** *129* (12), 3612-3620.

33. Bowmaker, G. A., Solvent-assisted mechanochemistry. *Chemical Communications* **2013,** *49* (4), 334-348.

34. Weyna, D. R.; Shattock, T.; Vishweshwar, P.; Zaworotko, M. J., Synthesis and structural characterization of cocrystals and pharmaceutical cocrystals: mechanochemistry vs slow evaporation from solution. *Crystal Growth and Design* **2009,** *9* (2), 1106-1123.

35. Prochowicz, D.; Sokołowski, K.; Justyniak, I.; Kornowicz, A.; Fairen-Jimenez, D.; Friščić, T.; Lewiński, J., A mechanochemical strategy for IRMOF assembly based on pre-designed oxo-zinc precursors. *Chemical Communications* **2015,** *51* (19), 4032-4035.

36. Seo, Y.-K.; Yoon, J. W.; Lee, J. S.; Lee, U.-H.; Hwang, Y. K.; Jun, C.-H.; Horcajada, P.; Serre, C.; Chang, J.-S., Large scale fluorine-free synthesis of hierarchically porous iron (III) trimesate MIL-100 (Fe) with a zeolite MTN topology. *Microporous and Mesoporous Materials* **2012,** *157*, 137-145.

37. Dhakshinamoorthy, A.; Alvaro, M.; Horcajada, P.; Gibson, E.; Vishnuvarthan, M.; Vimont, A.; Grenèche, J.-M.; Serre, C.; Daturi, M.; Garcia, H., Comparison of porous iron trimesates basolite F300 and MIL-100 (Fe) as heterogeneous catalysts for lewis acid and oxidation reactions: roles of structural defects and stability. *Acs Catalysis* **2012,** *2* (10), 2060-2065.

38. Tsao, C.-S.; Yu, M.-S.; Chung, T.-Y.; Wu, H.-C.; Wang, C.-Y.; Chang, K.-S.; Chen, H.-L., Characterization of pore structure in metal-organic framework by small-angle X-ray scattering. *Journal of the American Chemical Society* **2007,** *129* (51), 15997-16004.

39. Helfferich, F., Principles of adsorption & adsorption processes, by DM Ruthven, John Wiley & Sons, 1984, xxiv+ 433 pp. *AIChE Journal* **1985,** *31* (3), 523-524.

40. Reid, R.; Prausnitz, J., TK Sherwood The properties of gases and liquids. McGraw-Hill, New York: 1977.

41. Volkringer, C.; Leclerc, H.; Lavalley, J.-C.; Loiseau, T.; Férey, G. r.; Daturi, M.; Vimont, A., Infrared spectroscopy investigation of the acid sites in the metal–organic

framework aluminum trimesate MIL-100 (Al). *The Journal of Physical Chemistry C* **2012,** *116* (9), 5710-5719.

42. Petit, C.; Bandosz, T. J., Synthesis, characterization, and ammonia adsorption properties of mesoporous metal–organic framework (MIL (Fe))–graphite oxide composites: exploring the limits of materials fabrication. *Advanced Functional Materials* **2011,** *21* (11), 2108-2117.

43. Park, E. Y.; Hasan, Z.; Khan, N. A.; Jhung, S. H., Adsorptive removal of bisphenol-a from water with a metal-organic framework, a porous chromium-benzenedicarboxylate. *Journal of nanoscience and nanotechnology* **2013,** *13* (4), 2789-2794.

44. Zhou, M.; Wu, Y.-n.; Qiao, J.; Zhang, J.; McDonald, A.; Li, G.; Li, F., The removal of bisphenol A from aqueous solutions by MIL-53 (Al) and mesostructured MIL-53 (Al). *Journal of colloid and interface science* **2013,** *405*, 157-163.

45. Huo, S.-H.; Yan, X.-P., Metal–organic framework MIL-100 (Fe) for the adsorption of malachite green from aqueous solution. *Journal of Materials Chemistry* **2012,** *22* (15), 7449-7455.

Chapter 4: Mechanochemical Reactivity of Ni(II) building blocks with 4,4'-Bipyridine for the solid state preparation of coordination polymers

This chapter is the result of the collaboration with: (i) another research group from the University of Cagliari (Headed by Prof. Aragoni) and (ii) UK National Crystallography Service, Chemistry, University of Southampton, Highfield Campus, Southampton, United Kingdom (Prof. S.Coles).

Part of this study is submitted to *CrystEngComm*.

V. Cabras, G. Ennas, M. Pilloni, A. Scano, R. Lai, M. C. Aragoni, S. J. Coles, "Mechanochemical Reactivity of Secondary Building Blocks for the Solid State Preparation of Coordination Polymers: The case of Nickel Diethyldithiophosphate and 4,4'-Bipyridine."

4 Mechanochemical Reactivity of Ni(II) building blocks with 4,4'-Bipyridine for the Solid State Preparation of Coordination Polymers

4.1 Introduction

The preparation of coordination polymers by the self-assembly of naked metal ions or neutral metal complexes and donor molecules via coordination bonds or secondary bonding interactions is an active topic in the field of crystal engineering. The resulting supramolecular assemblies are of great appeal due to a combination of their intrinsic beauty and promising applications in several differents fields such as gas storage, ion exchange, chemical sensing, catalysis, energy transfer, and separation.[1]

Multi-topic organic molecules are commonly used as spacers and an opportune choice of the number and position of donor atoms can be used to direct the network assembly, although factors such as flexibility of the ligand and different accessible conformations dictate product formation and need to be examined and taken into account during design.[2] The metal coordination environment is exceptionally difficult to control when "naked" metal ions are used as nodes and, in view of that, the use of neutral coordination complexes held together by additional donor molecules or secondary bonding interactions has gained striking importance.[3] In fact, by reducing the degrees of freedom of the system, for instance by using *cis*-protected metal building blocks in place of the naked metal ions, or by using a neutral, coordinatively unsaturated metal complex, less uncertainty can be expected. Moreover, the use of neutral synthons leads to self-reliant supramolecular assemblies that do not require the presence of a counterion and thus reduce the occurrence of isomerism.

A typical example of this building strategy has been reported successfully by Aragoni et.al.[4] by using neutral coordinatively unsaturated phosphonodithioato Ni(II) complexes, as neutral building blocks and bipyridyl-type as neutral ligands in a solution-based batch process. However, the properties of these crystalline

materials are critically dependent on the deliberate creation of a crystalline network structure, planned using properly designed building blocks and this continues to be a challenge. The aspects to be evaluated in developing a network based on coordination polymers are the building blocks, i.e. metal nodes and organic spacers, the metal coordination environments, and also the formation conditions such as solvent, temperature, metal-ligand molar ratio, and weak secondary interactions.

Recently, mechanochemical methods based on grinding or ball-milling of the reactants have also been exploited in the field of crystal engineering.[5] These approaches have the aim of breaking and forming supramolecular interactions with no need for the intermediacy of a solvent, thus providing an alternative and green way to crystal engineering.

Mechanosynthesis, briefly defined by IUPAC as *a chemical reaction that is induced by the direct absorption of mechanical energy*,[6] is emerging as a powerful synthetic technique for environmentally-friendly and energy-efficient synthesis. It offers short reaction times, low-cost starting materials and avoids large quantities of solvent and high temperatures compared to conventional solvent-based methods.[7] Mechanosynthesis typically rapidly promotes solid state reactions and sometimes can induce improved reactivity of reagents resulting in new and unexpected reaction products. Furthermore, there are encouraging recent demonstration of industrial scale up.[8]

While mechanochemistry goes back nearly two centuries,[9] it is only in the last 30 years that the method has been developing in different broad areas of chemistry ranging from inorganic chemistry,[10] to organic,[11] supramolecular chemistry[9b] including the synthesis of coordination polymers,[12] and pharmaceutical solids.[13]

As already explain in Chapter 2, mechanosynthesis can be carried out using manual (mortar and pestle) or non-manual methods such as extrusion or ball milling, the latter being the most widely used in the research laboratory. Two different ball milling synthetic methods, called Neat Grinding (NG) and Liquid-Assisted Grinding (LAG or ILAG for ion LAG),[14] are known.[15] NG is a solvent-free method while in the LAG method small amounts of solvent are added to the solid reaction mixture. The reaction kinetics is often favoured by the presence of a

liquid phase[15a, 16] and different structures can be obtained from the same precursors by changing solvents.[17] A careful solvent selection, as well as its accurate dosing, is therefore required.[18]

Mechanochemical methods normally provide microcrystalline powders and therefore single crystal diffraction methods can not usually be applied for structural characterization. X-ray powder diffraction is the main technique used to characterize microcrystalline powders. Although, it remains more challenging than single crystal structure analysis in terms of deriving accurate structural information.[6]

The problem can often be solved by growing single crystals by conventional solution-based methods and then comparing the resulting structure, via simulation of powder XRD patterns, with that formed by solid–solid mechanosynthesis (scheme 1).[7] It is worth noting that crystallization from solution and mechanical methods do not always yields the same product, especially when solvate species are formed and when nucleation of crystals is under solubility control.[8]

Under these considerations and with the aim of finding new systems that could yield more predictable results, a systematic study to explore the mechanochemical reactions between neutral pre-formed coordination compounds and organic spacers was undertaken. Despite the mechanosynthesis of coordination polymers has already been extensively investigated (Chapter 2, 2.6), to the best of our knowledge the mechanochemical synthesis by using neutral coordinatively unsaturated dithiophosphato/ dithiophosphonato Ni(II) complexes has never been investigated before and could extend the reach of this field.

This chapter relates to the use of mechanochemical approach for reactions between neutral coordinatively unsatured O,O'- dithiophosphato and O,O'-dithiophosphonate Ni(II) complexes $[((EtO)_2PS_2)_2Ni]$ (**1**), $[((MeO)_2PS_2)_2Ni]$ (**2**), $[((MeO\text{-}C_6H_4)(EtO))PS_2)_2Ni]$ (**3**), $[((MeO\text{-}C_6H_4)(MeO))PS_2)_2Ni]$ (**4**), and 4,4'-bipyridine (**L1**), to yield coordination polymers $(\mathbf{1}\cdot\mathbf{L1})_\infty$. $(\mathbf{2}\cdot\mathbf{L1})_\infty$ $(\mathbf{3}\cdot\mathbf{L1})_\infty$ $(\mathbf{4}\cdot\mathbf{L1})_\infty$. In parallel, traditional solution based synthesis (also called "conventional synthesis") of $(\mathbf{1}\cdot\mathbf{L})_\infty$ and $(\mathbf{2}\cdot\mathbf{L1})_\infty$ were performed by Prof. Aragoni group at University of Cagliari. The X-Ray crystal structure of polymers obtained as single crystals by Prof. S.Coles group at University of Southampton UK, were

compared to the mechanochemical data. The single crystal data of $(\mathbf{3}\cdot\mathbf{L1})_\infty$ are already published[4a] while a partial structure determination of $(\mathbf{4}\cdot\mathbf{L1})_\infty$ from XRPD data is here reported.

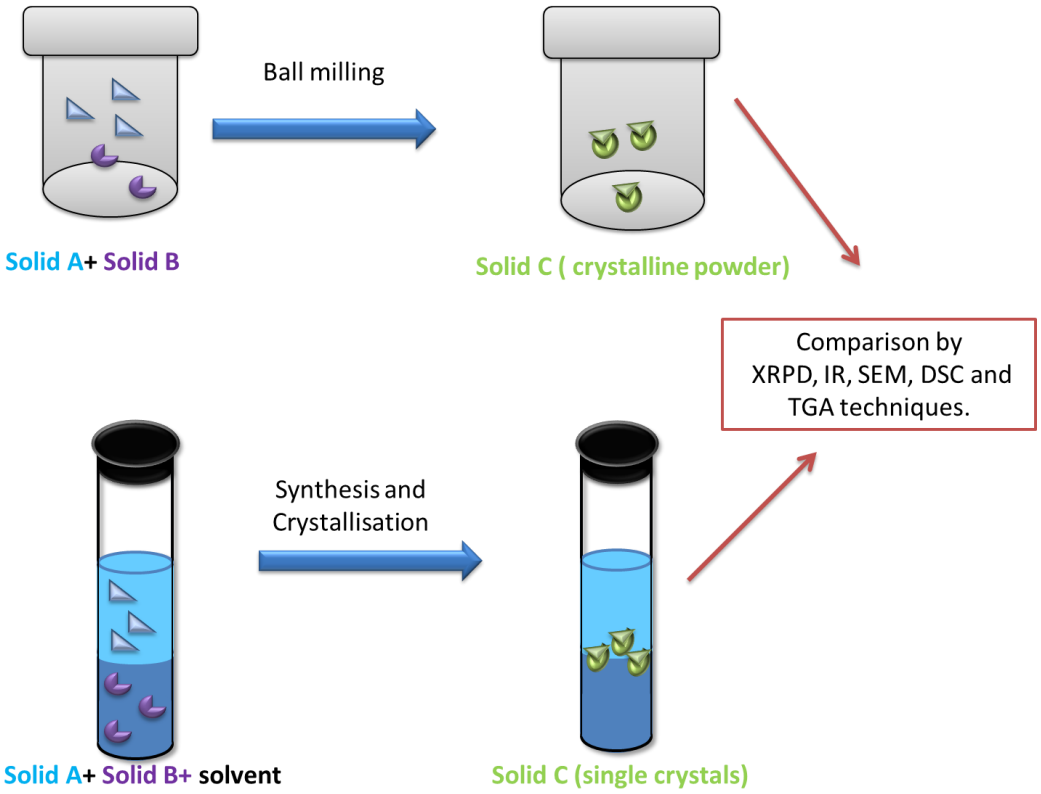

Scheme 4.1. Schematic representation of the procedure adopted to characterize mechanichemical products. The crystalline powder obtained by grinding reactions is compared with the solid obtained through crystallization by XRPD, IR, SEM, DSC and TG techniques.

The evolution of the reactants during the mechanosynthesis process and the influence of the synthesis parameters on the chemical, structural, and thermal properties of the samples were investigated by XRPD, IR, SEM, TG and DSC techniques (Scheme 4.1).

4.2 Experimental section

4.2.1 Materials and Methods

4,4'-bipyridine ($C_{10}H_8N_2$, 99%, Sigma-Aldrich) was used as received without further purification. The dithiophosphate and dithiophosphonate complex $[((EtO)_2PS_2)_2Ni]$ (**1**),), $[((MeO)_2PS_2)_2Ni]$ (**2**), $[((MeO\text{-}C_6H_4)(EtO))PS_2)_2Ni]$ (**3**), $[((MeO\text{-}C_6H_4)(MeO))PS_2)_2Ni]$ (**4**) were synthesized according to the literature procedure.[9] The mixture of reagents was milled using a shaker ball-mill (Spex 8000, CertiPrep, Metuchen, NJ) in a 30 mL teflon coated stainless-steel grinding jar. Two 5 mm diameter zirconia balls (0.40 g for each ball) were used. In order to prevent excessive overheating of the jar the experiments were carried out alternating milling and rest period at 5 min intervals. In the LAG synthesis ethanol (96%, Sigma-Aldrich, without further purification), methanol (for analysis ACS, Carlo Erba) and chloroform (HPLC grade, ACS, Sigma-Aldrich) were used as solvents. The effect of milling was monitored by X-ray powder diffraction (XRPD) performed on small portions of the powder sampled at different milling times.

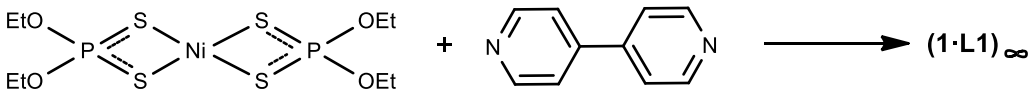

$[((EtO)_2PS_2)_2Ni]$ (**1**) 4,4'-bipyridine (**L1**)

Scheme 4.2. General scheme of the reaction between complex **1** and ligand **L1** to give $\mathbf{(1{\cdot}L1)}_\infty$ coordination polymer **.**

XRPD patterns were recorded at 40 kV and 30 mA on a Seifert X3000 diffractometer using CuK_α radiation in Bragg Brentano geometry and equipped with a graphite monochromator and scintillation counter. The data were collected between 5.00 and 80.00° 2θ, with a 0.05° 2θ step size. In order to obtain a satisfactory signal-to-noise ratio in the X-ray pattern an appropriate acquisition time was selected. The CSD [10] was used to compare experimental and deposited structures. The Maud software [11] was used for Rietveld refinements, and the peak profiles were modelled by using the pseudo-Voigt profile function. Recommended

fitting procedures were adopted and the instrumental profile broadening was derived from the fitting of XRPD data obtained from standard samples.[12] The scale factor, background contribution, lattice parameter, unit cell, average crystallite size, micro-strain were refined. The R_{wp}-factor was used as an indicator of goodness of fit.

X-ray structure determinations and crystallographic data for compound $(\mathbf{1{\cdot}L1})_{\infty}$, $(\mathbf{2{\cdot}L1})_{\infty}$ were collected at 120(2) K by means of combined phi and omega scans on a Bruker-Nonius Kappa CCD area detector, situated at the window of a FR591 rotating anode (graphite Mo-K_α radiation, λ = 0.71073Å). The structures were solved by direct methods, SHELXS-97 and refined on F^2 using SHELXL.[13]

Anisotropic displacement parameters were assigned to all non-hydrogen atoms. Hydrogen atoms were included in the refinement, but thermal parameters and geometry were constrained to ride on the atom to which they are bonded. The data were corrected for absorption effects using SORTAV.[14]

The structure has been deposited with the Cambridge Crystallographic Data Centre: deposition number CCDC 1517440.

Sample morphology was observed using scanning electron microscopy (SEM) (S-4100, HITACHI). The samples were fixed on a brass stub using carbon double-sided, coated with gold blazers SCD 004 sputter coater for 2 min and observed under an excitation voltage of 10 kV.

FT-Infrared spectra were recorded on a Thermo Nicolet 5700 spectrometer at room temperature using a flow of dried air. Middle IR spectra (resolution 4 cm^{-1}) were recorded as KBr pellets, with a KBr beam-splitter and KBr windows ($(\mathbf{1{\cdot}L1})_{\infty}$ samples). For $(\mathbf{2{\cdot}L1})_{\infty}$, $(\mathbf{3{\cdot}L1})_{\infty}$, $(\mathbf{4{\cdot}L1})_{\infty}$ samples a Bruker Vector-22 equipped with a diamond single-reflection ATR accessory (Platinum ATR module) and a liquid nitrogen cooled MCT detector is adopted.

FT-Raman spectra (resolution of 4 cm^{-1}) were recorded as KBr solid mixture on a Bruker RFS100 FT-Raman spectrometer, fitted with an In-Ga-As detector (room temperature) operating with a Nd-YAG laser (excitation wavelength 1064 nm) with a 180° scattering geometry. The excitation power was modulated between 100 and 250 mW.

Elemental analyses were performed with an EA1108 CHNS-O Fisons instrument.

Differential scanning calorimetry (DSC) measurements were performed at atmospheric pressure using a Perkin-Elmer instrument model DSC7 having a maximum temperature detectable of 600°C and 725°C using aluminum or platinum crucible respectively. The measurements were performed under Ar flow (40 mL min^{-1}). Samples of 5 mg were encapsulated in aluminum crucibles and scanned in the temperature range of 40–360 °C (where the most significant transformations are present) with a heating rate of 10°C min^{-1}. The calorimeter was calibrated by measuring the melting temperature of metallic indium and zinc (99.999 mass% purity) and the temperature was obtained with an accuracy of ±0.5 °C. Thermogravimetric analysis was carried out on a TGA-SDTA 851 Mettler-Toledo instrument (T_{max}=1100°C) using an alumina sample pan under Argon flow (50 mL min^{-1}) with a heating rate of 10 K min^{-1}. All the measures were performed in the range 35-1000°C. The instrument was calibrated with zinc and iron standard samples and the temperature was obtained with an accuracy of ±2 °C.

4.2.2 Synthesis

Syntheses of $[((EtO)_2PS_2)_2Ni\cdot(4,4'\text{-bipyridine})]_\infty$, $(1\cdot L1)_\infty$.

Conventional synthesis: complex **1** (0.0214 g, 0.05 mmol) and **L1** (0.0078 g, 0.05 mmol) were reacted at 140 °C in a high pressure Aldrich tube in 30 mL of EtOH. After complete dissolving of the reagents, the reaction mixture was slowly cooled to room temperature. Few days later $(\mathbf{1\cdot L1})_\infty$ (0.0130 g, 0.02 mmol, 47% yield) was obtained as green crystals suitable for X-ray analysis. M.p.: 210 °C (d). Elemental analysis found (calc. for $C_{18}H_{26}N_2O_4P_2S_4Ni$; formula mass = 585.31 u): C, 36.98 (36.94); H, 4.40 (4.82); N, 4.83 (4.79); S, 19.71 (21.91). FT-IR (KBr, 4000-400 cm^{-1}): 2974 vw, 2284 vw, 1608 s, 1535 vw, 1490 w, 1409 m, 1388 w, 1221 m, 1160 w, 1070 vw, 1042 s, 1018 vs, 956 vs, 815 vs, 774 s, 729 w, 682 s, 665 m, 634 vm, 552 w, 482 vm, 470 m, 452 w, 440 w 426 m, 412 w cm^{-1}. FT-Raman (3500-100 cm^{-1}, 200 mW, solid in KBr, relative intensities between parentheses related to the highest peak taken equal to 10.0): 2928 (3.5), 1614 (10), 1295 (9.8), 1022 (7.2), 550 (3.5), 92 (6.3) cm^{-1}.

NG synthesis: equimolar quantities of complex **1** (0.1712g, 0.4 mmol) and **L1** (0.0637g, 0.4mmol) were placed in the jar along with two 5 mm diameter balls. Powder was collected after selected time intervals. The NG synthesis was also performed in the 2:1 (**L1**:**1**) molar ratio, and the resulting product compared to those obtained by conventional and equimolar NG synthesis.

LAG synthesis: equimolar quantities of complex **1** (0.1712g, 0.4 mmol) and **L1** (0.0637g, 0.4mmol) were placed in the jar along with two 5 mm diameter balls and 50 μL of ethanol.

Syntheses of $[((MeO)_2PS_2)_2Ni\cdot(4,4'\text{-bipyridine})]_\infty$, $(2\cdot L1)_\infty$.

Conventional synthesis of $(2\cdot L1)_\infty$: complex **2** (0.0187 g, 0.05 mmol) and **L1** (0.0078 g, 0.05 mmol) were reacted at 130 °C in a high pressure Aldrich tube in 10 mL of $CHCl_3$ and 20 mL of MeOH. After complete dissolving of the reagents, the reaction mixture was slowly cooled to room temperature. After a few days $(\mathbf{2\cdot L1})_\infty$ (0.0177 g, 0.03 mmol, 78.8% yield) was obtained as green crystals suitable for X-ray analysis. M.p.: 195 °C (d). Elemental analysis found (calc. for $C_{14}H_{20}N_2O_4P_2S_4Ni$; formula mass = 530.01 u): C, 31.65 (31.77); H, 3.77 (3.81); N, 5.29 (5.29); S, 23.71 (24.24). FT-IR (4000-600): 3080 vw, 3010 vw, 2988 vw, 2941 w, 1608 s, 1547 vw, 1536 vw, 1489 w, 1451 m, 1406 m, 1225 m, 1164 m, 1073 m, 1064 vm, 1044vw, 1002 vs, 791v s, 730 w, 678 s, 656 vs, 633 vm. cm^{-1}. FT-Raman (3500-100 cm^{-1}, 200 mW, solid in KBr, relative intensities between parentheses related to the highest peak taken equal to 10.0): 1614 (10.0), 1521 (0.4), 1467 (0.8), 1295 (9.4), 1245 (1.2), 1230 (1.4), 1090 (2), 1023 (6.2), 788 (0.6), 640 (1), 514 (4.6), 393 (2), 367 (1.9), 265 (2.4), 113 (5.4), 38 (0.9) cm-^{1}

NG synthesis of $(2\cdot L1)_\infty$: complex **2** [$((MeO)_2PS_2)_2$ Ni] 0.1496g, 0.4 mmol) and **L1** 4,4'-bipyridine (0.0637g, 0.4mmol) mixture was placed in the jar along with two 5 mm diameter balls. Powder was collected after selected time intervals.

LAG synthesis of $(2\cdot L1)_\infty$: Two LAG synthesis were also carried out: in the first one 50 μL of methanol were added, in the second one the same volume of chloroform $CHCl_3$ was added. Samples were collected at different milling times.

The synthesized ball milling samples have been compared to the corresponding samples prepared by conventional approach.

Synthesis of $[(MeO\text{-}C_6H_4)(EtO))PS_2)_2Ni]\cdot(4,4'\text{-bipyridine})]_\infty$, $(3\cdot L1)_\infty$.

Conventional synthesis of $(3\cdot L1)_\infty$: The sample having formula $C_{28}H_{32}N_2O_4P_2S_4Ni$ was prepared in the conventional manner according to previously reported procedure.[4a] Spectral data are in agreement with the literature Ref:4a.

NG synthesis of $(3\cdot L1)_\infty$: complex **3** $[(MeO\text{-}C_6H_4)(EtO))PS_2)_2Ni]$ (0.2213g, 0.4mmol) and **L1** 4,4'-bipyridine (0.0637g, 0.4mmol) mixture was placed in the jar along with two 5 mm diameter balls. Powder was collected after selected time intervals.

LAG synthesis of $(3\cdot L1)_\infty$: Two LAG synthesis were also carried out: in the first one 50 μL of ethanol was added, in the second one the same volume of chloroform $CHCl_3$ was added. Samples were collected at different milling times.

Synthesis of $[(MeO\text{-}C_6H_4)(MeO))PS_2)_2Ni]$ (4,4'-bipyridine)]$_\infty$, $(4\cdot L1)_\infty$.

Conventional synthesis of $(4\cdot L1)_\infty$: In the conventional synthesis, complex **4** $[(MeO\text{-}C_6H_4)(MeO))PS_2)_2Ni]$ (0.0262 g, 0.05 mmol) and **L1** (4,4'-bipyridine , 0.0078 g, 0.05 mmol) were reacted at 150°C in a high-pressure Aldrich tube in 30 mL of and MeOH/$CHCl_3$ (1:1 v/v) mixture. After the reagents were completely dissolved, the reaction mixture was slowly cooled to room temperature. The product was obtained (0.0272 g, 0.04 mmol, 80% yield) as a green powder not suitable for single crystal analysis. M.p.: 283 °C (d). Elemental analysis found (calc. for $C_{26}H_{28}N_2O_4\ S_4P_2Ni$; formula mass = 680.57 u): C, 44.40 (45.83); H, 4.07 (4.14); S, 17.41 (18.82). FT-IR (4000-600): 3073 vw, 2939 vw, 2838 vw, 2349 vw, 1604 s ν(C=N), 1591 s, 1565 vw, 1532 vw ν(C=C, conj), 1498 m, 1484 w, 1453 m, 1444 m, 1404 m, 1293 vm, 1258 s, 1213 vm,1178 vm, 1111 s, 1062 w, 1018 vs (pirydine breathing mode), 969 w, 835 m, 809 s, 778vs, 729 w, 658 s, 644 vs, 626 s cm^{-1}. FT-Raman (3500-100 cm^{-1}, 200 mW, solid in KBr, relative intensities between parentheses related to the highest peak taken equal to 10.0): 3074 (2.1), 2938 (2.1), 2836 (1.5), 1068 (10.0), 1289 (9.6), 1237 (1.8), 1177 (0.9),

1110 (4.5), 1083 (2.1), 1021 (6.9), 801 (1.5), 657 (1.8), 541 (5.7), 365 (1.8), 292 (2.1), 118 (5.4) cm^{-1}.

NG synthesis of $(4\cdot L1)_\infty$: In the NG synthesis, complex **4** [(MeO-C_6H_4)(MeO))$PS_2)_2$Ni] (0.2102g, 0.4mmol) and **L1** 4,4'-bipyridine (0.0637g, 0.4mmol) mixture was placed in the jar along with two 5 mm diameter balls. Powder was collected after selected time intervals.

LAG synthesis of $(4\cdot L1)_\infty$: Three LAG synthesis were also carried out adding a) 50 μL of methanol CH_3OH , b) 50 μL of chloroform $CHCl_3$ and c) 50 μL of a mixture (1:1 v/v) of methanol and chloroform. Samples were collected at different milling times.

4.3 Results and discussion

4.3.1 $[((EtO)_2PS_2)_2Ni]\cdot$(4,4'-bipyridine)$]_\infty$, $(1\cdot L1)_\infty$

4.3.1.1 Structure and morphology

The reaction of 4,4'-bipyridine (**L1**) and the nickel dithiophosphato complex $[Ni((EtO)_2PS_2)_2]$ (**1**) under solvothermal conditions afforded a crystalline compound which was isolated and identified by means of single crystal X-ray diffraction as the coordination polymer of formula $(\mathbf{1\cdot L1})_\infty$. Crystallographic data are reported in Table 4.1 and the asymmetric unit with selected bond lengths and angles in Figure 4.1.

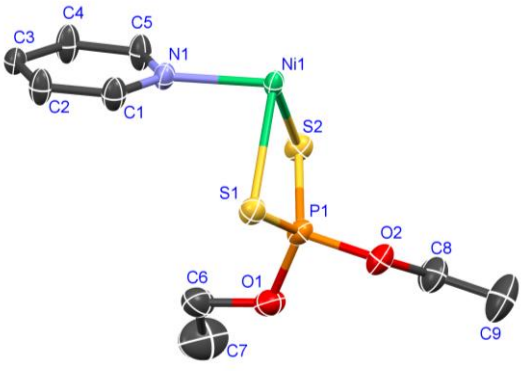

Figure 4.1: Ellipsoid drawing (70% probability level) of the asymmetric unit of $(\mathbf{1\cdot L1})_\infty$, with atom numbering scheme. Selected bond lengths and angles: Ni1─S1, 2.5057(8); Ni1─S2, 2.4948(7); Ni1─N1, 2.0750(17); P1─S1, 1.9769(8); P1─S2, 1.9821(8) Å; S1─Ni1─S2, 82.01(3); S1─Ni1─N1, 88.76(5); S2─Ni1─N1, 90.21(5)°.

Examination of the data reported in Table 4.1 shows a good agreement between the single crystal and powder data with minor discrepancies especially evident in the higher values of the c lattice parameter in the powder data. These differences can be ascribed to the free rotation of the ethoxy P-substituents that is evident even at 120 K (see thermal ellipsoid displacements of atoms C6-C9 in Figure 4.1) and become more evident at the temperature at which XRPD patterns were recorded (298 K) giving rise to increasing disorder and therefore a minor packing efficiency.

Compound $(\mathbf{1}\cdot\mathbf{L1})_\infty$ is a mono-dimensional rigid polymer formed by axial coordination of **L1** to the Ni^{II} ion of the square-planar dithiophosphato complex **1**. The $[Ni(EtOPS_2)_2]$ units are bridged by the organic spacers **L1** to form neutral parallel chains –**L**–$[Ni(EtOPS_2)_2]$–**L**–$[Ni(EtOPS_2)_2]$–**L**– as shown in Figure 4.2. The coordination environment around the nickel ion results in a distorted octahedron with four sulfur atoms from two bidentate dithiophosphato units in the equatorial plane and two nitrogen atoms, from different bipyridine units, occupying the axial positions. The coordination of the neutral donor **L1** induces variations in the bond distances and angles in the NiS_4 coordination framework similar to those found for analogous molecular adducts between phosphonodithioato complexes and pyridine derivatives, which is ascribed to the reduced net positive charge on the central Ni.[4b] As shown in Figure 4.2a, the main structural feature of $(\mathbf{1}\cdot\mathbf{L1})_\infty$ is the presence of linear chains, that closely resemble the analogous polymer $[Ni(EtOdtp)_2\ \mathbf{L1}]_\infty$[4a] with Ni···Ni distances between bridged dithiophosphato units of 11.24 Å very similar to those of 11.38 Å found in $[Ni(EtOdtp)_2\ \mathbf{L1}]_\infty$. The chains are aligned in planes that pack in an antiparallel fashion (shown in blue and yellow in Figure 4.2b) due to the presence of glide planes perpendicular to the (010) direction with glide component (1/2, 0, 1/2).

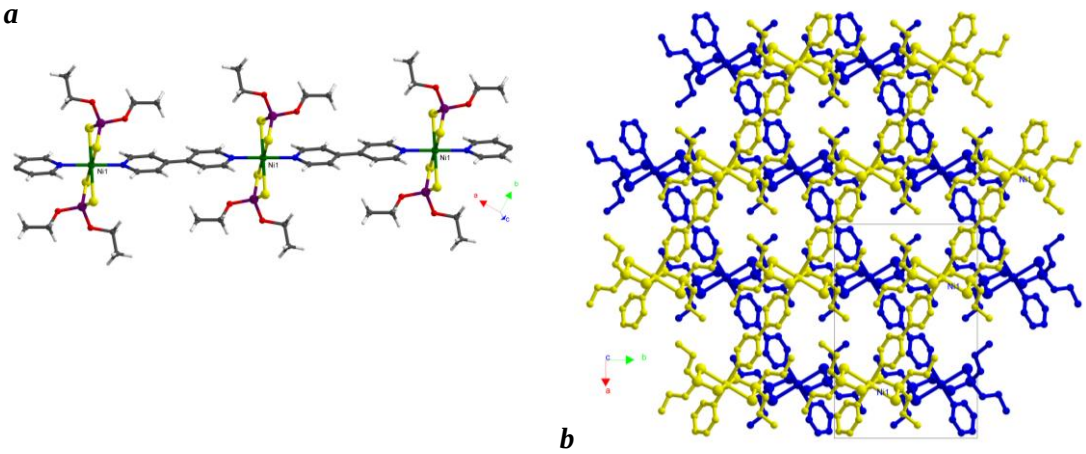

Figure 4.2. Packing views of $(\mathbf{1}\cdot\mathbf{L1})_\infty$ showing the linear polymeric chain (***a***) and the parallel planes packing in the different directions (evidenced in blue and yellow color) due to the presence of glide planes perpendicular to the (010) direction with glide component (1/2, 0, 1/2) (***b***).

In order to optimize the ball mill process, previous general mechanochemical studies were carried out (data not shown). During these studies the volume of the jar, the ball milling apparatus, and the mass of reagents were kept constant while the number of balls (2, 4 or 28) and their diameters (5 or 10 mm) was varied. Thus, different values for the mass, collision frequency, and free path of the balls were obtained, consequently changing the kinetic energy involved in the collisions. The complexity of the milling process can be simplified in two different elemental mechanical actions by which energy is transferred from the milling tools to the milled powder: collision and attrition. The mechanism of collision prevails when the milling device contains a limited number of balls. On the contrary it is expected that the attrition mechanism prevails when the mill begins to be filled up with balls.[15] In all our experiments the collision regime is dominant respect to the attrition one.[16] The results of the above described studies revealed that the use of two 5 mm diameter balls is the optimal condition to reach the desired product in the shortest time. For this reason, in all the mechanochemical synthesis reported in this thesis two zirconia balls of 5mm diameter were used.

The XRPD patterns recorded on NG samples at different selected time intervals during the mechanosynthesis are shown in Figure 4.3. After 5 minutes of milling the pattern (showed in Figure 4.3a) indicates the almost complete formation of coordination polymer $(\mathbf{1}\cdot\mathbf{L1})_\infty$. However, small peaks due to reagents were barely

evident, particularly faint peaks at 8.78, 12.19 and 13.51 2θ degrees due to nickel complex **1** and peaks at 12.57 and 25.62 2θ degree belonging to **L1**. After 10 min milling the complete conversion of reagents into the green colored $(\mathbf{1}\cdot\mathbf{L1})_{\infty}$ compound was achieved. Its pattern corresponds to that recorded for the coordination polymer obtained by conventional methods (Figure 4.4c and a, respectively), with no residual peaks due to unreacted reagents detectable.

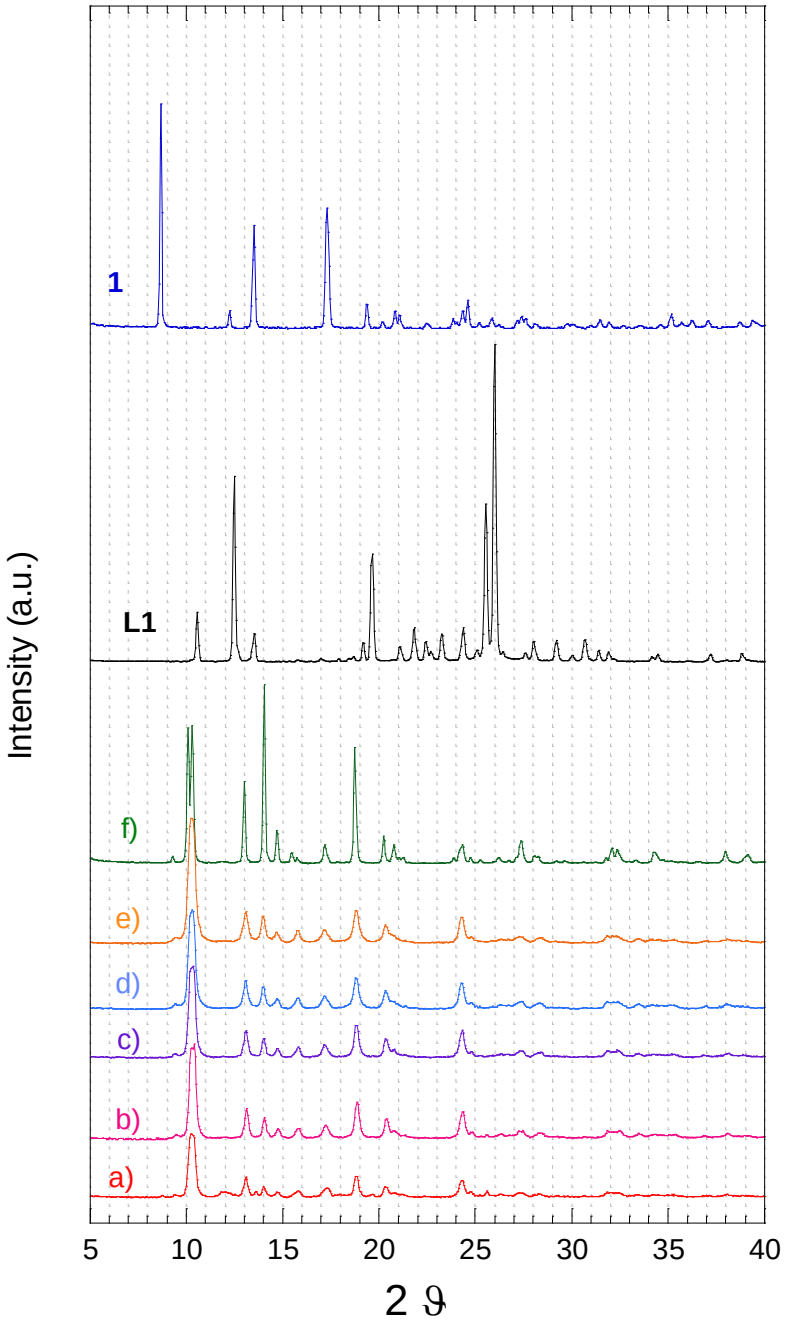

Figure 4.3. Comparison of XRPD patterns for compound $(\mathbf{1}\cdot\mathbf{L1})_{\infty}$ obtained by NG synthesis: a) sample after 5 minutes grinding, b) after 10 minutes grinding, c) after 20 minutes grinding, d) 25 minutes grinding, e) 30 minutes grinding and f) conventional synthesis samples. Reagents **L1** and **1** are reported to comparison

Table 4.1. Summary of X-Ray single crystal and powder data and structure refinements parameters for compound $(\mathbf{1}\cdot\mathbf{L1})_\infty$ obtained by conventional and grinding methods (NG 10 min and LAG 5 min). (<D> average crystal size; **σ** microstrain).

Compound	$(\mathbf{1}\cdot\mathbf{L1})_\infty$ conventional	$(\mathbf{1}\cdot\mathbf{L1})_\infty$ conventional	$(\mathbf{1}\cdot\mathbf{L1})_\infty$ NG 10 min	$(\mathbf{1}\cdot\mathbf{L1})_\infty$ LAG 5 min
XRD method	single crystal	powder	powder	powder
Crystal system	monoclinic	monoclinic	monoclinic	monoclinic
Space group	C 2/c	C 2/c	C 2/c	C 2/c
a / Å	19.099(4)	19.71(2)	19.78(2)	19.74(2)
b / Å	11.842(2)	11.25(2)	11.24(2)	11.23(2)
c / Å	12.957(3)	14.15(2)	14.36(2)	14.24(2)
β / °	112.93(3)	116.7(5)	116.8(5)	116.7(5)
V / $Å^3$	2698.9(11)	2776(3)	2848(3)	2820(3)
Z	4	4	4	4
T / K	120	298	298	298
D_{calc} /g cm^{-3}	1.441	-	-	-
θ min-max /°	3.3-27.5	5-80	5-80	5-80
<D> / nm	-	>100	37	60
σ / %	-	<0.1	0.6	0.4
Wavelength/ Å	0.71073 (MoKα)	1.54056(CuKα)	1.54056 (CuKα)	1.54056(CuKα)
R indices (all data)	R_1 = 0.030; wR_2 = 0.0705	R_{wp}=10.0	R_{wp}=9.2	R_{wp}=5.8

$$w^{-1} = \left[\sigma^2\left(F_{exp}^2\right) + (0.0320P)^2 + 2.1046P\right] \; where \; P = [F_{exp}^2 + 2F_{calc}^2]$$

$$R_1 = \sum_{i=1}^{n} (|F_{exp,i}| - |F_{calc,i}|) / \sum_{n=1}^{\infty} |F_{exp,i}|$$

$$wR_2 = \left\{ \sum_{i=1}^{n} [w(F_{exp,i}^2 - F_{calc,i}^2)^2] / \sum_{n=1}^{\infty} [w(F_{exp,i}^2)^2] \right\}^{1/2}$$

$$R_{wp} = 100 * \sum_{i=1}^{n} w_i \left(I_i^{exp} - I_i^{calc}\right)^2 / \sum_{i=1}^{n} \left(w_i I_i^{exp}\right)^2 \quad .$$

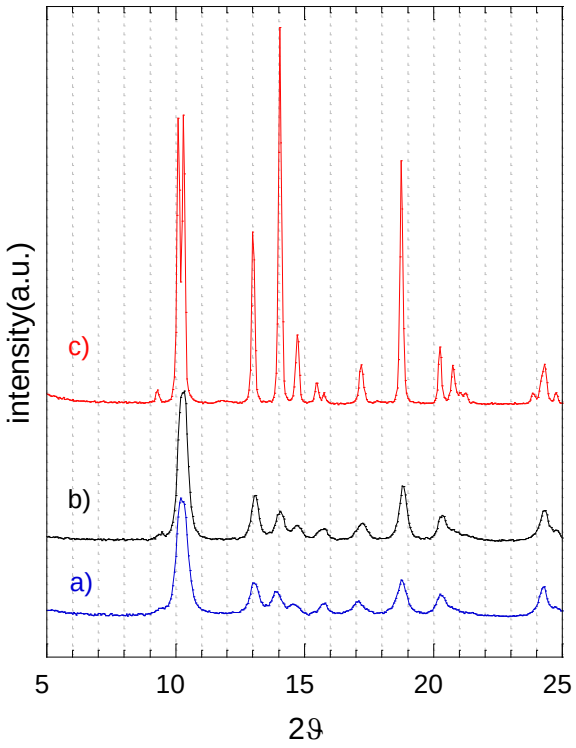

Figure 4.4. Comparison of XRPD patterns for compound $(\mathbf{1}\cdot\mathbf{L1})_{\infty}$ obtained by a) NG after 10 minutes grinding, b) LAG after 5 minutes grinding and c) conventional synthesis samples.

Further milling of the powder did not change the structure of the products. Therefore at 10 min of milling the synthesis can be considered as having concluded (Figure 4.3a-e). It is noteworthy that the XRPD peaks for the NG 10 minute sample are in the same position as the conventionally prepared sample, but the intensity and width, and therefore size and strain, are significantly different. This can be explained by the continuous reduction of crystallite grain size, due to the repeated fracture of the powders induced by milling, accompanied by progressive dispersion and intimate mixing at the atomic level, which promotes interdiffusion of the starting compounds and their solid state reaction. Moreover, milling induces structural disorder giving broader peaks with different intensities.

With the aim of optimizing the synthesis, we also explored the LAG method by adding a few microlitres of ethanol, normally used as solvent in the conventional synthesis, to the starting powder reagents. Examination of Figure 4.4b shows that the use of solvent reduced the reaction times: LAG mechanosynthesis can be

considered concluded after 5 minutes of milling (Figure 4.5a-d). The 5 minute LAG XRPD pattern is very similar to the 10 minute NG synthesis (Figure 4.4a-b).

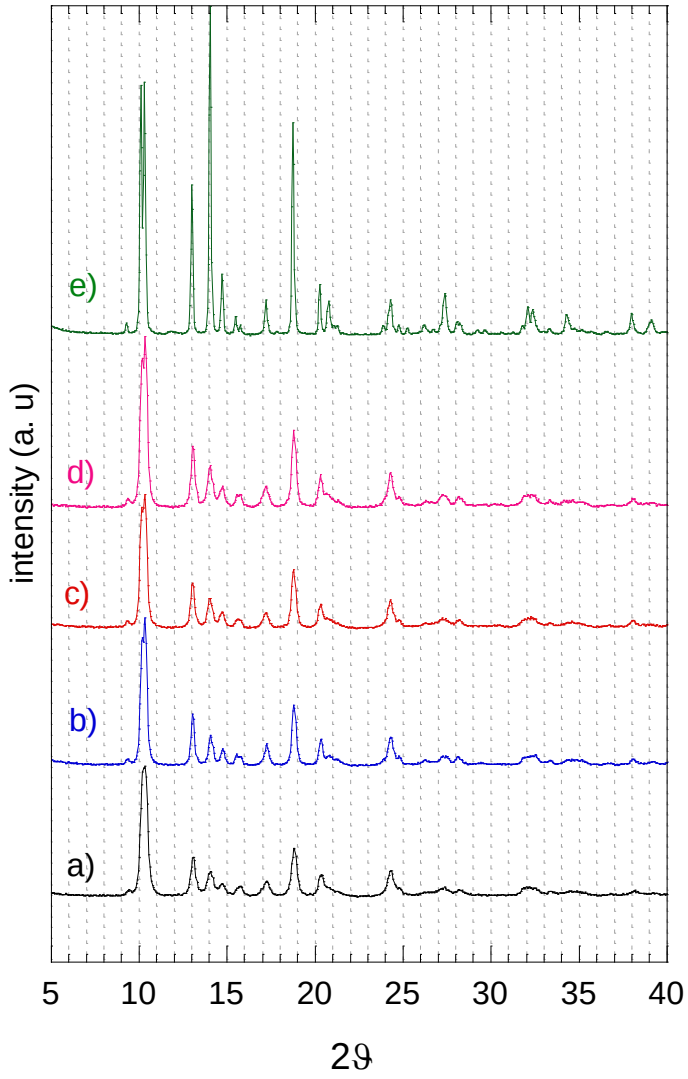

Figure 4.5. Comparisons of XRPD patterns for LAG synthesis of $(\mathbf{1}\cdot\mathbf{L1})_\infty$: a) sample after 5 minutes of milling, b) after 10 minutes, c) after 15 minutes, d) after 20 minutes and e) conventional method sample.

Rietveld refinement (Figure 4.6 and Table 4.1) of the LAG sample indicated an average crystal size of 60 nm, which is slightly bigger than the NG sample. The microstrain of the LAG sample is very similar to the corresponding NG sample.

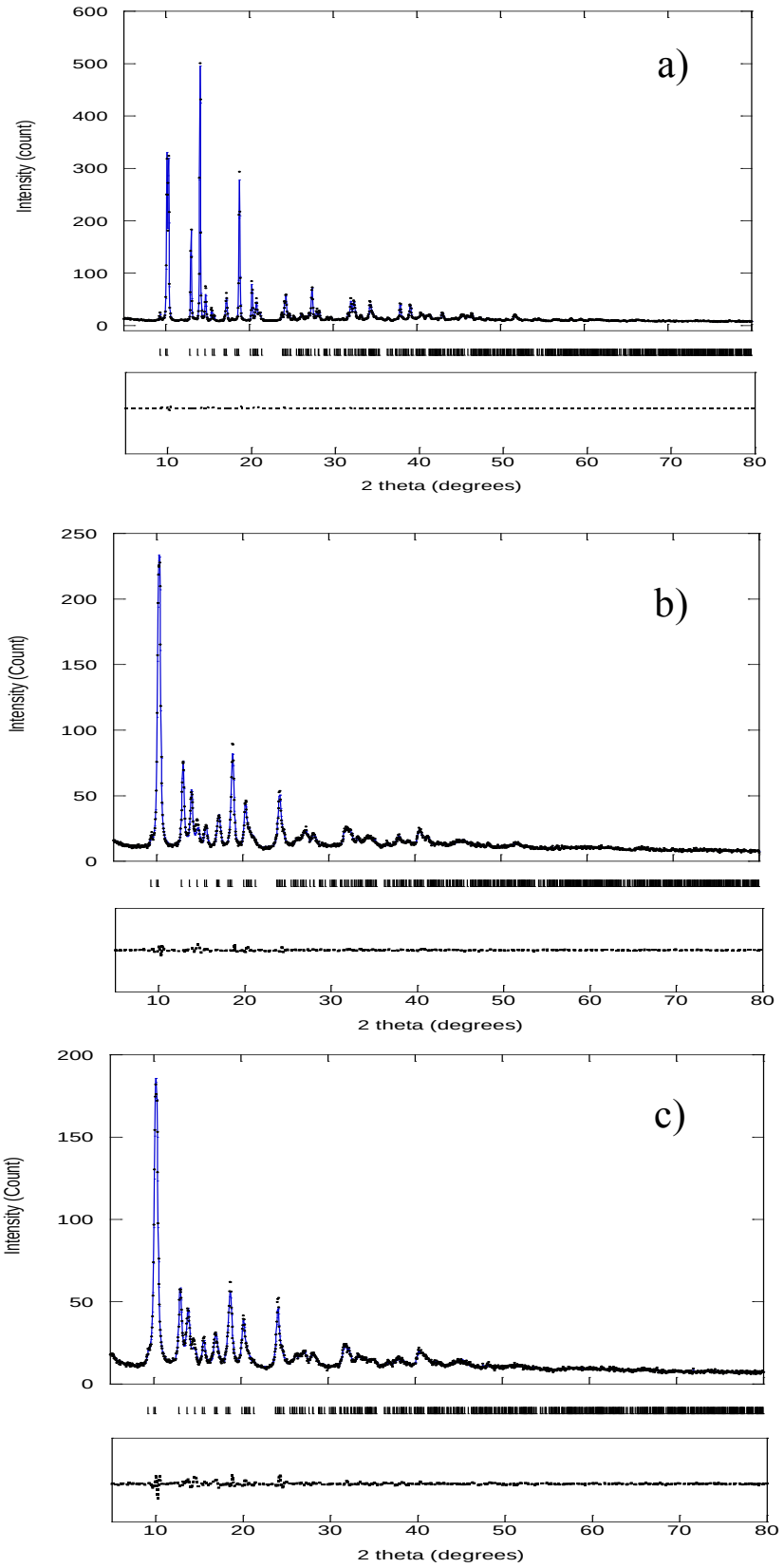

Figure 4.6. Rietveld refinement for conventional (a), LAG (b) and (c) NG samples : experimental (dots), simulated curve (solid lines) and curva difference (dashed line). Vertical bars represent reflection position of $(\mathbf{1}\cdot\mathbf{L1})_{\infty}$ phase obtained by single crystal data.

SEM micrographs of the compound $(\mathbf{1}\cdot\mathbf{L1})_\infty$ prepared by conventional synthesis and using NG and LAG mechanosyntesis methods highlight the different morphology of the samples (Figure 4.7). The conventional sample is mainly constituted of well-defined microcrystals (left), whilst NG and LAG samples show irregular shaped aggregates of nanocrystals with rough surfaces. Moreover the LAG sample forms as smaller aggregates in comparison to the NG sample.

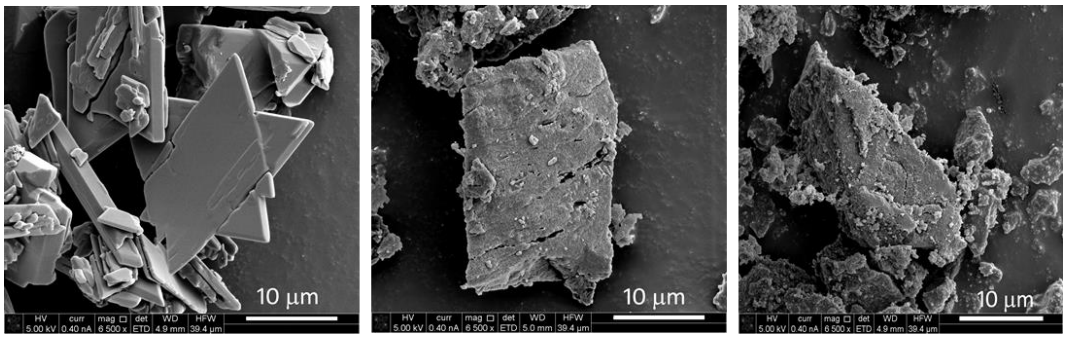

Figure 4.7. SEM images of compound $(\mathbf{1}\cdot\mathbf{L1})_\infty$: micro-crystals from conventional synthesis (left), NG sample after 10 minutes grinding (middle), LAG sample after 5 minutes grinding (right). Magnifications are reported in the bottom of the micrograph (bar= 10µm).

The FTIR spectra of the samples obtained by NG, LAG and conventional methods are reported in Figure 4.8. The most characteristic ring vibration ν(C-N), ν(C-C) and pirydine breathing mode can be observed in the range (cm^{-1}): 1600.0-1608.9, 1533.4-1537.5 and 1006.8-1018.3, respectively. These bands are shifted at higher frequencies compared to free 4,4'-bipy,[17] thus confirming 4,4'-bipy coordination to the nickel metal complex.

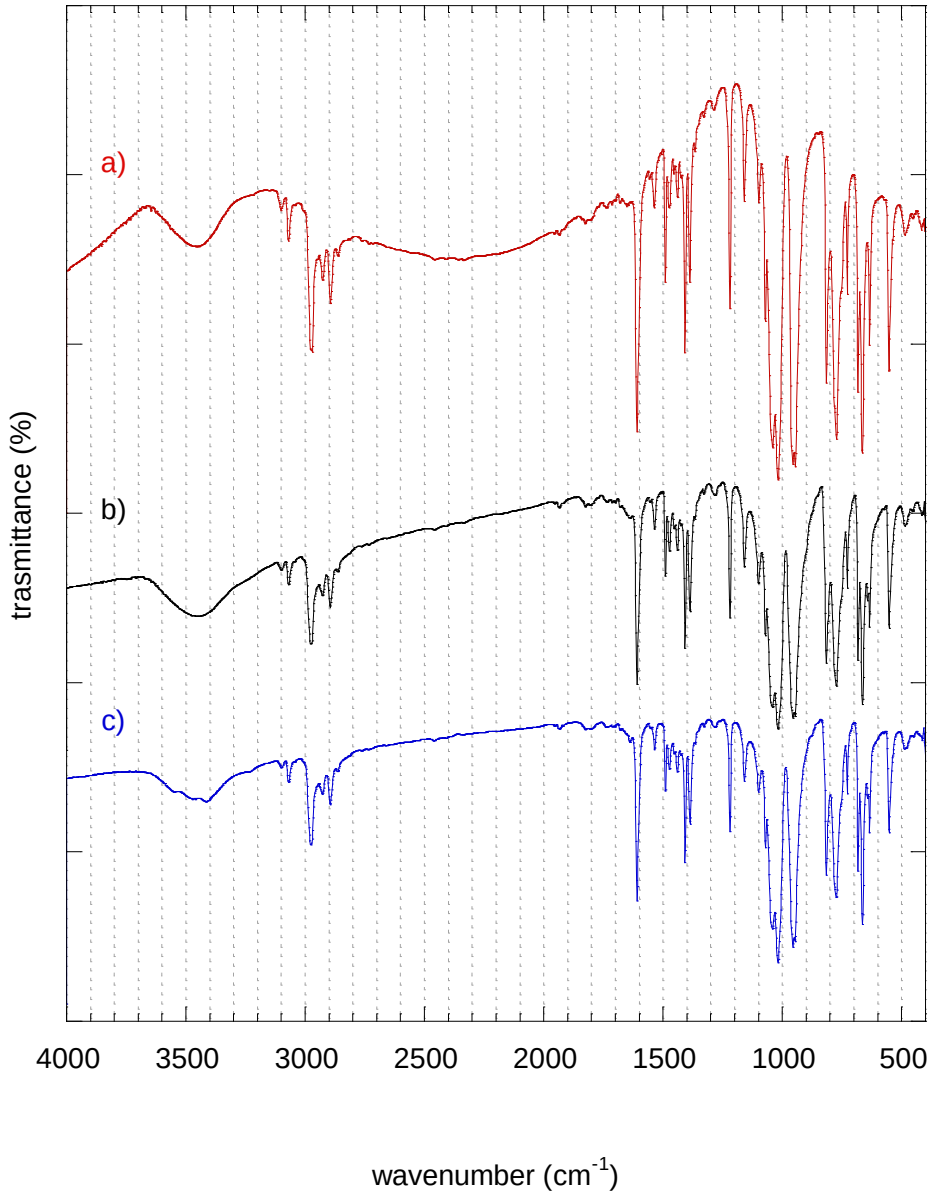

Figure 4.8. IR spectra of compound $(\mathbf{1}\cdot\mathbf{L1})_{\infty}$: a) conventional synthesis, b) NG and c) LAG samples.

4.3.1.2 Thermal stability $(\mathbf{1}\cdot\mathbf{L1})_\infty$

In order to determine the thermal behavior of the samples TGA and DSC measurements were conducted on compound $(\mathbf{1}\cdot\mathbf{L1})_\infty$ prepared by conventional, and mechanochemical NG and LAG methods (Figure 4.9). TG and the corresponding derivative dTG curve of the sample prepared by conventional synthesis (Figure 4.8a left) shows three main mass loss (and dTG peaks) in the temperature range of 217-241°C, (ii) 339-466 °C and (iii) 780-957°C respectively. The first and second mass loss of the TG curve reflect thermal decomposition of the organic parts of $(\mathbf{1}\cdot\mathbf{L1})_\infty$; the mass remaining after the first step (73.9%) corresponds, as expected, to the loss of **L1**. The plateau observed from 466 to 780 °C is consistent with the presence of the bis(dithio-metaphosphato) nickel(II) $[Ni(S_2PO)_2]$ moiety, in agreement with the data reported in literature for the analogous $[Pt(EtOPS_2)_2]$ platinum complex.[18]

At higher temperature (do not detectable with DSC7 apparatus), decomposition of the sample is observed with TGA, with formation of a residue product identified as nickel phosphate $Ni_2P_2O_7$ by XRPD analysis (data not shown).

In Figure 4.9 (right side) DSC thermograms of $(\mathbf{1}\cdot\mathbf{L1})_\infty$ samples are also reported, along with those of **L1** and **1** reagents for comparison. In agreement with the TG analysis, the DSC curve of the conventional sample shows a no reversible asymmetric exothermic peak at 223°C due to decomposition of $(\mathbf{1}\cdot\mathbf{L1})_\infty$ into $[Ni(S_2PO)_2]$. No peaks are observed in the DSC curve at temperatures lower than 220°C indicating that the polymer $(\mathbf{1}\cdot\mathbf{L1})_\infty$ is stable up to this temperature.

Similar thermal behaviors were observed for the samples obtained by mechanochemical NG (b) and LAG (c) methods. Figure 4.9 (left) shows the formation of the same degradation compounds with small differences only in the temperature of the first mass loss, which is slightly lower (196 °C) in comparison to that found for the conventionally prepared sample (220 °C). The corresponding DSC exothermic peaks are also in agreement, showing a shift of temperature from 223 to 209 °C. Moreover, in ball milled samples, particularly in the NG one, the DSC peaks related to the polymer decomposition are broader than those recorded

for the conventional sample, which is consistent with smaller and/or more disordered (**1**·**L1**)$_\infty$ particles.

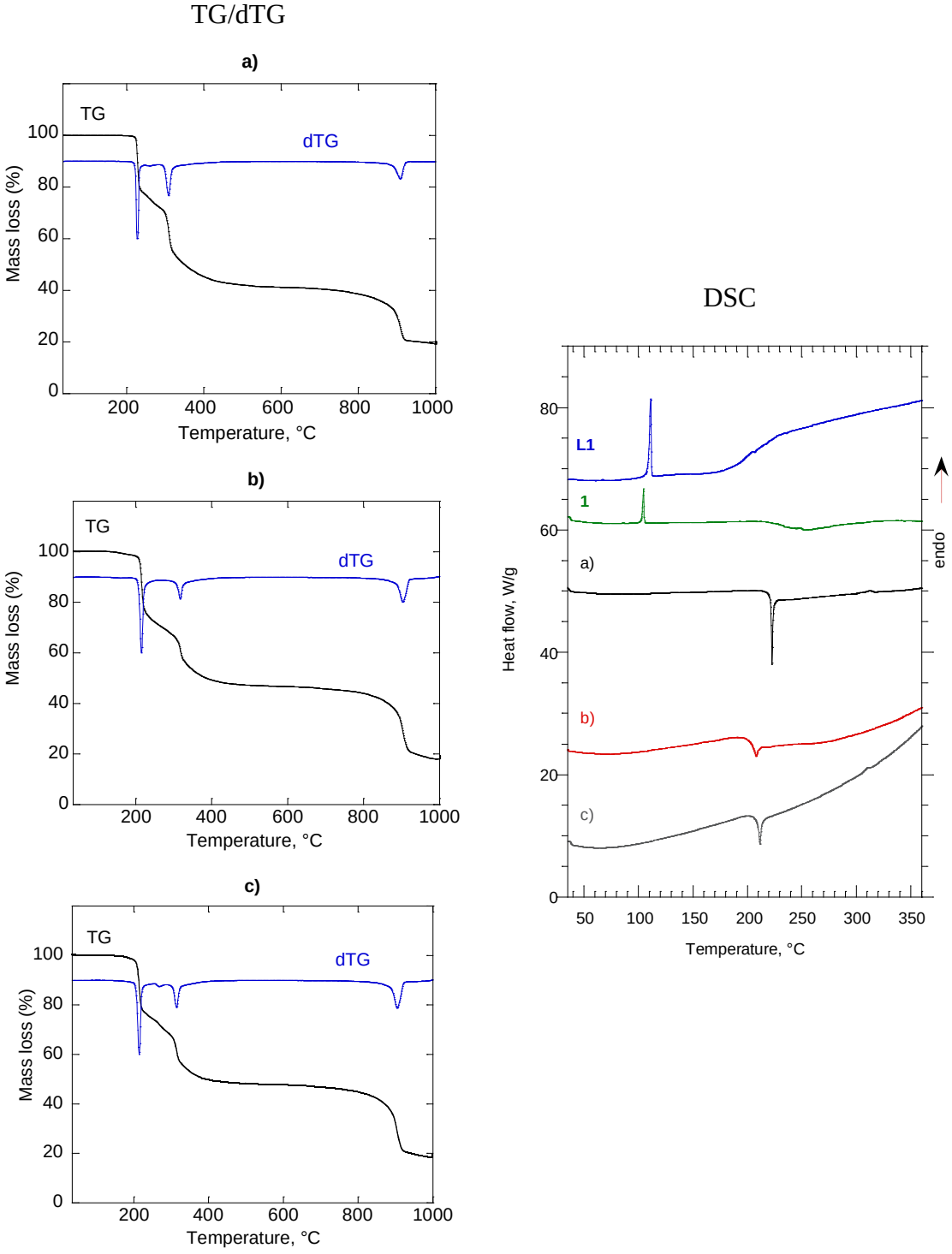

Figure 4.9. TG and dTG curves (left side) and DSC (right side) of compound (**1**·**L1**)$_\infty$ obtained with a) conventional, b) NG and c) LAG methods. In DSC plots, **L1** and **1** thermograms were also reported for comparison.

Synthesis with a 2:1 – **L1**:**1** molar ratio was also carried out in order to evaluate the existence of compounds with different stoichiometry, but even after a long milling time (20 minutes) coordination polymer $(\mathbf{1}\cdot\mathbf{L1})_\infty$ was the only compound obtained. The XRPD pattern of this sample (Figure 4.10 left) shows peaks due to excess of **L1**, thus confirming the presence of unreacted reagent. DSC measurement (Figure 4.10 right) confirmed the presence of unreacted **L1**, showing an endothermic peak assignable to **L1** melting. Moreover, after washing with ethanol and drying, the milled powder was analyzed by XRPD and DSC (figure 4.10 left and right) confirming its $(\mathbf{1}\cdot\mathbf{L1})_\infty$ nature.

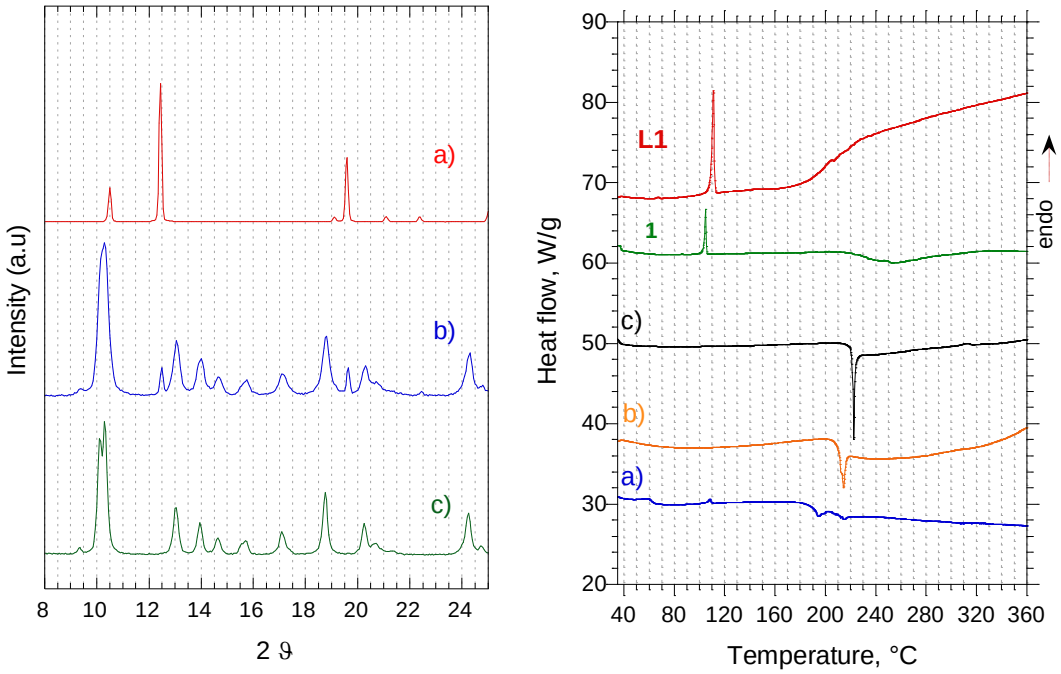

Figure 4.10. XRPD patterns for NG synthesis performed in the 2:1 (**L1**:**1**) molar ratio(left side): b) NG sample after 20 minutes grinding and c) NG 20 minutes sample washed with ethanol. For comparison **L** (4,4'-bipyridine) pattern is reported (a). On the right side DSC curves of compound $(\mathbf{1}\cdot\mathbf{L1})_\infty$ are reported: a) NG 20 minutes sample performed in the 2:1 (**L**:**1**) molar ratio, b) the same sample washed with ethanol, c) conventionally prepared $(\mathbf{1}\cdot\mathbf{L1})_\infty$ sample. Reagents **L1** (4,4'-bipyridine) and **1** for comparison.

4.3.2 [((MeO)$_2$PS$_2$)$_2$Ni]·(4,4'-bipyridine)]$_\infty$, (2·L1)$_\infty$

4.3.2.1 Structure and morphology, (2·L1)$_\infty$

The reaction of 4,4'-bipyridine (**L1**) and the nickel dithiophosphato complex [Ni((MeO)$_2$PS$_2$)$_2$] (**2**) under solvothermal conditions afforded a crystalline compound which was isolated and identified by means of single crystal X-ray diffraction as the coordination polymer of formula (**2**·**L1**)$_\infty$. Crystallographic data are reported in Table 4.2, and the asymmetric unit together with the 1D polymeric chain is reported in Figure 4.11. The central ion Ni(II) displays a distorted octahedral geometry with the equatorial plane occupied in isobidentate bonds with two dithiophosphoric ligands and the pyridine rings belonging to **L1** axially bridging adjacent Ni(II) ions to form infinite polymeric chains. The coordination of **L1** leads to an increase of Ni-S bond, which went from 2.219 and 2.225 Å in the square planar complex **2** to the value of 2.494 Å in the octahedral compound. Also the bond angles of the NiS$_2$P coordination ring are subject to significant variations similar to those found for analogous molecular adducts between phosphonodithioato complexes and pyridine derivatives, which is ascribed to the reduced net positive charge on the central Ni.[4b] The resulting neutral parallel chains –**L**–[Ni(MeOPS$_2$)$_2$]–**L**–[Ni(MeOPS$_2$)$_2$]–**L**– display Ni···N of 11.23 Å. Good agreement between single crystal and the XRPD data are observed. Minor discrepancy is observed respect to (**1**·**L1**)$_\infty$ case study, in particular in the value of c lattice parameter indicating a more rigid methoxy P-substituent group in (**2**·**L1**)$_\infty$ respect to free rotation of ethoxy in (**1**·**L1**)$_\infty$

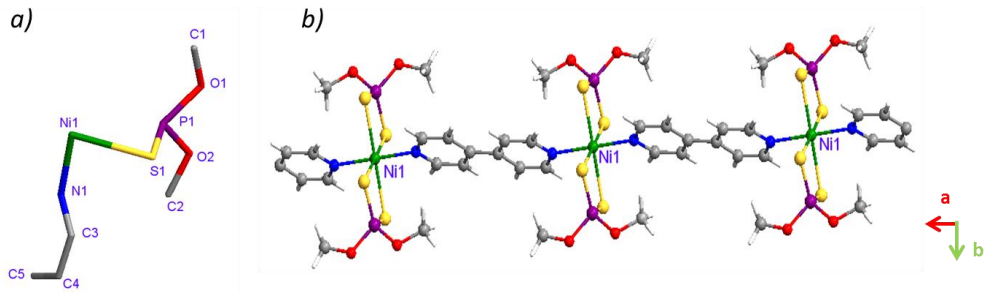

Figure 4.11. asymmetric unit of (**2**·**L1**)$_\infty$ *(a)* and packing views of (**2**·**L1**)$_\infty$ showing the linear polymeric chain (***b***).Selected bond lengths and angles: Ni1─S1, 2.4942(5); Ni1─S2, 2.4942(5); Ni1─N1, 2.084(2); P1─S1, 1.9809(7); P1─S2, 1.9823(7) Å; S1─Ni1─S2, 81.95(2); S1─Ni1─N1, 90.36(6); S2─Ni1─N1, 89.64(5)°.

Table 4.2. Summary of X-Ray single crystal and powder data and structure refinements parameters for compound $(\mathbf{2}\cdot\mathbf{L})_\infty$ obtained by conventional and grinding methods (NG 30-40 min and LAG 20-30 min). (<D> average crystal size; σ microstrain).

Compound	$(\mathbf{2}\cdot\mathbf{L1})_\infty$ conventional	$(\mathbf{2}\cdot\mathbf{L1})_\infty$ conventional	$(\mathbf{2}\cdot\mathbf{L1})_\infty$ NG 40 min	$(\mathbf{2}\cdot\mathbf{L1})_\infty$ LAG 20 min
XRD method	single crystal	powder	powder	powder
Crystal system	orthorombic	orthorombic	orthorombic	orthorombic
Space group	P n n m	P n n m	P n n m	P n n m
a / Å	11.2320(3)	11.301 (1)	11.29(1)	11.284(3)
b / Å	11.3060(3)	11.577(1)	11.59(1)	11.568(21)
c / Å	8.3430(4)	8.412 (1)	8.42(1)	8.415(2)
V / $Å^3$	1059.47 (11)	1100(2)	1101(2)	1098(2)
Z	2	2	2	2
T / K	120	298	298	298
D_{calc} /g cm^{-3}	1.441	-	-	-
θ min-max /°	3.3-27.5	5-80	5-80	5-80
<D> / nm	-	>100	28(3)	36(3)
σ / %	-	<0.17(2)	0.9(4)	0.4 (3)
Wavelength/Å	0.71073(MoKα)	1.54056(CuKα)	1.54056(CuKα)	1.54056(CuKα)
R indices (all data)	R_1 = 0.030; wR_2 = 0.0705	R_{wp}=2.0	R_{wp}=2.4	R_{wp}=4.8

$$w^{-1} = \left[\sigma^2\left(F_{exp}^2\right) + (0.0320P)^2 + 2.1046P\right] \; where \; P = [F_{exp}^2 + 2F_{calc}^2]$$

$$R_1 = \sum_{i=1}^{n} \left(\left|F_{exp,i}\right| - \left|F_{calc,i}\right|\right) / \sum_{n=1}^{\infty} \left|F_{exp,i}\right|$$

$$wR_2 = \left\{ \sum_{i=1}^{n} \left[w\left(F_{exp,i}^2 - F_{calc,i}^2\right)^2\right] / \sum_{n=1}^{\infty} \left[w\left(F_{exp,i}^2\right)^2\right] \right\}^{1/2}$$

$$R_{wp} = 100 * \sum_{i=1}^{n} w_i \left(I_i^{exp} - I_i^{calc}\right)^2 / \sum_{i=1}^{n} \left(w_i I_i^{exp}\right)^2$$

The XRPD patterns taken at selected time intervals during the mechanosynthesis NG are shown in Figure 4.12. After 20 minutes milling the pattern indicates the almost complete formation of coordination polymer $(\mathbf{2}\cdot\mathbf{L1})_{\infty}$. However, small peaks due to a new unidentified phase were evident at 14.53, 17.35, 20.46, 21.92, 23.0, 23.18, 28.72 2ϑ degree, and no peaks belong to **2** and **L1** were observed.

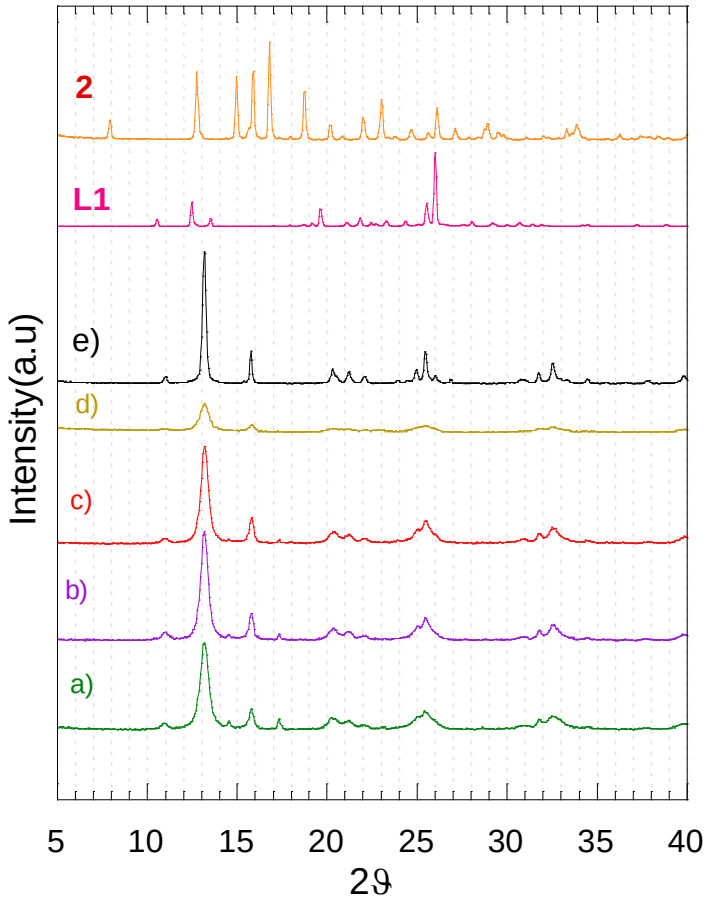

Figure 4.12. Comparisons of XRPD patterns for NG synthesis of $(\mathbf{2}\cdot\mathbf{L1})_{\infty}$: a) sample after 20 minutes of milling, b) after 25 minutes, c) after 30 minutes, d) after 40 minutes and e) conventional method sample.

A careful look of Figure 4.12 indicates that XRPD peaks of NG 30-40 minute sample are in the same position of conventional sample, but the peaks intensity and width, and therefore size and strain, are significantly different. This can be explained by taking in account the continuous reduction of crystallite grain size, due to the repeated fracture of the powders induced by milling, accompanied by progressive dispersion and intimate mixing at atomic level, which promotes interdiffusion of the starting compounds and their solid state reaction. Moreover milling induces structural disorder giving broader and changed intensities peaks.

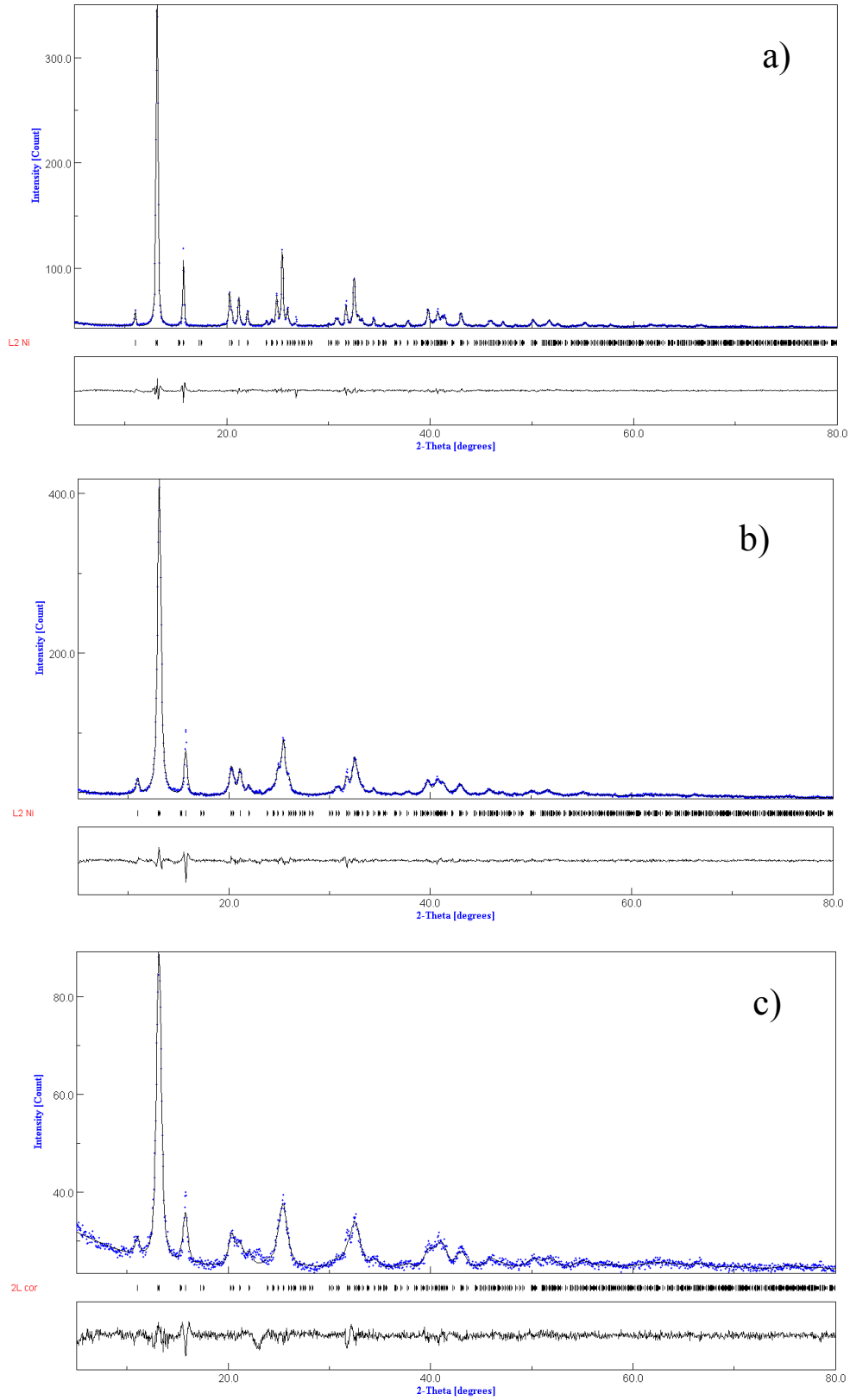

Figure 4.13. Rietveld refinement for conventional (a); LAG (b); NG (c) samples: experimental (dots), simulated curve (solid lines) and curva difference (dashed line). Vertical bars represent reflection position of $(\mathbf{2{\cdot}L1})_{\infty}$ phase obtained by single crystal data.

After 40 minutes milling time (Figure 4.12d), the synthesis can be considered concluded, and all peaks belong to the coordination polymer. The complete conversion into $(\mathbf{2}\cdot\mathbf{L1})_\infty$ polymer was gained and no peaks due to the new unidentified phase were present. Rietveld refinement of NG 40 minutes XRPD pattern (Figure 4.13) indicated a good agreement with experimental structure obtained by powder data of conventional sample (table 4.2). The isotropic size-strain model indicated an average crystal size of 28 nm and a 0.9% of microstrain for NG sample.

In Figure 4.14 the XRPD pattern of the NG sample milled 40 minutes is compared to those of the conventional synthesis, to the LAG:MeOH and to the LAG:$CHCl_3$ samples after 20 minutes of grinding.

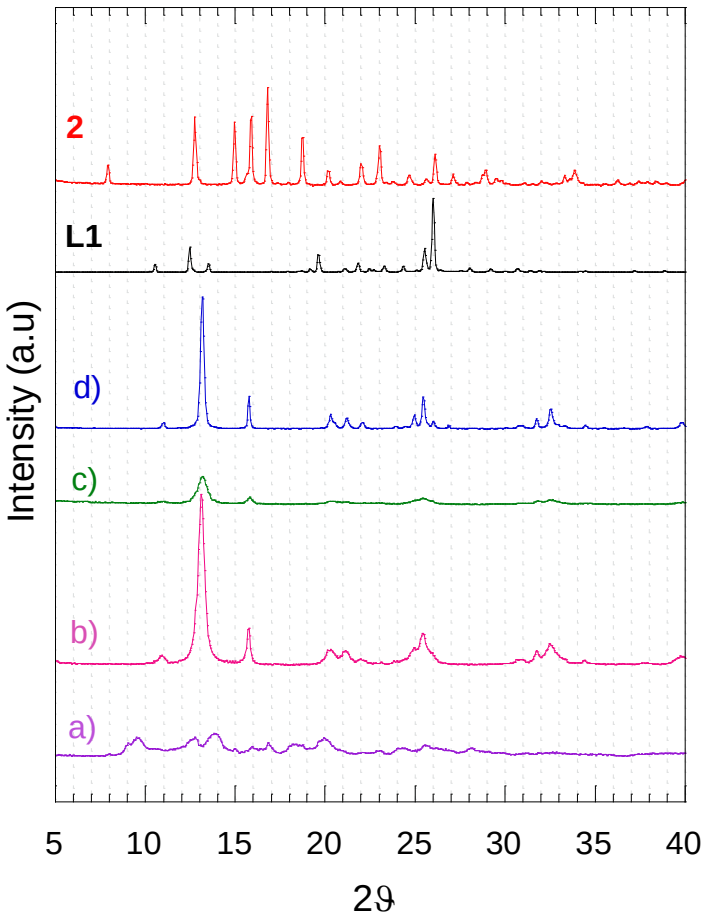

Figure 4.14. Comparison of XRPD patterns for compound $(\mathbf{2}\cdot\mathbf{L1})_\infty$ obtained by a) LAG:$CHCl_3$ after 20 minutes grinding, b) LAG:MeOH after 20 minutes grinding, c) SF after 40 minutes and d) conventional synthesis samples.

With the aim to optimize the synthesis we continued our experimentation adopting the LAG method adding to the starting powder reagents 50 μL of solvent. Adopting chloroform as solvent after several grinding times (Figure13a) the XRPD pattern of the sample shows typical feactures of amorphous/very disordered phase and no peaks due to $(\mathbf{2}\cdot\mathbf{L1})_{\infty}$ are present. Therefore the LAG experimentation was performed adopting MeOH solvent. This LAG mechanosynthesis can be considered concluded after 20 minutes of milling. Figure 4.15 reported the complete milling time samples, where the LAG:MeOH XRPD patterns are very similar to those of the NG synthesis (Figure 4.12).

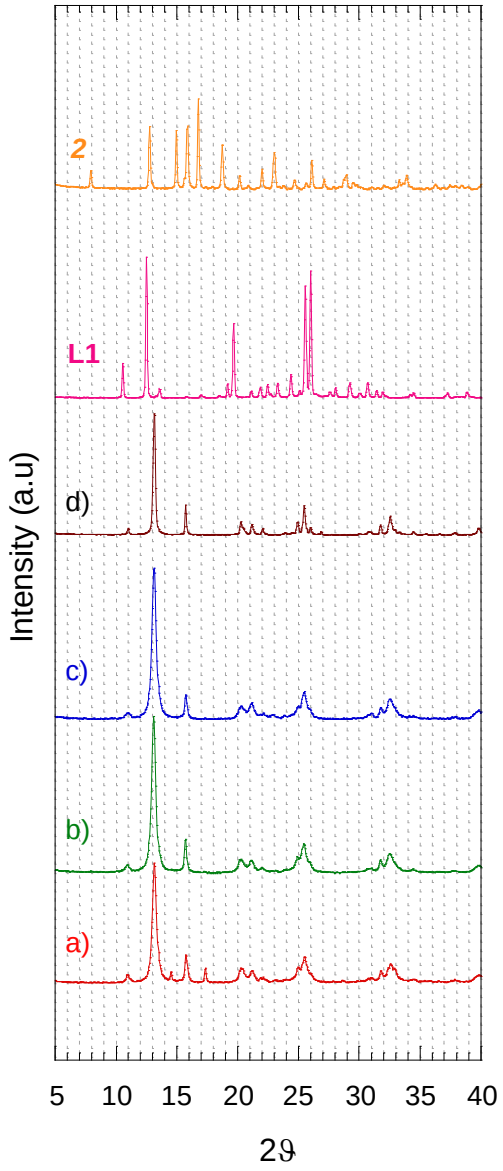

Figure 4.15. Comparisons of XRPD patterns for LAG:MeOH synthesis of $(\mathbf{2}\cdot\mathbf{L1})_{\infty}$: a) sample after 10 minutes of milling, b) after 20 minutes, c) after 30 minutes and d) conventional method sample. Reagents 2 and **L1** are reported for comparison.

It is noteworthy that in the first grinding times of NG and LAG-MeOH samples, we observed in XRPD pattern beside the formation of the expected polymer, seven new peaks (14.53, 17.35, 20.46, 21.92, 23.0,23.18, 28.72° 2ϑ degree) due to an unidentified phase. In our opinion, these peaks can be attributed to the **metal complex-L_2** monomer /adduct. This formation is in agreement with solution titration results of similar Ni(II) polymers.[19] In fact, in solution the formation of an **"metal complex·L_2"** monomer /adduct formed through the addition of two **L1** ligands to the central Ni(II) ion was observed. The coordination of the second pyridyl group to another **metal complex** moiety leads to the formation of the coordination polymer that precipitates from the solution as a green powder. An alternative explanation is the formation of an unstable polymorphic form of $(\mathbf{2}\cdot\mathbf{L1})_\infty$ polymer which evolves towards the more stable polymorphic form after further milling times.

Rietveld refinement (Figure 4.13 and Table 4.2) of LAG:MeOH sample indicated an average crystal size of 36 nm, slightly bigger than NG sample and the microstrain of LAG sample is 0.4%. This value is lower than the NG corresponding sample (0.9%) and it may be due to a more ordered crystalline phase in the synthesis with the addition of a small amount of methanol.

The SEM micrographs of the compound $(\mathbf{2}\cdot\mathbf{L1})_\infty$ prepared by conventional synthesis and using NG and LAG:MeOH mechanisyntesis method highlight the different morphology of the samples (Figure 4.16). Microcrystals are present in the conventional sample, while NG and LAG:MeOH samples generally shown irregular shaped crystals with rough surfaces and submicron particles. However in NG sample few hedgehog/whisker needles arise from the rough surface.

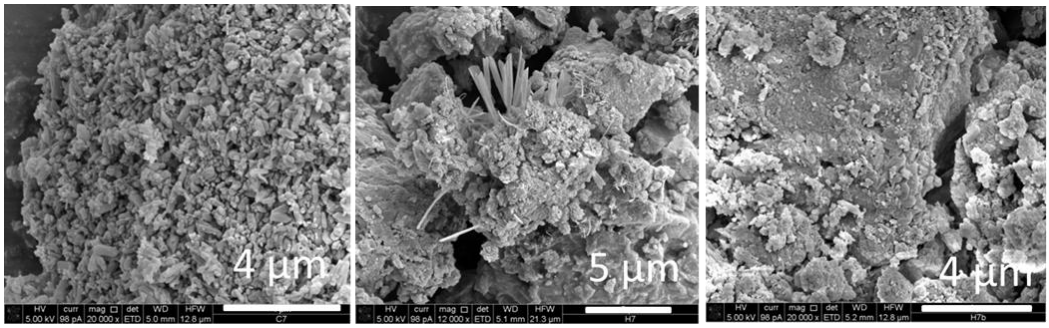

Figure 4.16. SEM images of compound $(\mathbf{2}\cdot\mathbf{L1})_{\infty}$: micro-crystals from conventional synthesis (left), NG sample after 40 minutes grinding (middle), LAG sample after 20 minutes grinding (right). Magnifications are reported in the bottom of the micrograph (bar= 4µm (conventional and LAG sample) bar= 5 µm (NG sample)).

FTIR-ATR (4000-600 cm^{-1}) for $(\mathbf{2}\cdot\mathbf{L1})_{\infty}$ conventional sample, NG and LAG mechanosintetical samples: 3080 vw, 3010 vw, 2988 vw, 2941 w, 1608 s ν(C=N), 1547 vw, 1536 vw ν(C=C, conj), 1489 w, 1451 m, 1406 m, 1225 m, 1164 m, 1073 m, 1064 vm, 1044vw, 1002 vs (pirydine breathing mode) , 791v s, 730 w, 678 s, 656 vs, 633 vm. cm^{-1}. The most characteristic ring vibration for free **L1** (ν(CN), ν (CC) and pyridine breathing mode) were observed to be ≤ 1600, ≤ 1530 and ≤ 1000 (cm^{-1}). When **L1** is coordinated to metal ions the same bands of free **L1** are shifted at higher frequencies in the following range: 1600.0-1608.9, 1533.4-1537.5 and 1006.8-1018.3 cm^{-1}, respectively.[17] IR spectra of $(\mathbf{2}\cdot\mathbf{L1})_{\infty}$ conventional sample, NG and LAG mechanosintetical samples indicate that **L1** is coordinated to metal complex demonstrated by the bands at 1608, 1536 and 1002 cm^{-1} .

4.3.2.2 Thermal stability $(\mathbf{2}\cdot\mathbf{L1})_\infty$

Examination of the thermal behavior of $(\mathbf{2}\cdot\mathbf{L1})_\infty$ samples was carried out by TGA and DSC measurements. TG and corresponding derivative dTG curve of $(\mathbf{2}\cdot\mathbf{L1})_\infty$ prepared by conventional synthesis (Figure 17) shows three main mass loss (and peaks in dTG) in the temperature range of: i) 160-210 °C, (ii) 210-510 °C and (iii) 680-960°C. The first and second steps of TG curve reflect thermal decomposition of the organic parts of $(\mathbf{2}\cdot\mathbf{L1})_\infty$ complex. The mass remaining after the second step (55.6%) and the plateau observed from 510 to 680 °C appears consistent with the presence of bis(dithio-metaphosphato) nickel(II) $[Ni(S_2PO)_2]$. This phase is in agreement with the data reported in the literature.[18] The first step corresponds to the loss of one molecule of **L1** any two Ni complex suggesting the breakage of the polymeric structure giving rise to a **metal complex$_2$-L** adduct. The residue product after 960°C was found to be nickel fosfate $Ni_2P_2O_7$ as confirmed by XRPD analysis (data not shown).

In figure 4.17 (right side) DSC thermograms of $(\mathbf{2}\cdot\mathbf{L1})_\infty$ samples and **L1** and **2** reagents were reported. In agreement with TG analysis, DSC curve of conventional sample shown a no reversible asymmetric exothermic peak starting at 181°C (centered at 195°C) due to decomposition of $(\mathbf{2}\cdot\mathbf{L1})_\infty$ indicating that the polymer $(\mathbf{2}\cdot\mathbf{L1})_\infty$ was stable up to this temperature.

For NG and LAG samples (Figure 4.17), compared to conventional one, similar thermal behaviour were observed with the same degradation compounds. However first step in TG is less steep, with a broader peak in dTG, and the temperature slightly lower (150 °C) than the conventional one. DSC exotherm peaks in ball milled samples was also shifted at lower temperature.

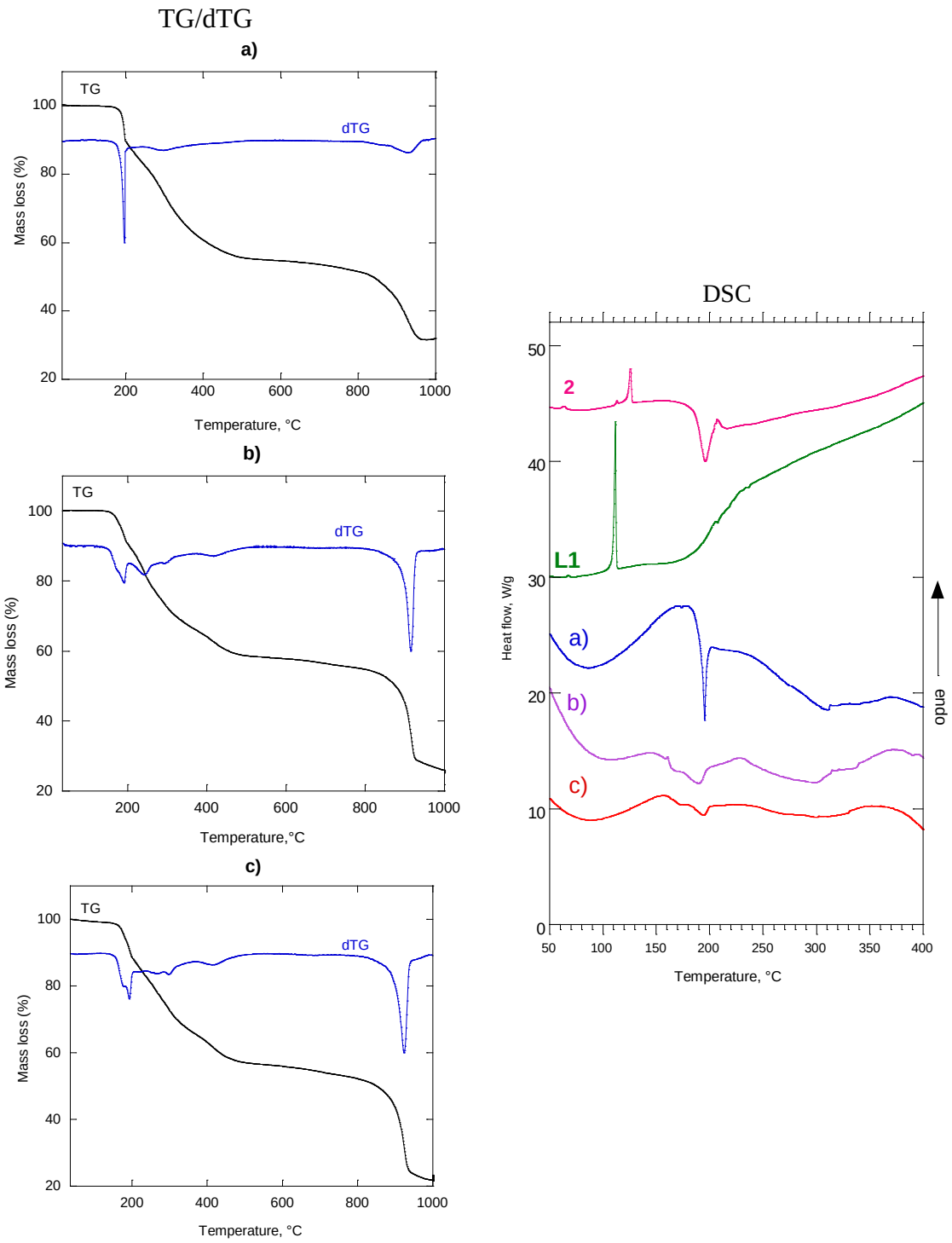

Figure 4.17. TG and dTG curves (left side) and DSC (right side) of compound (**2**·**L1**)$_\infty$ obtained with a) conventional, b) NG and c) LAG:MeOH methods. In DSC plots, **L1** and **2** thermograms were also reported for comparison.

4.3.3 [(MeO-C_6H_4)(EtO))PS_2)$_2$Ni]·4,4'-bipyridine)]$_\infty$, (3·L1)$_\infty$

4.3.3.1 Structure and morphology, (3·L1)$_\infty$

The reaction of 4,4'-bipyridine (**L1**) and the nickel dithiophosphonato complex [(MeO-C_6H_4)(EtO))PS_2)$_2$Ni] (**3**) under solvothermal conditions, as already reported, gives rise to a crystalline coordination polymer of formula (**3**·**L1**)$_\infty$.[4a] X-ray single crystal and powder data of conventional sample are reported in Table 4.3 and the structure is shown in figure 4.18. In (**3**·**L1**)$_\infty$ the nickel ion displays a distorted octahedral environment and the two bidentate phosphonodithioato units occupy the equatorial positions. Each pyridine unit of **L1** is axially coordinated to the Ni(II) ion of two [(MeO-C_6H_4)(EtO))PS_2)$_2$Ni] (**3**) units [Ni-N: 2.136(2) Å], thus forming polymeric structures.

The structural feature of (**3**·**L1**)$_\infty$ is the presence of [(MeO-C_6H_4)(EtO))PS_2)$_2$Ni]–**L1**–[(MeO-C_6H_4)(EtO))PS_2)$_2$Ni]–**L1**– neutral parallel chains running in linear and zigzag lines with an Ni-Ni distance, through coordinate bonds, of 11.38 Å . Weak hydrogen bond, particularly of the C-H···S type between the 3 units connect the linear polymer in 2D rhombic grid. The high stability of this is confirmed by the very similar structure obtained for the analogous polymer with cadmium instead of nickel ion.[20]

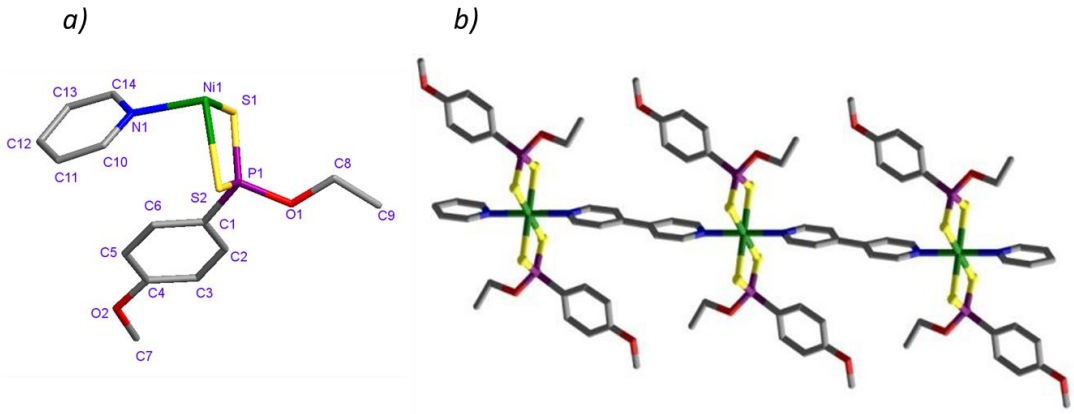

Figure 4.18. asymmetric unit of (**3**·**L1**)$_\infty$ *(a)* and packing views of (**3**·**L1**)$_\infty$ showing the linear polymeric chain (***b***).

Table 4.3. Summary of X-Ray single crystal (CSD RefCode EYEQUU) and powder data and structure refinements parameters for compound $(\mathbf{3}\cdot\mathbf{L1})_\infty$ obtained by conventional and LAG methods (LAG 10 min). (<D> average crystal size; σ microstrain)

Compound	$(\mathbf{3}\cdot\mathbf{L1})_\infty$ conventional (EYEQUU)	$(\mathbf{3}\cdot\mathbf{L1})_\infty$ conventional	$(\mathbf{3}\cdot\mathbf{L1})_\infty$ LAG 10 min
XRD method	single crystal	powder	powder
Crystal system	triclinic	triclinic	triclinic
Space group	P -1	P-1	P -1
a / Å	8.123(3)	8.197(1)	8.184(2)
b / Å	9.910(3)	10.099(2)	10.091(4)
c / Å	10.126(3)	10.148(2)	10.144(5)
α /°	89.479(7)	88.84(1)	88.83(2)
β/°	76.330(5)	76.02(1)	76.08(2)
γ /°	77.675(6	76.94(1)	76.69(2)
V / $Å^3$	773.0 (4)	794(1)	790(1)
Z	1	1	1
T / K	120	298	298
D_{calc} /g cm^{-3}	1.524	-	-
θ min-max /°	3.3-27.5	5-80	5-80
<D> / nm	-	68(1)	57(1)
σ / %	-	<0.26(1)	0.30(1)
Wavelength/ Å	0.71073 (MoKα)	1.54056 (CuKα)	1.54056 (CuKα)
R indices (all data)	R_1 = 0.0397; wR_2 = 0.0884	R_{wp}=6.2	R_{wp}=6.6

$$w^{-1} = \left[\sigma^2\left(F_{exp}^2\right) + (0.0320P)^2 + 2.1046P\right] \; where \; P = [F_{exp}^2 + 2F_{calc}^2]$$

$$R_1 = \sum_{i=1}^{n} \left(\left|F_{exp,i}\right| - \left|F_{calc,i}\right|\right) / \sum_{n=1}^{\infty} \left|F_{exp,i}\right|$$

$$wR_2 = \left\{\sum_{i=1}^{n} [w(F_{exp,i}^2 - F_{calc,i}^2)^2] / \sum_{n=1}^{\infty} [w(F_{exp,i}^2)^2]\right\}^{1/2}$$

$$R_{wp} = 100 * \sum_{i=1}^{n} w_i \left(I_i^{exp} - I_i^{calc}\right)^2 / \sum_{i=1}^{n} \left(w_i I_i^{exp}\right)^2$$

The NG mechanosynthesis of 4,4'-bipyridine (**L1**) and the nickel dithiophosphonato complex [(MeO-C_6H_4)(EtO))$PS_2)_2$Ni] (**3**) doesn't led to (**3**·**L1**)$_\infty$ coordination polymer. In fact, as shown in figure 4.19, after 10 min (and further milling time) an XRPD pattern typical of amorphous/very disordered materials is obtained.

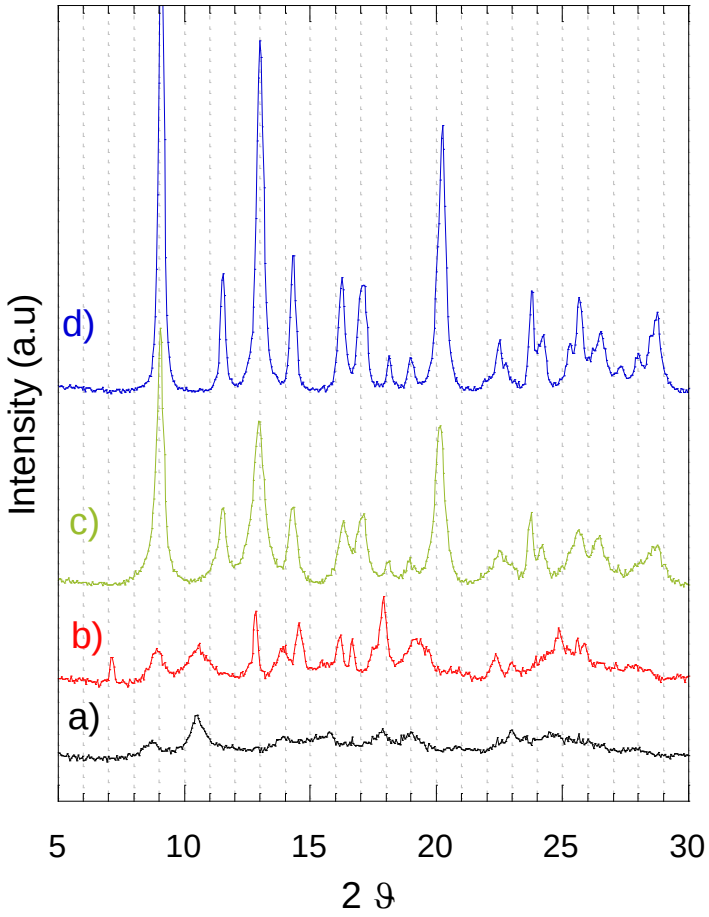

Figure 4.19. Comparison of XRPD patterns for compound (**3**·**L1**)$_\infty$ obtained by a) NG after 10 minutes, b) LAG:EtOH after 10 minutes grinding, c) LAG:$CHCl_3$ after 10 minutes grinding and d) conventional synthesis samples.

As already seen in other systems, the coordination polymer synthesis is favored by the presence of a liquid phase.[21] Therefore, we continued our experimentation adopting the LAG method adding 50 μL of ethanol to the starting powder reagents. When using EtOH solvent undesired and unidentified product is obtained as well as in the NG synthesis. Adopting chloroform as solvent, after 10 minutes of grinding (Figure 4.19c), the XRPD pattern of the sample shows typical features of (**3**·**L1**)$_\infty$ obtained in the conventional manner. Progressive milling times for LAG:$CHCl_3$ experiment (Figure 4.20) do not change substantially the

features of the reaction product indicating a relative stability of the $(\mathbf{3}\cdot\mathbf{L1})_\infty$ polymer. XRPD peaks of $(\mathbf{3}\cdot\mathbf{L1})_\infty$ LAG:$CHCl_3$ sample (10 minutes) are in the same position of the conventionally obtained one, but the peaks intensity and width, and therefore size and strain, are different.

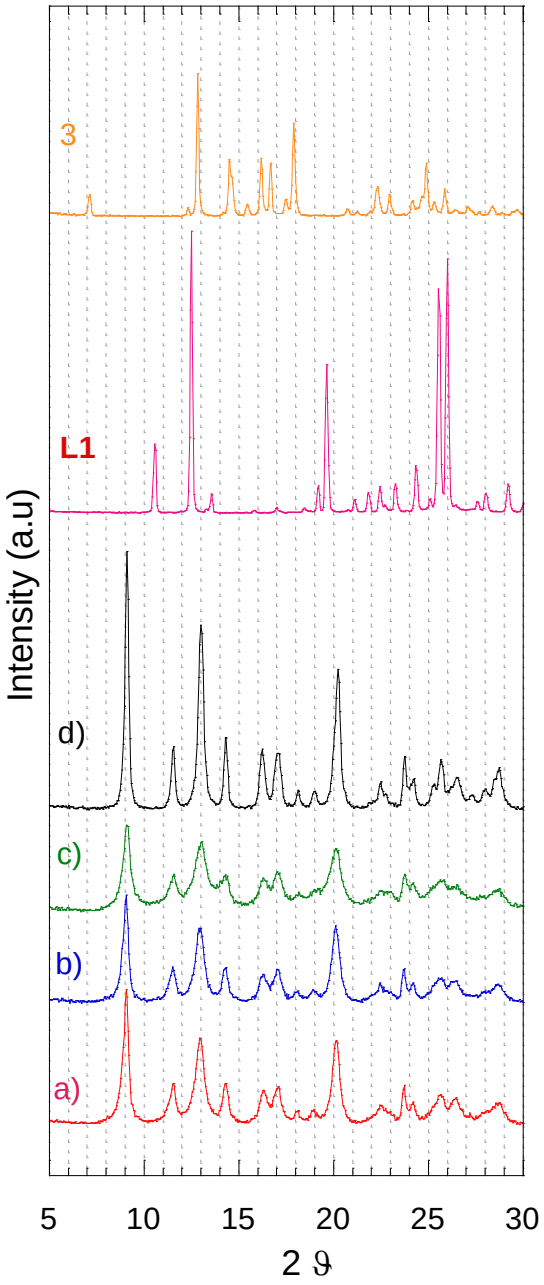

Figure 4.20. Comparisons of XRPD patterns for LAG:$CHCl_3$ synthesis of $(\mathbf{3}\cdot\mathbf{L1})_\infty$: a) sample after 10 minutes of milling, b) after 20 minutes, c) after 30 minutes and d) conventional method sample. Reagents **3** and **L1** are reported for comparison.

Rietveld refinement (Figure 4.21 and Table 4.3) of LAG sample indicated an average crystal size of 57 nm, slightly smaller than conventional sample (60 nm). Microstrain of LAG sample is very similar to the sample obtained in the conventional manner.

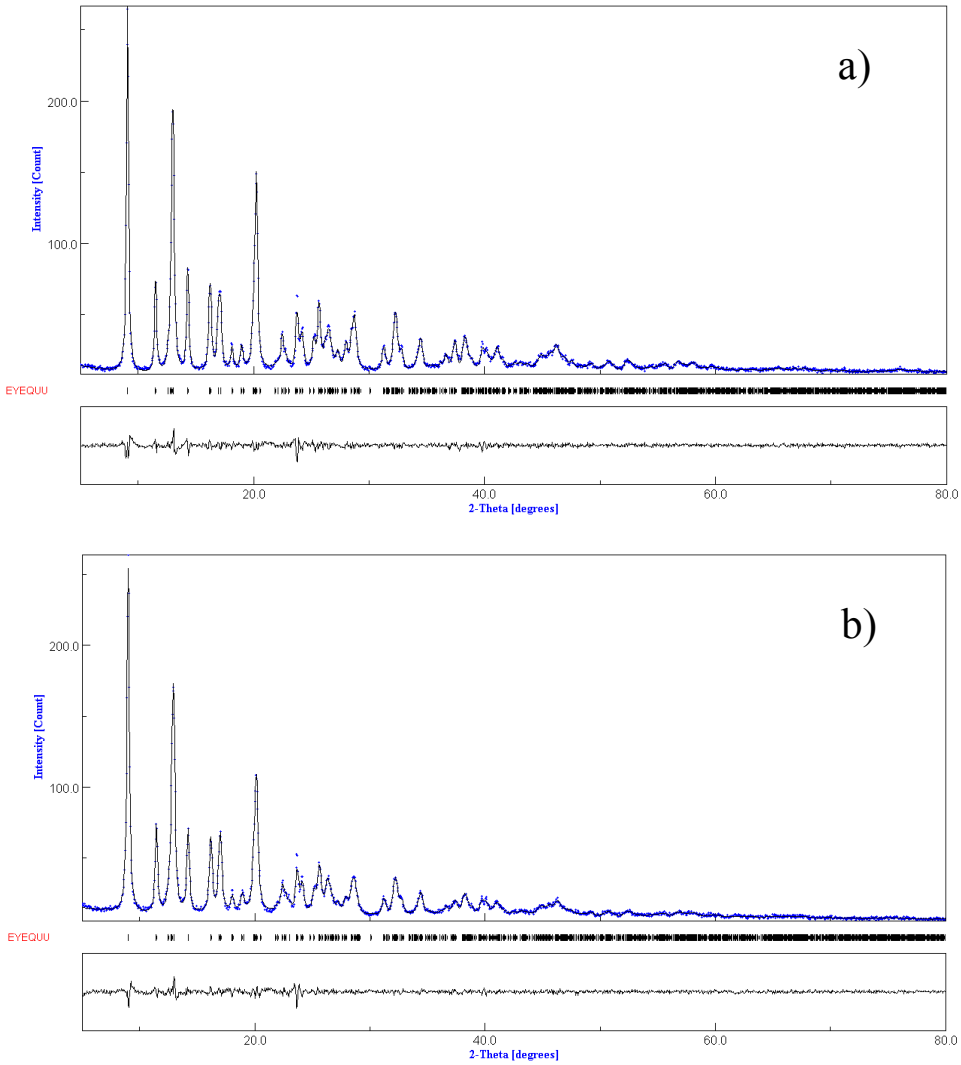

Figure 4.21. Rietveld refinement for conventional (a); LAG (b) samples: experimental (dots), simulated curve (solid lines) and curva difference (dashed line). Vertical bars represent reflection position of $(\mathbf{3{\cdot}L1})_\infty$ phase obtained by single crystal data (EYEQUU).

FTIR-ATR (4000-600 cm^{-1}) for $(\mathbf{3{\cdot}L1})_\infty$ conventional sample and LAG:$CHCl_3$ samples: 3067 vw, 2982 vw, 2892 vw, 2838 vw, 1600 s ν(C=N), 1568 vw, 1531 vw ν(C=C, conj), 1500 m, 1484m, 1400 m, 1300 vm, 1261s, 1216 m, 1178m, 1116s, 1064 m, 1026 vs, 1004 vw (pirydine breathing mode), 947 vs, 778v s, 728 w, 661m, 644 vs, 628 s cm^{-1}. The most characteristic ring vibration for free **L1**

(ν(CN), ν (CC) and pyridine breathing mode) were observed to be ≤ 1600, ≤ 1530 and ≤ 1000 (cm^{-1}). When **L1** is coordinated to metal ions the same bands of free **L1** are shifted at higher frequencies[17] as can be observed for $(\mathbf{3}\cdot\mathbf{L1})_\infty$ coordination polymer: 1600 s ν(C=N), 1531 vw ν(C=C, conj), 1004 vw (pyridine breathing mode).

The SEM micrograph of the compound $(\mathbf{3}\cdot\mathbf{L1})_\infty$ prepared by conventional synthesis shows regular elongated/acicular microcrystals of few microns. In the LAG:$CHCl_3$ sample very different morphology is observed with rough surfaces and submicron crystallites (Figure 4.22).

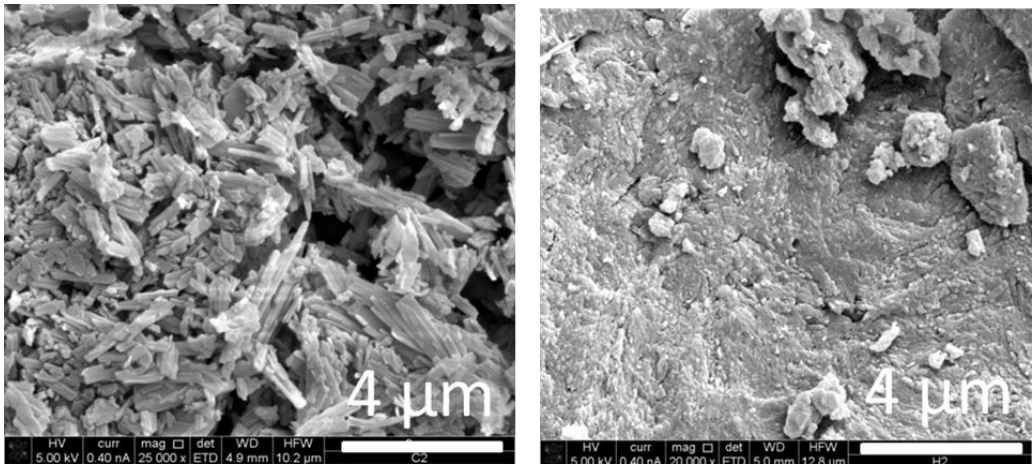

Figure 4.22. SEM images of compound $(\mathbf{3}\cdot\mathbf{L1})_\infty$**:** conventional synthesis sample (left), LAG sample in $CHCl_3$ after 10 minutes grinding (right). Magnifications are reported in the bottom of the micrograph(3µm for conventional sample and 4 µm for LAG:$CHCl_3$ sample).

4.3.3.2 Thermal stability $(\mathbf{3}\cdot\mathbf{L1})_\infty$

TG and corresponding derivative dTG curves of $(\mathbf{3}\cdot\mathbf{L1})_\infty$ prepared in the conventional manner (Figure 4.23a left side) shows three main mass loss (and peaks in dTG) in the temperature range of: i) 142-359, (ii) 359-558 °C and (iii) 767-981°C. The first and second steps of TG curve reflect thermal decomposition of the organic parts of $(\mathbf{3}\cdot\mathbf{L1})_\infty$ polymer. The first corresponds to **L1** lost while the mass remaining after the second step (36.5%), and the plateau observed from 558 to 767 °C appears consistent with the presence of bis(dithio-metaphosphato)

nickel(II) $[Ni(S_2PO)_2]$.[18] As expected, the residue product after 981°C , was found to be nickel fosfate $Ni_2P_2O_7$.

DSC curve of conventionally prepared sample (Figure 4.23a right) shows a very weakly non reversible exothermic peak centered at 176°C, due to decomposition of $(\mathbf{3}\cdot\mathbf{L1})_\infty$ followed by a sharp exothermic step centered at 239°C that corresponds to the temperature of the first dTG peak .

As already seen in $(\mathbf{2}\cdot\mathbf{L1})_\infty$, $(\mathbf{3}\cdot\mathbf{L1})_\infty$ LAG sample has similar thermal behavior (TG and DSC Figure 4.23b) compared to conventional one with the same degradation compounds but with lower slightly shifted temperatures.

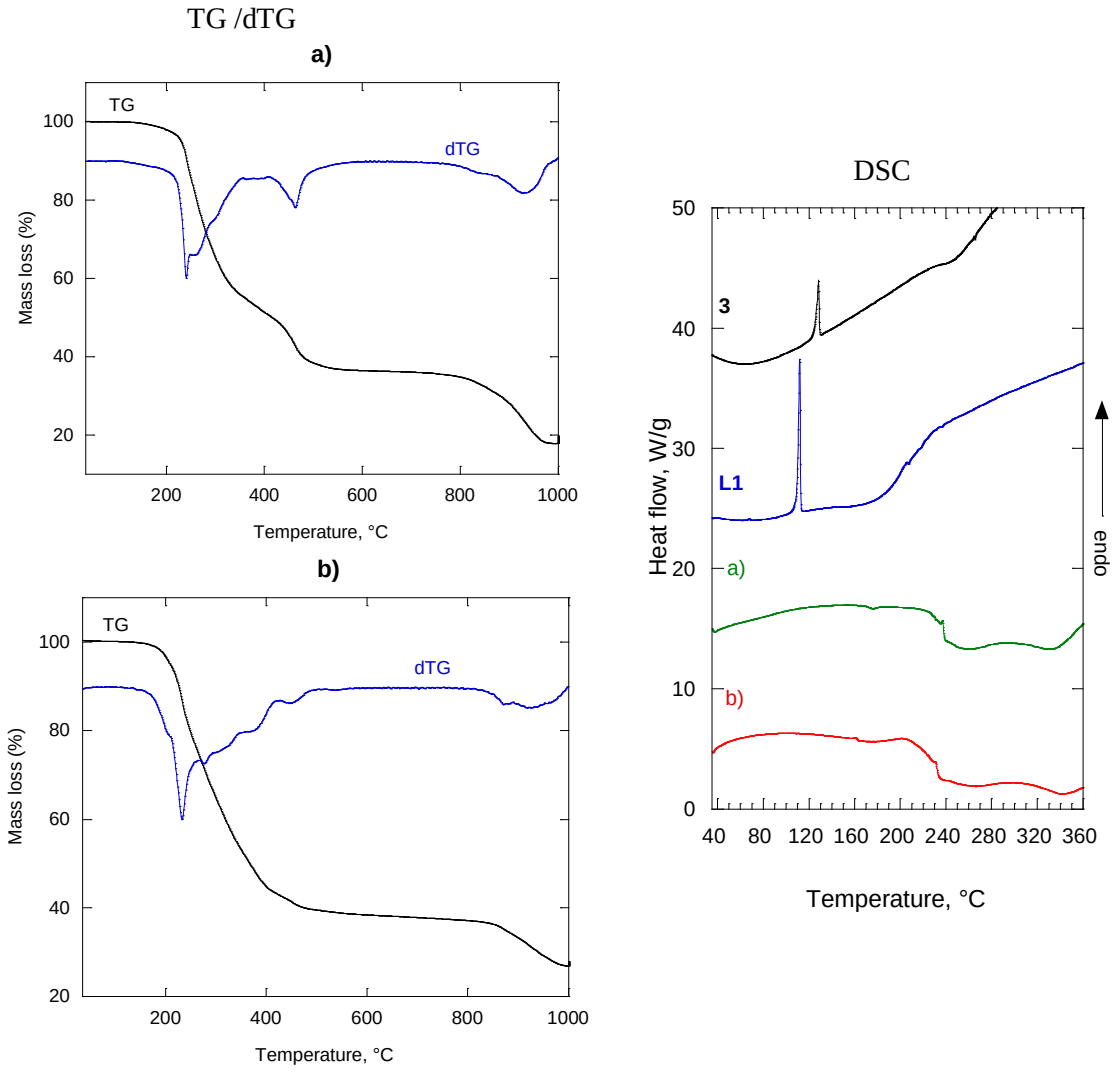

Figure 4.23. TG and dTG curves (left side) and DSC (right side) of compound $(\mathbf{3}\cdot\mathbf{L1})_\infty$ obtained with a) conventional and b) LAG:$MCHCl_3$ methods. In DSC plots, **L1** and **3** thermograms were also reported for comparison.

4.3.4 [(MeO-C_6H_4)(MeO))PS_2)$_2$Ni]·4,4'-bipyridine)]$_\infty$, (4·L1)$_\infty$

4.3.4.1 Structure and morphology, (4·L1)$_\infty$

The solution based reaction using 4,4'-bipyridine (**L1**) and the nickel complex [(MeO-C_6H_4)(MeO))PS_2)$_2$Ni] (**4**) was performed resulting in a new powder product, the coordination polymer of formula [(MeO-C_6H_4)(MeO))PS_2)$_2$Ni]·4,4'-bipyridine)]$_\infty$, **(4·L1)**$_\infty$ which has not been characterised by single crystal X-ray diffraction. Therefore, we started the structural investigation of **(4·L1)**$_\infty$ using the structural model of the analogous coordination polymer obtained with cadmium instead of nickel ion.[20] However, the XRPD pattern of conventionally prepared **(4·L1)**$_\infty$ sample reported in figure 4.24, showing features that are not isostructural with the same Cd polymer. The **(4·L1)**$_\infty$ crystal lattice, cell parameters and average crystal size with relative strain were obtained by using McMaille software[22] and results are reported in Table 4.4. Complete crystal refinement using DASH software is in progress.

Table 4.4. Summary of X-Ray powder data and structure parameters for compound $(\mathbf{4{\cdot}L1})_\infty$ obtained by conventional and LAG:MeOH/$CHCl_3$ methods (LAG:50 min). (<D> average crystal size; σ microstrain).

Compound	$(\mathbf{4{\cdot}L1})_\infty$ conventional	$(\mathbf{4{\cdot}L1})_\infty$ LAG 50 min
XRD method	powder	powder
Crystal system	triclinic	triclinic
Space group	P-1	P-1
a / Å	10.223(6)	10.206(8)
b / Å	10.309(5)	10.323(7)
c / Å	7.857(4)	7.852(5)
α /°	115.57(3))	115.57(4)
β/°	104.03(4)	103.76(4)
γ /°	81.19(5)	81.43(6)
V / $Å^3$	723.97(6)	723.8 (1)
Z	1	1
T / K	298	298
θ min-max /°	5-80	5-80
<D> / nm	50(2)	60(2)
σ / %	0.35(1)	0.38(1)
Wavelength/ Å	1.54056 (CuKα)	1.54056 (CuKα)

The mechanosynthesis experiments using NG and LAG (with different solvents) methods to obtain $\mathbf{(4{\cdot}L1)}_\infty$ polymer were carried out. The NG experiment does not led the required coordination polymer but an unidentified mixture of several phases, including $\mathbf{(4{\cdot}L1)}_\infty$ and an amorphous contribution were observed (Figure 4.24a). In Figure 4.24b is also reported the XRPD pattern of LAG:$CHCl_3$ sample at 50 minutes grinding time showing the almost completely formation of $\mathbf{(4{\cdot}L1)}_\infty$ structure but with very broadened peaks. Using methanol as liquid phase, the XRPD pattern of the 35 minute LAG:MeOH sample (Figure 4.24c) appears almost completely coincidence with the typical phase of $\mathbf{(4{\cdot}L1)}_\infty$. Anyway it shows very broad peaks and the contribution of another unidentified phase

(clearly visible peaks of this phase at 7.96 and 15.97 2ϑ). Therefore, the LAG experiment using the same solvent mixture adopted for the solvothermal synthesis, MeOH:$CHCl_3$ (1:1v/v), was performed. The XRPD pattern of LAG: MeOH/$CHCl_3$ sample milled 50 minutes (Figure 4.24d) can be considered very similar to that of the conventionally synthesized sample and therefore, the reaction after 50 minutes milling can be considered concluded. XRPD patterns of LAG: MeOH/$CHCl_3$ samples at several milling time are reported in figure 4.25.

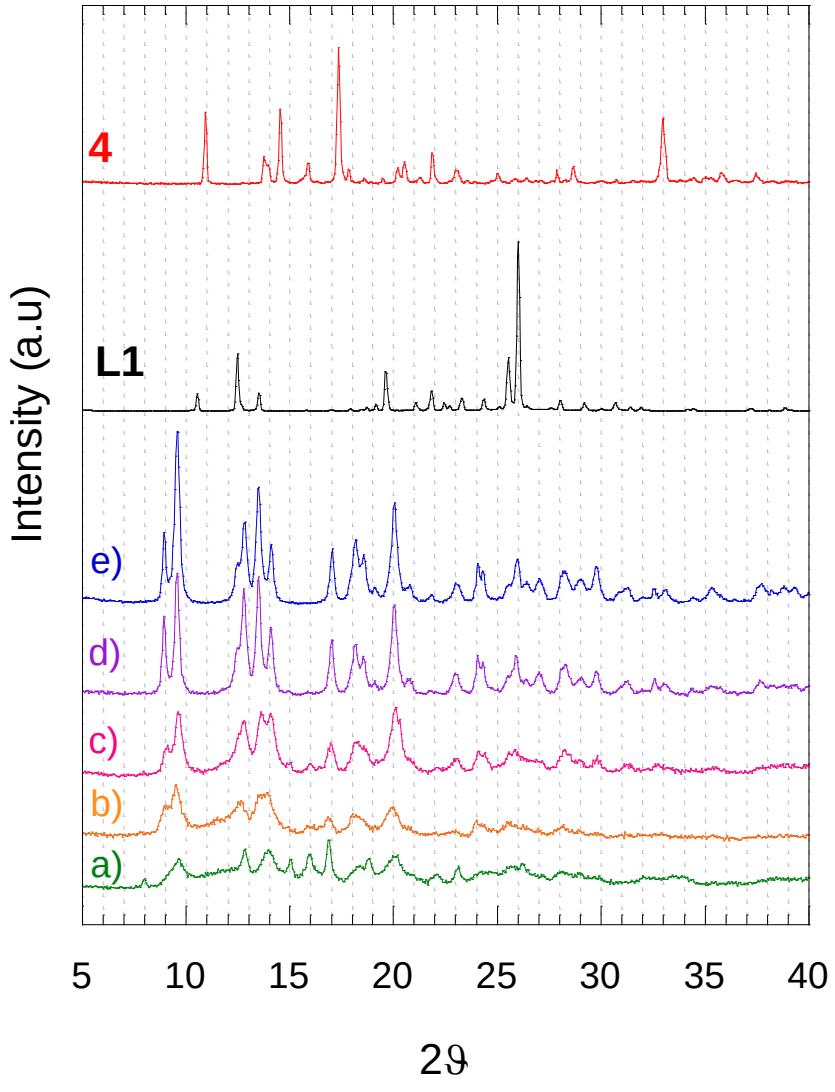

Figure 4.24. Comparison of XRPD patterns for compound (**4**·**L1**)$_\infty$ obtained by a) NG after 40 minutes, b) LAG:$CHCl_3$ after 50 minutes grinding, c) LAG:MeOH after 10 minutes grinding and d) LAG:MeOH/$CHCl_3$ after 50 minutes grinding, e) conventional synthesis samples. Reagents **4** and **L1** are reported for comparison.

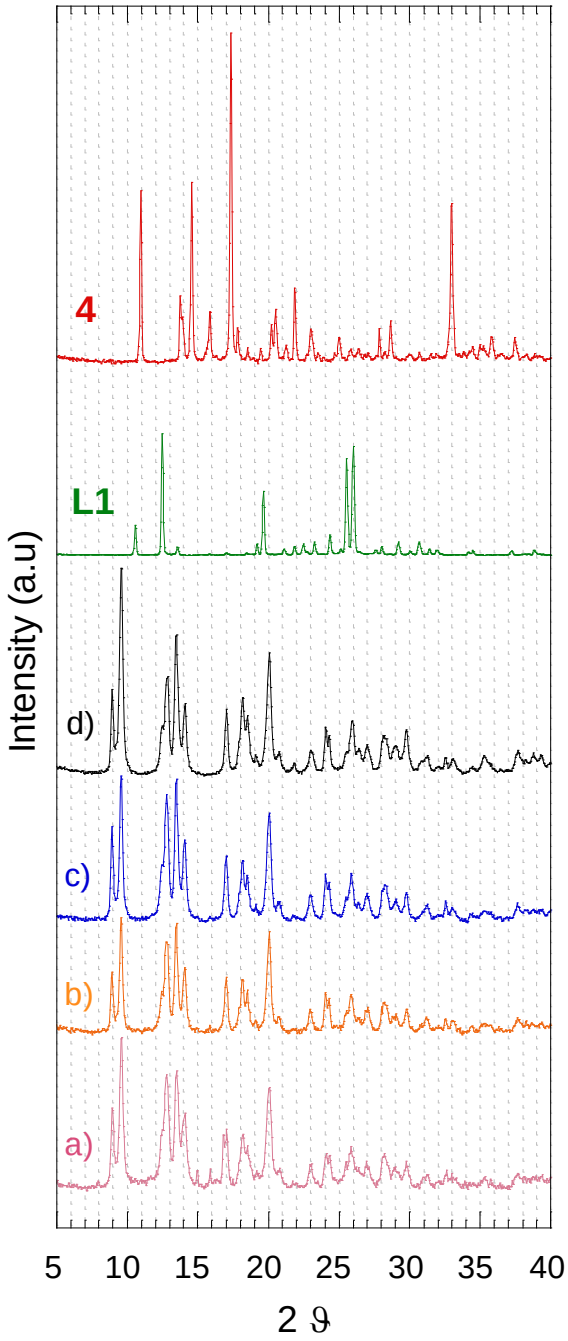

Figure 4.25. Comparisons of XRPD patterns for LAG:MeOH/$CHCl_3$ synthesis of $(\mathbf{4}\cdot\mathbf{L1})_\infty$: a) sample after 30 minutes of milling, b) after 40 minutes, c) after 50 minutes and d) conventional method sample. Reagents **4** and **L1** are reported for comparison.

FTIR-ATR (4000-600 cm^{-1}) for $(\mathbf{4}\cdot\mathbf{L1})_\infty$ conventional and LAG mechanosintetical samples: 3073 vw, 2939 vw, 2838 vw, 2349 vw, 1604 s ν(C=N), 1591 s, 1565 vw, 1532 vw ν(C=C, conj), 1498 m, 1484 w, 1453 m, 1444 m, 1404 m, 1293 vm, 1258 s, 1213 vm,1178 vm, 1111 s, 1062 w, 1018 vs (pirydine breathing mode), 969 w, 835 m, 809 s, 778vs, 729 w, 658 s, 644 vs, 626 s cm^{-1}.

As observed for the previously analyzed coordination polymers, the most characteristic ring vibration for free **L1** (ν(CN), ν (CC) and pyridine breathing mode) are shifted at higher frequencies [17] confirming that **L1** is coordinated to the metal complex **4.**

SEM micrographs of $(\mathbf{4}\cdot\mathbf{L1})_\infty$ show different morphological features between the conventional synthesis and LAG: MeOH/$CHCl_3$ samples (Figure 4.26). As already observed previously, the conventional sample is formed by regular shaped tiny microcrystals, while the LAG sample shows irregular shaped crystals with rough surfaces.

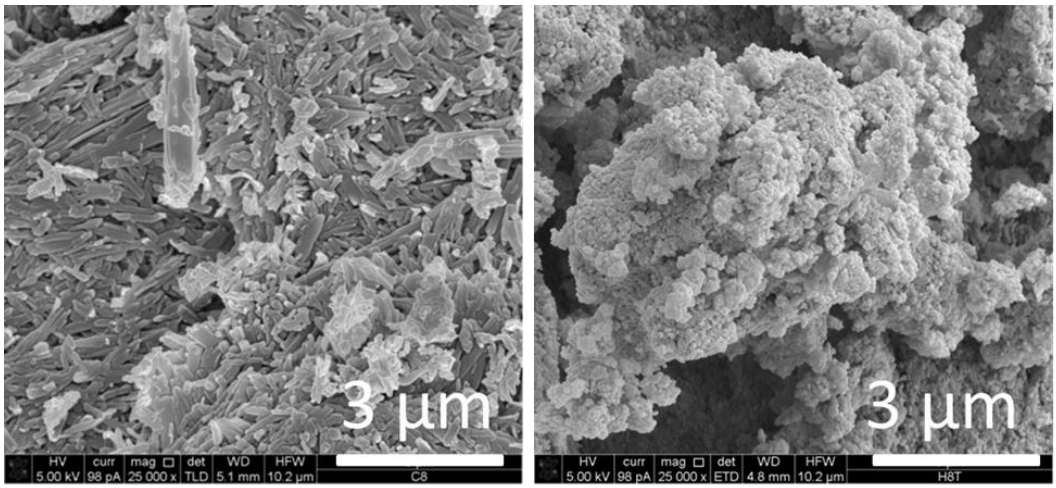

Figure 4.26. SEM images of $(\mathbf{4}\cdot\mathbf{L1})_\infty$ samples: conventional synthesis sample (left), LAG: MeOH/CHCl3 after 50 minutes grinding (right). Magnifications are reported in the bottom of the micrograph (bar=3µm).

4.3.4.2 Thermal stability $(\mathbf{4{\cdot}L1})_\infty$

The thermal characterization of $(\mathbf{4{\cdot}L1})_\infty$ samples was carried out by TG and DSC measurements. TG and corresponding derivative dTG curve of conventional synthesis sample $(\mathbf{4{\cdot}L1})_\infty$ (Figure 4.27a left) shows three substantial mass loss (and peaks in dTG) in the temperature range of: i) 75-418, (ii) 418-544 °C and (iii) 694-1000°C. The first and second steps of TG curve reflect thermal decomposition of the organic parts of $(\mathbf{4{\cdot}L1})_\infty$ polymer. In particular, the first step (weight loss of 53.5%) is consistent with the loss of **L1** and the two (-$C_6H_4OCH_3$) substituents at the phosphorus atom. The mass remaining after the second step (38.4%) and the plateau observed from 544 to 694 °C appears consistent with the presence of bis(dithio-metaphosphato) nickel(II) [$Ni(S_2PO)_2$]. The residue product after 1000°C was found to be mainly nickel fosfate $Ni_2P_2O_7$ as confirmed by XRPD analysis (data not shown). Faint peaks due to Ni_2P_5, NiO and $Ni_3(PO_4)_2$ phases are also found in this XRPD pattern.
DSC thermograms for $(\mathbf{4{\cdot}L1})_\infty$ samples and reagents (**L1** and **4)** are also reported (Figure 4.27 right). In agreement with TG analysis, DSC curve of conventional sample shown a no reversible asymmetric and broadened exothermic peak centered at 283°C due to $(\mathbf{4{\cdot}L1})_\infty$ decomposition (Figure 4.27a right).

Comparing the thermal behavior of $(\mathbf{4{\cdot}L1})_\infty$ LAG:MeOH/$CHCl_3$ sample with that of conventional sample, the same degradation compounds are observed in TG measurement (Figure 4.27b left). DSC curve of LAG: MeOH/$CHCl_3$ sample is also similar to the conventional one with more broadened and shifted at lower temperature exothermic peak (~230 °C) (Figure 4.27b right).

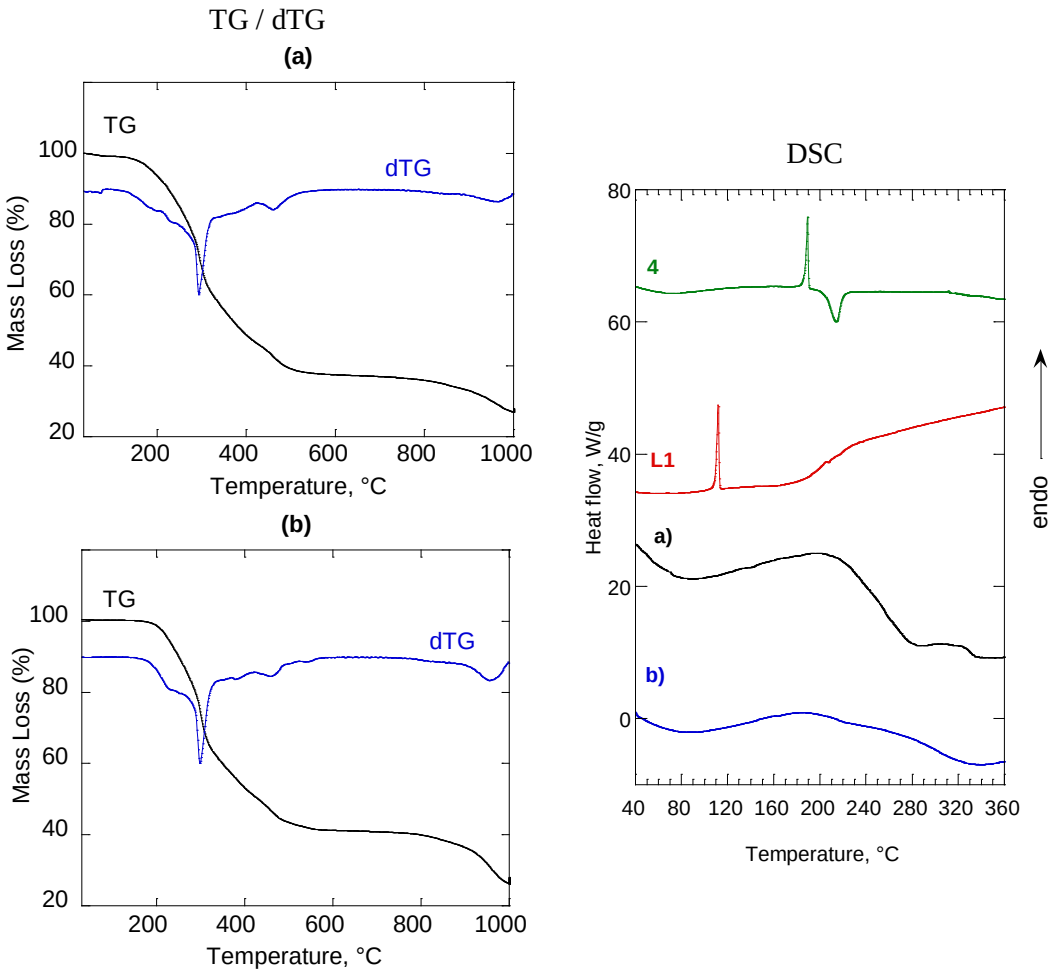

Figure 4.27. TG and dTG curves (left side) and DSC (right side) of compound (**4**·**L1**)$_\infty$ obtained with a) conventional and b) 50 minute LAG:MeOH/$CHCl_3$ methods. In DSC plots, **L1** and **4** thermograms were also reported for comparison.

4.4 Conclusion

Mechanochemical reactions of neutral O,O'-diethyldithiophosphato/ O,O'-diethyldithiophosphonato Ni^{II} complex (**1**), (**2**), (**3**), (**4**) with 4,4'-bipyridine (**L1**) allow the formation of mono dimensional coordination polymers $(\mathbf{1}\cdot\mathbf{L1})_\infty$, $(\mathbf{2}\cdot\mathbf{L1})_\infty$, $(\mathbf{3}\cdot\mathbf{L1})_\infty$, $(\mathbf{4}\cdot\mathbf{L1})_\infty$ respectively. An environmental friendly one pot mechanosynthesis of coordination polymers (CP) starting from neutral secondary building blocks has been developed by milling reactants. The mechanichemical protocol developed gave $(\mathbf{1}\cdot\mathbf{L1})_\infty$ polymer with significant benefits compared to solution-based protocols and confirmed the 'green' nature of this methodology: reactions are much faster (less than one hour compared to several hours) and the use of high temperatures and solvents are avoided. With regard to $(\mathbf{1}\cdot\mathbf{L1})_\infty$ and $(\mathbf{2}\cdot\mathbf{L1})_\infty$, the NG mechanochemical approach gives yields comparable to those obtained from LAG (using ethanol and methanol for $(\mathbf{1}\cdot\mathbf{L1})_\infty$ and $(\mathbf{2}\cdot\mathbf{L1})_\infty$ respectively), the latter is more efficient at reducing the reaction time. Moreover, as well known from the literature,[23] the solvent acts as a 'lubricant' for kinetic acceleration of the reaction, as a heat sink for exothermic reactions, as a dispersant for product removal from the reaction sites, as a suspending agent for the reactants, and as a crystallization promoter. As a consequence, the average crystal size in the LAG sample is slightly larger than that obtained in NG samples. For $(\mathbf{3}\cdot\mathbf{L1})_\infty$ and $(\mathbf{4}\cdot\mathbf{L1})_\infty$ the mechanosynthesis is possible only by LAG method suggesting that in some cases the addition of a liquid phase can enable mechanochemical reactions. In several case studies NG and LAG mechanosynthesis can lead to a mixture of phases and does not progresses. While using a specific solvent or a suitable mixture of solvents can result in the desired product with a yield equal to 100%. The ability of different liquid phases in the LAG synthesis to steer the formation of various coordination polymers structures has been already demonstrated.[24]

Further systematic work is now in progress in our laboratory with the aim of studying mechanochemical synthesis of coordination polymers starting from different metal complexes with different bipyridyl-based spacers.

4.5 References

1. (a) Fernández-Catalá, J.; Casco, M. E.; Martínez-Escandell, M.; Rodríguez-Reinoso, F.; Silvestre-Albero, J., HKUST-1@ACM hybrids for adsorption applications: A systematic study of the synthesis conditions. *Microporous and Mesoporous Materials* **2017,** *237*, 74-81; (b) Gao, Y.; Li, S.; Li, Y.; Yao, L.; Zhang, H., Accelerated photocatalytic degradation of organic pollutant over metal-organic framework MIL-53(Fe) under visible LED light mediated by persulfate. *Applied Catalysis B: Environmental* **2017,** *202*, 165-174; (c) Yin, N.; Wang, K.; Wang, L.; Li, Z., Amino-functionalized MOFs combining ceramic membrane ultrafiltration for Pb (II) removal. *Chemical Engineering Journal* **2016,** *306*, 619-628.

2. (a) Chand, D. K.; Fujita, M.; Biradha, K.; Sakamoto, S.; Yamaguchi, K., Metal driven self-assembly of pyridine appended ligands with cis-protected/naked Pd (II) ion: a comparative study. *Dalton Transactions* **2003,** (13), 2750-2756; (b) Fujita, M., Metal-directed self-assembly of two-and three-dimensional synthetic receptors. *Chemical Society Reviews* **1998,** *27* (6), 417-425; (c) Leininger, S.; Olenyuk, B.; Stang, P. J., Self-assembly of discrete cyclic nanostructures mediated by transition metals. *Chemical Reviews* **2000,** *100* (3), 853-908; (d) Olenyuk, B.; Whiteford, J., A. Fechtenk ötter and PJ Stang. *J. Chem. Soc., Dalton Trans* **1998,** *1707*; (e) MacGillivray, L. R., *Metal-organic frameworks: design and application*. John Wiley & Sons: **2010**.

3. (a) Aakeröy, C. B.; Desper, J.; Valdés-Martínez, J., Controlling molecular and supramolecular structure of hydrogen-bonded coordination compounds. *CrystEngComm* **2004,** *6* (69), 413-418; (b) Aragoni, M. C.; Arca, M.; Devillanova, F. A.; Hursthouse, M. B.; Huth, S. L.; Isaia, F.; Lippolis, V.; Mancini, A.; Soddu, S.; Verani, G., Investigation into the reactivity of the coordinatively unsaturated phosphonodithioato [Ni (MeOpdt) 2] towards 2, 4, 6-tris (2-pyridyl)-1, 3, 5-triazine: goals and achievements. *Dalton Transactions* **2007,** (21), 2127-2134; (c) Biradha, K.; Sarkar, M.; Rajput, L., Crystal engineering of coordination polymers using 4, 4'-bipyridine as a bond between transition metal atoms. *Chemical Communications* **2006,** (40), 4169-4179; (d) Braga, D.; Brammer, L.; Champness, N. R., New trends in crystal engineering. *CrystEngComm* **2005,** *7* (1), 1-19; (e) Brammer, L., Developments in inorganic crystal engineering. *Chemical Society Reviews* **2004,** *33* (8), 476-489; (f) Braun, M. E.; Steffek, C. D.; Kim, J.; Rasmussen, P. G.; Yaghi, O. M., 1, 4-Benzenedicarboxylate derivatives as links in the design of paddle-wheel units and metal–organic frameworks. *Chemical Communications* **2001,** (24), 2532-2533; (g) Chen, Z.-F.; Zhang, S.-F.; Luo, H.-S.; Abrahams, B. F.; Liang, H., Ni 2 (R* COO) 4 (H 2 O)(4, 4'-bipy) 2—a robust homochiral quartz-like network with large chiral channels. *CrystEngComm* **2007,** *9* (1), 27-29; (h) Cheng, A.-L.; Liu, N.; Yue, Y.-F.; Jiang, Y.-W.; Gao, E.-Q.; Yan, C.-H.; He, M.-Y., Unprecedented 3D entanglement of 1D zigzag coordination polymers leading to a robust microporous framework. *Chemical Communications* **2007,** (4), 407-409; (i) Cotton, F. A.; Lin, C.; Murillo, C. A., Supramolecular arrays based on dimetal building units. *Accounts of chemical research* **2001,** *34* (10), 759-771; (j) Gao, E.-Q.; Bai, S.-Q.; Wang, Z.-M.; Yan, C.-H., One-and two-dimensional metal–dicyanamido complexes with a flexible bridging co-ligand: structural and magnetic properties. *Dalton Transactions* **2003,** (9), 1759-1764; (k) Goldberg, I., Crystal engineering of porphyrin framework solids. *Chemical communications* **2005,** (10), 1243-1254; (l) Kitagawa, S.; Kitaura, R.; Noro, S. i., Functional porous coordination polymers. *Angewandte Chemie International Edition* **2004,** *43* (18), 2334-2375; (m) Lu,

W.; Wei, Z.; Gu, Z.-Y.; Liu, T.-F.; Park, J.; Park, J.; Tian, J.; Zhang, M.; Zhang, Q.; Gentle III, T., Tuning the structure and function of metal–organic frameworks via linker design. *Chemical Society Reviews* **2014,** *43* (16), 5561-5593; (n) O'Keeffe, M.; Eddaoudi, M.; Li, H.; Reineke, T.; Yaghi, O. M., Frameworks for extended solids: geometrical design principles. *Journal of Solid State Chemistry* **2000,** *152* (1), 3-20; (o) Rather, B.; Zaworotko, M. J., A 3D metal-organic network,[Cu 2 (glutarate) 2 (4, 4'-bipyridine)], that exhibits single-crystal to single-crystal dehydration and rehydration. *Chemical Communications* **2003,** (7), 830-831; (p) Rosi, N. L.; Eddaoudi, M.; Kim, J.; O'Keeffe, M.; Yaghi, O. M., Advances in the chemistry of metal–organic frameworks. *CrystEngComm* **2002,** *4* (68), 401-404; (q) Sain, S.; Maji, T. K.; Mostafa, G.; Lu, T.-H.; Chaudhuri, N. R., A novel layered and pillared topology in a 3D open framework: synthesis, crystal structure and magnetic properties. *New Journal of Chemistry* **2003,** *27* (2), 185-187.

4. (a) Aragoni, M. C.; Arca, M.; Champness, N. R.; Chernikov, A. V.; Devillanova, F. A.; Isaia, F.; Lippolis, V.; Oxtoby, N. S.; Verani, G.; Vatsadze, S. Z., Designed Assembly of Low-dimensional Molecular Units: Novel Neutral Coordination Polymers Based on (Phosphonodithioato) NiII Complexes. *European Journal of Inorganic Chemistry* **2004,** *2004* (10), 2008-2012; (b) Aragoni, M. C.; Arca, M.; Champness, N. R.; De Pasquale, M.; Devillanova, F. A.; Isaia, F.; Lippolis, V.; Oxtoby, N. S.; Wilson, C., Synthesis and structural characterisation of coordination polymers designed using discrete phosphonodithioato Ni II complexes and dipyridyl donor ligands. *CrystEngComm* **2005,** *7* (60), 363-369.

5. Aboutorabi, L.; Morsali, A., Structural transformations and solid-state reactivity involving nano lead (II) coordination polymers via thermal, mechanochemical and photochemical approaches. *Coordination Chemistry Reviews* **2016,** *310*, 116-130.

6. McNaught, A. D.; Wilkinson, A., Compendium of chemical terminology. IUPAC recommendations. **1997**.

7. Prochowicz, D.; Sokołowski, K.; Justyniak, I.; Kornowicz, A.; Fairen-Jimenez, D.; Friščić, T.; Lewiński, J., A mechanochemical strategy for IRMOF assembly based on pre-designed oxo-zinc precursors. *Chemical Communications* **2015,** *51* (19), 4032-4035.

8. Carli, F., *Proc. Int. Symp. Controlled Release Bioact. Mater.* **1999,** *26*, 873.

9. (a) Bowmaker, G. A., Solvent-assisted mechanochemistry. *Chemical Communications* **2013,** *49* (4), 334-348; (b) James, S. L.; Adams, C. J.; Bolm, C.; Braga, D.; Collier, P.; Friščić, T.; Grepioni, F.; Harris, K. D.; Hyett, G.; Jones, W., Mechanochemistry: opportunities for new and cleaner synthesis. *Chemical Society Reviews* **2012,** *41* (1), 413-447.

10. Pilloni, M.; Nicolas, J.; Marsaud, V.; Bouchemal, K.; Frongia, F.; Scano, A.; Ennas, G.; Dubernet, C., PEGylation and preliminary biocompatibility evaluation of magnetite–silica nanocomposites obtained by high energy ball milling. *International journal of pharmaceutics* **2010,** *401* (1), 103-112.

11. Chen, L.; Lemma, B. E.; Rich, J. S.; Mack, J., Freedom: a copper-free, oxidant-free and solvent-free palladium catalysed homocoupling reaction. *Green Chemistry* **2014,** *16* (3), 1101-1103.

12. (a) Braga, D.; Giaffreda, S. L.; Grepioni, F.; Pettersen, A.; Maini, L.; Curzi, M.; Polito, M., Mechanochemical preparation of molecular and supramolecular organometallic materials and coordination networks. *Dalton transactions* **2006,** (10), 1249-1263; (b) Pilloni, M.; Padella, F.; Ennas, G.; Lai, S.; Bellusci, M.; Rombi, E.; Sini, F.; Pentimalli, M.; Delitala, C.; Scano, A., Liquid-assisted mechanochemical synthesis of an iron carboxylate Metal Organic Framework and its evaluation in diesel fuel desulfurization. *Microporous and Mesoporous Materials* **2015,** *213*, 14-21.

13. (a) Braga, D.; Maini, L.; Grepioni, F., Mechanochemical preparation of co-crystals. *Chemical Society Reviews* **2013,** *42* (18), 7638-7648; (b) Pilloni, M.; Ennas, G.; Casu, M.; Fadda, A. M.; Frongia, F.; Marongiu, F.; Sanna, R.; Scano, A.; Valenti, D.; Sinico, C., Drug silica nanocomposite: preparation, characterization and skin permeation studies. *Pharmaceutical development and technology* **2013,** *18* (3), 626-633.

14. Friščić, T.; Trask, A. V.; Jones, W.; Motherwell, W., Screening for inclusion compounds and systematic construction of three-component solids by liquid-assisted grinding. *Angewandte Chemie* **2006,** *118* (45), 7708-7712.

15. (a) Friščić, T.; Fábián, L., Mechanochemical conversion of a metal oxide into coordination polymers and porous frameworks using liquid-assisted grinding (LAG). *CrystEngComm* **2009,** *11* (5), 743-745; (b) Pichon, A.; James, S. L., An array-based study of reactivity under solvent-free mechanochemical conditions—insights and trends. *CrystEngComm* **2008,** *10* (12), 1839-1847.

16. (a) Friščić, T.; Reid, D. G.; Halasz, I.; Stein, R. S.; Dinnebier, R. E.; Duer, M. J., Ion-and Liquid-Assisted Grinding: Improved Mechanochemical Synthesis of Metal–Organic Frameworks Reveals Salt Inclusion and Anion Templating. *Angewandte Chemie* **2010,** *122* (4), 724-727; (b) Shan, N.; Toda, F.; Jones, W., Mechanochemistry and co-crystal formation: effect of solvent on reaction kinetics. *Chemical Communications* **2002,** (20), 2372-2373.

17. Yang, H.; Orefuwa, S.; Goudy, A., Study of mechanochemical synthesis in the formation of the metal–organic framework Cu 3 (BTC) 2 for hydrogen storage. *Microporous and Mesoporous Materials* **2011,** *143* (1), 37-45.

18. Yuan, W.; Friščić, T.; Apperley, D.; James, S. L., High reactivity of metal–organic frameworks under grinding conditions: parallels with organic molecular materials. *Angewandte Chemie* **2010,** *122* (23), 4008-4011.

19. Braga, D.; Maini, L.; de Sanctis, G.; Rubini, K.; Grepioni, F.; Chierotti, M. R.; Gobetto, R., Mechanochemical Preparation of Hydrogen-Bonded Adducts Between the Diamine 1, 4-Diazabicyclo [2.2. 2] octane and Dicarboxylic Acids of Variable Chain Length: An X-ray Diffraction and Solid-State NMR Study. *Chemistry–A European Journal* **2003,** *9* (22), 5538-5548.

20. Trask, A. V.; van de Streek, J.; Motherwell, W. S.; Jones, W., Achieving polymorphic and stoichiometric diversity in cocrystal formation: importance of solid-state grinding, powder X-ray structure determination, and seeding. *Crystal growth & design* **2005,** *5* (6), 2233-2241.

21. (a) Albano, V. G.; Aragoni, M. C.; Arca, M.; Castellari, C.; Demartin, F.; Devillanova, F. A.; Isaia, F.; Lippolis, V.; Loddo, L.; Verani, G., An unprecedented example of a cis-phosphonodithioato nickel (II) complex built by an extensive hydrogen bonding supramolecular network. *Chemical Communications* **2002,** (11), 1170-1171; (b) Aragoni, M. C.; Arca, M.; Devillanova, F. A.; Ferraro, J. R.; Isaia, F.; Lelj, F.; Lippolis, V.; Verani, G., An experimental and theoretical approach to phosphonodithioato complexes: molecular orbital analysis by hybrid-DFT and EHT calculations on trans-bis [O-alkyl-phenylphosphonodithioato] NiII, and vibrational assignments. *Canadian Journal of Chemistry* **2001,** *79* (10), 1483-1491; (c) Caria Aragoni, M.; Arca, M.; Demartin, F.; Devillanova, F. A.; Graiff, C.; Isaia, F.; Lippolis, V.; Tiripicchio, A.; Verani, G., Ring-opening of Lawesson's reagent: New syntheses of phosphono- and amidophosphono-dithioato complexes - structural and CP-MAS 31P-NMR characterization of [p-CH3OPh(X)PS2]2M (X = MeO, /PrNH; M = NiII, PdII, and PtII). *European Journal of Inorganic Chemistry* **2000,** (10), 2239-2244.

22. Groom, C. R.; Bruno, I. J.; Lightfoot, M. P.; Ward, S. C., The Cambridge structural database. *Acta Crystallographica Section B: Structural Science, Crystal Engineering and Materials* **2016,** *72* (2), 171-179.

23. Lutterotti, L.; Matthies, S.; Wenk, H., MAUD: a friendly Java program for material analysis using diffraction. *IUCr: Newsletter of the CPD* **1999,** *21* (14-15).

24. Young, R., Introduction to the Rietveld method. *The Rietveld Method* **1993,** *5*, 1-38.

25. (a) Sheldrick, G., Foundations of crystallography. *Acta Crystallographica A* **2008,** *64*, 112-122; (b) Sheldrick, G. M., Crystal structure refinement with SHELXL. *Acta Crystallographica Section C: Structural Chemistry* **2015,** *71* (1), 3-8.

26. (a) Blessing, R. H., An empirical correction for absorption anisotropy. *Acta Crystallographica Section A: Foundations of Crystallography* **1995,** *51* (1), 33-38; (b) Blessing, R. H., Outlier treatment in data merging. *Journal of Applied Crystallography* **1997,** *30* (4), 421-426.

27. Magini, M.; Iasonna, A., Energy transfer in mechanical alloying (overview). *Materials Transactions, JIM* **1995,** *36* (2), 123-133.

28. Yadav, T. P.; Yadav, R. M.; Singh, D. P., Mechanical milling: a top down approach for the synthesis of nanomaterials and nanocomposites. *Nanoscience and Nanotechnology* **2012,** *2* (3), 22-48.

29. Czakis-Sulikowska, D.; Kałużna, J., Synthesis and thermal behaviour of 4, 4'-bipyridyl and 2, 4' bipyridyl complexes of Co (II), Ni (II) and Cu (II) thiocyanates. *Journal of Thermal Analysis and Calorimetry* **1996,** *47* (6), 1763-1776.

30. Rodina, T. A.; Ivanov, A. V.; Gerasimenko, A. V.; Lutsenko, I. A.; Ivanov, M. A.; Hanna, J. V.; Antzutkin, O. N.; Sergienko, V. I., Crystalline O, O'-di-sec-butyl and O, O'-diethyl dithiophosphate platinum (II) complexes: Synthesis, 13 C and 31 P CP/MAS NMR, single crystal X-ray diffraction studies and thermal behaviour. *Polyhedron* **2011,** *30* (13), 2210-2217.

31. Lai, R., Crystal engineering of MOF based on polypyridyl ligands and coordinatively unsatured NiII ions. **2016**.

32. Desogus, D., Progettazione e Assemblaggio di Nuovi Polimeri di Coordinazione a partire da Ditiofosfonati di Cadmio e Leganti Polipiridinici. **2005**.

33. Le Bail, A., Monte carlo indexing with mcmaille. *Powder Diffraction* **2004,** *19* (03), 249-254.

34. Friščić, T.; James, S. L.; Boldyreva, E. V.; Bolm, C.; Jones, W.; Mack, J.; Steed, J. W.; Suslick, K. S., Highlights from Faraday discussion 170: Challenges and opportunities of modern mechanochemistry, Montreal, Canada, 2014. *Chemical Communications* **2015,** *51* (29), 6248-6256.

35. Friščić, T.; Childs, S. L.; Rizvi, S. A.; Jones, W., The role of solvent in mechanochemical and sonochemical cocrystal formation: a solubility-based approach for predicting cocrystallisation outcome. *CrystEngComm* **2009,** *11* (3), 418-426.

Chapter 5:

Mechanochemical Reactivity of Ni(II) building blocks with Polypyridyl ligands

This part of the PhD project has been carried out with the collaboration of the research group of Prof. M.C. Aragoni, *Chemistry Department, University of Cagliari*.

5 Mechanochemical Reactivity of Dithiophosphate and Dithiophosphonate Ni(II) complexes with Polypyridyl ligands

5.1 Introduction

As already widely discussed in the previous chapters, the field of crystal engineering regarding the building of coordination polymers is an evolving topic. In order to predict the topology of the resulting coordination polymer the choice of the ligands used as spacers between the Ni^{II} complexes is essential. The primary structure of the resulting coordination polymer directly depends on the geometry and topology of the molecules used as spacers. Therefore, in this chapter the mechanochemical reactivity of the metal complexes (**1**),(**2**), (**3**) e (**4**) with the 1,4-bis(3-pyridyl)-butadiyne (**L2**), 2,5-bis(4-pyridyl)-4-thia-1,3-thiazolidine (**L3**) and 2,5-bis(3-pyridyl)-4-thia-1,3-thiazolidine (**L4**) polydentate ligands is investigated. The nitrogen donors have been selected according to their rigidity, conformation, number and position of donor atoms. We used two different typologies of ligands: bidentate rigid spacers such as (**L2**) and semi-rigid bidentate spacers: (**L3**) and (**L4**) (Figure 5.1).

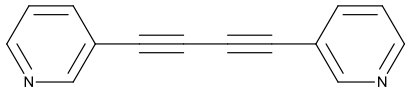

1,4-bis(3-pyridyl)-butadiyne (**L2**)

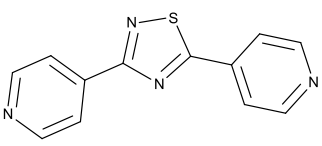

2,5-bis(4-pyridyl)-4-thia-1,3-thiazolidine (**L3**)

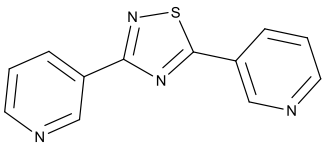

2,5-bis(3-pyridyl)-4-thia-1,3-thiazolidine (**L4**)

Figure 5.1 Formula structures of polypyridyl ligands used as organic linkers.

Ligand **L2,** consists of a buta-1,3-diyne chain with 1,4-substitution at position 3 in both pyridine rings. It belongs to the category of bis(aryl)diacetylenes ligands, which are well known in literature as building blocks for the synthesis of polymers, supramolecular materials and drugs.[1,2] They are extensively investigated with regard to the strong tendency of the diacetylene moiety to arrange into columnar systems thus leading to polymeric conjugated systems which display interesting optical properties.[3] **L2** exhibits a convergent or a divergent configuration of the pyridyl moieties depending on the relative orientation of the nitrogen donor atoms (Figure 5.2).

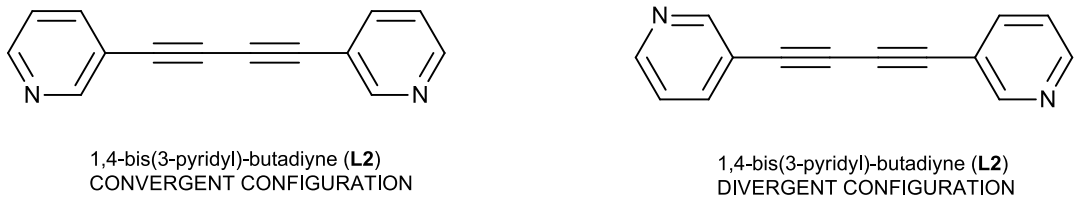

Figure 5.2. Convergent and divergent configuration of **L2**.

L3 and **L4**, are *bis*- functional ligands firstly isolated by Meltzer and coworkers in 1955.[4] Both **L3** and **L4** contain two pyridyl groups linked by a 1,2,4-thiadiazole group acting as a rigid, non-reactive spacer. Compared with 4,4′-dipyridine, **L1**, the pyridyl rings in **L3** and **L4** feature different space directions and separation lengths (9.599 and 9.962 Å, respectively).[5] Moreover, due to the different positions of the nitrogen atoms in **L3** and **L4** and to the different rotational conformations possible for the pyridyl rings, several orientations of the binding sites can be expected.

Solvothermal reaction between ligand **L2** and the nickel dithiophosphato and dithiophosphonato Ni^{II} complexes $[((EtO)_2PS_2)_2Ni]$ (**1**), $[((MeO)_2PS_2)_2Ni]$ (**2**), $[((MeO\text{-}C_6H_4)(EtO))PS_2)_2Ni]$ (**3**), $[((MeO\text{-}C_6H_4)(MeO))PS_2)_2Ni]$ (**4**), were performed. The solid and crystalline afforded compounds have been isolated and characterized (Elemental Analysis, Single Cristal X-ray diffraction, Spectrophotometric titrations, NMR, IR, Raman and Fluorescence studies) by Prof. M.C Aragoni and described in R. Lai PhD thesis.[6] Single crystal X-ray

diffraction performed on the coordination polymers **(1·L2)**$_\infty$, **(2·L2)**$_\infty$, **(3·L2)**$_\infty$, **(4·L2)**$_\infty$ result in polymeric chains where the pyridine units of **L2** are axially coordinated to the Ni^{II} ion of two different dithiophosphato or dithiophosphonato complex units. All polymers **(1·L2)**$_\infty$, **(2·L2)**$_\infty$, **(3·L2)**$_\infty$, **(4·L2)**$_\infty$ present very similar structure with a primary structure characterized by the infinite repetition of metal centers and **L2** molecules in a zig-zag fashion where ligands **L2**, in the divergent configurations, bridge two Ni^{II} complex units. (Figure 5.3, a-b). It is interesting to note that the alkoxy substituents at the phosphorous atoms point the hydrogens of the carbon atoms directly bound to the oxygen atoms point towards the pyridyl rings. This implies that OMe and OEt substituents are oriented towards and forwards the coordination plane, respectively, and therefore only OEt P-substituents are available to engage intermolecular interactions and contribute to the packing of the polymeric chains.[6]

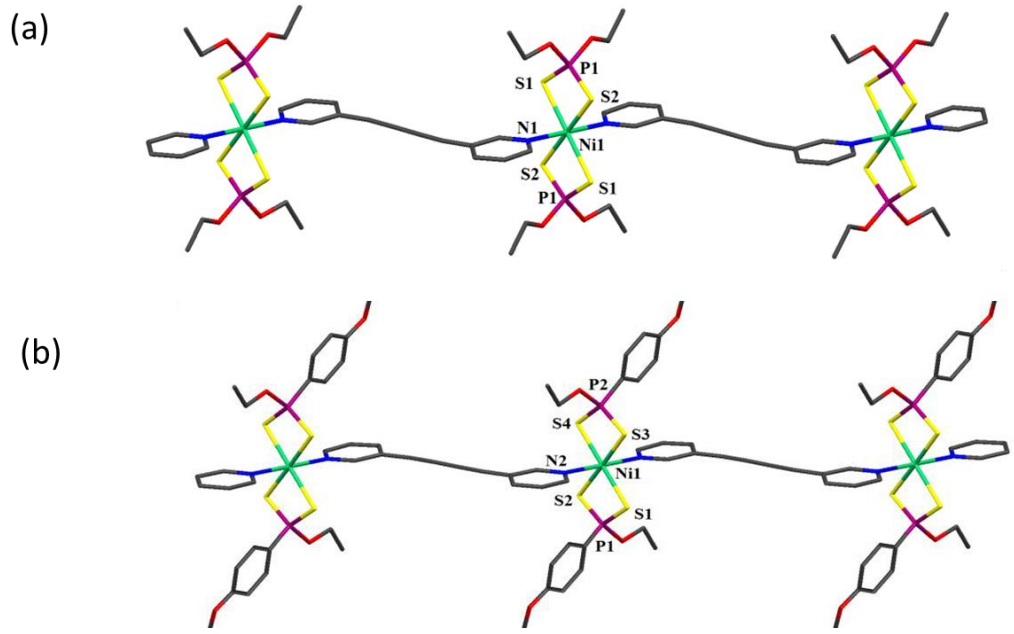

Figure 5.3 Zig zag chains of coordination polymers **L2** based, **(a)** and **(b)** represent **(1·L2)** $_\infty$ and **(3·L2)** $_\infty$ respectively [6]

Solvothermal reactions resulting in **(2·L3)**$_\infty$, **(4·L3)**$_\infty$, **(1·L4)**$_\infty$, **(3·L4)**$_\infty$ coordination polymers were performed and afforded crystalline compounds have been isolated and characterized by Elemental Analysis, Single Cristal X-ray Diffraction, NMR, IR, Raman and Fluorescence studies.[7]

Ligands **L3** and **L4** are less rigid with respect to **L2** and the predictability of the coordination polymers resulting is affected to the existence of different conformations available for these ligands. **L3** and **L4** are structural isomers which differ for the position of the nitrogen atoms in the pyridine rings. For **L3** an unique conformation is available whilst for **L4** two planar isomers, cissoid and transoid are possible. This is due to the different position of the nitrogen atoms in **L4** in comparison with **L3** and as a consequence of the different rotational conformations allowed for the pyridyl rings. Therefore, ligand **L3** leads to highly predictable linear coordination polymers due to the unique coordination conformation available. On the contrary, a convergent or a divergent coordination can be expected for **L4** leading to either dimeric or polymeric structures (Figure 5.4, a-b).[6]

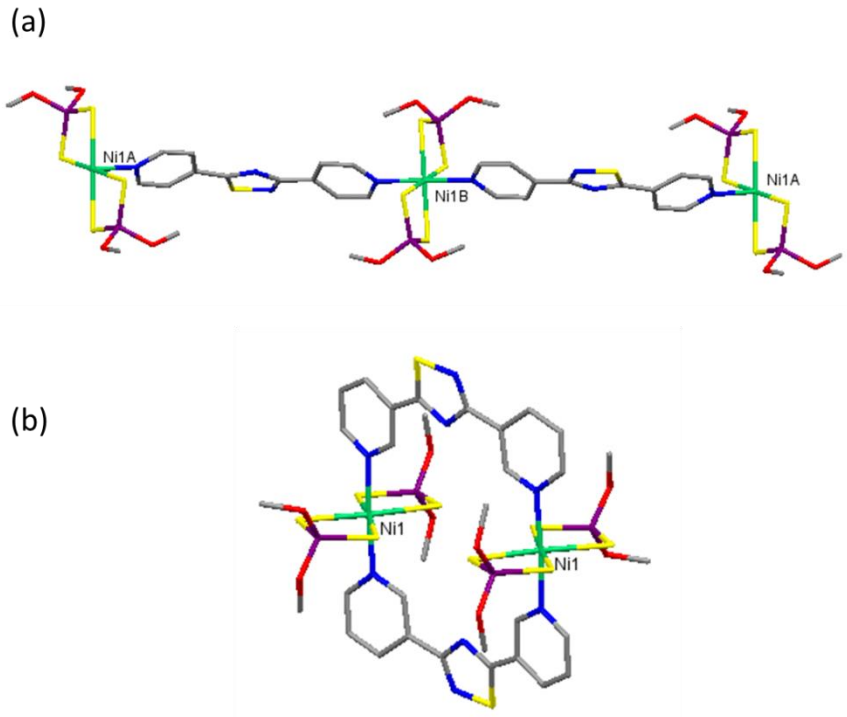

Figure 5.4 (a) polymeric structure of$(2\cdot L3)_{\infty}$ and (b) dimeric structure of $(1\cdot L4)_2$.[7]

Aim of this study is the environmental friendly mechanosynthesis of **$(1\cdot L2)_{\infty}$**, **$(2\cdot L2)_{\infty}$**, **$(3\cdot L2)_{\infty}$**, **$(4\cdot L2)_{\infty}$**, **$(2\cdot L3)_{\infty}$**, **$(4\cdot L3)_{\infty}$**, **$(1\cdot L4)_{\infty}$**, **$(3\cdot L4)_{\infty}$** coordination polymers by milling the neutral square planar Ni^{II} complexs $[((EtO)_2PS_2)_2Ni]$ (**1**), $[((MeO)_2PS_2)_2Ni]$ (**2**), $[((MeO\text{-}C_6H_4)(EtO))PS_2)_2Ni]$ (**3**), [((MeO-

$C_6H_4)(MeO))PS_2)_2Ni]$ (**4**), and 1,4-bis(3-pyridyl)-butadiyne (**L2)**, 2,5-bis(4-pyridyl)-4-thia-1,3-thiazolidine (**L3**) and 2,5-bis(3-pyridyl)-4-thia-1,3-thiazolidine (**L4**) polydentate ligands at room temperature. Mechanochemical synthesis provides powder samples (usually as polycrystalline material). Therefore, in order to obtain accurate structural information analogue single crystals grown from solution of this set of eight compounds was performed, and fully characterized.[6] In this PhD thesis a mechanochemical approach is investigated and **(1·L2)**$_\infty$, **(2·L2)**$_\infty$, **(3·L2)**$_\infty$, **(4·L2)**$_\infty$, **(2·L3)** $_\infty$, **(4·L3)**$_\infty$, **(1·L4)$_2$**, **(3·L4)** $_\infty$ solvothermal samples and their resulting structure are compared, via X-Ray Powder Diffraction, with that formed by mechanosynthesis. The evolution of the reactants during the synthesis process and the influence of the synthesis parameters on the chemical, structural, and thermal properties of the samples were investigated.

5.2 Experimental section

5.2.1 Materials and Methods

All commercially available compounds were used as received. The ligand 1,4-di-3-pyridyl-1,3-butadiyne (**L2**) was synthesized optimizing the literature method[8] as reported by Lai.[6] The Ni^{II} complexes (**1**),(**2**),[9] (**3**) e (**4**)[10] and the *bis*- functional ligands **L3** and **L4** [4] were synthesized according to previously reported procedures [4,9,10].

The mechanochemical experiments were carried out on the Spex 8000 shaker ball-mill (CertiPrep, Metuchen, NJ) in a 30 mL teflon coated stainless-steel grinding jar. Two 5 mm diameter zirconia balls (0.40 g single ball) were used. In order to prevent excessive overheating of the jar the experiments were carried out alternating milling and rest period at 5 min intervals. In the LAG synthesis ethanol (96%, Sigma-Aldrich, without further purification), methanol (for analysis ACS,Carlo Erba) and chloroform (HPLC grade, ACS, Sigma-Aldrich) was used as the solvents. With the purpose to track the progress of reactions during the milling process, samples at different milling time were synthetized.

Samples reported in this chapter were characterized by X-ray Powder Diffraction, Infrared Spectroscopy, Scanning Electron Microscopy, Thermogravimetry and

Differential Scanning Calorimetry techniques. Specifications of these instruments are reported in 4.2.1. For this set of samples the Rietveld refinement is not shown because still in progress in our laboratories, but it is mandatory to obtain more information about the structure of the milled samples. The average crystal size of the samples is calculated by Scherrer equation.

5.2.2 Synthesis

Synthesis of $[((EtO)_2PS_2)_2Ni]\cdot$(1,4 bis (3-pyridyl)butadiyne)]$_\infty$, (1·L2) $_\infty$. (56.8 mg, 0.13mmol) of **1** and (51.0 mg, 0.25 mmol) of **L2** , were reacted at 130 °C in a high pressure Aldrich tube in 15 mL of EtOH and 15 ml of $CHCl_3$. After complete dissolving of the reagents, the reaction mixture was transferred in a small vial and slowly cooled at room temperature. Two weeks later very few green palette crystals of (**1·L2**)$_\infty$ suitable for X-ray analysis ware obtained (yield:58%). This sample was characterized by Elemental Analysis, Single Cristal X-ray Diffraction, NMR, IR, Raman and Fluorescence techniques in the PhD thesis of R. Lai from the research group of Prof. M.C Aragoni (University of Cagliari).[6]

NG synthesis of (1·L2)$_\infty$. Equimolar quantities of $[((EtO)_2PS_2)_2Ni]$ **1** complex (0.1712g, 0.4 mmol) and 1,4-bis(3-pyridyl)-butadiyne **L2** (0.0817g, 0.4mmol) were placed in the jar along with zirconia balls. FT-IR (4000-600 cm^{-1}) for (**1·L2**)$_\infty$ NG and LAG samples: 2977 m, 2927 m, 1738 w, 1595 m ν(C=N), 1564 m ν (C=C, conj), 1476 vm, 1440 w, 1409 vm, 1387 vm, 1324 w, 1181 vm, 1102 s, 1023 vs (pirydine breathing mode) , 957 vs, 797 vs, 690 s, 657 vs, 640 vs cm^{-1}.

In order to explore the possibility to obtain different stoichiometry of compounds the NG synthesis was also performed in the 2:1 (**L2**:**1**) molar ratio, and the resulting product compared to those obtained by conventional and equimolar NG synthesis.

LAG synthesis of (1·L2)$_\infty$. equimolar quantities of complex **1** (0.1712g, 0.4 mmol) and **L2** (0.0817g, 0.4mmol) were placed in the jar along with zirconia balls and 50 μL of ethanol.

Synthesis of $[((MeO)_2PS_2)_2Ni]\cdot$(1,4 bis (3-pyridyl)butadiyne)]$_\infty$, (2·L2) $_\infty$. The conventional synthesis was performed in the same way of **(1·L2)** $_\infty$ reacting 0.08 mmol of **2** and 0.15 mmol of **L2** at 130 °C in high pressure Aldrich tube with 15 mL of MeOH and 15 mL of $CHCl_3$. After complete reagents dissolvation, the reaction mixture was transferred in a vial, and slowly cooled at room temperature. After two weeks green needles crystals of **(2·L2)** $_\infty$, suitable for X-ray analysis have been obtained (yield:55%) and fully characterized.[6]

NG synthesis of (2·L2)$_\infty$. Equimolar quantities of $[((MeO)_2PS_2)_2Ni]$ **2** (0.1492g, 0.4 mmol) and **L2** (0.0817g, 0.4mmol) were placed in the jar along with zirconia balls.

LAG synthesis of (2·L2)$_\infty$. (0.1492g, 0.4 mmol) of complex **2** and (0.0817g, 0.4mmol) **L2** were placed in the jar along with zirconia balls and 50 μL of chloroform. The same LAG synthesis was carried out with the same amount of reagents and milling conditions in methanol. FT-IR (4000-600cm^{-1}) for **(2·L2)**$_\infty$ LAG sample: 3072 vw, 3009 vw, 2978 w, 2939 m, 1594 m ν(C=N), 1567 m ν (C=C, conj), 1472 m, 1450 w, 1405 s, 1328 w, 1228 w, 1172 s, 1094 s, 1033 m (pirydine breathing mode) , 1005 vs, 794 vs, 683 s, 650 vs cm^{-1}.

Synthesis of $[(MeO\text{-}C_6H_4)(EtO))PS_2)_2Ni]\cdot$(1,4 bis (3-pyrdyl)butadiyne)]$_\infty$, (3·L2) $_\infty$. The solvothermal reaction consists in 0.65 mmol of **3** and 0.12 mmol of **L2** that have been reacted at 50 °C in a flask with 13 mL of EtOH and 15 mL of $CHCl_3$. After complete dissolving of the reagents, the reaction mixture was slowly cooled at room temperature. After 24 hours a green microcristalline powder of **(3·L2)**$_\infty$ was filtered from solution. Green crystals suitable for X-ray analysis have been obtained by reacting in Aldrich high pressure tube the same quantity of reagents and solvents. After complete reagent dissolving, the reaction mixture was transferred in a vial and slowly cooled at room temperature. The sample obtained (yield 32%) was fully characterized. [6]

NG synthesis of (3·L2) $_\infty$. (0.2213 g, 0.4 mmol) of $[(MeO\text{-}C_6H_4)(EtO))PS_2)_2Ni]$ **3** and (0.0817g, 0.4mmol) **L2** were placed in the jar along with zirconia balls.

LAG synthesis of (3·L2) $_\infty$. Ni^{II} complex **3** (0.2213g, 0.4 mmol) and **L2** (0.0817g, 0.4mmol) mixture were placed in the jar along with zirconia balls. LAG synthesis

were carried out using i) 50 μL of ethanol and ii) the same volume of chloroform. FT-IR (4000-600cm^{-1}) for (**3**·**L2**)$_\infty$ LAG:$CHCl_3$ sample: 3060 vw, 2970 m, 2910 m, 2830 w, 1590 s ν(C=N), 1570 m ν(C=C, conj), 1470 m, 1410 w, 1380 w, 1290 m, 1250 s, 1110 vs, 1030 s (pirydine breathing mode) , 930 vs, 800 m, 690 m, 640 s cm^{-1}.

Synthesis of [(MeO-C_6H_4)(MeO))$PS_2)_2$Ni] ·(1,4 bis (3-pyrdyl)butadiyne)]$_\infty$, (4·L2) $_\infty$. The solution-based reaction was obtained using 0.18 mmol of **4** and 0.35 mmol **L2** and reacting these reactants at 50 °C in a flask with 15 mL of MeOH and 15 mL of $CHCl_3$. After complete dissolving of the reagents, the reaction mixture was slowly cooled at room temperature. After 24 hours a green microcristalline powder of **(4·L2)** $_\infty$ is precipitated from solution. Green crystals suitable for X-ray analysis were obtained by preparing a solution of **4** in 5 mL of $CHCl_3$ in a small vial which was then introduced into a bigger one containing **L2** solution in 10 mL of MeOH, and left to stand at room temperature for a week. The resulting sample (yield 89%) was characterized in detail in the PhD thesis of R. Lai. [6]

NG synthesis of (4·L2) $_\infty$. (0.1712g, 0.4 mmol) of [(MeO-C_6H_4)(MeO))$PS_2)_2$Ni] **4** and (0.0817g, 0.4mmol) **L2** were placed in the jar along with zirconia balls.

LAG synthesis of (4·L2) $_\infty$. Ni^{II} complex **4** (0.1712g, 0.4 mmol) and **L2** (0.0817g, 0.4mmol) mixture were placed in the jar along with zirconia balls. Three LAG synthesis were carried out using i) 50 μL of methanol, ii) the same volume of chloroform and iii) a mixture of 50 μL of methanol/ 50 μL of chloroform. FT-IR (4000-600cm^{-1}) for (**4**·**L2**)$_\infty$ LAG:$CHCl_3$ sample: 3060 vw, 2928 m, 2894 m, 2857 w, 1600 s ν, 1561 m ν, 1444 m, 1405 w, 1294 m, 1252 s, 1178s, 1115 vs, 1026 s, 1006 vs, 828 m, 793 m, 645 s, 622m cm^{-1}

Synthesis of [((MeO)$_2$$PS_2)_2$Ni]·2,5-bis(4-pyridyl)-4-thia-1,3-thiazolidine]$_\infty$, (2·L3) $_\infty$**.** [Ni((MeO)$_2$$PS_2)_2$] (18.6 mg, 0.05 mmol) 2) and 2,5-bis(4-pyridyl)-4-thia-1,3-thiazolidine (**L3**) (12.0 mg, 0.05 mmol) were reacted at 130 °C in a high pressure Aldrich tube in 30 mL of MeOH. After complete dissolving of the reagents, the reaction mixture was transferred in a small vial and

slowly cooled at room temperature. Five days later **(2·L3)**$_\infty$ few green crystals suitable for X-ray analysis were obtained (yield: 20%)and fully characterized in [6].

LAG synthesis of (2·L3)$_\infty$. (0.0746g, 0.2 mmol) of [Ni((MeO)$_2$PS$_2$)$_2$] **2** and (0.0502g, 0.2mmol) **L3** were placed in the jar along with zirconia balls and 50 μL of methanol. FT-IR (4000-600cm^{-1}) for (**2·L3**)$_\infty$ LAG:MeOH sample: 2936 w, 2833 vw, 1608 m ν(C=N), 1569 w ν(C=C, conj), 1458 m, 1409 m, 1333 w, 1293 vw, 1213 w, 1173w, 1133 m, 1000 vs (pyridine breathing mode), 822 m, 795 s, 777 vs, 702 s, 675 s, 648m cm^{-1}.

Synthesis of [(MeO-C$_6$H$_4$)(MeO))PS$_2$)$_2$Ni]· 2,5-bis(4-pyridyl)-4-thia-1,3-thiazolidine]$_\infty$, (4·L3)$_\infty$. [(MeO-C$_6$H$_4$)(MeO))PS$_2$)$_2$Ni] (**4**) (26.2 mg, 0.05 mmol) and 2,5-bis(4-pyridyl)-4-thia-1,3-thiazolidine (**L3**) (12.0 mg, 0.05 mmol) were reacted at 100 °C in a high pressure Aldrich tube in 30 mL of MeOH. After complete dissolving of the reagents, the reaction mixture was slowly cooled at room temperature. A week later, **(4·L3)**$_\infty$ was obtained (yield 88%) as green crystals suit-able for X-ray analysis. A complete characterization is reported in [6].

LAG synthesis of (4·L3)$_\infty$. (0.1838g, 0.35 mmol) of [Ni((MeO)$_2$PS$_2$)$_2$](**2**) and (0.0841g, 0.35mmol) 2,5-bis(4-pyridyl)-4-thia-1,3-thiazolidine (**L3**) were placed in the jar along with zirconia balls and 50 μL of methanol. FT-IR (4000-600cm^{-1}) for (**4·L3**)$_\infty$ LAG:MeOH sample: 2933 w, 2830 vw, 1590 m ν(C=N), 1567 m ν (C=C, conj), 1500 m, 1460 m, 1436 w, 1410 m, 1336 w, 1267 m, 1250 s, 1177 m, 1110 s, 1060 w, 1030 vs, 1013 vs (pyridine breathing mode), 940 w, 903 w, 830 vm, 773 vs, 750 w, 730 w, 707 w, 690 w, 653 s, 640 vs, 620 s cm^{-1}.

Synthesis of [((EtO)$_2$PS$_2$)$_2$Ni]·2,5-bis(3-pyridyl)-4-thia-1,3-thiazolidine]$_2$, (1·L4)$_2$. A solution of [Ni((EtO)$_2$PS$_2$)$_2$] (**1**) (10.3 mg, 0.02 mmol) was prepared in 0.5 mL of CH_2Cl_2 in a small vial. This vial was then introduced into a bigger one containing a solution of 2,5-bis(3-pyridyl)-4-thia-1,3-thiazolidine (**L4**) (10.0 mg, 0.04 mmol) in 10 mL of MeOH, and left to stand at room temperature for several weeks. Green crystals of **(1·L4)$_2$** suitable for X-ray

analysis have been obtained (yield:50%) and a complete characterization is reported in [6].

LAG synthesis of $(\mathbf{1{\cdot}L4})_\infty$. (0.0856g, 0.2 mmol) of $[Ni((EtO)_2PS_2)_2]$ (**1**) and (0.0480g, 0.2mmol) 2,5-bis(3-pyridyl)-4-thia-1,3-thiazolidine **(L4)** were placed in the jar along with zirconia balls and 50 μL of dichloromethane. FT-IR (4000-600cm^{-1}) for $(\mathbf{1{\cdot}L4})_\mathbf{2}$ LAG:EtOH sample: 2977 w, 2891 vw, 1601 m ν(C=N), 1580 m ν (C=C, conj), 1500 m, 1465 m, 1426 m, 1399 vm, 1329 w, 1302 w, 1298 m, 1185 m, 1127 m, 1096 s, 1014 s (pyridine breathing mode), 948 vs, 816 m, 773 s, 726 w, 695 w, 653 m, 672 vs cm^{-1}.

Synthesis of $[(EtO\text{-}C_6H_4)(MeO))PS_2)_2Ni]\cdot$ 2,5-bis(3-pyridyl)-4-thia-1,3-thiazolidine]$_\infty$, $(\mathbf{3{\cdot}L4})_\infty$. $[(EtO\text{-}C_6H_4)(MeO))PS_2)_2Ni]$ (**3**) (27.7 mg, 0.05 mmol) and 2,5-bis(3-pyridyl)-4-thia-1,3-thiazolidine (**L4**) (12.0 mg, 0.05 mmol) were reacted at 130 °C in a high pressure Aldrich tube in 15 mL of EtOH and 25 mL of $CHCl_3$. After complete dissolving of the reagents, the reaction mixture was slowly cooled at room temperature. A week later, $(\mathbf{3{\cdot}L4})_\infty$ was obtained (yield:54%) as green crystals suitable for X-ray analysis and fully characterized. [6]

LAG synthesis of $(\mathbf{3{\cdot}L4})_\infty$. (0.1107g, 0.2 mmol) of **3** and (0.0480g, 0.2mmol) **L4** were placed in the jar along with zirconia balls and 50 μL of chloroform. FT-IR (4000-600cm^{-1}) for $(\mathbf{3{\cdot}L4})_\infty$ LAG:$CHCl_3$ sample: 2969 w, 2891 vw, 1604 m ν(C=N), 1570 w ν (C=C, conj), 1500 m, 1471 m, 1404 vm, 1337 m, 1292 vm, 1250 s, 1195 w, 1170 w, 1127 m, 1104 s, 1016 vs (pyridine breathing mode), 938 s, 908 w, 821 m, 800 m, 775 s, 733 m, 688 s, 646 vs, 621 s cm^{-1}.

5.3 Results and Discussion

Profiting of the expertise acquired in the mechanochemical synthesis of similar coordination polymers (Chapter 4), this part of the research concerns the investigation of a matrix of eight products, involving the same four Ni^{II} complexes adopted in chapter 4, this time reacting with a set of two different typologies of ligands: bidentate rigid (**L2**) and semi-rigid bidentate (**L3**) and (**L4**). Several mechanochemical reactions were performed in NG and LAG (with

different solvents) approaches. In all the cases the powder of conventional solution materials were previously identified by comparison of its XRPD pattern with single-crystal X-ray data.[6]

Table 5.1 Schematic representation of the mechanosynthesis reported in this chapther. (Symbols: √ for milled samples isostructurals with the crystallographic data, × for mechanochemical reactions for which a different structure is observed, - these synthesis are not performed).

	1				**2**			**3**			**4**			
	EtOH	*$CHCl_3$*	*NG*	*CH_2Cl_2*	*MeOH*	*$CHCl_3$*	*NG*	*EtOH*	*$CHCl_3$*	*NG*	*MeOH*	*$CHCl_3$*	*MeOH/ $CHCl_3$*	*NG*
L2	√	-	√	-	√	×	×	×	√	×	×	×	×	×
L3	-	-	-	-	√	-	-	-	-	-	√	-	-	-
L4	-	-	-	√	-	-	-	-	√	-	-	-	-	-

5.3.1 Structure and morphology of (1·L2)$_\infty$, (2·L2)$_\infty$, (3·L2)$_\infty$, (4·L2)$_\infty$

The occurrence of a mechanochemical reaction was ascertained by comparison of the XRPD pattern of the grinded samples with those of the solution-based material and reactants. The results are summarized in table 5.1. The observations vary from quantitative formation of products to partial reactions. In some case amorphous products are obtained, while other times a mixture of unknown phases is observed. The examination of these four cases: **(1·L2)**$_\infty$, **(2·L2)**$_\infty$, **(3·L2)**$_\infty$, **(4·L2)**$_\infty$ highlights that in the first three cases a quantitative reaction occurred to give the desired product. In the case of **(1·L2)**$_\infty$, the complete conversion of reactants into coordination polymer (**1·L2**)$_\infty$ was gained in quantitative yield in 30 minutes (Figure 5.5c) (for XRPD patterns of NG products at several time intervals see section 5.6, Figure 5.17). The comparison between the XRPD pattern of the milled product and of the solution-based reaction (Figure 5.5a) shows a close correspondence. The same correspondence is observed with the XRPD pattern of LAG sample after 10 minutes of milling (Figure 5.5b). As already observed for the coordination polymers studied in Chapter 4, the XRPD peaks for the milled sample correspond to these of the conventionally prepared sample, but the intensity and width, and therefore size and strain, are significantly different. This

is due to the continuous reduction of crystallite grain size induced by milling. The average crystal size of samples, calculated by Scherrer equation, correspond to 24nm and 33 nm for NG and LAG sample respectively while, as expected, the conventionally prepared is microcrystalline.The LAG method was carried out by adding a few microlitres of ethanol. As already observed for the LAG synthesis of $(\mathbf{1}\cdot\mathbf{L1})_\infty$ coordination polymer obtained by reacting **L1** with **1** (see Chapter 4), the use of solvent reduced the reaction time.

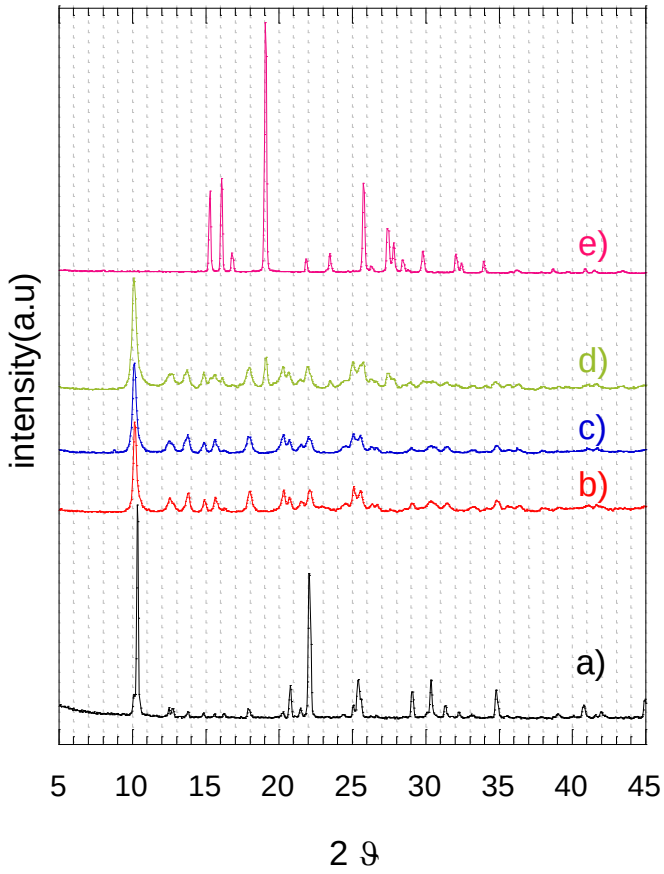

Figure 5.5. Comparison of XRPD patterns for compound $(\mathbf{1}\cdot\mathbf{L2})_\infty$ obtained by a) conventional synthesis, b) LAG after 10 minutes grinding, c) NG after 30 minutes grinding, d) NG performed in the 2:1 (**L2**:**1**) molar ratio after 10 minutes grinding samples and e) **L2** ligand.

In the case of **(1·L2)** $_\infty$ LAG mechanosynthesis the reaction can be considered concluded after 10 minutes of milling (for XRPD patterns of LAG products at several time intervals see section 5.6, Figure 5.18) while for the (**1**·**L1**)$_\infty$ LAG mechanosynthesis was concluded after only 5 minutes of grinding (4.3.1). The same result was observed in NG synthesis of (**1**·**L1**)$_\infty$ in comparison with (**1**·**L2**)$_\infty$, that have been concluded at 10 and 30 minutes for (**1**·**L1**)$_\infty$ and (**1**·**L2**)$_\infty$ respectively. A possible explanation for this difference, using the same coordinatively unsatured Ni (II) complex **1** (with identical milling conditions and apparatus) can be provided to the difference in the melting points for **L1** (111-114°C) and **L2** (149-155°C) ligands**.** Pichon and coworkers have studied the reactivity under mechanochemical conditions of a set of reactions and have discerned some trends. In particular, they observed a general inverse correlation between melting point of ligands and reactivity.[11] As already discussed in Chapter 2, reaction between organic solids (co-crystals reactions) have been study in order to investigate the mechanism of mechanosynthesis. In some cases examinations have suggested that an high mobility of molecules within solid crystals occurs, while in other cases was found that the reaction proceed via intermediate eutectic phases which are liquid during the reaction. The inverse correlation studied by Pichon is consistent with both of these descriptions. Low reactant melting points can make the reactions more thermodynamically favourable, this is correlate with low lattice energy in the starting materials. Furthermore, low reactant melting points can favour faster kinetics since they can lead to greater molecular mobility.[11] In this light **L1** is the most reactive of the ligands investigated (Table 5.2) and this is in agreement with the results observed for (**1**·**L1**)$_\infty$ and (**1**·**L2**)$_\infty$ milled samples.[11] In figure 5.5 is also reported the XRPD pattern of NG synthesis in the 2:1 (**L2**/**1**) molar ratio. This reaction was performed with the aim to investigate if other polymeric stoichiometry were possible starting from the same reagents. The XRPD pattern highlights, in addition to the peaks coincident with the (**1**·**L2**)$_\infty$ coordination polymer phase, peaks due to **L2** phase at 16.02, 19.07, 23.47, 27.37, 27.88 2ϑ degree which remain at higher milling times. This is an evidence that the stoichiometry of the (**1**·**L2**)$_\infty$ coordination polymer is 1:1 (**L2**/**1**) and the excess amount of ligand remains unreacted.

Table 5.2 Melting points of reagents.

Reagent	Melting Point (°C)
$[((EtO)_2PS_2)_2Ni]$, **1**	95
$[((MeO)_2PS_2)_2Ni]$, **2**	120
$[((MeO\text{-}C_6H_4)(EtO))PS_2)_2Ni]$, **3**	128
$[((MeO\text{-}C_6H_4)(MeO))PS_2)_2Ni]$, **4**	189
4,4'- bipyridine, **L1**	110
1,4-bis(3-pyridyl)-butadiyne, **L2**	155
2,5-bis(4-pyridyl)-4-thia-1,3-thiazolidine, **L3**	197
2,5-bis(3-pyridyl)-4-thia-1,3-thiazolidine, **L4**	137

In the mechanochemical case study of $\mathbf{(2\cdot L2)}_\infty$, the NG approach and two LAG experiments were performed by adding to the starting powder reagents few microlitres of chloroform for the first experiment and of methanol for the second. The conventionally obtained sample was performed in a mixture of $CHCl_3$ and MeOH. As observed in the XRPD patterns of Figure 5.6 the NG (Figure 5.6a) and LAG:$CHCl_3$ (Figure 5.6b) experiments did not led to the $\mathbf{(2\cdot L2)}_\infty$ structure.We can observed an analogy (i) and a difference (ii) with the mechanosynthesis carried out for the $\mathbf{(2\cdot L1)}_\infty$ coordination polymer investigated in Chapter 4. The analogy (i) consists of the liquid phase used (methanol) that has the possibility to drive the reaction through the quantitative formation of $\mathbf{(2\cdot L2)}_\infty$ in 10 minutes (for complete XRPD patterns of LAG products Figure 5.19 of section 5.6). The pattern of this sample matched very closely with that of the conventional synthesis (Figure 5.6c-d). The average crystal size of the milled sample, calculated by Scherrer equation, corresponds to 60nm. Examining $\mathbf{(2\cdot L1)}_\infty$ case (Chapter 4) is

possible to note the same evidence in LAG experiment which performed in methanol leads the expected pattern phase while in chloroform did not lead to the **(2·L1)**$_\infty$ structure. On the other hand, (ii) the discrepancy is observed in NG synthesis that in the case of **(2·L1)**$_\infty$ gives rise to the desired structure after 20 minutes of milling and in the case of **(2·L2)**$_\infty$ did not give the desired structure. This is probably due to the higher melting point of **L2** in comparison with **L1** resulting in a less thermodynamically favourite NG reaction for **(2·L2)**$_\infty$.[11]

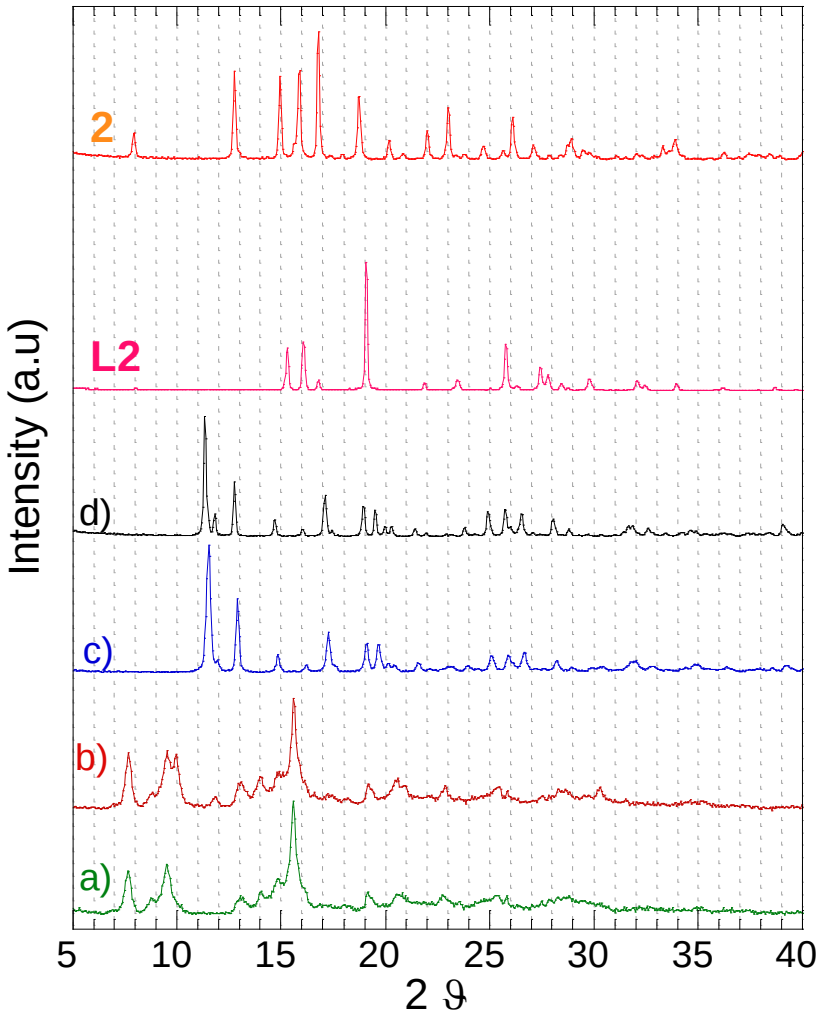

Figure 5.6. Comparison of XRPD patterns for compound (**2·L2**)$_\infty$ obtained by a) NG after 20 minutes grinding, b) LAG: $CHCl_3$after 20 minutes grinding, c) LAG: MeOH after 20 minutes grinding d) conventional synthesis. Reagents **2** and **L2** for comparison.

The mechanochemical study of $(\mathbf{3{\cdot}L2})_\infty$ coordination polymer has been carried out by a variety of NG and LAG experiments. As observed in Figure 5.7c the complete formation of the $\mathbf{(3{\cdot}L2)}_\infty$ structure is achieved after 40 minutes of milling in LAG: MEOH synthesis (Figure5.7d), with peaks in the XRPD pattern placed in the same position observed in the pattern of the conventionally prepared sample (for complete XRPD patterns of LAG products see figure 5.20 of section 5.6). However, as observed also for the $\mathbf{(2{\cdot}L2)}_\infty$ milled sample, broader peaks in the LAG sample are due to the smaller particle size (76nm by Scherrer equation). There are clear discrepancies between the pattern of the conventionally prepared sample and the NG and LAG:EtOH samples after 30 minutes of grinding (Figure 5.7). These differences are unchanged in samples collected at higher grinding times (data not shown). In the XRPD patter of the NG sample (Figure 5.7a) the presence of an amorphous phase is observed. It is also possible to observe an analogy with the mechanosynthesis carried out for the $\mathbf{(3{\cdot}L1)}_\infty$ coordination polymer investigated in Chapter 4. The analogy consists of the liquid phase (chloroform) used that drives the reaction through the $\mathbf{(3{\cdot}L2)}_\infty$ formation. The LAG experiment with chloroform for $\mathbf{(3{\cdot}L1)}_\infty$ (Chapter 4) leads the expected pattern phase, the same experiment performed by adding ethanol did not lead to the $\mathbf{(3{\cdot}L1)}_\infty$ structure.

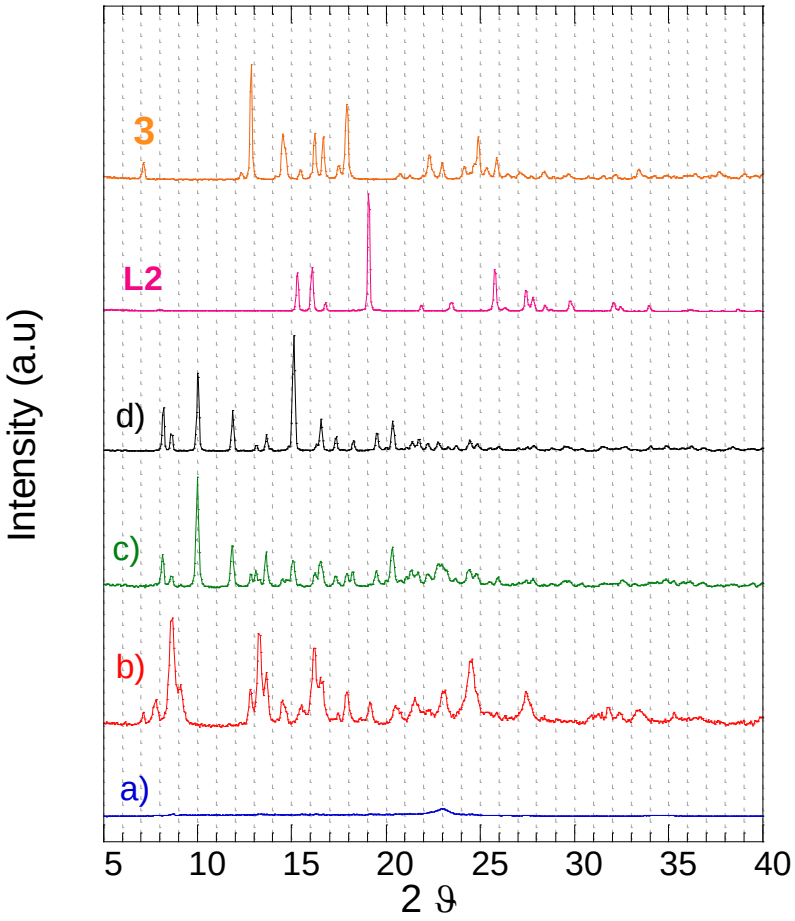

Figure 5.7. XRPD patterns for $(\mathbf{3}\cdot\mathbf{L2})_\infty$: a) NG after 30 minutes, b) LAG: EtOH after 30 minutes, c) LAG:$CHCl_3$ after 40 minutes and d) $(\mathbf{3}\cdot\mathbf{L2})_\infty$ conventional synthesis samples. In the pattern **3** and **L2** are reported to comparison.

Interesting to note is that all the mechanochemical reactions investigated for $\mathbf{(4\cdot L2)}_\infty$ highlight discrepancies from the conventionally prepared sample. The mechanochemical study of $(\mathbf{4}\cdot\mathbf{L2})_\infty$ coordination polymer was carried out adopting NG and LAG experiments. LAG syntheses were performed by adding to the starting powder reagents few microlitres of chloroform in the first experiment and methanol in the second. These two syntheses do not lead to the desired $\mathbf{(4\cdot L2)}_\infty$ structure, therefore the LAG experiment in a mixture of chloroform and methanol was carried out according to the conventional synthesis which was performed in a $CHCl_3$:MeOH (50:50 v/v) mixture. In Figure 5.8 experimental XRPD patterns of $\mathbf{(4\cdot L2)}_\infty$ conventionally synthesized and milled samples are reported. XRPD pattern of conventional sample corresponds to the

calculated pattern using single crystal data.[6] The XRPD pattern of LAG:MeOH/$CHCl_3$ sample is in clear discrepancies with the pattern of the conventional sample (it only matches with the most intense peak at 15.4° 2ϑ of the **(4·L2)**$_\infty$ conventional). Furthermore, peaks of this LAG sample did not match with starting materials. Additional peaks are visible suggesting a partial formation of an unknown product or the occurrence of a mixture of phases. A careful observation of the Figure 5.8 shows that also the other mechanochemical reactions were inefficient to obtain the **(4·L2)**$_\infty$ conventional structure. No one of the four milled samples is exactly identical to another one. There are difference in peaks position and intensity, suggesting that NG and LAG:MeOH, LAG:$CHCl_3$ and LAG:MeOH/$CHCl_3$ methods resulted in different and at the same time unknown products or their mixtures. In this case the mechanosynthesis can be considered inefficient to obtain the same sample of solution-based reactions.[12] As demonstrated by Pichon and coworkers, an important issue of mechanochemistry is the possibility to obtain products not formed using conventional solvent-based crystallization.[11] Different polymer connectivities are obtained on the precise process condition adopted, and especially from the solvent which act as templating agent supporting the foregoing discussion reported in section 4.3 of this PhD thesis. Several examples for the solvent effects are reported in this PhD thesis. For **(1·L1)**$_\infty$ and **(1·L2)**$_\infty$ the appropriate solvent for the known phase is ethanol, for **(2·L1)**$_\infty$ and **(2·L2)**$_\infty$ is methanol, while for **(3·L1)**$_\infty$ **(3·L2)**$_\infty$ is chloroform. Considering this partial trend, and observing that for the case of **(4·L1)**$_\infty$ the appropriate solvent was the mixture of methanol and chloroform, we would expect the same behavior for **(4·L2)**$_\infty$ sample. It is therefore interesting to note that in the LAG mechanosynthesis (with the MeOH/$CHCl_3$ mixture) an alternative, unknown phase was observed, presumably due to the absence of an appropriate templating solvent for the known phase. Moreover, Pichon and coworkers have demonstrated a mechanochemical trend about the general inverse correlation between melting point of reactants and reactivity. The Ni^{II} complexes presented in this PhD thesis have a proper melting point (Table 5.2), for instance 189°C for **4** and 95°C for **1**. Based on the trend observed by Pichon about the correlation between reactivity and melting point of ligands, probably this may be

the explanation of the more difficult ability of obtaining coordination polymers with Ni^{II} complex **4.**

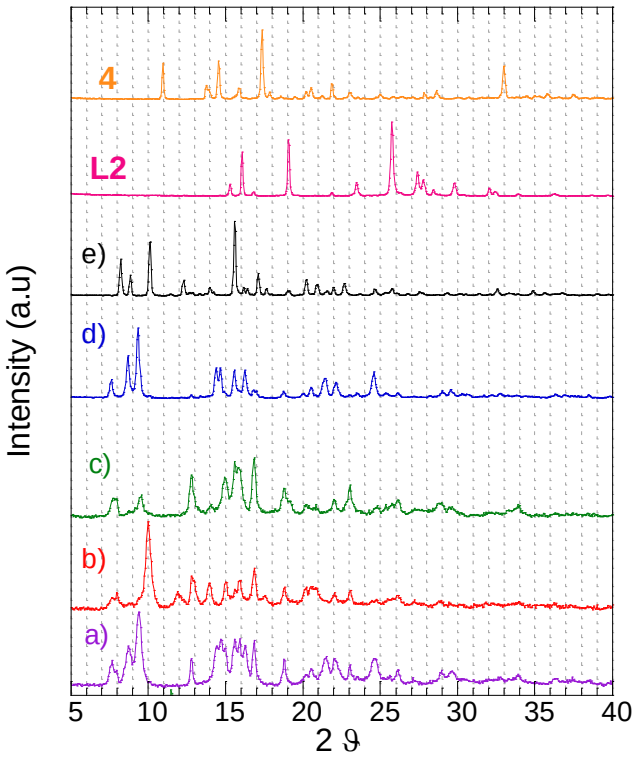

Figure 5.8. XRPD patterns for $(\mathbf{4}\cdot\mathbf{L2})_\infty$: a) LAG: MeOH after 40 minutes, b) LAG:$CHCl_3$ after 40 minutes, c) NG after 40 minutes and d) LAG:MeOH/$CHCl_3$ after 30 minutes, e) $(\mathbf{4}\cdot\mathbf{L2})_\infty$ conventional synthesis samples. XRPD patterns of **4** and **L2** are reported to comparison.

With regard to FT-IR characterization of milled samples, **L2** has two pyridine rings space by a buta-1,3-diyne chain therefore, it is possible to find an analogy with the most characteristic bands of the ligand complexed shifted at higher frequencies in comparison to free ligand as has been observed in the previous chapter for **L1**. The FT-IR spectra of $(\mathbf{1}\cdot\mathbf{L2})_\infty$, $(\mathbf{2}\cdot\mathbf{L2})_\infty$, $(\mathbf{3}\cdot\mathbf{L2})_\infty$, $(\mathbf{4}\cdot\mathbf{L2})_n$ milled samples present the most characteristic ring vibration ν(C-N), ν(C-C) and pyridine breathing mode shifted at higher frequencies compared to free **L2** (bands at: 1577, 1560 and 1020 cm^{-1}).[4] FT-IR bands for $(\mathbf{1}\cdot\mathbf{L2})_\infty$ at 1595, 1566, 1023 cm^{-1}, for $(\mathbf{2}\cdot\mathbf{L2})_\infty$ at 1594, 1567, 1033 cm^{-1} and for $(\mathbf{3}\cdot\mathbf{L2})_\infty$ 1590, 1570, 1030 cm^{-1}, thus confirming that **L2** is coordinated to the nickel metal complex. [8]

With regard to FT-IR (4000-600cm^{-1}) of $(\mathbf{4}\cdot\mathbf{L2})_n$ LAG:$CHCl_3$ sample: 3060 vw, 2928 m, 2894 m, 2857 w, 1600 s ν, 1561 m ν, 1444 m, 1405 w, 1294 m, 1252 s,

1178s, 1115 vs, 1026 s, 1006 vs, 828 m, 793 m, 645 s, 622m cm^{-1}. FT-IR bands of conventional sample are (KBr, 4000-400 cm^{-1}): 1598 vs, 1568 w, 1531 vw, 1500 s, 1455 w, 1440 w, 1389 w, 1297 ms, 1259 s, 1216 mw, 1178 mw, 1114 vs, 1064 w, 1029 vs, 949 s, 830 w, 810 mw, 646 s, 628 mw, 545 ms, 521 w, 500 vw, 472 mw, 438 vs, 383 vs, 383 s, 326 vw, 301 w, 287 vw, 235 s, 199 mw, 167 vs, 112 ms, 102 s cm^{-1}. Most of the bands are present in both samples and this is due to the presence of the same functional groups in both of them. However, as observed in the XRPD pattern the resulting structure from the milling experiments are different from the conventional solution base reaction.

SEM images of this set of samples (prepared by solution-based reactions and mechanosynthesis) are reported in figure 5.9. As already observed for the other milled samples investigated in Chapter 4 and for other cases presented in the literature,[13,14] generally the effect of the grinding results in a crystal fracturing and particle size reduction. An example of this general trend is observed for the compound $(\mathbf{1}\cdot\mathbf{L2})_\infty$ prepared by conventional synthesis, NG and LAG mechanosyntesis (Figure 5.9a, b and c respectively). Different morphology are observed and in particular the conventional sample is mainly constituted of well-defined microcrystals. On the other hand NG and LAG samples have similar morphologies, appearing as irregular shaped aggregates of nanocrystals with rough surfaces. The LAG sample shows bigger aggregates in comparison to the NG sample. Probably this is due to the different average crystal size calculated to be 33 nm for the LAG and 24nm for the NG samples. That affects the dimension of the aggregates of nanocrystals resulting bigger for the LAG sample in comparison with the NG sample. The 40 minute $(\mathbf{3}\cdot\mathbf{L2})_\infty$ LAG:$CHCl_3$ milled sample (Figure 5.9g) appears as well-definite crystal shape in comparison with the other milled samples (Figure 5.9 b, c, e, i). It is in agreement with the average crystal size of this sample (76 nm) that is consistent with the biggest crystal size observed in all LAG experiments reported in this thesis.

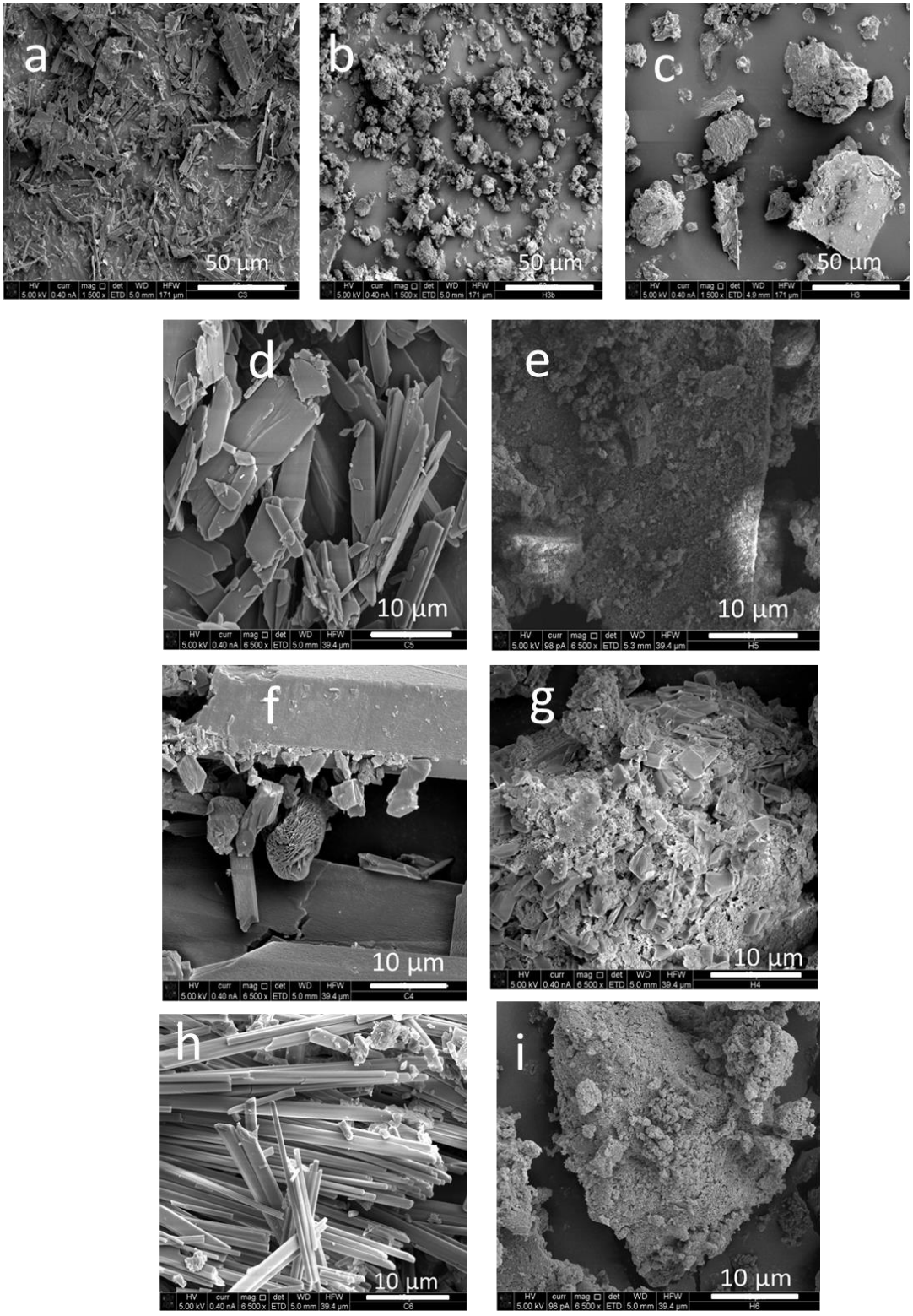

Figure 5.9. SEM images of compounds, $(\mathbf{2{\cdot}L2})_\infty$, $(\mathbf{3{\cdot}L2})_\infty$, $(\mathbf{4{\cdot}L2})_\infty$: (a) $(\mathbf{1{\cdot}L2})_\infty$ from conventional synthesis, (b) $(\mathbf{1{\cdot}L2})_\infty$ NG sample after 20 minutes grinding, (c) $(\mathbf{1{\cdot}L2})_\infty$ LAG sample after 10 minutes grinding, (d) $(\mathbf{2{\cdot}L2})_\infty$ conventional synthesis, (e) $(\mathbf{2{\cdot}L2})_\infty$ LAG sample after 30 minutes grinding, (f) $(\mathbf{3{\cdot}L2})_\infty$ conventional synthesis, (g) $(\mathbf{3{\cdot}L2})_\infty$ LAG:$CHCl_3$ sample after 40 minutes grinding, (h) $(\mathbf{4{\cdot}L2})_\infty$ conventional synthesis and (i) $(\mathbf{4{\cdot}L2})_\infty$ LAG:$CHCl_3$ sample after 40 minutes grinding. Magnifications are reported in the bottom of the micrograph (bar:(a-c)= 50µm or bar:(d-1)= 10µm).

5.3.2 Structure and morphology of *(2·L3)$_\infty$ and (4·L3)$_\infty$*

The mechanochemical study adopting **L3** as semi-rigid bidentate ligand, highlights some analogies and differences with respect to the set of polymers with **L1** and **L2** ligands. We studied two mechanochemical cases reacting **L3** with the dithiophosphate complex (**1)** in the first case, and the dithiophosphonato (**3**) in the second, resulting respectively in **(2·L3)** $_\infty$ and **(4·L3)** $_\infty$ coordination polymers. In both cases the conventional solution-based reaction was carried out adopting 30 mL of MeOH. Therefore, we performed directly LAG experiments using 50 μL of MeOH. In table 5.1 these mechanochemical synthesis are summarized.

Experimental XRPD patterns of **(2·L3)** $_\infty$ obtained by conventional synthesis and by LAG mechanosynthesis taken at selected time intervals are reported (Figure 5.10). After 10 minutes milling the almost complete conversion of reagents into the green colored (**2·L3**)$_\infty$ compound was achieved. However, in the 10 minute milled sample is observed a small peak at 10.81 2ϑ degree due to unreacted **2** (Figure 5.10a)**.** The complete conversion into coordination polymer (**2·L3**)$_\infty$ was gained with the 20 minutes milled sample (Figure 5.10b) which pattern corresponds to that recorded for the experimental coordination polymer obtained by conventional method (Figure 5.10e), with no residual peaks belong to unreacted reagents detectable. Further milling of the powder (30 and 40 minutes) did not change the structure obtained at 20 minutes of grinding showing that the coordination polymer is stable. The average crystal size of 20 minute sample is about 33 nm.

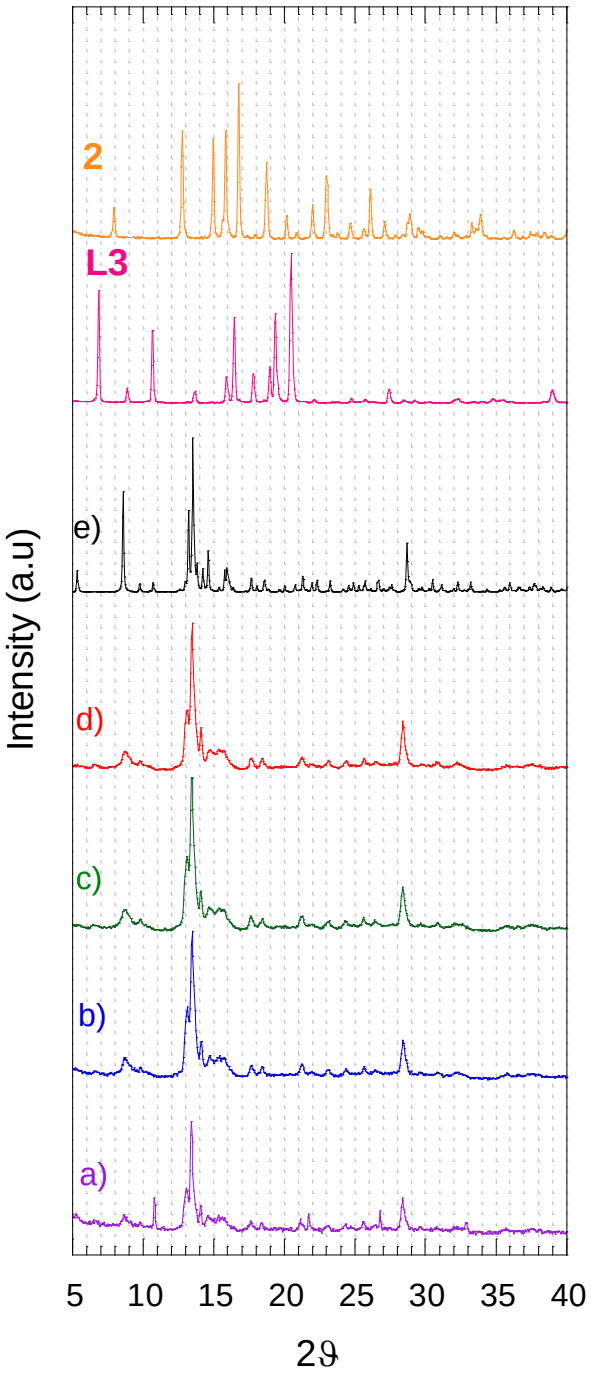

Figure 5.10. XRPD patterns for LAG: MeOH synthesis of $(\mathbf{2}\cdot\mathbf{L3})_{\infty}$: a-d) LAG samples at different milling times, from the bottom a) 10 minutes, b) 20 minutes, c) 30 minutes, d) 40 minutes and e) $(\mathbf{2}\cdot\mathbf{L3})_{\infty}$ conventional synthesis. In the pattern **2** and **L3** are reported to comparison.

In the case of $\mathbf{(4\cdot L3)}_{\infty}$ the XRPD pattern of LAG:MeOH sample suggests the quantitative formation of $\mathbf{(4\cdot L3)}_{\infty}$ within 20 minutes of milling (Figure 5.11a). The XRDP pattern of LAG:MeOH sample after 20 minutes milling corresponds to that recorded for the experimental coordination polymer obtained by conventional

method (Figure 24e), with an average crystal size of 67 nm. The XRPD pattern of the LAG:MeOH 10 minutes sample shows an unidentified and broader peak at 7.91 2ϑ (with small intensity), probably due to an intermediate compound that disappears with the evolving of the reaction. With regard to reactivity under mechanochemical conditions, **L3** and **4** have higher melting points (197°C and 189 °C respectively) in comparison to **L2** and the other metal complexes **1**, **2** and **3**. Therefore, for this compound the templating effect of solvent and not the melting point effect is the predominant effect that may promote the mechanochemical reaction.[11]

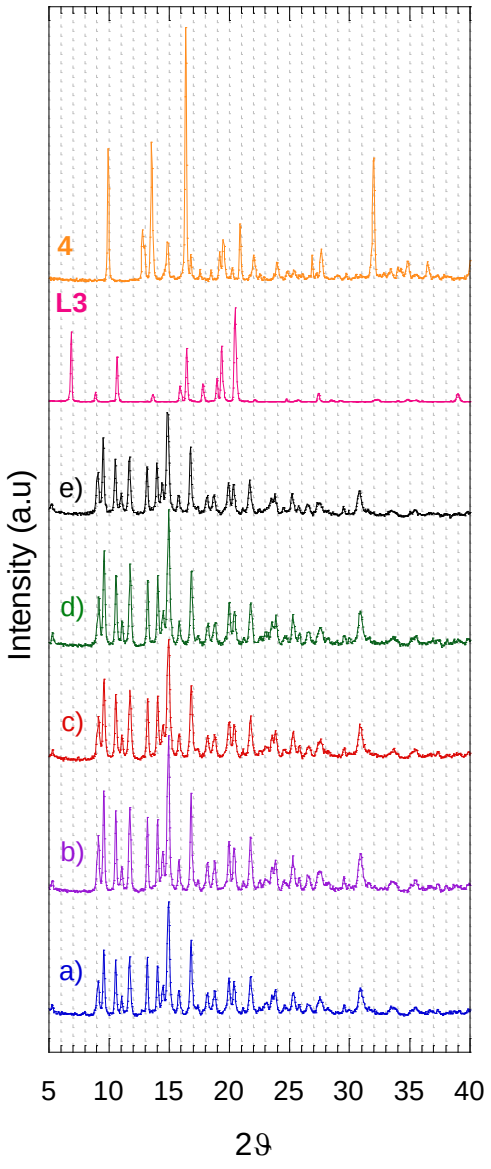

Figure 5.11. XRPD patterns for LAG: MeOH synthesis of $(\mathbf{4}\cdot\mathbf{L3})_\infty$: a-d) LAG samples at different milling times, from the bottom a) 10 minutes, b) 20 minutes, c) 30 minutes, d) 40 minutes and e) $(\mathbf{4}\cdot\mathbf{L3})_\infty$ conventional synthesis. In the pattern **4** and **L3** are reported to comparison.

The appropriate solvent trend observed for **(1·L1)**$_\infty$, **(2·L1)**$_\infty$, **(3·L1)**$_\infty$,**(4·L1)**$_\infty$,**(1·L2)**$_\infty$, **(2·L2)**$_\infty$, **(3·L2)**$_\infty$ can be considered appropriate also for **(2·L3)**$_\infty$ and **(4·L3)**$_\infty$,(where the solvent used to build up the isostructural phase to the solution-based sample is, as expected, methanol in both cases). **L3** is a polypyrdyl ligand as **L1** and **L2**. Therefore, it is possible to find an analogy with the most characteristic FTIR bands of the complexed ligand shifted at higher frequencies in comparison to free ligand as has been observed for **L1** and **L2**. IR spectra of these samples indicate that **L3** is coordinated to metal complex: bands at 1589, 1567 and 989 cm^{-1} in the free **L3**[6] are shifted at 1608, 1569 and 1000 cm^{-1} in the (**2·L3**)$_\infty$ and at 1590, 1567 and 1013 cm^{-1} in the (**4·L3**)$_\infty$ coordination polymers.

In Figure 5.12 SEM micrographs of the compounds based on **L3** are reported. The conventionally prepared (**2·L3**)$_\infty$ sample (Figure 5.12a) shows few regular elongated/acicular not well grown mixture of very tiny microcrystals. The SEM micrograph of the compound (**4·L3**)$_\infty$ prepared by conventional synthesis shows regular elongated and trabecular microcrystals (Figure 5.12c) In both the milled samples (Figure 5.12 b,d) very different morphology is observed with rough surfaces and submicron crystallites.

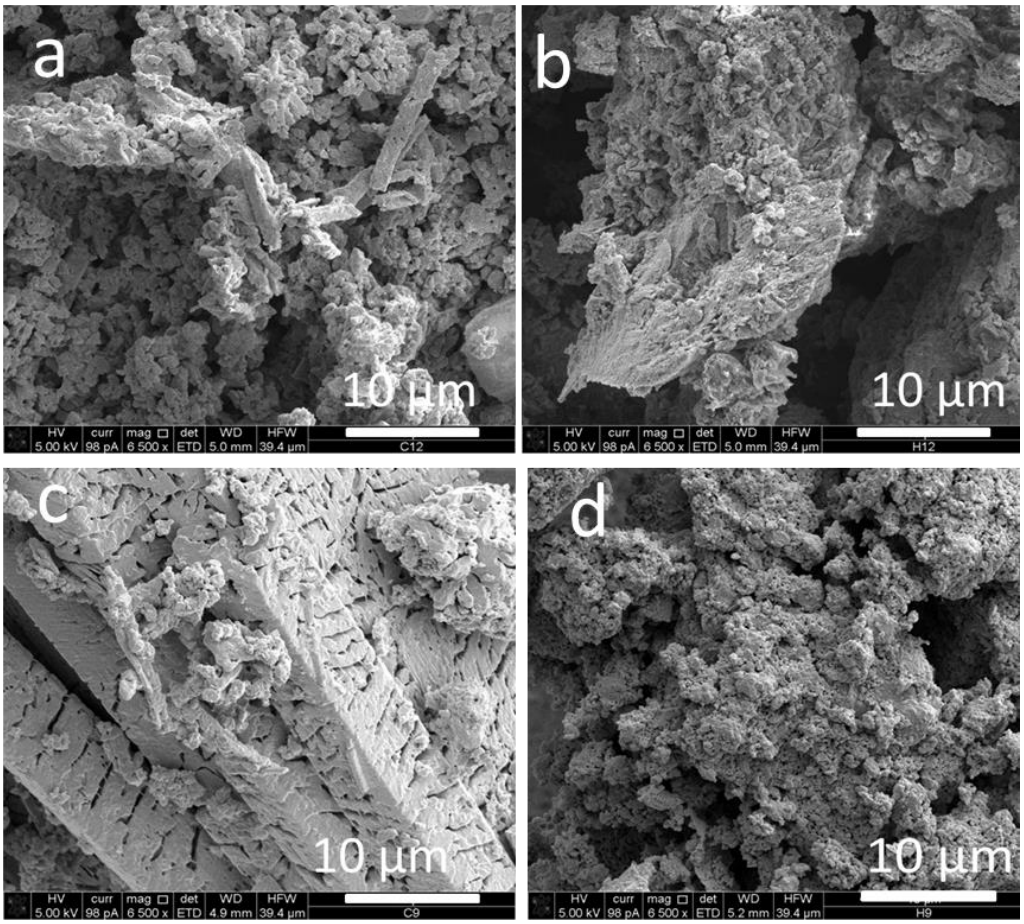

Figure 5.12. SEM images of compounds $(\mathbf{2}\cdot\mathbf{L3})_\infty$ and $(\mathbf{4}\cdot\mathbf{L3})_\infty$: (a) $(\mathbf{2}\cdot\mathbf{L3})_\infty$ from conventional synthesis (b) $(\mathbf{2}\cdot\mathbf{L3})_\infty$ LAG:MeOH sample after 40 minutes grinding, (c) $(\mathbf{4}\cdot\mathbf{L3})_\infty$ from conventional synthesis and (d) $(\mathbf{4}\cdot\mathbf{L3})_\infty$ LAG:MeOH sample after 40 minutes grinding. Magnifications are reported in the bottom of the micrograph (bar= 10µm).

5.3.3 Structure and morphology of $(1\cdot L4)_2$ and $(3\cdot L4)_\infty$

Ligand **L4** is very similar to **L3** excepts for the position of nitrogen atom in the pyridine rings (in position 3 and 4 for **L4** and **L3** respectively). Nevertheless, the use of **L4** as spacer in coordination polymers leads to less predictable final products if compared with the results obtained by using **L3.** It has already been noticed [7] that **L4** can exist either as a transoid or cissoids isomer, and in this last case can show a convergent or a divergent conformation depending on the orientation of N-atoms of the pyridyl rings that can point inwards or outwards with respect to the ligand bite angle. In the conventional synthesis of $(\mathbf{1}\cdot\mathbf{L4})_2$ the pyridyl rings of ligand **L4** are oriented in a convergent fashion leading to closed rings rather than polymeric chains.[7] In dimer $(\mathbf{1}\cdot\mathbf{L4})_2$ two **L4** spacers bridge two

dithiophosphato nickel complexes with openings of about 8 × 8 $Å^2$. On the contrary, adopting (**4**) as unsatured Ni^{II} complex the conventional synthesis leads to the **(3·L4)**$_\infty$ polymer structure with a divergent orientation of **L4** ligands.[7] With the aim to investigate the mechanochemical favorite structure, we reported two products reacting **L4** with the dithiophosphate complex (**1)** in the first case, and with the dithiophosphonato (**3**) in the second. For these samples we did not investigate the solvents trend (in LAG synthesis) because more interested in using the same solvents of conventional solution-based reactions with the aim to investigate the favorite structure. Therefore, the mechanosynthesis of **(1·L4)$_2$** and **(3·L4)**$_\infty$ were performed in dichloromethane and chloroform respectively.

In figure 5.13 XRPD patterns for the **(1·L4)$_2$** LAG:CH_2Cl_2 mechanosynthesis are reported indicating a close correspondence between the mechanochemical sample after only 10 minutes in comparison with the conventionally prepared sample. The mechanochemical reaction lead to the close ring structure such as the conventional synthesis (Figure 5.4b) suggesting that in both synthesis the convergent coordination is preferred, probably due to the small size of the substituents to the phosphorous atoms in Ni^{II} complex **1**. Further milling of the powder did not change the structure obtained at 10 minutes of grinding, the XRPD peaks for the LAG samples are in the same position as the conventionally prepared sample, but the intensity and width, and therefore size and strain, are different. The average crystal size of the milled sample, calculated by Scherrer equation, corresponds to 70 nm. With regard to reactivity under mechanochemical conditions the **L4** ligand and the metal complex **1** have a melting point of 137°C and 95°C respectively (Table 5.2). The general inverse correlation between melting point and reactivity can explain the quick formation of the dimers of **(1·L4)$_2$** after only 10 minutes of mechanochemical treatments.[11]

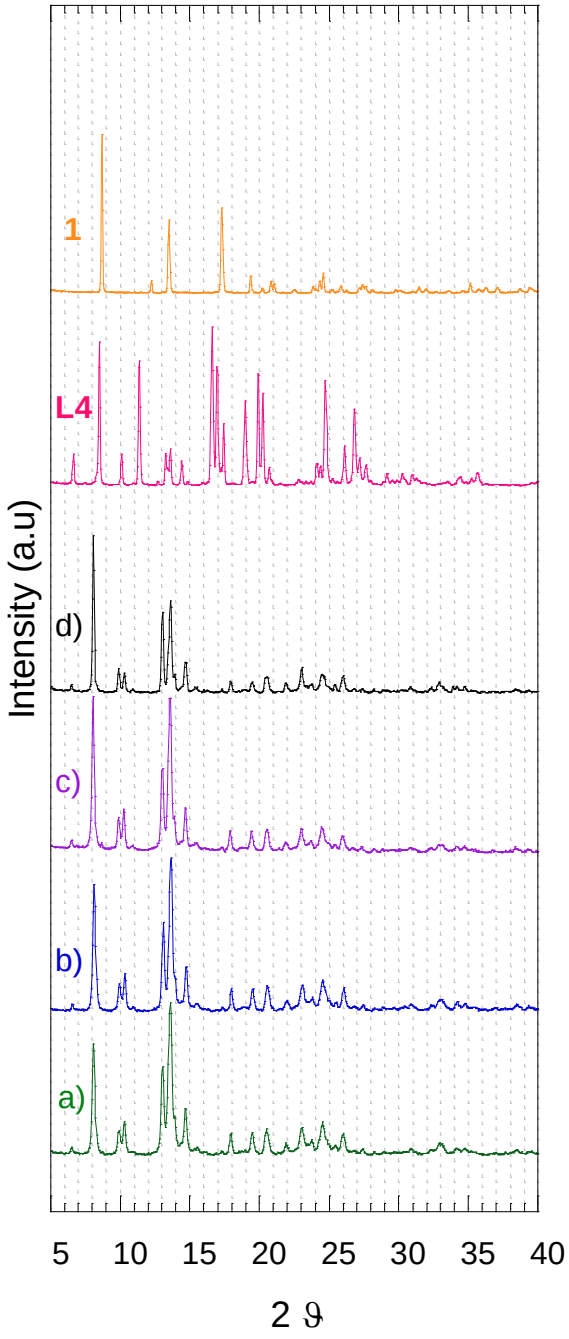

Figure 5.13. XRPD patterns for LAG: CH_2Cl_2 synthesis of (**1**·**L4**)$_2$: a-c) LAG:CH_2Cl_2 samples at different milling times, from the bottom a) 10 minutes, b) 20 minutes, c) 30 minutes and d) (**1**·**L4**)$_2$ conventional synthesis. In the pattern **1** and **L4** are reported to comparison.

With regard to (**3**·**L4**)$_\infty$ the XRPD pattern for the 20 minute LAG:$CHCl_3$ sample as shown in Figure 5.14a, reports peaks at 6.89 and 17.86 2ϑ due to unreacted **3**. These peaks disappear in the further milling time samples, this is due to the complete conversion of reagents into the (**3**·**L4**)$_\infty$ compound which corresponds to that recorded for the coordination polymer obtained by conventional method

(Figure 5.14d), with no residual peaks due to unreacted reagents detectable. Adopting mechanochemical conditions the ball milling reaction led to the isostructural compound resulting from the conventional synthesis. The coordination polymer packs in parallel chains with a divergent orientation of **L4** probably due to the bigger size of the substituents to the phosphorous atoms in Ni^{II} complex **3** in comparison to that of **1**.[6] The average crystal size of the milled sample, calculated by Scherrer equation, corresponds to 40nm.

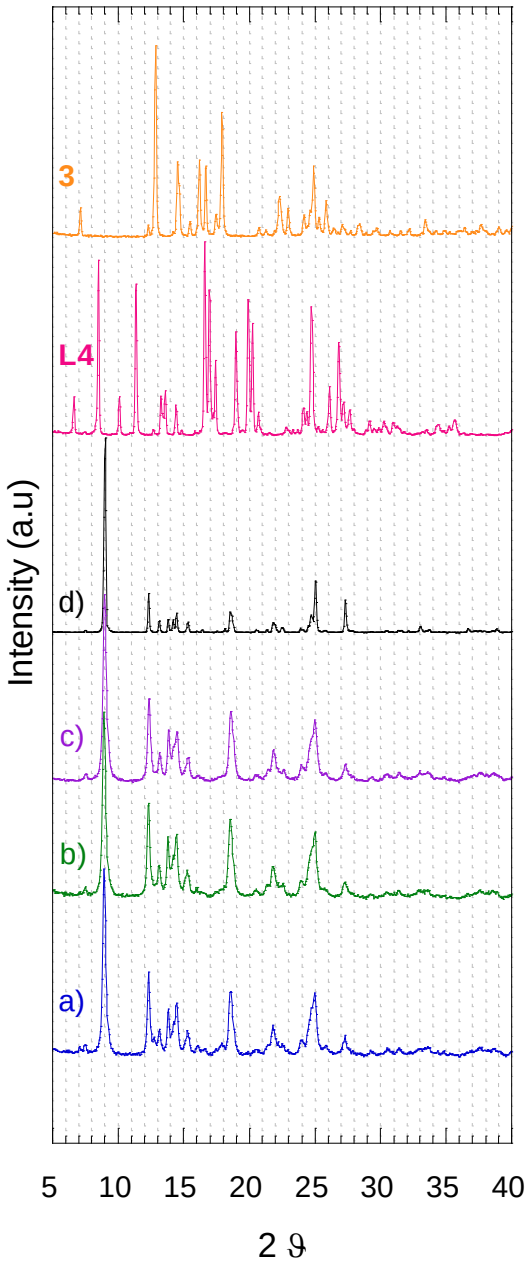

Figure 5.14. XRPD patterns for LAG: $CHCl_3$ synthesis of $(\mathbf{3}\cdot\mathbf{L4})_\infty$: a-c) LAG:$CHCl_3$ samples at different milling times, from the bottom a) 20 minutes, b) 30 minutes, c) 40 minutes and d) $(\mathbf{3}\cdot\mathbf{L4})_\infty$ conventional synthesis. In the pattern **3** and **L4** are reported to comparison.

L4 is a polypyrdyl ligand as **L1, L2** and **L3** therefore it is possible to find an analogy with the most characteristic IR bands of the ligand complexed shifted at higher frequencies in comparison to free ligand as has been observed for **L1**, **L2** and **L3**. IR spectra of samples indicate that **L4** is coordinated to metal complex: bands at 1598, 1567 and 107 cm^{-1} in the free **L4**[6] are shifted at 1601, 1580 and 1014 cm^{-1} in the $(\mathbf{1}\cdot\mathbf{L4})_2$ and at 1601, 1570 and 1016 cm^{-1} in the $(\mathbf{3}\cdot\mathbf{L4})_\infty$ compounds respectively.

SEM micrographs (Figure 5.15) of the compounds $(\mathbf{1}\cdot\mathbf{L4})_2$ and $(\mathbf{3}\cdot\mathbf{L4})_\infty$ prepared by conventional synthesis highlight a well-defined morphology as already observed in samples prepared by solvent-based reaction while milled samples (also obtained with LAG mechanosynthesis: 50 μL) show aggregates of nanocrystals with rough surfaces.

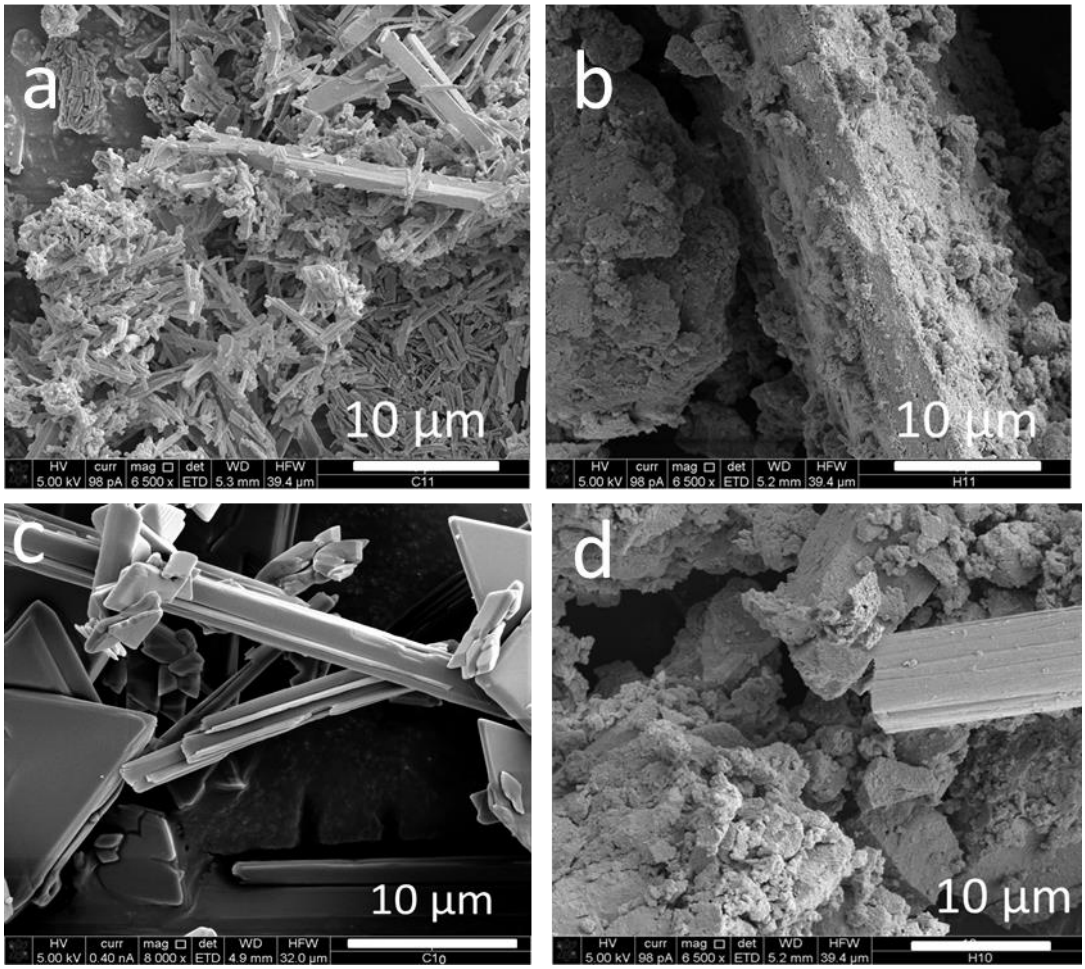

Figure 5.15. SEM images of compound $(\mathbf{1}\cdot\mathbf{L4})_2$ and $(\mathbf{3}\cdot\mathbf{L4})_\infty$: (a) $(\mathbf{1}\cdot\mathbf{L4})_2$ from conventional synthesis, (b) $(\mathbf{1}\cdot\mathbf{L4})_2$ LAG:CH_2Cl_2 sample after 10 minutes grinding, (c). $(\mathbf{3}\cdot\mathbf{L4})_\infty$ from conventional synthesis and (d) $(\mathbf{3}\cdot\mathbf{L4})_\infty$ LAG:$CHCl_3$ sample after 40 minutes grinding. Magnifications are reported in the bottom of the micrograph (bar= 10μm).

5.3.4 Thermal stability of (1·L2)$_\infty$, (2·L2)$_\infty$, (3·L2)$_\infty$, (4·L2)$_\infty$, (2·L3)$_\infty$, (4·L3)$_\infty$, (1·L4)$_\infty$, (3·L4)$_\infty$

The thermal behavior of the eight milled samples was investigated by Thermogravimetry and Differential Scanning Calorimetry techniques and for comparison the same measurements were performed on the conventional samples A similar thermal behavior was observed for each sample. For instance, for (**1**·**L2**)$_\infty$ conventional sample, TG and the corresponding derivative dTG curve (figure 5.16a left) show two main mass loss (and dTG peaks) in the temperature range of : (i) 182-448°C, (ii) 834-900°C. The weight loss of about 33 wt% observed in the first range is related to the thermal decomposition of the organic parts of (**1**·**L2**)$_\infty$ and reflect the mass loss of **L2**. In the range 448-834°C a gradual lost and no a plateau as the analogous (**1**·**L1**)$_\infty$ coordination polymer studied in chapter 4 is observed. This gradual lost is about 10 wt% which is consistent with the loss of CH_3CH_2 groups and with the presence of bis(dithio-metaphosphato) nickel(II) [$Ni(S_2PO)_2$] (mass remaining 55 wt %). As confirmed by XRPD pattern (data not shown) the latter at temperature higher than 834°C decomposes into nickel fosfate $Ni_2P_2O_7$ (mass remaining about 22 wt %).

DSC thermograms of (**1**·**L2**)$_\infty$ samples along with those of **L2** and **1** reagents are reported in figure 5.16 (right side). The conventional sample shows an irreversible net exothermic peak centered at 199°C due to decomposition of (**1**·**L2**)$_\infty$ in agreement with the TG analysis. No peaks are observed in the DSC curve at temperatures lower indicating that the polymer (**1**·**L2**)$_\infty$ is stable up to this temperature.

The (**1**·**L2**)$_\infty$ NG (Figure 5.16b, left) and LAG (Figure 5.16c, left) mechanochemical samples show similar thermal behaviors in comparison with the conventionally prepared sample. TG thermograms show the main two range of mass loss (i) in the range 182-448°C, (ii) and 834-900°C and the formation of the same degradation compounds of conventional sample. The corresponding DSC exothermic peaks are in agreement with the conventionally prepared sample. A slightly difference is consistent with the shift from 199 to 189 °C of the exothermic peak in the milled samples. This is due to the smaller features of the

nanocrystals of the milled sample (33 nm and 24 nm for LAG and NG samples respectively) in comparison with the conventionally obtained microcrystalline $(\mathbf{1}\cdot\mathbf{L2})_{\infty}$ sample. The DSC thermogram of NG sample with the 2:1 (**L2**/**1**) molar ratio is reported in Figure 5.16 (right). The endothermic peak at 153 °C is related to the fusion of **L2** indicating**,** the excess of unreacted reagent in agreement with XRPD pattern.

The other samples exhibit very similar thermal behavior with differences in the TG and DSC temperatures. Generally the first mass loss is consistent with the decomposition of the organic part of the molecule and the product at high temperature after complete decomposition is nickel fosfate $Ni_2P_2O_7$. The calculation of TG mass loss for $(\mathbf{2}\cdot\mathbf{L2})_{\infty}$, $(\mathbf{3}\cdot\mathbf{L2})_{\infty}$, $(\mathbf{4}\cdot\mathbf{L2})_{\infty}$, $(\mathbf{2}\cdot\mathbf{L3})_{\infty}$, $(\mathbf{4}\cdot\mathbf{L3})_{\infty}$, $(\mathbf{1}\cdot\mathbf{L4})_{\infty}$, $(\mathbf{3}\cdot\mathbf{L4})_{\infty}$ samples and DSC termograms are reported in the section 5.6 (5.22, 5.23, 5.24, 5.25, 5.26, 5.27, 5.28).

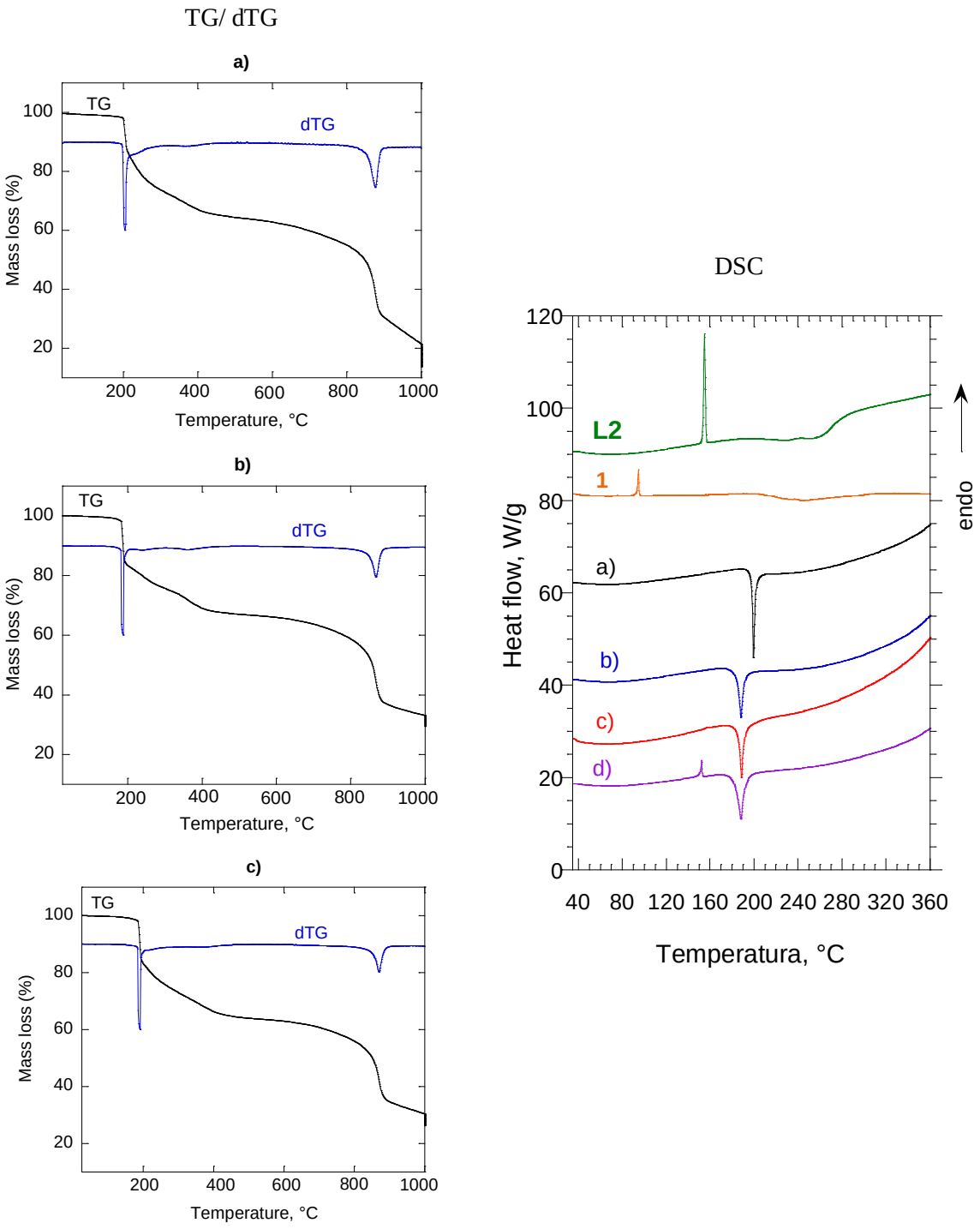

Figure 5.16. TG and dTG curves (left side) and DSC (right side) of compound $(\mathbf{1}\cdot\mathbf{L2})_{\infty}$ obtained with a) conventional, b) NG and c) LAG methods. In DSC plots, **L2**, **1** d) NG performed in the 2:1 (**L2**:**1**) molar ratio thermograms were also reported for comparison.

5.4 Conclusions

This survey of reactions between Ni^{II} metal complexes (**1**), (**2**), (**3**), (**4**) with different bipyridyl-based spacers (**L2**), (**L3**) and (**L4**) under mechanochemical conditions shows several advantages compared to traditional solution-based synthesis. Quantitative reactions occur under these conditions to give the desired polycrystalline product within minutes (less than one hour compared to several hours of conventional synthesis), in absence of liquid phase or using minimal amounts of solvent. The mechanochemical protocol developed in chapter 4 has also been applied here with significant benefits compared to solution-based protocols confirming the 'green' nature of this methodology. A variety of six coordination polymers $(\mathbf{1}\cdot\mathbf{L2})_\infty$, $(\mathbf{2}\cdot\mathbf{L2})_\infty$, $(\mathbf{3}\cdot\mathbf{L2})_\infty$, $(\mathbf{2}\cdot\mathbf{L3})_\infty$, $(\mathbf{4}\cdot\mathbf{L3})_\infty$, $(\mathbf{3}\cdot\mathbf{L4})_\infty$, one dimer $(\mathbf{1}\cdot\mathbf{L4})_2$ and an unknown phase $(\mathbf{4}\cdot\mathbf{L2})_n$ have been studied. We demonstrated that different conditions, and especially the solvent used in LAG synthesis, can lead to different phases. In several NG and LAG mechanosynthesis a mixture of phases rather than the desired one is obtained. The use of a specific solvent or a suitable mixture of solvents can result in the desired product with a yield equal to 100%. A trend of suitable solvent (ethanol, methanol, chloroform for **1**, **2**, **3** respectively) in relation with the adopted Ni^{II} metal complexes can be observed for $(\mathbf{1}\cdot\mathbf{L2})_\infty$, $(\mathbf{2}\cdot\mathbf{L2})_\infty$, $(\mathbf{3}\cdot\mathbf{L2})_\infty$, $(\mathbf{2}\cdot\mathbf{L3})_\infty$,$(\mathbf{3}\cdot\mathbf{L4})_\infty$ samples. Moreover, another mechanochemical trend concerning the general inverse correlation between melting point of reagents and reactivity has been observed according to literature data.[11] As already mentioned, we obtained for $(\mathbf{1}\cdot\mathbf{L4})_2$ a dimeric structure according to the structure obtained in solution-based reaction. With regard to $(\mathbf{4}\cdot\mathbf{L2})_n$, several NG and LAG synthesis were performed without obtaining the desired coordination polymer. An important issue regarding mechanochemistry is the possibility to obtain products not formed using conventional solvent-based crystallization and this is one of this case.[11] Further studies would be interesting to be developed concerning, for example, the better understanding of mechanism of reactions under mechanical conditions. The interest of this survey about coordination polymers based on dithiophosphato and dithiophospnonato complexes, regards the field of crystal engineering but further research will be applied concern the identification of other application fields.

5.5 General Remarks on all Mechanochemical Synthesis

Table 5.3 Schematic representation of the mechanosynthesis reported in Chapter 4 and Chapter 5. (Symbols: **√** for milled samples isostructurals with the crystallographic data, **√/~** for mechanochemical reactions occurred but with XRPD peaks profiles very broad, **×** for mechanochemical reactions for which a different structure is observed, - these synthesis are not performed).

	1				**2**			**3**			**4**			
	EtOH	*$CHCl_3$*	*NG*	*CH_2Cl_2*	*MeOH*	*$CHCl_3$*	*NG*	*EtOH*	*$CHCl_3$*	*NG*	*MeOH*	*$CHCl_3$*	*MeOH/ $CHCl_3$*	*NG*
L1	√	-	√	-	√	×	√	×	√	×	√/~	√/~	√	×
L2	√	-	√	-	√	×	×	×	√	×	×	×	×	×
L3	-	-	-	-	√	-	-	-	-	-	√	-	-	-
L4	-	-	-	√	-	-	-	-	√	-	-	-	-	-

In table 5.3 are schematically summarized all the mechanosynthesis performed using dithiophostato and dithiophosponato unsatured square planar Ni ^{II} complexes (**1**), (**2**), (**3**), (**4**) and ligands (**L1**), (**L2**), (**L3**), (**L4**). The reactions discussed in chapter 4 are also reported. Mechanochemichal synthesis for which the XRPD patter of milled samples are corresponding to the specific product (in particular to the simulated data results from conventionally prepared samples), are designated with the symbol **√.** The symbol **√/~** is adopted for mechanochemical reactions occurred but with XRPD peaks profiles very broad. For reactions in which a different structure has been obtained, the symbol **×** is adopted, and the mechanochemichal reactions indicated with - are not performed in this PhD thesis. In view of this table we can conclude that Pichon observations on the correlation between the melting point of ligands and the positive course of the synthesis were generally confirmed. However, some Ni^{II} complexes have similar or lower melting points than ligands (Table 5.2). In fact we observed that the correlation promote by Pichon should be extended to the unsatured square planar Ni ^{II} complexes studied in this PhD thesis. The higher the melting point of Ni^{II} complex the lower the mecanochemical reactivity of this reaction is. For instance, it has been highlighted that the mechanochemical reactivity between **1** and **L1** is

the highest compare to the other combinations of metal complexes and ligands. In the case study of $(\mathbf{1}\cdot\mathbf{L1})_{\infty}$, having **1** and **L1** the lowest melting points in comparison with the other used complexes and ligands, both the mechanochemical approaches NG and LAG have given rise to the desired product within different milling time depending on the mechanochemical method. On the contrary, for **3** and **4** complexes, having higher melting points than **1** and **2**, only LAG synthesis (and in some cases adopting a mixture of solvents) have led to the isostructural product of the conventionally synthesized. Nervertheless, based on these criteria the sample $(\mathbf{4}\cdot\mathbf{L2})_{n}$ does not respect this trend. We assume that on this case the absence of the templating effect of the solvent could/should have had a predominant role.

We suggest further investigation on this research topic. However, this PhD thesis can constitute an advance in the area of the crystal engineering field and in particular in the synthesis of the coordination polymer by no conventional /alternative synthetic methods. The mechanochemical synthesis of this particular type of coordination polymers using neutral pre-formed building blocks (dithiophospato and dithiophosponato Ni^{II}) may be suggest a fast and green synthetic process easy to be scaled up.

5.6 Compounds Characterization

In Figure 5.17 experimental XRPD pattern of **(1·L2)** $_\infty$ samples obtained by conventional synthesis and by NG mechanosynthesis taken at selected time intervals are reported. After 20 minutes of milling the almost complete conversion of reagents into the green colored $(\mathbf{1}\cdot\mathbf{L2})_\infty$ compound was achieved. However, small peaks at 8.60, 13.51, 17.30, 19.19 2ϑ degree due to unreacted **1** are observed in 5 minutes and 10 minutes NG samples. Trace amounts still remain at 20 minutes (Figure 5.17 a,b,c). which pattern corresponds to that recorded for the experimental coordination polymer obtained by conventional method (Figure 5.17 f) , with no detectable residual peaks belong to unreacted reagents. Therefore, at 30 minutes of milling the synthesis can be considered concluded.

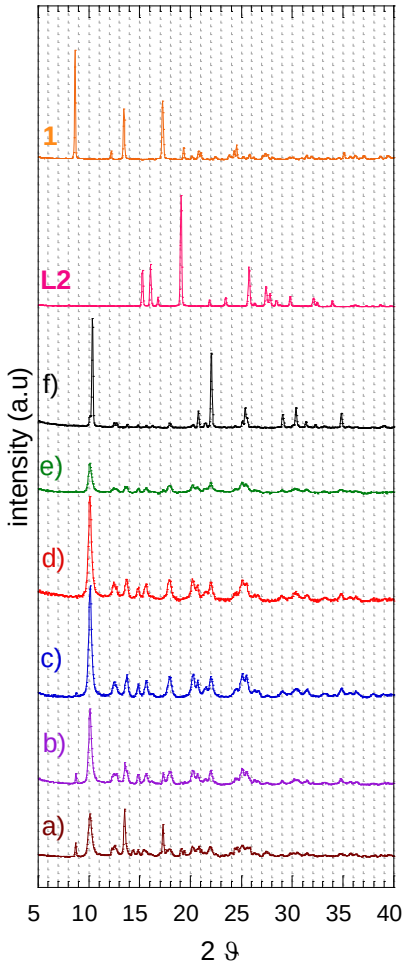

Figure 5.17 XRPD patterns for NG synthesis of $(\mathbf{1}\cdot\mathbf{L2})_\infty$: a-e) NG samples at different milling times, from the bottom a) 5 minutes, b) 10 minutes, c) 20 minutes, d) 30 minutes, e) 45 minutes samples respectively, f) $(\mathbf{1}\cdot\mathbf{L2})_\infty$ conventional synthesis. In the pattern **1** and **L2** are reported to comparison.

In Figure 5.18 experimental XRPD patterns of the **(1·L2)**$_\infty$ sample obtained by LAG mechanosynthesis and taken at selected time intervals are reported. The LAG synthesis was performed adding to the starting powder reagents 50 μL of ethanol, normally used as solvent in the conventional synthesis. The 5 minute (**1·L2**)$_\infty$ milled sample is reported and Bragg peaks (8.60, 13.51, 17.30, 19.19 2ϑ degree) belonging to unreacted **1** are observed. At higher grinding times, 30 and 40 minutes (Figure 5.18 c and d respectively), a small peak due to a new unidentified phase is evident at 22.97 2ϑ degree.

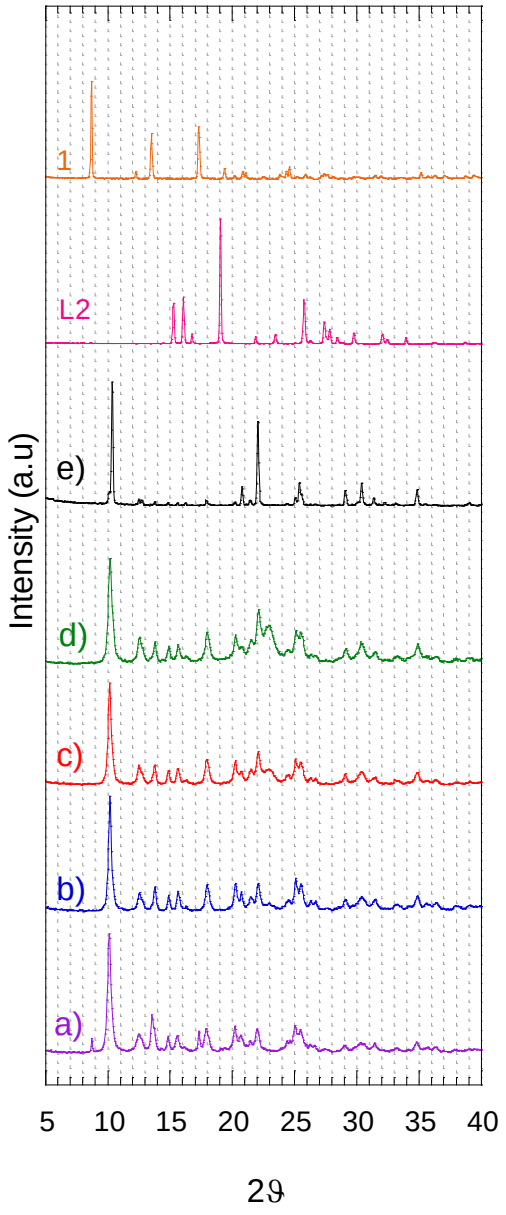

Figure 5.18. XRPD patterns for LAG synthesis of (**1·L2**)$_\infty$: a-d) LAG samples at different milling times, from the bottom a) 5 minutes, b) 10 minutes, c) 20 minutes and d) 30 minutes samples respectively, e) (**1·L2**)$_\infty$ conventional synthesis. In the pattern **1** and **L2** are reported to comparison.

In Figure 5.19 experimental XRPD patterns of **(2·L2)**$_\infty$ obtained by conventional synthesis and by LAG:MeOH mechanosynthesis taken at selected time intervals are reported. After only 10 minutes of milling the complete formation of the **(2·L2)**$_\infty$ structure is observed, with peaks in the XRPD pattern (Figure 5.19 a) placed in the same position observed for the conventionally prepared sample (Figure 5.19d). Further milling time did not change the structure of the products and therefore at 10 minutes of milling the synthesis can be considered concluded. Probably, milling the powder for 30 minutes can result in a well-defined and sharpest peaks shape as observed for the peak at 11.90° 2ϑ which has a better defined shape in the 30 minute milling sample compared with 10 and 20 minute samples. The average crystal size of the 30 minute LAG:MeOH sample, calculated by Scherrer equation, corresponds to 60nm.

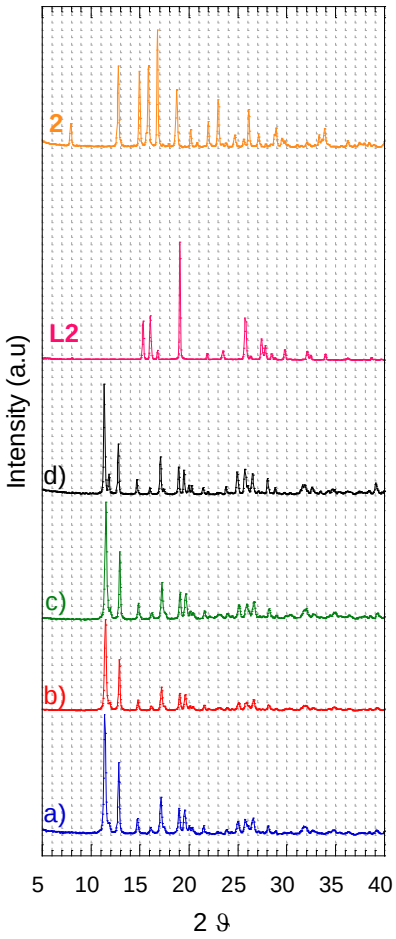

Figure 5.19. XRPD patterns for LAG: MeOH synthesis of **(2·L2)**$_\infty$: a-c) LAG samples at different milling times, from the bottom a) 10 minutes, b) 20 minutes, c) 30 minutes, d) **(2·L2)**$_\infty$ conventional synthesis. In the pattern **2** and **L2** are reported to comparison.

Experimental XRPD patterns of **(3·L2)**$_\infty$ samples conventionally synthesized and obtained by LAG:$CHCl_3$ mechanosynthesis at selected time intervals are reported (Figure 5.20). The XRPD patterns of LAG samples at 10, 20 and 30 minutes (Figure 5.20a-c) displace small peaks at 7.08, 12.84, 14.60, 17.84 2ϑ degree due to unreacted **3**. Some trace amounts of **3** still remain at 40 minutes.

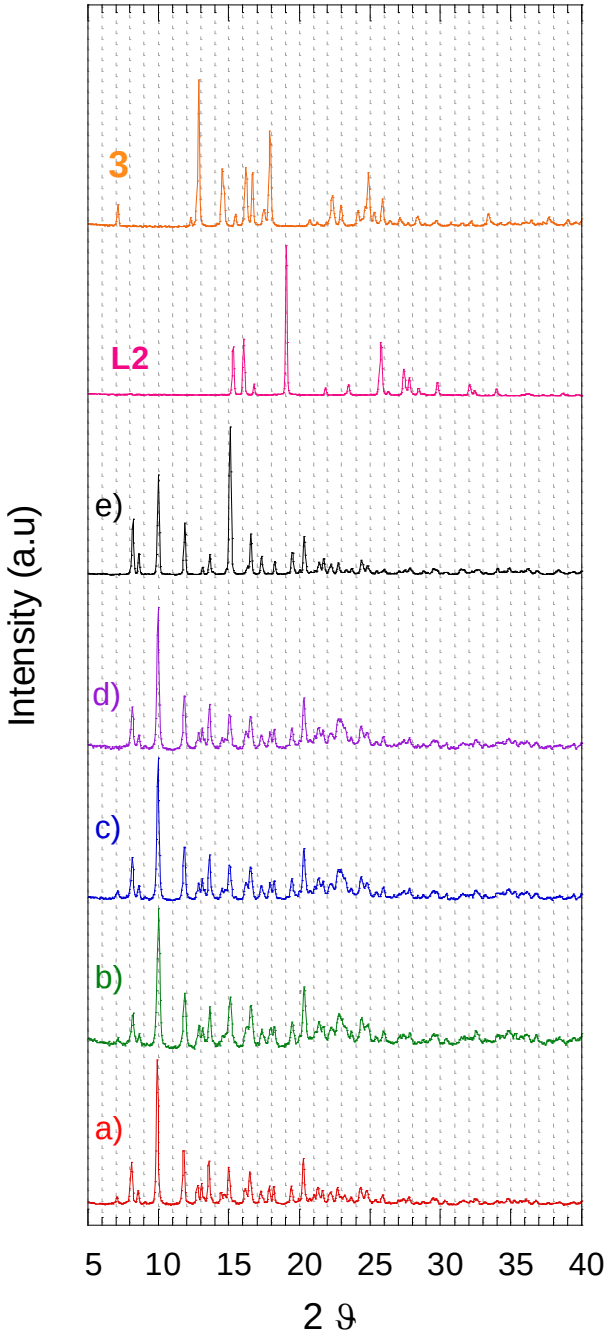

Figure 5.20. XRPD patterns for LAG: $CHCl_3$ synthesis of (**3·L2**)$_\infty$: a-d) LAG samples at different milling times, from the bottom a) 10 minutes, b) 20 minutes, c) 30 minutes, d) 40 minutes, e) (**2·L2**)$_\infty$ conventional synthesis. In the pattern **2** and **L2** are reported to comparison.

Experimental XRPD patterns of **(4·L2)**$_\infty$ samples adopting LAG:MEOH/$CHCl_3$ mechanosynthesis at selected time intervals are reported (Figure 5.21).

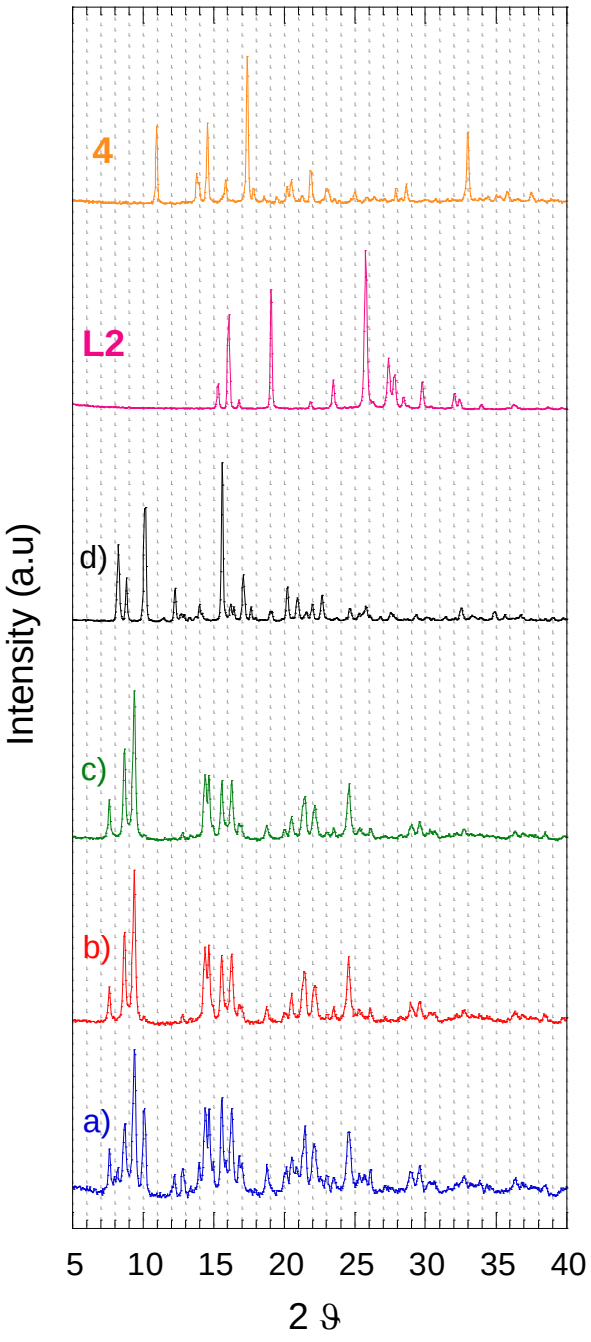

Figure 5.21. XRPD patterns for LAG: $CHCl_3$/MeOH synthesis of (**4·L2**)$_\infty$: a-c) LAG samples at different milling times, from the bottom a) 10 minutes, b) 20 minutes, c) 30 minutes, d) (**4·L2**)$_\infty$ conventional synthesis. XRPD pattern of **4** and **L2** are reported to comparison.

Figure 5.22 shows the thermal behavior investigated by Thermogravimetry and Differential Scanning Calorimetry techniques of coordination polymer (**2·L2**)$_\infty$. The thermogravimetric (TG) curves and the corresponding dTG for

conventionally prepared sample and for LAG sample are reported (Figure 5.22a-b left). For the sample prepared by conventional synthesis TG and the corresponding derivative dTG curve (Figure 5.22a left) show two main mass loss (and dTG peaks) in the temperature range of: (i) 166-339 °C, (ii) 794-945°C. The weight loss of about 35 wt % observed in the first range is related to the thermal decomposition of the organic parts of $(\mathbf{1}\cdot\mathbf{L2})_\infty$ and reflect the mass loss of **L2**. In the range 339-794°C a gradual lost is observed. It is consistent with the presence of bis(dithio-metaphosphato) nickel(II) $[Ni(S_2PO)_2]$. At higher temperature the decomposition into nickel fosfate $Ni_2P_2O_7$ (mass remaining about 28 wt %) is provided, as confirmed by XRPD pattern (data not shown).

DSC thermograms of $(\mathbf{2}\cdot\mathbf{L2})_\infty$ samples and reagents **L2** and **2** are reported (Figure 5.22 right side). In analogy with the previously characterized coordination polymer $(\mathbf{1}\cdot\mathbf{L2})_\infty$, the $(\mathbf{2}\cdot\mathbf{L2})_\infty$ conventional sample shows the characteristic exothermic peak due to $(\mathbf{2}\cdot\mathbf{L2})_\infty$ decomposition. However, it is possible to observed a spit in the exothermic peak (centered at 180°C and at 194°C respectively). This is in agreement with the first peak of the dTG that is splitted as well, and it is centered at the same values of temperature. No peaks are observed in the DSC curve at temperatures lower indicating that the polymer $(\mathbf{2}\cdot\mathbf{L2})_\infty$ is stable up to this temperature.

TG curve of $(\mathbf{2}\cdot\mathbf{L2})_\infty$ LAG sample (Figure 5.22b, left) shows similar thermal behavior in comparison with the conventionally prepared sample. TG thermogram shows the main two range of mass loss ((i) in the range 164-338°C, (ii) and 770-945°C), and the formation of the same degradation compounds of conventional sample. The DSC thermogram of $(\mathbf{2}\cdot\mathbf{L2})_\infty$ LAG sample shows a broader exothermic peak at 190°C instead of the splitted peak of the conventional sample in agreement with the TG (dTG) (Figure 5.22b left).

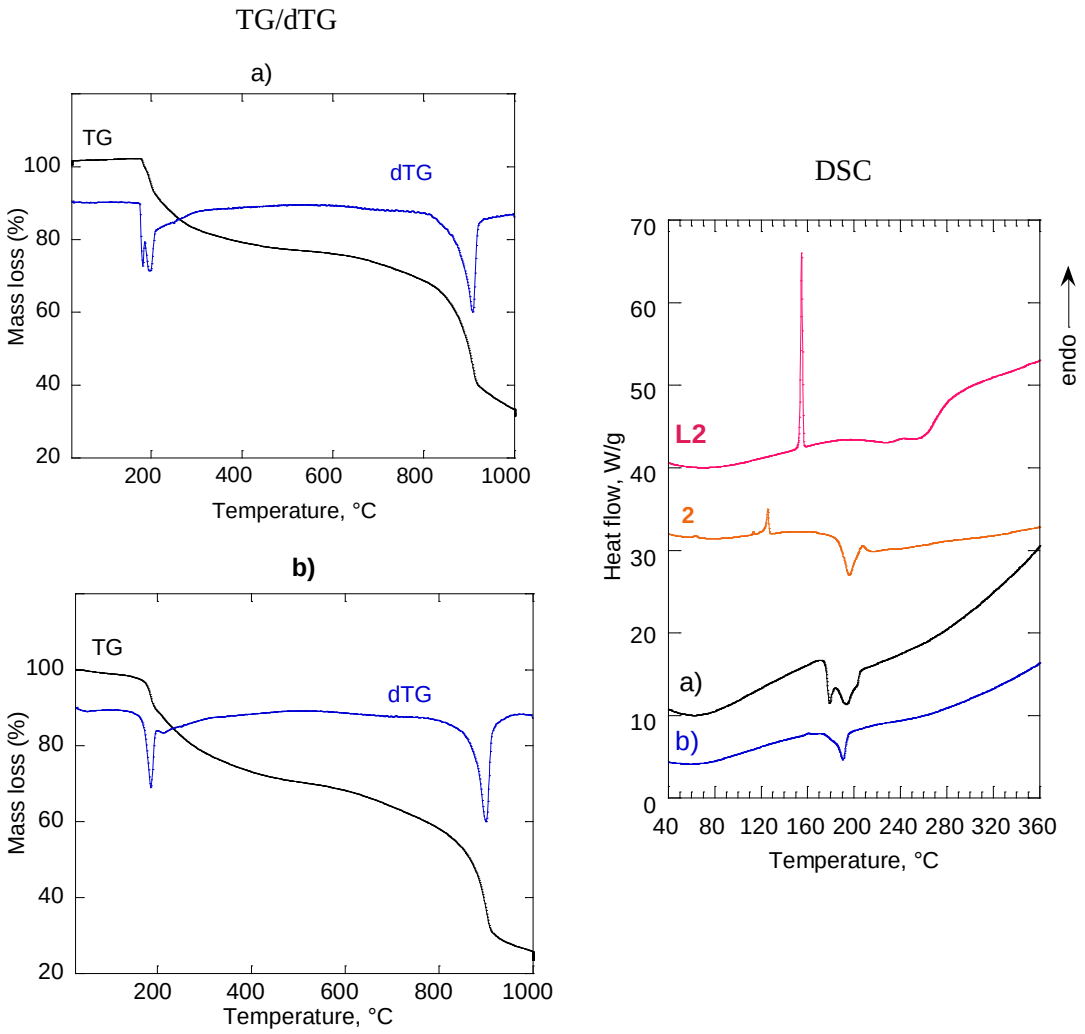

Figure 5.22. TG and dTG curves (left side) and DSC (right side) of compound (**2**·**L2**)$_\infty$ obtained with a) conventional and b) LAG methods. In DSC plots, **L2** and **2** thermograms were also reported for comparison.

TG and corresponding dTG curve of conventionally prepared sample (**3**·**L2**)$_\infty$ (Figure 5.23a, left side) shows five mass loss (and peaks in dTG). In the range of temperature 148-533°C, four mass losses centered in dTG at 195°C, 240°C, 292°C and 396 °C are observed, while the fifth is in the range 770-924°C. The first four steps of TG curve reflect thermal decomposition of the organic parts of (**3**·**L2**)$_\infty$ polymer (mass loss of 48%). It corresponds with the loss of **L2** and the organic part bonded to the P atoms of Ni^{II} complex **3**. The mass remaining (53%) before the fifth step (770°C) appears consistent with the presence of bis(dithio-metaphosphato) nickel(II) [$Ni(S_2PO)_2$]. As expected, the residue product after 924°C, was found to be nickel fosfate $Ni_2P_2O_7$.

DSC curve of conventionally prepared $(\mathbf{3}\cdot\mathbf{L2})_\infty$ sample, along with those of LAG: $CHCl_3$ 40 minute sample and reagents (**L2**, **3)** are reported (Figure 5.23, right side). In agreement with the TG analysis, the DSC curve of the conventional sample shows an irreversible exothermic peak at 197°C due to decomposition of $(\mathbf{3}\cdot\mathbf{L2})_\infty$. Therefore, the polymer $(\mathbf{3}\cdot\mathbf{L2})_\infty$ is stable up to this temperature.

The 40 minute $(\mathbf{3}\cdot\mathbf{L2})_\infty$ LAG:$CHCl_3$ sample presents similar thermal behavior in comparison with the sample conventionally prepared, with formation of the same degradation compounds. Slight differences are observed in the TG thermogram in the range of temperature 148-533°C where the four mass loss are centered in dTG curves at slightly lower temperatures: 182°C, 220°C, 290°C and 394 °C in comparison to that of conventional one (195°C, 240°C, 292°C and 396 °C) . The corresponding DSC exothermic peaks are in agreement, with a shift of temperature from 197 to 188 °C. Moreover, the DSC peak due to polymer decomposition is broader than that recorded for the conventional sample, which is consistent with smaller and/or more disordered $(\mathbf{3}\cdot\mathbf{L2})_\infty$ particles in the milled sample (76 nm instead of >100nm of the conventional sample).

TG/dTG

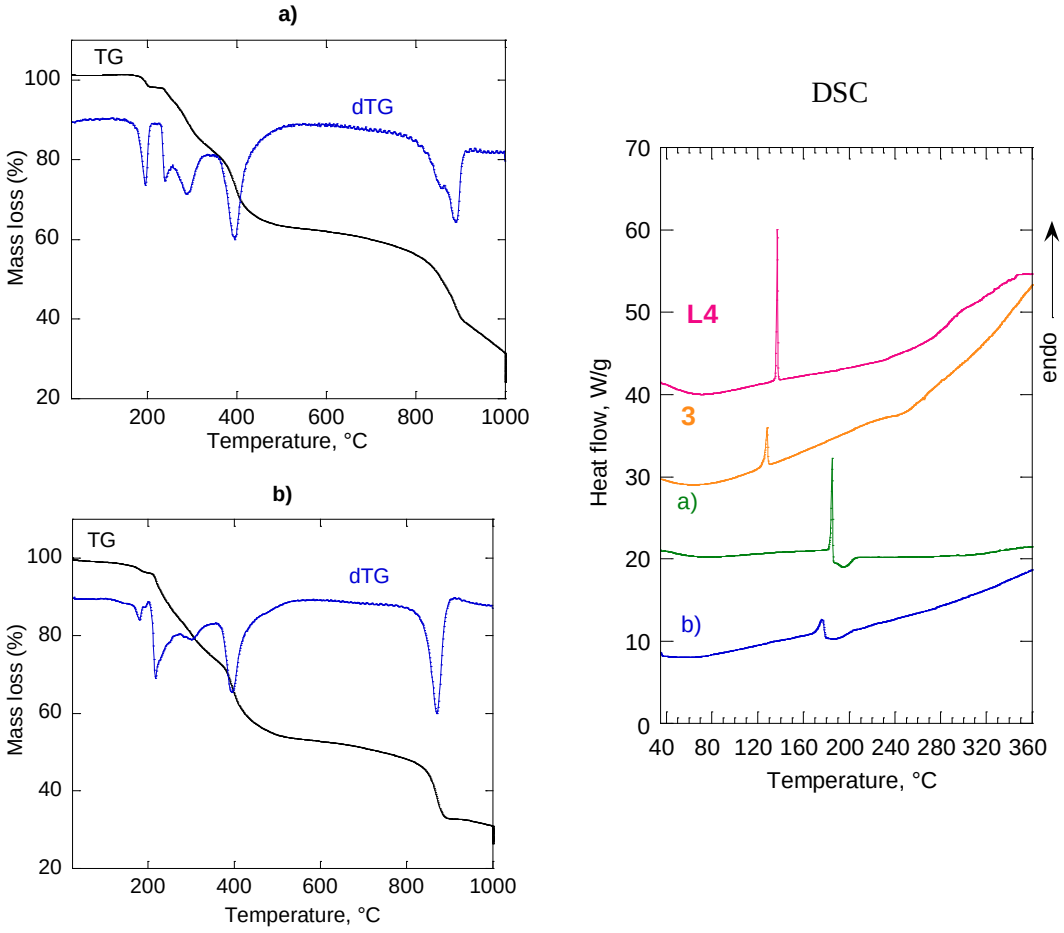

Figure 5.23. TG and dTG curves (left side) and DSC (right side) of compound $(\mathbf{3}\cdot\mathbf{L2})_\infty$ obtained with a) conventional and b) LAG methods. In DSC plots, **L2** and **3** thermograms were also reported for comparison.

The TG characterization of conventionally prepared $(\mathbf{4}\cdot\mathbf{L2})_\infty$ sample shows four main mass loss and corresponding peaks in dTG curve of Figure 5.24a, left. In the range of temperature 130-500°C three mass loss centered in dTG at 179°C, 290°C, 392°C are observed and the fourth is in the range 804-950°C. The first three steps of TG curve reflect thermal decomposition of the organic parts of $(\mathbf{4}\cdot\mathbf{L2})_\infty$ polymer (mass loss of 38%). It corresponds with the loss of **L2** and the (-CH_3) substituents bonded to the P atoms of Ni^{II} complex **4**. The mass remaining (63%) at 496°C appears consistent with the presence of $[Ni(OC_4H_6)(S_2PO_2)]$ that starting from 804°C decomposes to bis(dithio-metaphosphato) nickel(II) $[Ni(S_2PO)_2]$ (remaining mass 39%). As expected, the residue product after 924°C, was found to be nickel fosfate $Ni_2P_2O_7$.

DSC curve of conventionally prepared $(\mathbf{4}\cdot\mathbf{L2})_\infty$ sample, along with those of LAG:MeOH/$CHCl_3$ 40 minute sample and reagents (**L2**, **4)** are reported (Figure 5.24, right side). In agreement with the TG analysis, the DSC curve of the conventional sample shows a no reversible exothermic peak at 182°C due to decomposition of $(\mathbf{4}\cdot\mathbf{L2})_\infty$. Therefore, the polymer $(\mathbf{4}\cdot\mathbf{L2})_\infty$ is stable up to this temperature.

The 40 minute $(\mathbf{4}\cdot\mathbf{L2})_\infty$ LAG:MeOH/$CHCl_3$ sample presents similar thermal behavior in comparison with the sample prepared in the conventional manner, with formation of the same degradation compounds. Slight differences of temperature are observed in the TG/dTG thermogram: 172°C, 295°C, 402°C, 901°C in comparison to that of conventional one (179°C, 290°C, 392°C and 901 °C). The corresponding DSC exothermic peaks is centered at the same temperature of the conventional one. The thermal behavior of milled sample did not present the same differences observed on the XRPD analysis. Therefore, this can be explain with the formation of a different structure for the milled sample compared with the conventional one but with a very similar thermal behavior. Our hypothesis is that the LAG sample is the monomer (**4**·**L2**) that in the conventional synthesis is repeated indefinitely, building up the $(\mathbf{4}\cdot\mathbf{L2})_\infty$ coordination polymer. Further investigations are therefore needed.

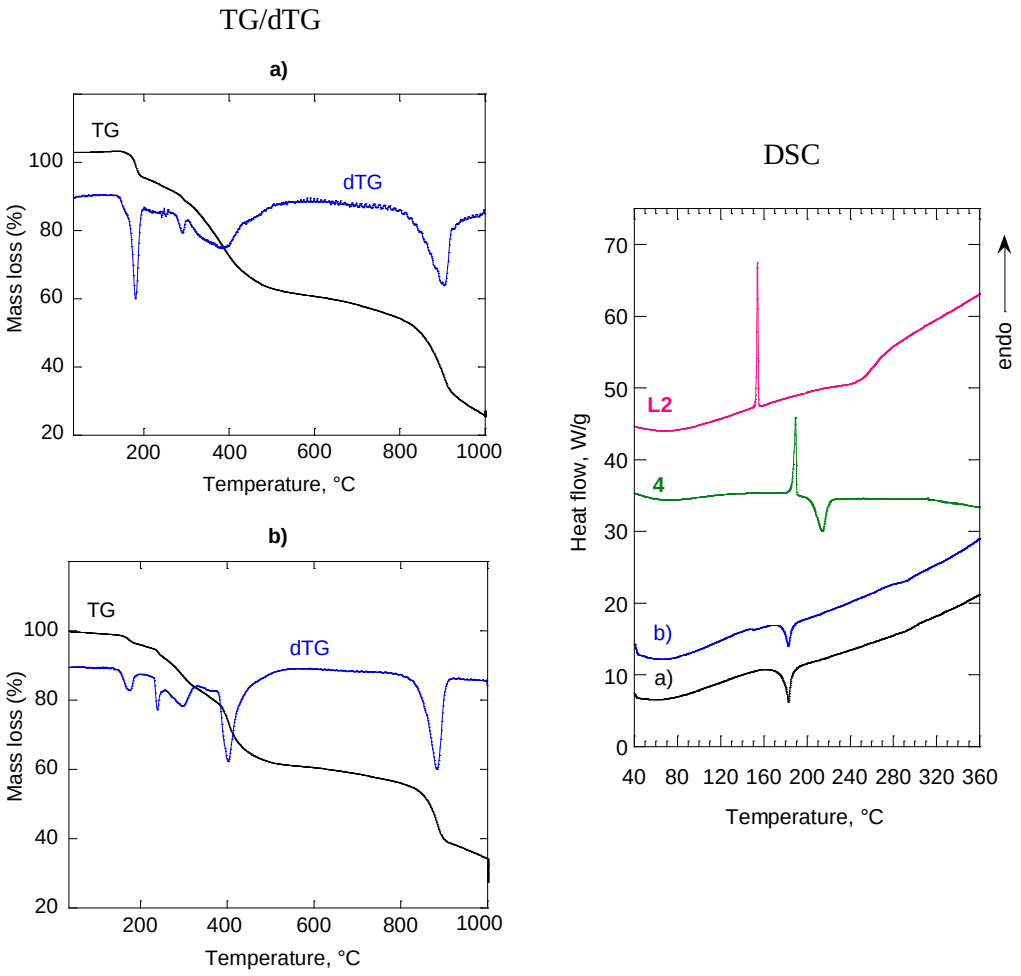

Figure 5.24. TG and dTG curves (left side) and DSC (right side) of compound $(\mathbf{4}\cdot\mathbf{L2})_\infty$ obtained with a) conventional and b) LAG methods. In DSC plots, **L2** and **4** thermograms were also reported for comparison.

TG and corresponding derivative dTG curves of $(\mathbf{2}\cdot\mathbf{L3})_\infty$ prepared in the conventional manner (Figure 5.25a left side) shows several mass loss (and peaks in dTG) in the temperature range of: i) 40-440, and (ii) 844-970°C. The mass loss in the first range of TG curve reflect thermal decomposition of the organic parts of $(\mathbf{2}\cdot\mathbf{L3})_\infty$ polymer: the ligand **L3** and the organic substituents at the phosphorus atoms of Ni^{II} complex **2.** The mass remaining (43%) after 440°C appears consistent with the presence of bis(dithio-metaphosphato) nickel(II) $[Ni(S_2PO)_2]$. As expected, the residue product after 970°C, was found to be nickel fosfate $Ni_2P_2O_7$.

DSC curve of conventionally prepared sample (Figure 5.25a right) shows an irreversible exothermic peak centered at 162°C, due to decomposition of $(\mathbf{2}\cdot\mathbf{L3})_\infty$.

As already seen in previously discussed mechanochemical samples, (**2**·**L3**)$_\infty$ LAG sample has similar thermal behavior (TG and DSC Figure 5.25b) compared to conventional one with the same degradation compounds but with lower slightly shifted temperatures (DSC exothermic peak is larger than the conventional one, centered at 151°C). This result is in agreement with the very small average crystal size of this milled sample (33 nm)

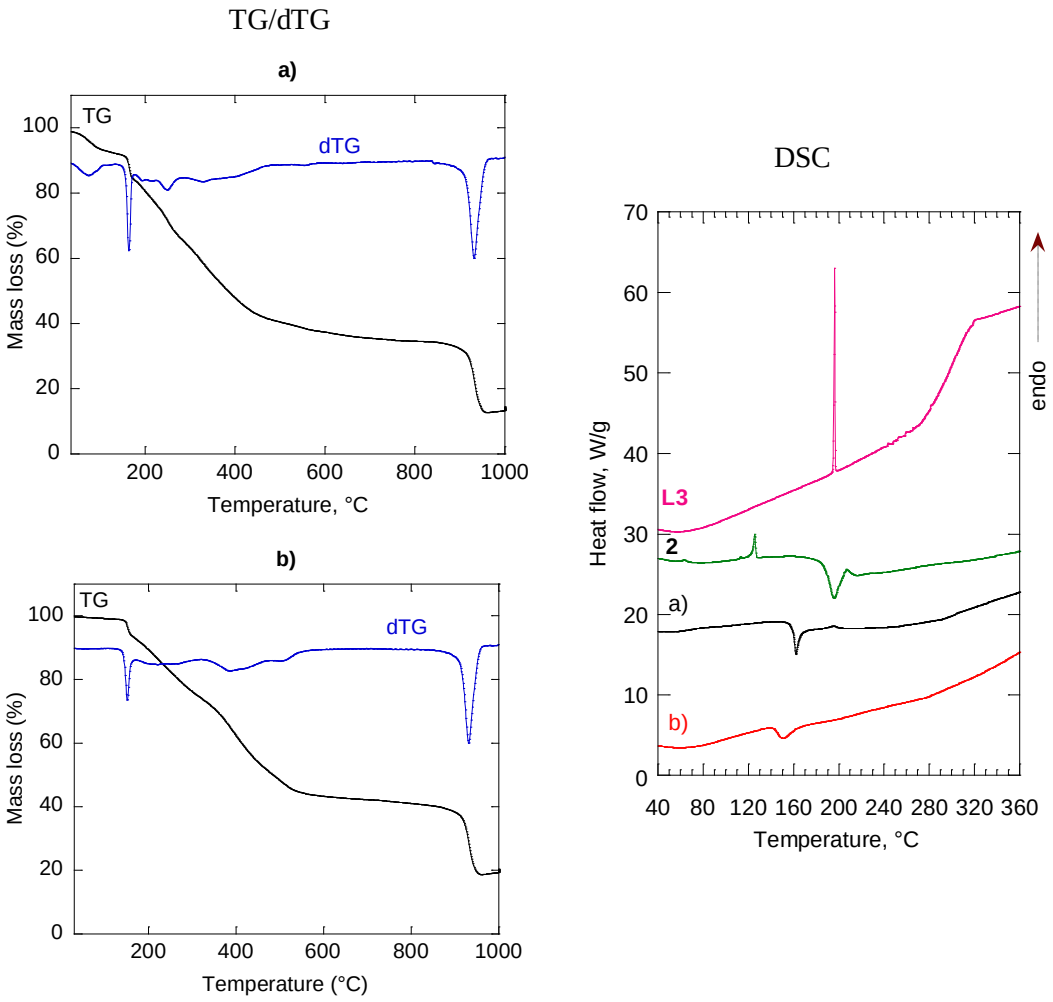

Figure 5.25. TG and dTG curves (left side) and DSC (right side) of compound (**2**·**L3**)$_\infty$ obtained with a) conventional and b) LAG:MCHCl$_3$ methods. In DSC plots, **L3** and **2** thermograms were also reported for comparison.

The TG characterization of conventionally prepared (**4**·**L3**)$_\infty$ sample shows three main mass loss (and several corresponding peaks in dTG curve) in the temperature range of(Figure 5.26a, left): i) 160-340, (ii) 340-545°C and (iii) 775-950°C. The mass loss in the first range (mass loss of 40%) corresponds with the

loss of **L3** and the (-CH_3) substituents bonded to the P atoms of Ni^{II} complex **4** and the mass remaining (60%) at 340°C appears consistent with the presence of [$Ni(OC_4H_6)(S_2PO_2)$]. The mass remaining after the second step (38%) and the plateau observed from 545 to 775 °C is consistent with the presence of the bis(dithio-metaphosphato) nickel(II) [$Ni(S_2PO)_2$] moiety, in agreement with the data reported in literature. As expected, the residue product after 950°C , was found to be nickel fosfate $Ni_2P_2O_7$.

DSC curve of conventionally prepared (**4**·**L3**)$_\infty$ sample, along with those of LAG:MeOH 40 minute sample and reagents (**L3**, **4)** are reported inFigure 5.26, right side. In agreement with the TG analysis, the DSC curve of the conventional sample shows an irreversible exothermic peak at 179°C due to decomposition of (**4**·**L2**)$_\infty$. Therefore, the polymer (**4**·**L2**)$_\infty$ is stable up to this temperature.

LAG:MeOH sample has similar thermal behavior (TG and DSC Figure 5.26b) compared to conventional one with the same degradation compounds but with lower slightly shifted temperatures (the DSC exothermic peaks is centered at 176°C).

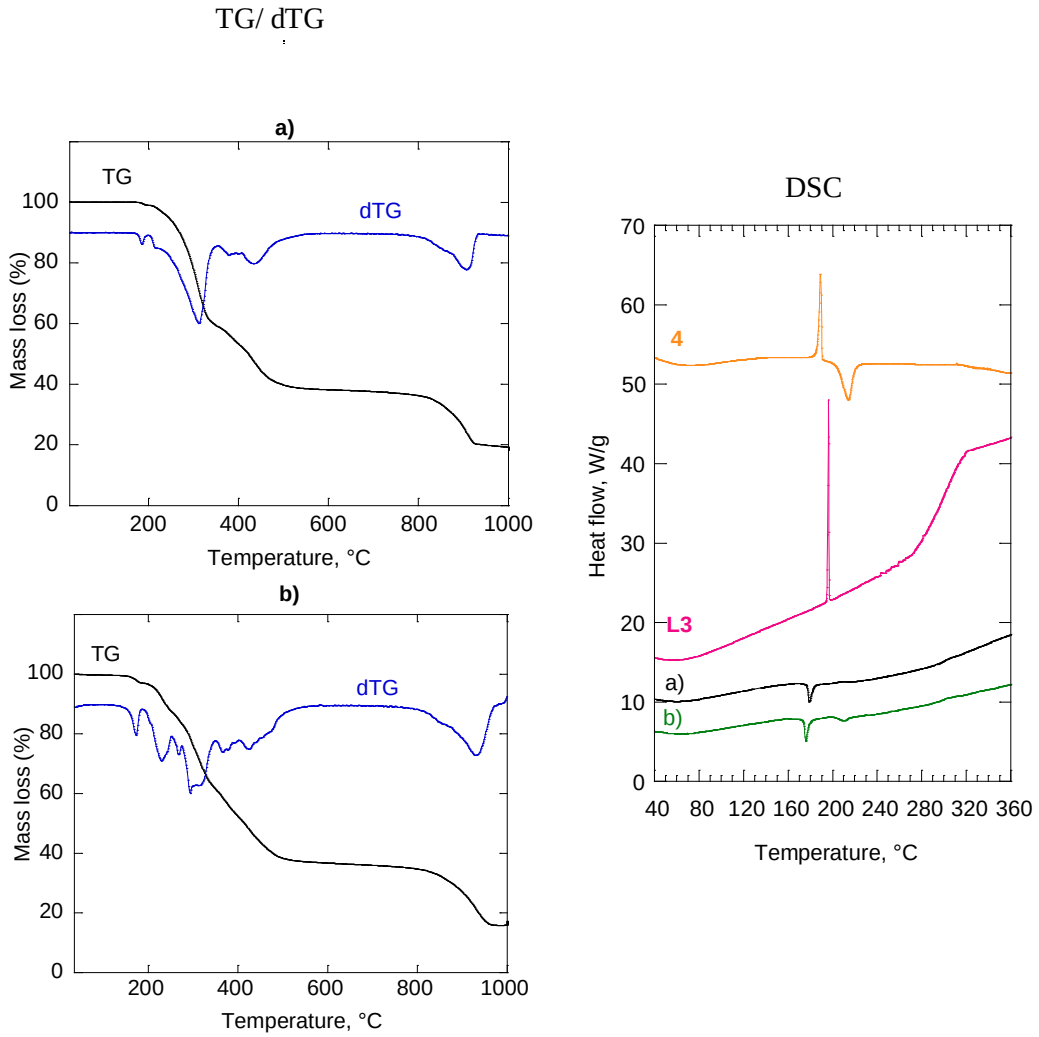

Figure 5.26. TG and dTG curves (left side) and DSC (right side) of compound (**4**·**L3**)$_\infty$ obtained with a) conventional and b) LAG:MeOH methods. In DSC plots, **L3** and4 thermograms were also reported for comparison.

The TG characterization of conventionally prepared (**1**·**L4**)$_2$ sample shows three main mass loss (and several corresponding peaks in dTG curve) in the temperature range of (Figure 5.27a, left): i) 160-240, (ii) 240-500°C and (iii) 680-860. The mass loss in the first and second range (mass loss of 60%) corresponds with the loss of **L4** and the (-CH_2CH_3) substituents bonded to the P atoms of Ni^{II} complex **1**. The mass remaining (40%) at 500°C is consistent with the presence of the bis(dithio-metaphosphato) nickel(II) [$Ni(S_2PO)_2$] moiety, in agreement with the data reported in literature. As expected, the residue product after 860°C , was found to be to be mainly nickel fosfate $Ni_2P_2O_7$ as confirmed by XRPD analysis

(data not shown). Faint peaks due to Ni_2P_5, NiO and $Ni_3(PO_4)_2$ phases are also found in this XRPD pattern.

DSC curve of conventionally prepared $(\mathbf{1}\cdot\mathbf{L4})_2$ sample, along with those of LAG:EtOH 10 minute sample and reagents (**L4**, **1)** are reported inFigure 5.27, right side. The DSC curve of the conventional sample shows an endothermic peak at 180°C immediately followed by an exothermic peak, this is the typical behavior of an incongruent melting. The LAG sample (TG and DSC Figure 5.27b) has similar thermal behavior compared to conventional one with the same degradation compounds (TG) but with lower slightly shifted temperatures (the DSC endothermic peak is centered at 177°C).

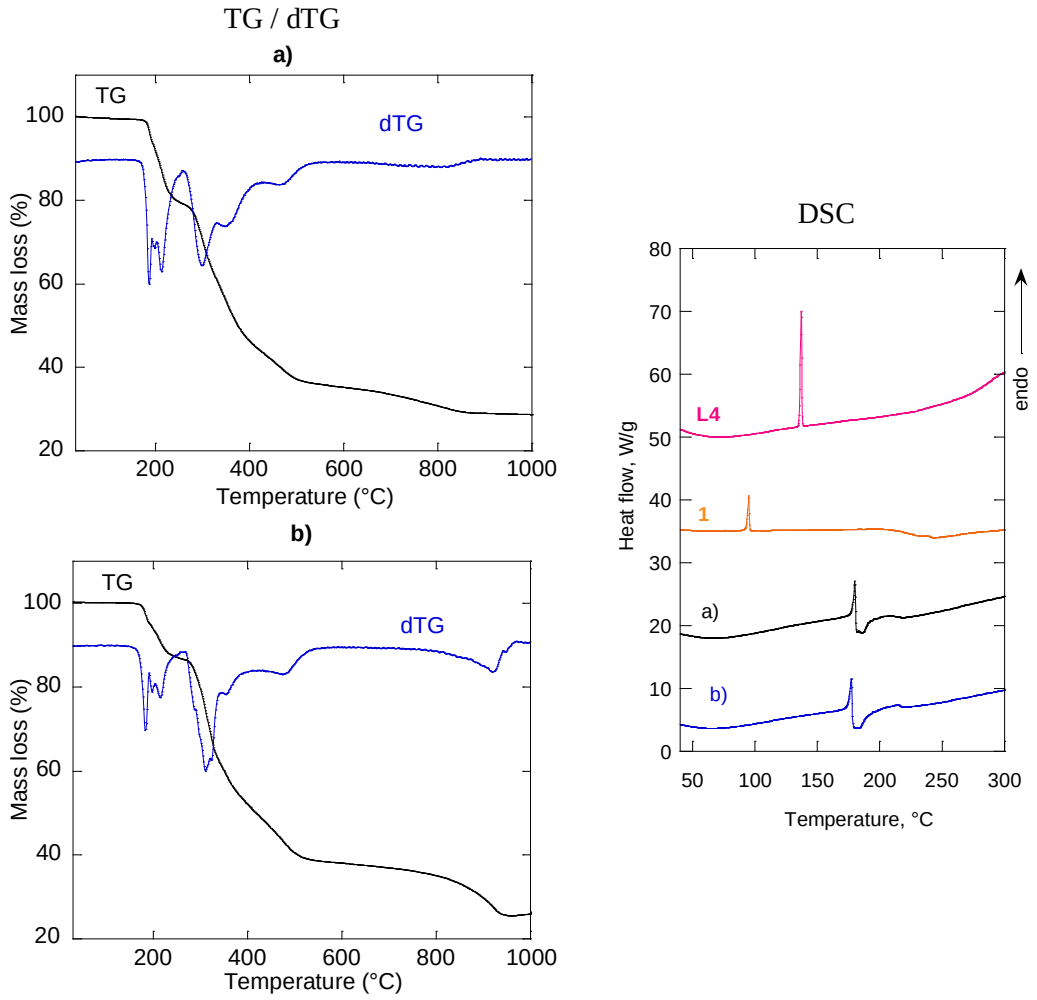

Figure 5.27. TG and dTG curves (left side) and DSC (right side) of compound $(\mathbf{1}\cdot\mathbf{L4})_2$ obtained with a) conventional and b) LAG:MeOH methods. In DSC plots, **L4** and **1** thermograms were also reported for comparison.

The TG characterization of conventionally prepared $(\mathbf{3}\cdot\mathbf{L4})_\infty$ sample shows three main mass loss (and several corresponding peaks in dTG curve) in the temperature range of (Figure 5.28a, left): i) 170-350°C, (ii) 350-540°C and (iii) 740-960°C.

The first and second steps of the TG curve reflect thermal decomposition of the organic parts of $(\mathbf{1}\cdot\mathbf{L})_\infty$. The mass remaining after the first step (60%) corresponds to the loss of **L4**. The plateau observed from 540 to 740 °C is consistent with the presence of the bis(dithio-metaphosphato) nickel(II) $[Ni(S_2PO)_2]$ compound (remaining mass 35%).[15] At higher temperature, decomposition of the sample is observed, with formation of a residue product identified as nickel phosphate $Ni_2P_2O_7$ by XRPD analysis (data not shown). The LAG sample has similar thermal behavior compared to conventional one with the same degradation compounds (Figure 5.28b, left).

DSC curve of conventionally prepared and LAG samples are reported in Figure 5.28, right side. As already observed for $(\mathbf{1}\cdot\mathbf{L4})_\infty$ samples, DSC curves of the $(\mathbf{3}\cdot\mathbf{L4})_\infty$ conventional and LAG samples show endothermic peaks at 185 and 175 °C respectively, immediately followed by an endothermic peak (incongruent melting). On the contrary the previously studied $(\mathbf{1}\cdot\mathbf{L1})_\infty$, $(\mathbf{2}\cdot\mathbf{L1})_\infty$, $(\mathbf{3}\cdot\mathbf{L1})_\infty$, $(\mathbf{4}\cdot\mathbf{L1})_\infty$, $(\mathbf{1}\cdot\mathbf{L2})_\infty$, $(\mathbf{2}\cdot\mathbf{L2})_\infty$, $(\mathbf{3}\cdot\mathbf{L2})_\infty$, $(\mathbf{4}\cdot\mathbf{L2})_\infty$, $(\mathbf{2}\cdot\mathbf{L3})_\infty$ and $(\mathbf{4}\cdot\mathbf{L3})_\infty$ samples show exothermic peaks of polymer degradation.

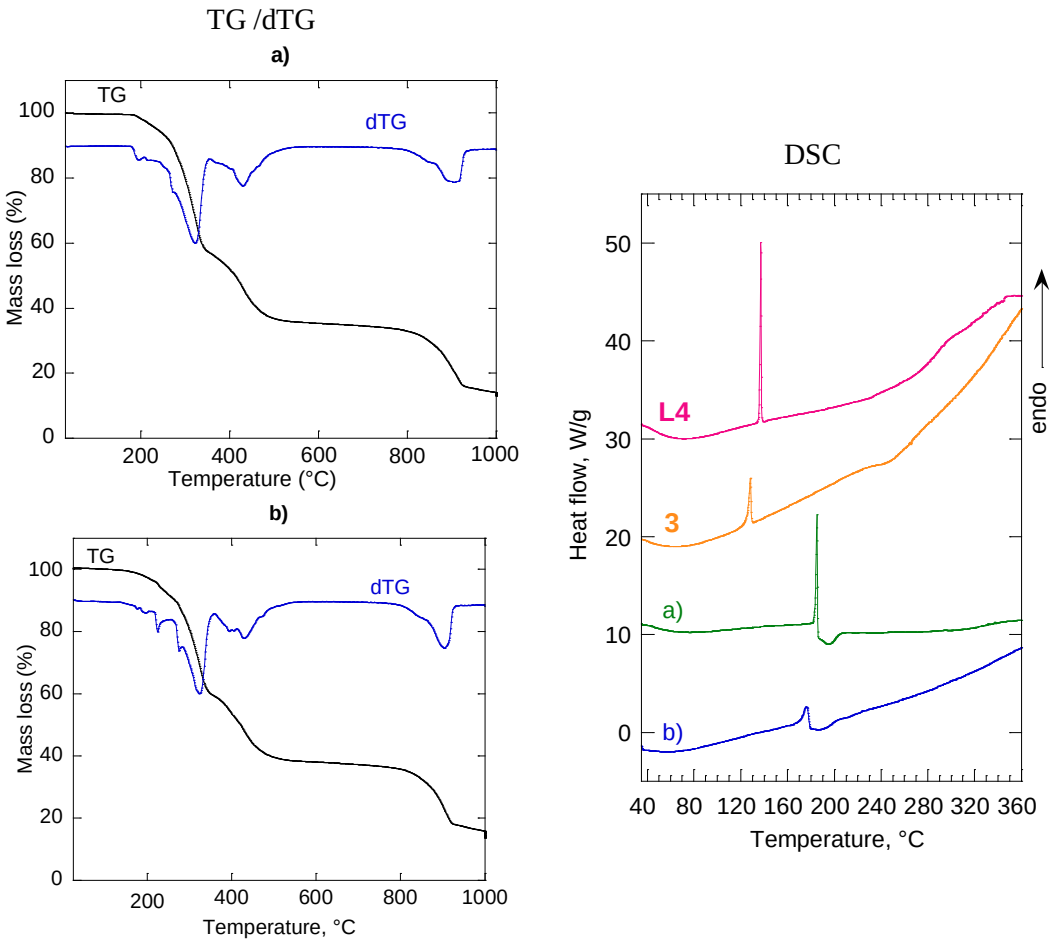

Figure 5.28. TG and dTG curves (left side) and DSC (right side) of compound $(\mathbf{3}\cdot\mathbf{L4})_{\infty}$ obtained with a) conventional and b) LAG:$CHCl_3$ methods. In DSC plots, **L4** and **3** thermograms were also reported for comparison.

5.7 References

1. Gleiter, R.; Werz, D. B., Alkynes between main group elements: from dumbbells via rods to squares and tubes. *Chem. Rev* **2010,** *110* (7), 4447-4488.

2. Schmidt, R.; Thorwirth, R.; Szuppa, T.; Stolle, A.; Ondruschka, B.; Hopf, H., Fast, Ligand-and Solvent-Free Synthesis of 1, 4-Substituted Buta-1, 3-diynes by Cu-Catalyzed Homocoupling of Terminal Alkynes in a Ball Mill. *Chemistry–A European Journal* **2011,** *17* (29), 8129-8138.

3. Chen, X.; Zhou, G.; Peng, X.; Yoon, J., Biosensors and chemosensors based on the optical responses of polydiacetylenes. *Chemical Society Reviews* **2012,** *41* (13), 4610-4630.

4. Meltzer, R. I.; Lewis, A. D.; King, J. A., Antitubercular Substances. IV. Thioamides. *Journal of the American Chemical Society* **1955,** *77* (15), 4062-4066.

5. Aragoni, M. C.; Arca, M.; Caltagirone, C.; Castellano, C.; Demartin, F.; Garau, A.; Isaia, F.; Lippolis, V.; Montis, R.; Pintus, A., Cationic and anionic 1D chains based on NH+⋯ N charge-assisted hydrogen bonds in bipyridyl derivatives and polyiodides. *CrystEngComm* **2012,** *14* (18), 5809-5823.

6. Lai, R., Crystal engineering of MOF based on polypyridyl ligands and coordinatively unsatured NiII ions. **2016**.

7. Aragoni, M. C.; Arca, M.; Coles, S.; Crespo-Alonso, M.; Coles, S.; Davies, R.; Hursthouse, M.; Isaia, F.; Lai, R.; Lippolis, V., Coordination polymers and polygons using di-pyridyl-thiadiazole spacers and substituted phosphorodithioato NiII complexes: potential and limitations for inorganic crystal engineering. *CrystEngComm* **2016**.

8. Rodríguez, J. G.; Martín-Villamil, R.; Cano, F. H.; Fonseca, I., Synthesis of 1, 4-di (n-pyridyl) buta-1, 3-diyne and formation of charge-transfer complexes. X-Ray structure of 1, 4-di (3-pyridyl) buta-1, 3-diyne. *Journal of the Chemical Society, Perkin Transactions 1* **1997,** (5), 709-714.

9. Aragoni, M. C.; Arca, M.; Crespo, M.; Devillanova, F. A.; Hursthouse, M. B.; Huth, S. L.; Isaia, F.; Lippolis, V.; Verani, G., Investigation on the reactivity of dithiophosphonato/dithiophosphato Ni II complexes towards 2, 4, 6-tris-2-pyridyl-1, 3, 5-triazine: developments and new perspectives. *Dalton Transactions* **2009,** (14), 2510-2520.

10. Aragoni, M. C.; Arca, M.; Demartin, F.; Devillanova, F. A.; Graiff, C.; Isaia, F.; Lippolis, V.; Tiripicchio, A.; Verani, G., Reactivity of phosphonodithioato Ni II complexes: solution equilibria, solid state studies and theoretical calculations on the adduct formation with some pyridine derivatives. *Journal of the Chemical Society, Dalton Transactions* **2001,** (18), 2671-2677.

11. Pichon, A.; James, S. L., An array-based study of reactivity under solvent-free mechanochemical conditions—insights and trends. *CrystEngComm* **2008,** *10* (12), 1839-1847.

12. Braga, D.; Grepioni, F., Reactions between or within molecular crystals. *Angewandte Chemie International Edition* **2004,** *43* (31), 4002-4011.

13. Garay, A. L.; Pichon, A.; James, S. L., Solvent-free synthesis of metal complexes. *Chemical Society Reviews* **2007,** *36* (6), 846-855.

14. Yuan, W.; Garay, A. L.; Pichon, A.; Clowes, R.; Wood, C. D.; Cooper, A. I.; James, S. L., Study of the mechanochemical formation and resulting properties of an archetypal MOF: Cu3 (BTC) 2 (BTC= 1, 3, 5-benzenetricarboxylate). *CrystEngComm* **2010,** *12* (12), 4063-4065.

15. Rodina, T. A.; Ivanov, A. V.; Gerasimenko, A. V.; Lutsenko, I. A.; Ivanov, M. A.; Hanna, J. V.; Antzutkin, O. N.; Sergienko, V. I., Crystalline O, O'-di-sec-butyl and O, O'-diethyl dithiophosphate platinum (II) complexes: Synthesis, 13 C and 31 P CP/MAS NMR, single crystal X-ray diffraction studies and thermal behaviour. *Polyhedron* **2011,** *30* (13), 2210-2217.

Chapter 6: Thio-functionalized Naphthalene Diimides ligands: design, synthesis and future application in coordination polymer architecture

This part of the PhD project has been carried out in the research group of Prof. Neil R. Champness at the *School of Chemistry, University of Nottingham* (UK).

6 Thio-functionalized Naphthalene Diimides ligands: design, synthesis and future application in coordination polymer architecture

6.1 Introduction

This part of the three years PhD thesis is focused on the conventional solution based synthesis of N-donors ligands to be used for the synthesis of coordination polymers. The project has concerned the investigation of naphthalene diimides (NDIs) as a noteworth class of organic molecules for application in the fields of material and supramolecular science.[1] Of interest is their application in the fields of conducting thin films and molecular sensors for their structure–function relationships.[2] Another field of NDIs interest is the areas of energy and electron transfer and in host-guest complexes for molecular switching devices. The naphthalene diimides are a compact, neutral, planar, chemically robust, redox-active, electron deficient class of aromatic compounds. Furthermore they have excellent oxidative and thermal stabilities, usually possessing high melting points; these characteristics make them promising candidates for organic electronics applications and photovoltaic devices.[3] In the design of electronic conducting functional materials, NDIs are among the most versatile and fascinating class of aromatic molecules. [4]

NDI molecules possess an imide and core region (Figure 6.1). Functionalization through the diimide nitrogens or substitution on the naphthalene core produces derivatives with variable absorption and emission properties that are. Substitution on the aromatic core of NDIs with one or more groups at the 2, 3, 6 and 7 positions is becoming increasingly popular and is emerging as a distinct class of material, with new and greatly different properties arising from this modification.[2] The substitution of the diimide nitrogens with aromatic functional groups give rise to non-fluorescent or weakly fluorescent compounds; while the substitution of the alkyl groups at the same positions lead to the typical fluorescence of this class of compound.

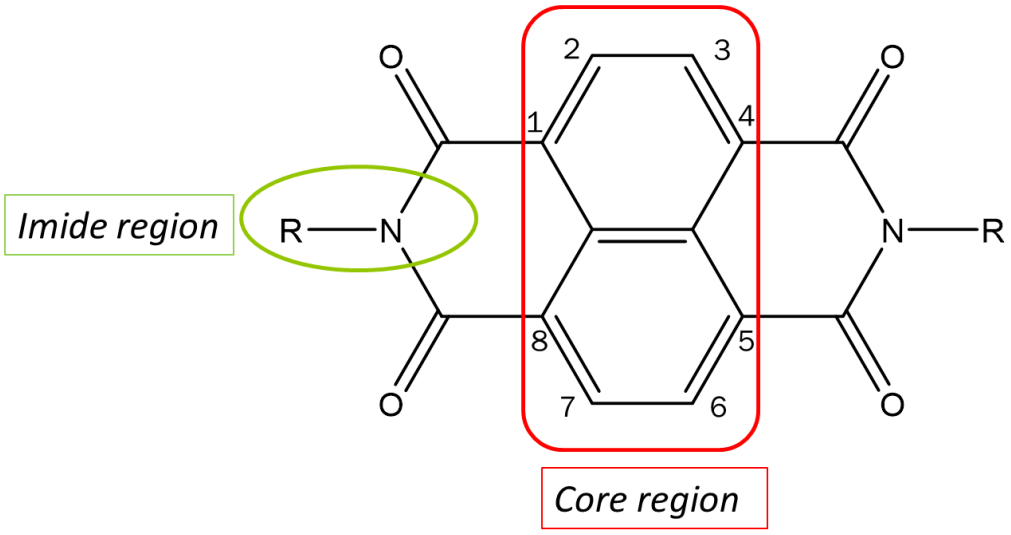

Figure 6.1. General structure and numbering system of NDIs highlighting the imide region (green) and core region (red).

Using NDIs, an electron donor-acceptor complex or charge transfer complex can be formed from an association of molecules that are capable of transferring a fraction of electronic charge which is transported from one part (the donor) to another (the acceptor). The donor and acceptor can be separate molecular entities, or attached to each other as two parts of a larger molecule as observed in this class of ligands.[5] The interest in NDI charge transfer systems is due to chemical and physical robustness and electronic complementarity to ubiquinones, biology's choice acceptor in photosynthetic reaction centres. NDIs can be reversibly reduced chemically or electrochemically at the fairly mild potential of -1.1 V vs. ferrocene Fc^+/Fc, forming stable radicals (for reference, trimethylbenzoquinone is reduced at -1.2 V vs. Fc^+/Fc).[2,6] For those properties NDIs are used as solar energy convertors and optoelectronic devices.

Several papers regarding the functionalization of NDIs (especially core substituted NDIs, cNDIs) are reported in literature[7,8] but only recently has emerged the reaction of NDIs with Lawesson's reagent resulting in the substitution of the carbonyl oxygen atoms with sulfur atoms to give thionated NDIs.[9] Group 16 elemental substitution is an effective means of modifying the optoelectronic properties of π- conjugated systems.[10] The principal advantage of this approach is that the frontier orbital energies can be altered without having to cause large-scale changes to the molecular structure. In particular, substitution with sulfur, known as thionation, has been used to change carbonyls groups into

thiocarbonyls. Relevant to note is that thioimide compounds have a tendency to be stable despite other thiocarbonyl systems.[11] The effect of sulfur atom substitution on the electronic structure was investigated by Tilley and coworkers and the schematic energy level of the nonthionated compound and the trithionated is reported in Figure 6.2.[12]

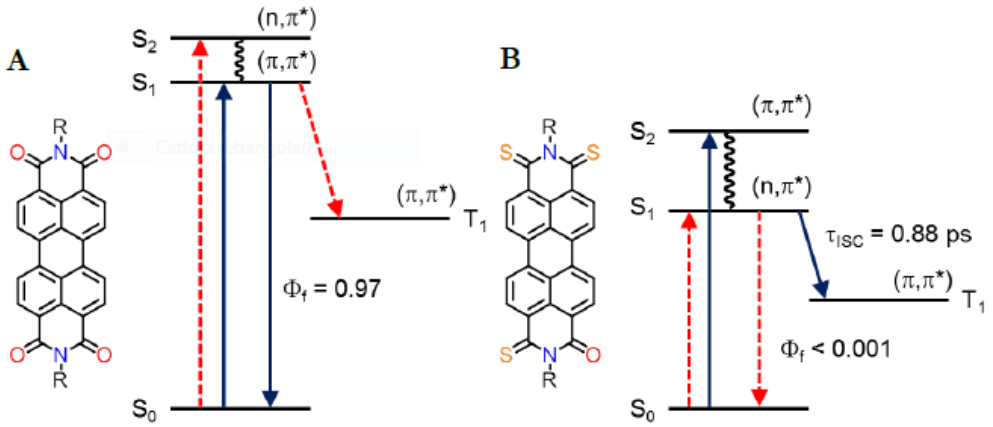

Figure 6.2: Energy level schematic proposed by Tilley.[12] Nonthionated PDI (A) and trithionated PDI (B). Blue arrows represent more likely electronic transitions, red arrows represent less likely transitions. R = 3-hexylundecyl.

It is possible to note a decrease in the energetic gap was observed in the trithionated compound. The introduction of sulfur atoms also lead to a variation in the absorption maximum that shifted from 526 nm in the nonthionated to a maximum of 706 nm in the tetrathionated sample. The LUMO energies decrease with increasing thionation (increased electron affinity), while the HOMO energies raise determining the red shift in optical absorption.[12]

In 2011 Facchetti and coworkers reported for the first time the successful thionation of a cyclohexyl substituted NDIs [13] (Figure 6.3). They effected the synthesis of monothionated and dithionated NDIs by reacting the cycloehxyl substituted NDIs with Davy reagent. Very recently, another example of thionation of a NDI compound has been reported and the full set of thionated NDIs was isolated.[5]

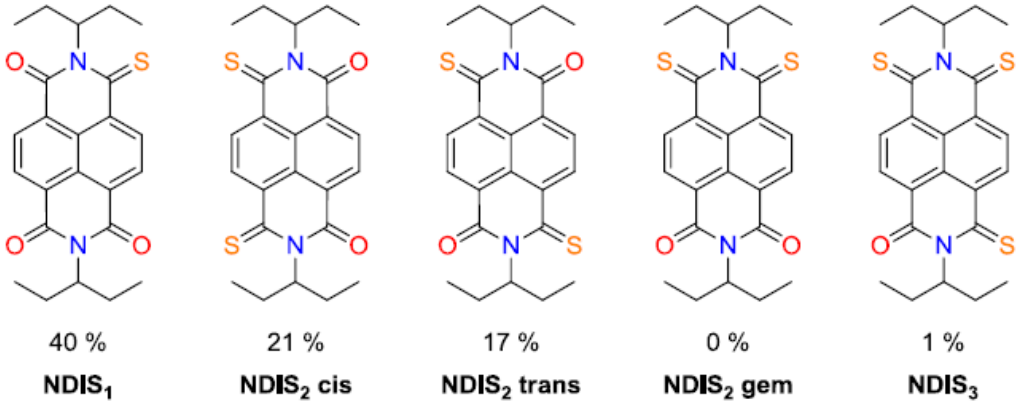

Figure 6.3. Structures of thionated NDI products described in ref:5.

The advantages observed following the thionation approach on the electrochemical and photophysical properties of thionated NDIs is the base on which this part of the project is focused. A selected series of diimide nitrogens substituted NDIs (nonthionated) are investigated especially for their use as electron acceptors which are able to lead to novel molecular assemblies and supramolecular ordered structures. The thionation approach was also adopted for these NDIs with the aim of improving the properties of these ligands. The final purpose of this project is to obtain Metal Organic Frameworks combining the electrochemical and photophysical properties of thionated NDIs with the porosity that can be obtained from coordination networks topology.

6.2 Experimental section

6.2.1 Materials and Methods

All chemical reagents were used as-purchased from Alfa Aesar, Fisher Scientific, Sigma-Aldrich, or VWR International, unless stated otherwise. Anhydrous toluene was dried by passing through a column packed with 4 Å molecular sieves, degassed and stored over a potassium mirror in a nitrogen atmosphere. Anhydrous dichloromethane was purchased from Sigma-Aldrich (Fluka) and stored over 4 Å

molecular sieves. Column chromatography was performed on Merck silica gel 60 (0.2-0.5 mm, 50 - 130 mesh).

NMR Spectroscopy: ^{1}H and $1^{3}C$ NMR spectra were recorded using either a Bruker AV(III)400 machine or a Bruker AV400 machine at room temperature. Chemical shifts are reported with respect to the $CDCl_3$ residual peak at 7.27 ppm (^{1}H).

Mass Spectrometry: MALDI-TOF M/S spectra were recorded with a Bruker Ultraflex III mass spectrometer using trans-2-[3-(4-tert-butylphenyl)-2-methyl-2-propenylidene]-malononitrile (DCTB) as the matrix. ESI M/S spectra were recorded with a Bruker MicroTOF.

Elemental Analysis: Elemental analysis was performed using an automated CE-440 Elemental Analyser.

X-ray Crystallography: Single crystal X-ray diffraction experiments were performed on an Oxford Diffraction SuperNova CCD area detector diffractometer at 120 K using monochromated Cu Kα radiation (λ = 1.5418 Å). The structures were solved by direct methods using either SHELXS or SHELXT[14] and refined with SHELXL[14] using a least squares method. OLEX2 software was used as the solution, refinement and analysis program.[15]

6.2.2 Synthesis

Synthesis of N, N'-di(4-pyridyl)-1,4,5,8-naphthalenediimide (DPNDI) ligand. A mixture of 1,4,5,8-naphthalene-tetracarboxylic dianhydride (NDA) (0.8g, 3mmol) and 4-aminopyridine (6mmol) in DMF (20mL) was heated under reflux for 8 h according to a previously reported procedure.[16] When the reaction mixture reached room temperature, a crystalline solid precipitated out, which was collected by filtration. The crude product was purified by recrystallization from DMF to obtain DPNDI as off-white crystalline solids (yield 86%). Spectral data are in agreement with the literature.[16]

Thionation of N, N'-di(4-pyridyl)-1,4,5,8-naphthalenediimide (DPNDI) ligand. DPNDI (0.5 g, 1.19 mmol) and Lawesson's reagent (2.88 g, 7.14 mmol) were dissolved in anhydrous toluene (50 mL) and heated (130°C) to reflux for 42 h. The solution was cooled to room temperature and concentrated under reduced pressure. The resulting brown residue was dissolved in chloroform (50 mL) and washed with NaOH (100 mM), sat. aq. $NaHCO_3$ and sat. aq. NaCl, dried over $MgSO_4$, filtered and concentrated. This product was treated by column chromatography (silica, gradient elution from 1:1 pentane:dichloromethane to dichloromethane).

The same amounts of reagents were reacted in toluene for 24 h and 48 h respectively adopting the same procedure. Several trial reaction was performed varying the solvent adopted: using 50 mL of tetrachloroethylene at 130°C or pyridine at 120°C. Other changes to this reaction were made using different thionation reagents: phosphorus pentasulphide and $[P_2S_5(pyridine)_2]$ in the same molar ratio of the previously reported reaction.

1,4,5,8-naphthalenetetracarboxydiimide (DPMNI). DPMNI was synthesized adapting the synthetic route of DPNDI with the synthesis reported in literature.[17] Briefly, 1,4,5,8-Naphthalenetetracarboxylic dianhydride (1.23 g, 4.6 mmol) and 4-(aminomethyl)pyridine (1.16 mL, 11.5 mmol) were refluxed in anhydrous DMF (20 mL) for 8 h, yielding an orange-brown product. The solid was isolated by vacuum filtration and washed with acetone and dried in vacuum. (yield 88%.). Spectral data are in agreement with the literature.[17]

Thionation of N, N'-di(4-pyridyl)-1,4,5,8-naphthalenediimide (DPMNI) ligand. DPMNI (0.30 g, 0.66 mmol) and Lawesson's reagent (1.44 g, 3.57 mmol) were dissolved in anhydrous toluene (25 mL) and heated (130°C) to reflux for 42 h. The solution was cooled to room temperature and concentrated under reduced pressure. The resulting brown residue was dissolved in chloroform (25 mL) and washed with NaOH (100 mM), sat. aq. $NaHCO_3$ and sat. aq. NaCl, dried over $MgSO_4$, filtered and concentrated. This mixture of products was treated by

column chromatography (silica, gradient elution from 1:1 pentane:dichloromethane to dichloromethane).

Thionation of Naphthalene-1,4,5,8-tetracarboxylic dianhydride (NDA) precursor. The commercially available NDA (0.32 g, 1.19 mmol) and Lawesson's reagent (2.88 g, 7.14 mmol) were dissolved in anhydrous toluene (50 mL) and heated to reflux for 48 h. The solution was cooled to room temperature and concentrated under reduced pressure. The resulting dark residue was dissolved in chloroform (50 mL) and washed with NaOH (100 mM), sat. aq. $NaHCO_3$ and sat. aq. NaCl, dried over $MgSO_4$, filtered, concentrated and MALDI-TOF characterized.

Synthesis of N,N′-Bis(4-nitrobenzene)-1,4,5,8-naphthalene tetracarboxy diimide (DBNDI). DBNDI was synthesized adapting the synthetic route of DPNDI with a previously reported procedure.[18] 1,4,5,8-Naphthalenetetracarboxylic dianhydride (0.80 g, 3.0mmol) and 4-aminobenzonitrile (0.71 g, 6.0 mmol) were refluxed in anhydrous DMF (20 mL) for 8 h. The crude product was purified by recrystallization from DMF to obtain yielding an orange-yellow product not suitable for Single Crystal X-ray Diffraction. (yield 78%) Spectral data are in agreement with the literature.[18]

Thionation of N,N′-Bis(4-nitrobenzene)-1,4,5,8-naphthalene tetracarboxy diimide (DBNDI). DBNDI (0.31 g, 0.66 mmol) and Lawesson's reagent (1.44 g, 3.57 mmol) were dissolved in anhydrous toluene (25 mL) and heated (125°C) to reflux for 48 h. The solution was cooled to room temperature and concentrated under reduced pressure. The resulting dark blue residue was dissolved in chloroform (25 mL) and washed with NaOH (100 mM), sat. aq. $NaHCO_3$ and sat. aq. NaCl, dried over $MgSO_4$, filtered and concentrated. The mixture of products was treated by column chromatography (silica, gradient elution from 1:1 hexane: chloroform to chloroform).

Solvothermal synthesis of (DPNDI·CuI)n. DPNI (0.011 g, 0.025mmol) and CuI (0.019 g, 0.1mmol) were mixed with 2 mL DMF solution in a scintillation vial, which was capped and heated to 100 ℃ in oven for 3 days, and then cooled to room-temperature. Tiny crystals of the product were formed and collected after several weeks.

.

6.3 Result and discussion

The synthesis of symmetric NDI compounds is a one-step procedure obtained by reacting the commercially-available naphthalene-1,4,5,8-tetracarboxylic dianhydride (NDA) with an appropriate primary amine in a high boiling solvent, usually DMF. The naphthalene-1,4,5,8-tetracarboxylic dianhydride is condensed with 4-aminopyridine (Scheme 6.1) giving rise to N, N'-di(4-pyridyl)-1,4,5,8-naphthalenediimide (DPNDI) ligand.

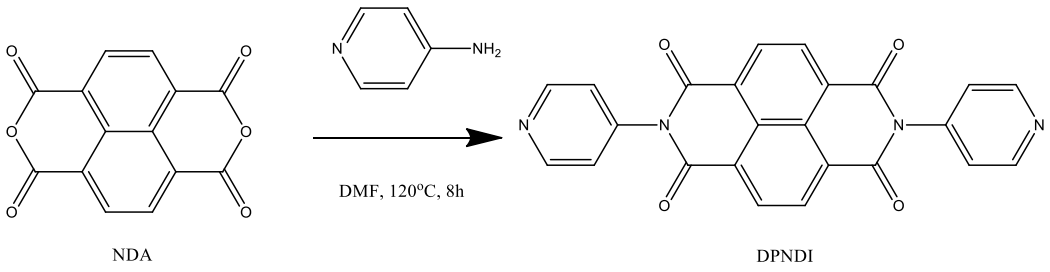

Scheme 6.1. Synthesis of DPNDI

The solid product was collected as an off-white crystalline solids, isolated and identified by single crystal X-ray diffraction (Figure 6.4) confirming the structure deposited in CDS with the Ref. Code: GATXAB01.

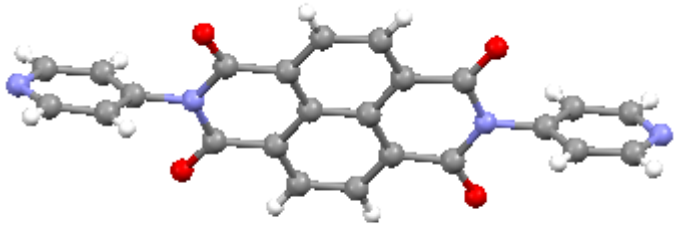

Figure 6.4. X-ray crystal structures of DPNDI molecule (Ref. Code: GATXAB01)[19]

The thionation reaction of carried out on the DPNDI molecule was performed by treatment with Lawesson's reagent, which is able to convert the NDI carbonyls into thiocarbonyls, in toluene (Scheme 6.2).

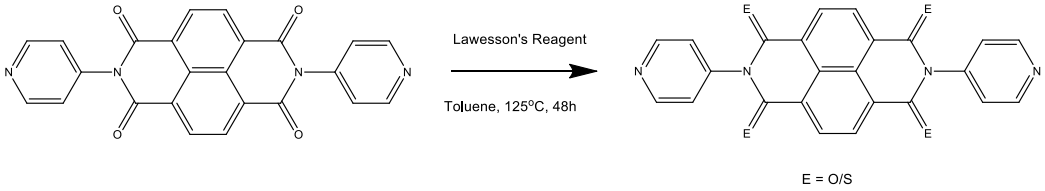

Scheme 6.2. Thionation of DPNDI

It has been demonstrated that recrystallization of the Lawesson's reagent will improve thionation yields,[12] so prior to use, the Lawesson's reagent was recrystallized from toluene and stored under nitrogen. The thionation approach was carried out under vacuum and inert atmosphere. Several different conditions of thionation were investigated in order to promote the reaction. For instance, different solvents (anhydrous toluene, tetrachloroethylene, pyridine, acetonitrile) were used, the solvent choice was evaluated on the basis of the solvents used in the literature for similar reactions. Furthermore, products after different reaction times (24, 48 or 72 hours) of thionation were examined and also various thionation reagents such as the more commonly used Lawesson's reagent but also P_2S_5 and [P_2S_5(pyridine)$_2$] were adopted, in order to promote the reaction towards the formation of the desired products. Unfortunately, only little traces of

monothionated DPNDI were observed and it was not successfully purified and isolated by column chromatography. In order to verify if the unsuccessful thionation could be attributed to the steric encumbrance of the DPNDI on the carbonyls positions, we performed another attempted thionation of the N, N'-di(4-pyridyl-methyl)-1,4,5,8-naphthalenediimide DPMNI. It was synthesized by reacting 1,4,5,8-naphthalenetetracarboxylic dianhydride and 4-aminopicolamine. The thionation of DPNDI is carried out with the same condition of the previous reaction. Scheme 6.3 reports the thionation in toluene for 48 hours but reactions with the previously conditions were also performed.

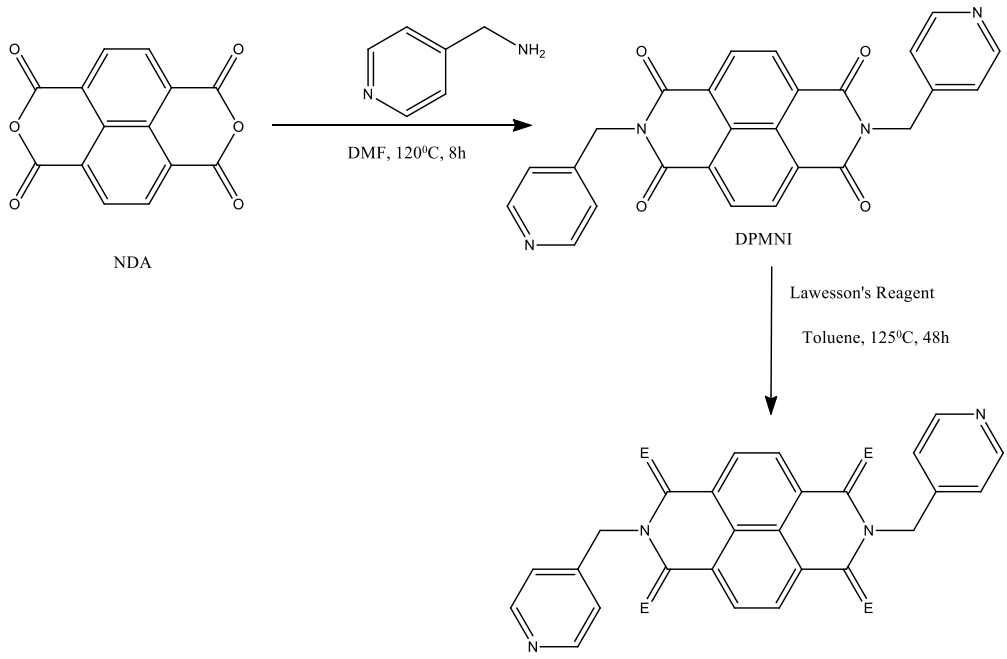

Scheme 6.3 Synthesis and thionation of DPMNI

Figure 6.5 reports the MALDI-TOF mass spectrum of the product after thionation showing the starting material peak and another low intensity peak that could be assigned to the dithionated ligand. In other to separate the non thionated from the presumed dithionated product a straightforward silica gel column chromatography, using a gradient elution from 1:1 pentane:dichloromethane to neat dichloromethane was performed according with the procedure adopted from

the thionation of a similar NDI. Unfortunately also in this case through the column we have not been able to separate the compounds.

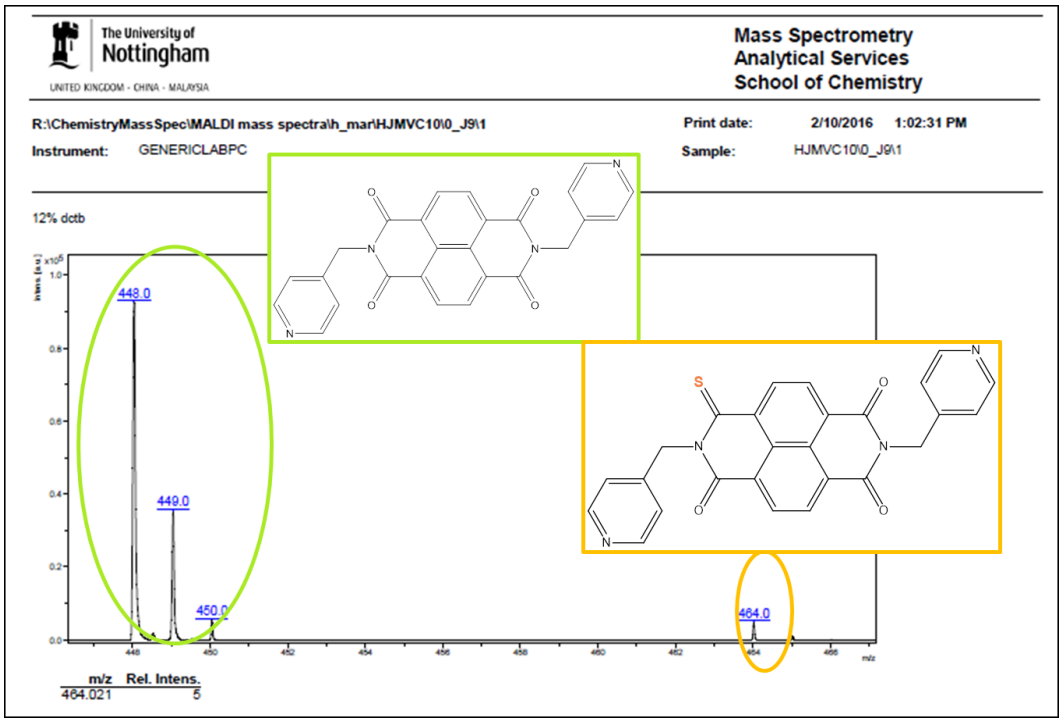

Figure 6.5. MALDI-TOF mass spectrum of products after the thionation of DPMNI.

The thionation of the naphthalene-1,4,5,8-tetracarboxylic dianhydride , NDA was also performed but the MALDI-TOF spectrum shows only the starting material (see 6.5, Figure 6.10) and no trace of minimal amount of thionated products is provided. Therefore, under the belief that probably the pyridine rings of DPNDI and DPMNI play a not entirely clear role on the thionation reaction we changed the functionalization at the diimide nitrogens of NDI molecule, reacting the NDA with a different primary amine, the 4-aminobenzonitrile (Scheme 6.4). Another NDI ligand named N, N'-di(4-benzonitrile)-1,4,5,8-naphthalenediimide (DBNDI) with formula: $C_{28}H_{12}N_4O_4$ was obtained and characterized in agreement with literature [18].

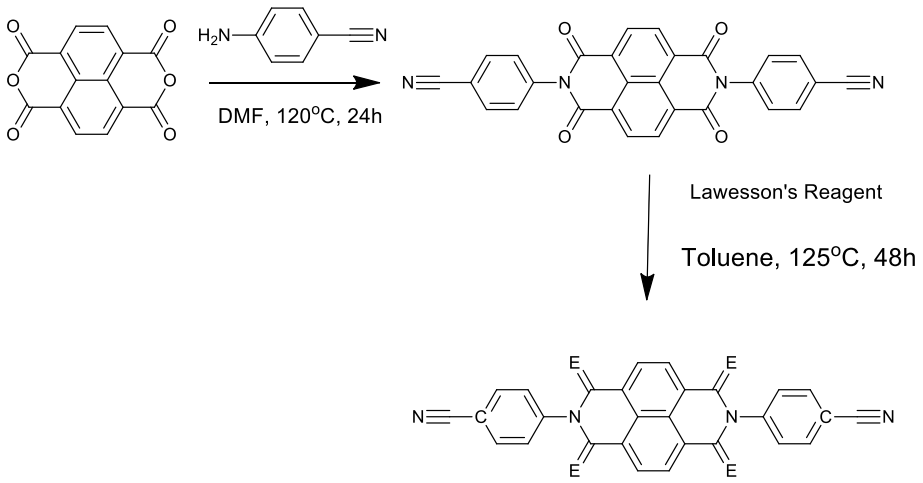

Scheme 6.4. Synthesis and thionation of DBMNDI

The thionation of this ligand was carried out adopting as a thionation medium Lawesson' reagent in toluene. In this case on the MALDI-TOF spectrum (Figure 6.6) it is possible to discriminate peaks due to the non thionated DBNDI, the monothionated and the dithionated products.

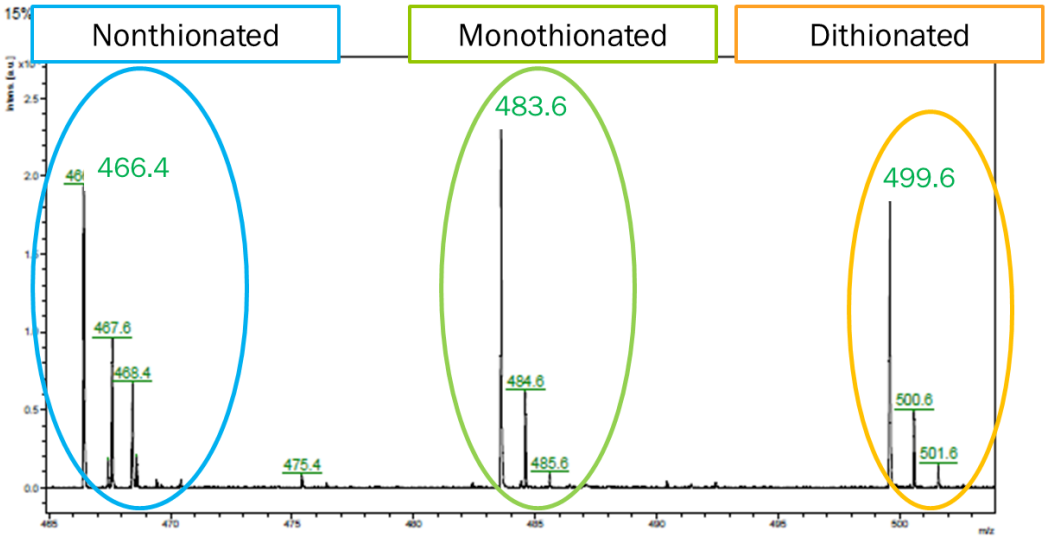

Figure 6.622. MALDI-TOF mass spectrum of products after the thionation of DBNDI.

The silica gel column chromatography, using a gradient elution from 1:1 hexane:chloroform to neat chloroform, was performed. Likely due to the higher reactivity of the sulfur atoms over the oxygen atoms, the monothionated was observed with very low yields (see 6.5, Figure 6.12 and 6.13). Further experiments regarding the development of a protocol of better separation and purification of the thionated compounds are in progress.

In order to verify the possibility of obtaining MOFs or coordination polymer architecture by using the previously discussed thionated compounds, a preliminary solvothermal synthesis adopting the DPNDI ligand and Cupper(I) iodide (CuI) was performed. In the literature, MOF materials consisting of CuI clusters and organic ligands with confirmed porosity (by surface area measurements or adsorption experiments), are very rare. [20,21] Because of the coordination geometry of Cu(I) and the potential bridging capability of the iodide anion, CuI has capability to form rhomboid (Cu_2I_2 dimer), stepped-cubane (Cu_4I_4 tetramer), prismane (Cu_6I_6 hexamer), and double-cubane (Cu_8I_8 octamer) clusters.[22] These clusters transmit rigidity to the framework and also can impart the desired photophysical properties of the framework. The preliminary reaction between DPNDI ligand and CuI was performed with a 1(DPNDI):4(CuI) stoichiometry in DMF solution at 100 °C for 3 days. Very tiny crystals were collected and the crystallographic characterization by Single Crystal X-ray Diffraction was performed. A preliminary image from Mercury software is reported (Figure 6.7) and a polymeric structure were DPNDI molecule bridge two CuI clusters is observed. However a refinement of this preliminary structure is mandatory in order to determine the correct tridimensional packing and chains interactions.

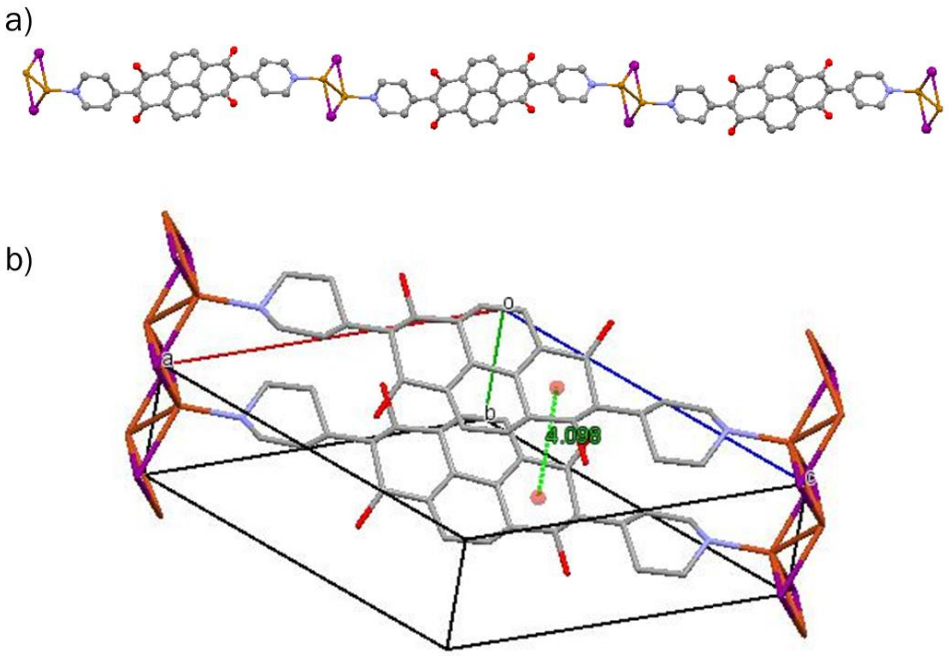

Figure 6.7. Structure of the polymeric chains of the product obtained reacting 1(DPNDI):4(CuI) (a). distance between two chains (b). (A more detailed description is mandatory after complete resolution of the structure).

With the aim to establish the homogeneity of this compound the XRPD measurement was performed and the pattern is reported in Figure 6.8.

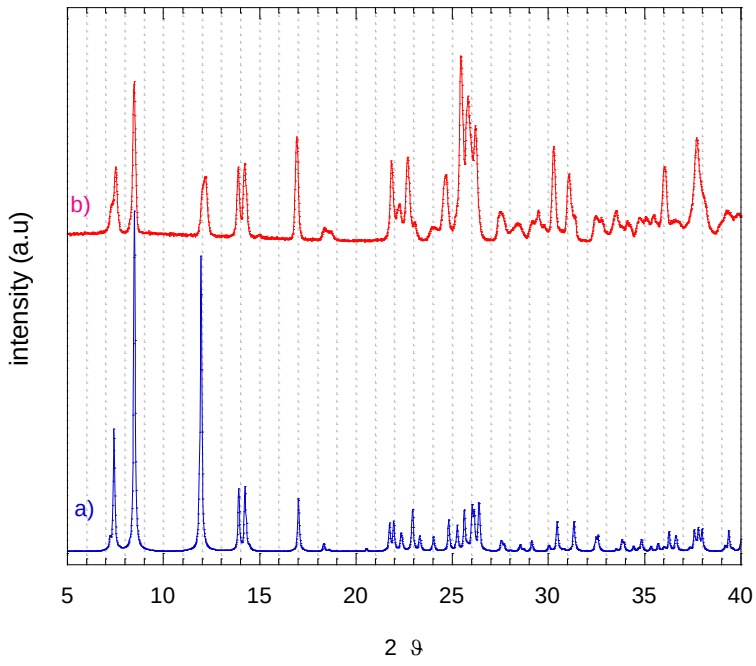

Figure 6.8. XRPD patterns of: a)powder product and b) simulated by single crystal data.

6.4 Conclusions

The thionation approach is an efficient strategy that does not perturb the NDIs molecular structure but improves the electron ability and reactivity of NDIs. The higher reactivity of these molecules due to the sulfur atom substitution may be not only an advantage for NDIs properties but it is also a disadvantage in the phase of purification of thionated compounds. In this chapter we have demonstrated that after several trials in NDIs molecules thionation showed promising results in N, N'-di(4-benzonitrile)-1,4,5,8-naphthalenediimide (DBNDI) where thionation was observed whit the partial purification of two thionated products: mono and disubstituted. In the light of these preliminary results future research concerning an efficient and systematic method to isolate thionated compounds is necessary. The ability to isolate these thio-substituted DBNDI products and isolate them in good yields may set the bases for the production of MOFs with thionated ligands. In this regard a prototypal structure adopting the DPNDI ligand (non-thionated) and Cupper(I) iodide (CuI) was performed in order to improve the optical properties of the product. Refinement of its preliminary structure is mandatory in order to determine the correct tridimensional packing and to study the properties resulting from an hybrid structure between an NDIs ligand and CuI that may improve This early work certainly needs further and future evidence to confirm the first results obtained and to develop others.

6.5 Compounds Characterization

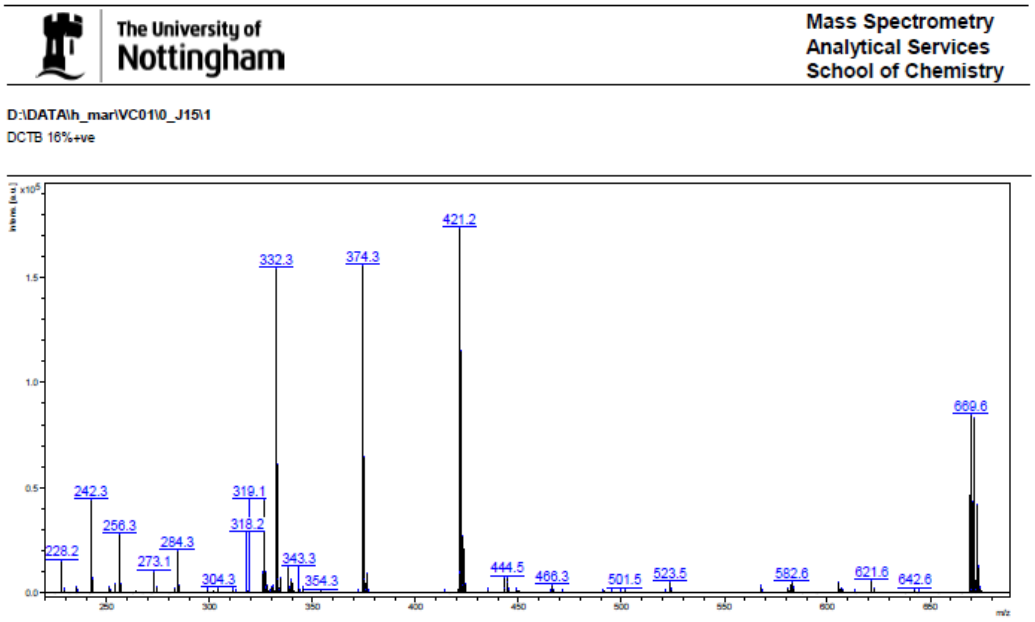

Figure 6.9: MALDI-TOF of (DPNDI) ligand.

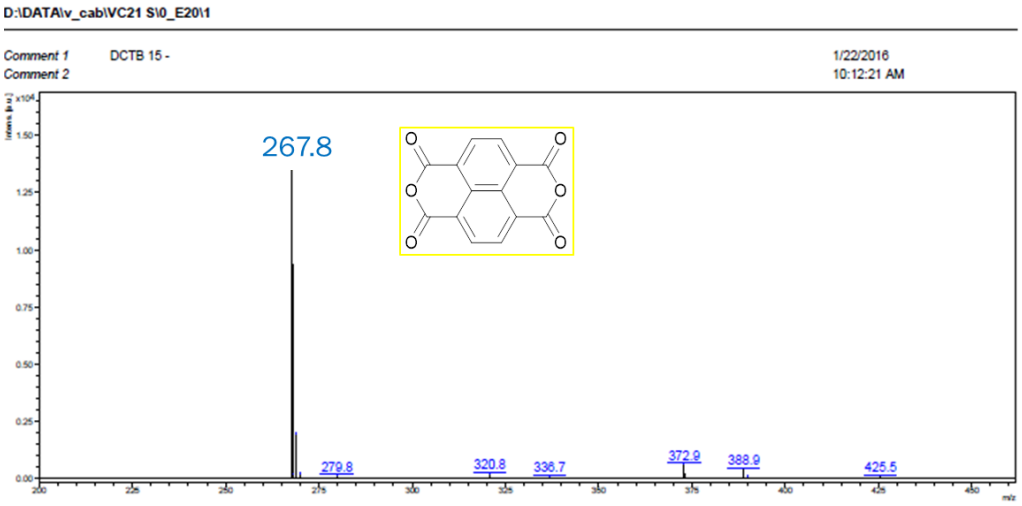

Figure 6.10: MALDI-TOF of NDA.

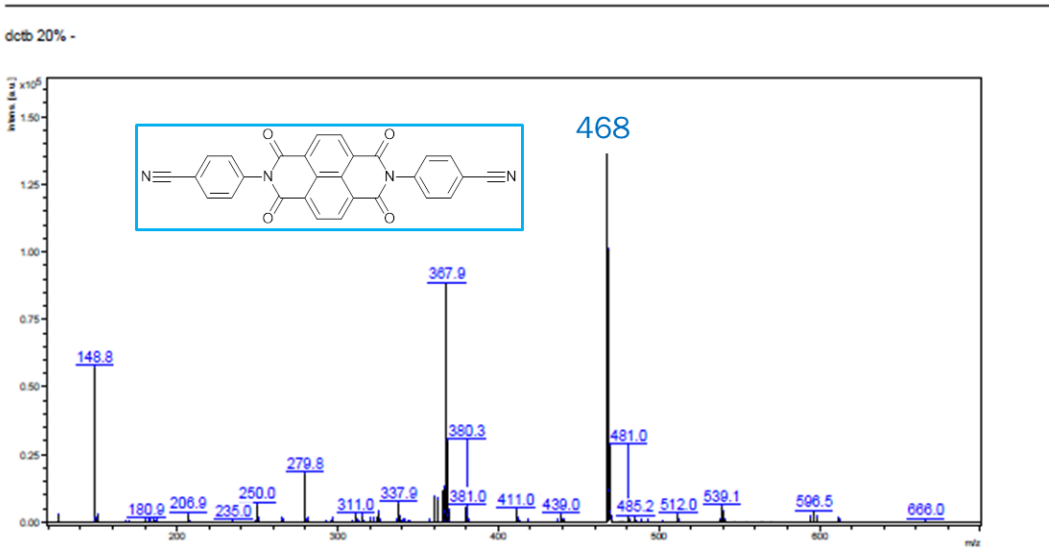

Figure 6.11: MALDI-TOF of DBNDI

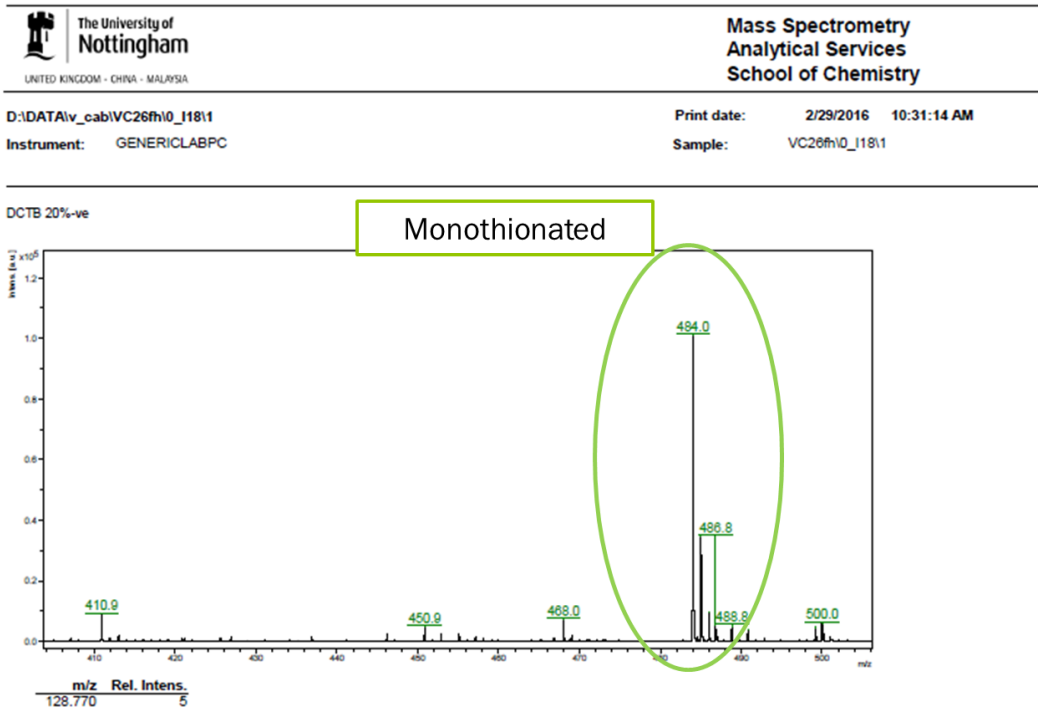

Figure 6.12: MALTI-TOF of the monothionated DBNDI

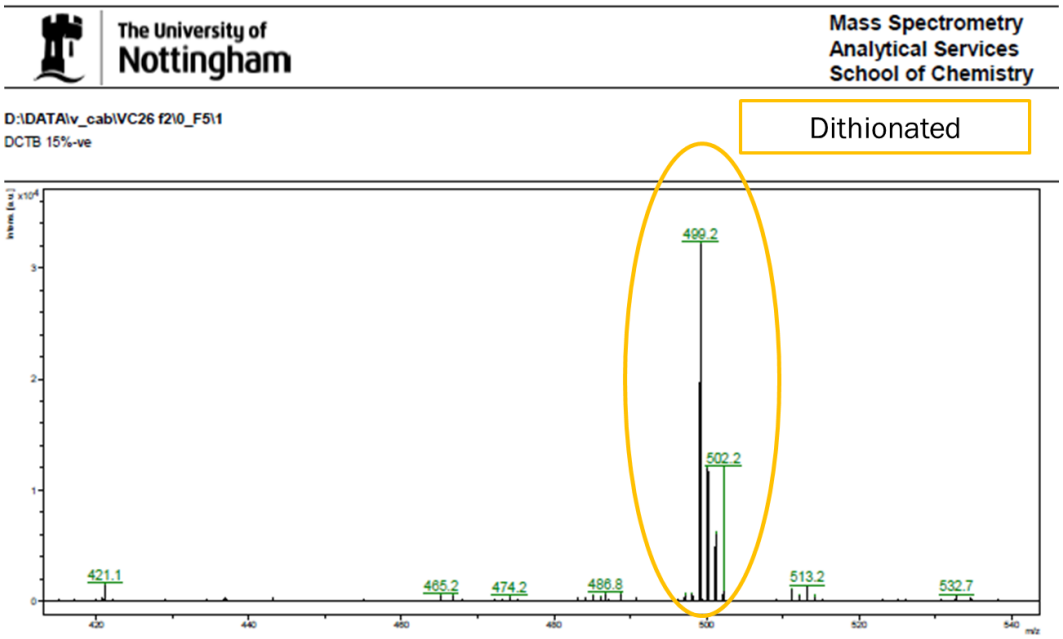

Figure 6.13: MALDI-TOF of dithionated DBNDI

6.6 References

1. Würthner, F., Perylene bisimide dyes as versatile building blocks for functional supramolecular architectures. *Chemical communications* **2004,** (14), 1564-1579.

2. Bhosale, S. V.; Jani, C. H.; Langford, S. J., Chemistry of naphthalene diimides. *Chemical Society Reviews* **2008,** *37* (2), 331-342

3. Würthner, F.; Stolte, M., Naphthalene and perylene diimides for organic transistors. *Chemical Communications* **2011,** *47* (18), 5109-5115.

4. Kobaisi, M. A.; Bhosale, S. V.; Latham, K.; Raynor, A. M.; Bhosale, S. V., Functional Naphthalene Diimides: Synthesis, Properties, and Applications. *Chemical Reviews* **2016,** *116* (19), 11685-11796.

5. Nicholas Pearce, Thionation of Asymmetric Rylene Diimides.

6. Bauscher, M.; Mäntele, W., Electrochemical and infrared-spectroscopic characterization of redox reactions of p-quinones. *The Journal of Physical Chemistry* **1992,** *96* (26), 11101-11108.

7. Würthner, F.; Ahmed, S.; Thalacker, C.; Debaerdemaeker, T., Core-Substituted Naphthalene Bisimides: New Fluorophors with Tunable Emission Wavelength for FRET Studies. *Chemistry–A European Journal* **2002,** *8* (20), 4742-4750.

8. Bhosale, S.; Sisson, A. L.; Talukdar, P.; Fürstenberg, A.; Banerji, N.; Vauthey, E.; Bollot, G.; Mareda, J.; Röger, C.; Würthner, F., Photoproduction of proton gradients with π-stacked fluorophore scaffolds in lipid bilayers. *Science* **2006,** *313* (5783), 84-86.

9. Gibson, G. L.; McCormick, T. M.; Seferos, D. S., Effect of Group-14 and Group-16 Substitution on the Photophysics of Structurally Related Donor–Acceptor Polymers. *The Journal of Physical Chemistry C* **2013,** *117* (32), 16606-16615.

10. Lévesque, S.; Gendron, D.; Bérubé, N.; Grenier, F. o.; Leclerc, M.; Côté, M., Thiocarbonyl Substitution in 1, 4-Dithioketopyrrolopyrrole and Thienopyrroledithione Derivatives: An Experimental and Theoretical Study. *The Journal of Physical Chemistry C* **2014,** *118* (8), 3953-3959.

11. Melon-Ksyta, D.; Orzeszko, A.; Borys, W.; Czupryński, K., Synthesis and liquid crystalline properties of monothio-and dithioimides with chiral N-substituents. *Journal of Materials Chemistry* **2002,** *12* (5), 1311-1315.

12. Tilley, A. J.; Pensack, R. D.; Lee, T. S.; Djukic, B.; Scholes, G. D.; Seferos, D. S., Ultrafast Triplet Formation in Thionated Perylene Diimides. *The Journal of Physical Chemistry C* **2014,** *118* (19), 9996-10004.

13. 9 J. Quinn, Y. Z., Z. Chen, H. Usta, C. Newman, H. Yan and A. Facchetti, US Pat., 062 365, 2010.

14. Sheldrick, G. M., Crystal structure refinement with SHELXL. *Acta Crystallographica Section C: Structural Chemistry* **2015,** *71* (1), 3-8.

15. Dolomanov, O. V.; Bourhis, L. J.; Gildea, R. J.; Howard, J. A.; Puschmann, H., OLEX2: a complete structure solution, refinement and analysis program. *Journal of Applied Crystallography* **2009,** *42* (2), 339-341.

16. Liao, J.-Z.; Dui, X.-J.; Zhang, H.-L.; Wu, X.-Y.; Lu, C.-Z., Polyoxometalate anion–π interaction-directed assembly of a three-dimensional hydrogen-bonded supramolecular framework with nanoscale porosity. *CrystEngComm* **2014,** *16* (46), 10530-10533

17. Leong, C. F.; Chan, B.; Faust, T. B.; Turner, P.; D'Alessandro, D. M., Electronic, optical, and computational studies of a redox-active napthalenediimide-based coordination polymer. *Inorganic chemistry* **2013,** *52* (24), 14246-14252.

18. Mastalerz, M.; Oppel, I. M., Rational construction of an extrinsic porous molecular crystal with an extraordinary high specific surface area. *Angewandte Chemie International Edition* **2012,** *51* (21), 5252-5255.

19. Fang, X.; Yuan, X.; Song, Y.-B.; Wang, J.-D.; Lin, M.-J., Cooperative lone pair–π and coordination interactions in naphthalene diimide coordination networks. *CrystEngComm* **2014,** *16* (38), 9090-9095.

20. Wang, J.; Luo, J.; Luo, X.; Zhao, J.; Li, D.-S.; Li, G.; Huo, Q.; Liu, Y., Assembly of a three-dimensional metal–organic framework with copper (I) iodide and 4-(pyrimidin-5-

yl) benzoic acid: controlled uptake and release of iodine. *Crystal Growth & Design* **2015,** *15* (2), 915-920.

21. Luo, X.; Sun, L.; Zhao, J.; Li, D.-S.; Wang, D.; Li, G.; Huo, Q.; Liu, Y., Three Metal–Organic Frameworks Based on Binodal Inorganic Building Units and Hetero-O, N Donor Ligand: Solvothermal Syntheses, Structures, and Gas Sorption Properties. *Crystal Growth & Design* **2015,** *15* (10), 4901-4907.

22. Hou, Q.; Jia, M.-J.; Zhao, J.-J.; Jin, J.; Yu, J.-H.; Xu, J.-Q., Two new 3-D photoluminescence metal–organic frameworks based on cubane Cu 4 I 4 clusters as tetrahedral nodes. *Inorganica Chimica Acta* **2012,** *384*, 287-292.